Imperial College London

EFFECT OF AGE AND SPECIES ON BLOOD FLOW PATTERNS AT ARTERIAL BRANCHES IN RELATION TO ATHEROSCLEROSIS

A THESIS SUBMITTED TO THE

UNIVERSITY OF LONDON FOR THE

DEGREE OF DOCTOR OF PHILOSOPHY

Andrew Richard Bond

September 2007

Abstract

The location of atherosclerotic lesions around arterial branches changes with age in rabbits; this is thought to reflect a change in the pattern of haemodynamic shear stress (frictional force per unit area) exerted by the flow of blood on the arterial wall. Lesions around branches in mice do not change location significantly with age and have a more uniform distribution around the branch ostium. The discrepancy may reflect the presence of different flow patterns from those in the rabbit. Endothelial cells (EC) and their nuclei (ECn) elongate with increased shear stress and align with mean flow direction. They were used to assess flow patterns in mice and rabbits of different ages. Techniques were developed to a) image EC and ECn, without imaging nuclei from underlying tissue, using confocal microscopy, and through the development of a modified Häutchen ("EStAR") technique, b) analyse the morphology of the cells and nuclei, and c) produce spatially accurate maps of cell and nuclear dimension and alignment for regions around intercostal branch ostia. Significant differences were found in the elongation of EC and ECn around branches, and significant changes occurred with age, in the rabbit. In mice, however, there were fewer differences around ostia and no significant change with age. A triangular arterial cushion surrounded the upstream part of most ostia in mice, and nuclear orientations suggested blood flow was being diverted around this cushion and the ostium. Orientations in rabbits were consistent with blood being drawn into the ostium from surrounding regions. They were also consistent with helical flow down the aorta. Our data suggest that shear stress patterns around branch ostia differ between species, and that in rabbits they reverse with age. These findings correlate with changes in lesion distribution between ages and species, but contradict current theories about lesion development and shear stress.

Publications and Awards

Publications

- Bond AR & Weinberg PD. Variation in blood flow patterns around arterial branches with age. *Heart* 2007; 93: e2 (Abstract)

- Bond AR. Variation in blood flow patterns around arterial branches with age. *The Bulletin (of the BSCR)* 2007; 20: 13-15

- Bond AR & Weinberg PD. Haemodynamic stresses and wall structure can account for the pattern of lipid deposition around aortic branches in mice. *Atherosclerosis* 2006; Suppl 7:200 (Abstract)

Awards

- British Society for Cardiovascular Research Young Investigator Award 2006

- First Prize – Poster competition at the Third Physiological Flow Meeting, Oxford, UK, April 2006. Physiological Flow Network

Acknowledgements

I would like to thank all the following people, without whom this would not have been possible:

A huge thank you to Ali for being there through all the highs and lows, motivating me through to the end, listening to my moaning, and just being there when I needed her the most.

Dr. Peter Weinberg for his expert guidance and support throughout this project.

Stephen Pountney at the University of Reading for his assistance with confocal microscopy.

Dr. Rini de Crom for supplying eNOS-GFP mice

Dr Chris Jackson at the Bristol Heart Institute, University of Bristol, for providing the silver staining technique.

Dr Mike Toscano, University of Bristol, for supplying the pig aortas (and being an excellent house mate).

I would like to thank all the past and present members of the PDW group for their help and support throughout the whole of this project.

Thank you to Sophie, Michael, Sarah, Chris, Nina, Steph, Melina, and Marzena for providing the comfiest beds, floors and sofas in the whole of London.

Thanks to my family for their support and at least pretending to understand what I've been doing for the past few years.

Finally, we are extremely grateful to the British Heart Foundation for funding this project.

Table of Contents

List of Figures

Chapter 1

Chapter 2

List of Tables

Abbreviations

AC	Arterial Cushion
$AgNO_3$	Silver nitrate
AO	Acridine Orange
ApoE	Apolipoprotein E
BAEC	Bovine aortic endothelial cells
CCD	Charge couple device
CHD	Coronary heart disease
CFD	Computational Fluid Dynamics
CT	Computed tomography
CVD	Cardiovascular disease
D	Downstream
EBA	Evans Blue Albumin
ECM	Extracellular matrix
ECn	Endothelial cell nuclei
EC(s)	Endothelial cell(s)
EL(s)	Endothelial Layer(s)
eNOS	Endothelial nitric oxide synthase
eNOS-GFP	Endothelial nitric oxide synthase-Green fluorescent protein
EStAR	Endothelial stick and rip
GPCR	G-protein coupled receptors
Hb	Haemoglobin
HDL	High density lipoprotein
HRP	Horseradish peroxidise
JAM	Junctional adhesion molecule
L	Left
LDL	Low density lipoprotein
L-NMMA	N^{ω}-monomethyl-L-arginine
LW	Length to width ratio
MAPK	Mitogen-activated protein kinases
MCP-1	Monocyte chemotactic protein-1
MF(s)	Microfilament(s)

MRI	Magnetic Resonance Imaging
MTOC	Microtubule organising centre
NO	Nitric Oxide
NZW	New Zealand White
PBS	Phosphate Buffered Saline
PCP	Planar cell polarity
PECAM-1	Platelet endothelial cell adhesion molecule
PI	Propidium Iodide
R	Right
RNase	Ribonuclease
SMCn	Smooth muscle cell nuclei
SMC(s)	Smooth muscle cell(s)
TGF-β	Transforming growth factor-β
TIFF	Tagged-image file format
U	Upstream
VCAM-1	Vascular cell adhesion molecule-1
VEGF	Vascular endothelial growth factor
VLDL	Very low density lipoprotein
WT	Wild-type
ZO-1	Zonula occludens-1

Chapter 1: Main Introduction

1.1 Why study atherosclerosis?

Heart disease is the world's biggest killer, causing one in three deaths, and affecting both men and women (World Heart Organisation, 2000). Cardiovascular disease (CVD) is the broad term used to describe coronary heart disease (CHD, i.e. myocardial infarction), strokes (cerebral infarction and haemorrhages) and all other disease of the circulatory system (i.e. peripheral arterial disease). In the UK alone in 2004, CVD was the cause of 216,000 deaths (37%), 60,000 of which were premature (deaths before the age of 75). Overall it is estimated to cost the UK economy approximately £26 billion (British Heart Foundation, 2004). The underlying cause of much CVD is atherosclerosis.

1.2 What is atherosclerosis?

Atherosclerosis is a chronic inflammatory disease that affects medium and large systemic arteries (Cai *et al.*, 2002), and is thought to be the main contributor to the pathogenesis of myocardial and cerebral infarction, gangrene and loss of function of the extremities (Ross, 1993). In healthy arteries, blood flows around the body supplying the organs with oxygenated blood, thus maintaining a fully functional system. However, in atherosclerosis the flow of blood can be seriously compromised. This is predominantly due to the thickening of the intima of the arterial walls, caused by the build up of fatty deposits and other components within the wall. A number of pathogenetic processes can all be involved in the initiation and progression of atherosclerotic lesions and shall be discussed in detail later. These include macrophage foam cell formation and death, accumulation of extracellular lipid, chronic inflammation, and formation and transformation of haematoma and thrombus to fibromuscular tissue (Stary, 2000).

1.3 Why should we be concerned about atherosclerosis?

Atherosclerosis itself does not always cause death. In the earlier stages, the blood vessel can remodel to maintain its lumen diameter and counteract the intimal thickening (Ward *et al.*, 2000). If the lumen does get smaller, the flow of oxygenated blood to the organs gets restricted leading to e.g. angina (heart pain). However, more significant problems occur if the atherosclerotic lesion develops a fibrous plaque (advanced lesion) that ruptures. This exposes the blood to components of the wall and may lead to thrombus

(blood clot) formation which may further impinge on the flow of blood. It has been suggested that a thrombus over an atherosclerotic plaque in the carotid arteries can reduce blood flow downstream of the thrombus to less than 10% of its normal volume (Levick, 2003). In the worst case scenario, the thrombus may embolise and become lodged in the smaller arteries completely occluding flow. If this occurs in the carotid arteries it can trigger strokes or even death, and if it occurs in the coronary arteries it can lead to a myocardial infarction.

1.4 Types of lesions

Current theory suggests there are two broad lesion groups, early and advanced (or raised) lesions. Using current technology it is not possible to track arterial disease accurately within the same patients, so it is unknown whether later lesion types are a development of early lesions, or whether they are actually a totally new disease. Early lesions are present in everyday life, even without the influence of external risk factors, and are thought to be a protective response to potential damage to the endothelium and underlying smooth muscle cells (SMC) of the arteries, by the migration of monocytes and T-lymphocytes between the endothelial cells (EC). This takes place under the influence of growth-regulatory molecules and chemo-attractants (Ross, 1993). The American Heart Association (AHA) (Stary et al., 1994, Stary et al., 1995) has further classified lesion types depending on their histological characteristics. Lesions are designated by Roman numerals (I-VI), which give an indication of the usual sequence of lesion development and progression. Lesion types I and II are the early lesions and generally are the only types found in children and infants, although they can also occur in adults, type III are intermediate lesions (preatheroma) and evolve soon after puberty, and lesion types IV, V and VI are advanced lesions. Type I to III lesions are thought of as clinically silent and are always relatively small (Stary, 2000).

1.4.1 Type I lesions

Type I lesions, or initial lesions, contain atherogenic lipoproteins in large enough quantities to cause an increase in macrophages and formation of scattered macrophage foam cells. They are the first microscopically detectable lesion type, however they may still be undetectable to the naked eye (Stary *et al.*, 1994).

1.4.2 Type II lesions

Type II lesions consist primarily of macrophage foam cells, as in type I lesions, but also contain lipid-laden SMC, and due to this they are also named 'fatty streaks'. Historically the fatty streak was named and identified by its gross appearance. T-lymphocytes have also been observed in these lesions although they are not as numerous as macrophages (Stary et al., 1994, Stary et al., 1995). Virmani *et al* (2000) proposed the term "intimal xanthoma" instead of fatty streak, as xanthoma is a general pathological term that describes focal accumulations of fat-laden macrophages.

1.4.3 Type III lesions

Type III lesions apply solely to lesions that form the bridging gap between clinically silent early lesions and advanced lesions, both morphologically and chemically. They contain in addition to the lipid-laden cells of type II, scattered collections of extracellular lipid droplets and particles that separate and disrupt the layers of intimal SMC (Stein and Stein, 2001).

1.4.4 Type IV lesions

Type IV lesions, or atheroma, are the first lesion type considered to be advanced by histological criteria because of their dense lipid core. Lipid cores thicken the artery wall and are generally large enough to be visible to the naked eye when the cut surface is examined. Between the lipid core and the endothelial surface, the intima contains macrophages and SMC with and without lipid droplet inclusions, lymphocytes and mast cells (Stary *et al.*, 1995).

1.4.5 Type V lesions

If a lesion progresses to a type V lesion then it can be termed atherosclerosis, or an atherosclerotic plaque. These lesions are recognised when prominent new fibrous connective tissue has formed, referred to as a fibroatheroma, which may cause arteries to become narrower, generally to a greater extent than with type IV lesions, and develop fissures, hematoma, and or thrombus, and are therefore clinically significant.

1.4.6 Type VI lesions

The final types of lesions are referred to as complicated lesions as they contain one or more of either disruptions to the lesion surface, hematoma or hemorrhage, and thrombotic deposits (Stary *et al.*, 1995).

1.5 Risk Factors for atherosclerosis

The exact mechanism(s) behind the formation of atherosclerotic lesions are unknown, hence the reason for the large amount of ongoing research in this field. Numerous risk factors for the disease have been identified, many of which are common to most CVD. These include modifiable factors such as hypercholesterolemia, hypertension, diabetes mellitus, obesity, smoking, physical inactivity, and blood viscosity (Levick, 2003). However, there is also a group of non-modifiable risk factors that include age, male gender, a family history of CHD, and the menopause (Eriksson, 2002).

1.6 Methods for detecting sites susceptible to lesion formation

Sites susceptible to the formation of atherosclerotic lesions can be determined by looking at the permeability of the endothelium, and infiltration of fatty deposits into the arterial wall. A method commonly used to detect sites of altered permeability is to use Evans Blue Albumin (EBA) as a circulatory tracer, since once transported across the wall it permanently stains sites of uptake blue. Quantifying the concentration of EBA in the wall when viewed using digital imaging fluorescence microscopy can determine the rate of uptake (Chuang et al., 1990, Lin et al., 1990, Patterson et al., 1992, Lin, 1996). Rhodamine-labelled albumin (Staughton *et al.*, 2001), radio-labelled low density lipoprotein (125I-LDL) (Truskey *et al.*, 1992) and labelled horseradish peroxidase (HRP) (Chuang *et al.*, 1990) are also used in permeability studies as they too can be detected, quantified and mapped. Techniques available for detecting lesions are intravascular ultrasound (*in vivo*) (Frimerman et al., 1999, Chandran et al., 2003), and oil red O to detect lipid within lesions in *ex vivo* tissue (Barnes and Weinberg, 1998, Kratky *et al.*, 1993).

1.7 The Location of Lesions

Lesions do not occur randomly in the vasculature, but are localized at bends, bifurcations and T-junctions (Asakura and Karino, 1990). Using the methods previously mentioned, the location of atherosclerotic lesions has been further elucidated. One important feature of atherosclerosis is that it occurs in systemic arteries but not in veins or pulmonary arteries. This suggests that hemodynamic factors, wall properties and pressure play a pivotal role in lesion formation as both vessel types are exposed to blood with comparable chemical constituents (e.g. plasma, white and red blood cells), lipid composition, and viscosity, although gaseous concentrations will vary. In 1969, Caro (Caro *et al.*, 1969) predicted that fatty streaking would occur at areas with relatively thick fluid dynamic boundary layers (the region of fluid near the wall that is affected by viscous interaction with the wall) i.e. the outer walls of daughter vessels, and that a new boundary layer would develop in the parent vessel downstream of the flow divider and be expected to inhibit atheroma development. Caro's results for post-mortem human tissue showed that the inner wall of the vessel (a, Fig. 1.1), where shear stress (which shall be discussed later) is greater, is much less affected than the other walls, particularly the outer.

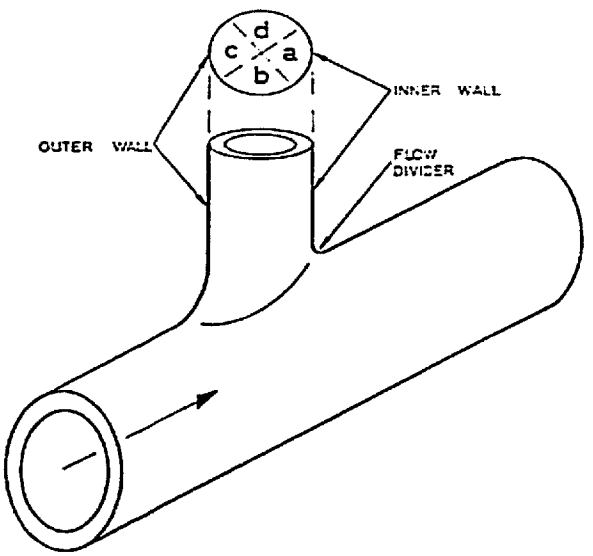

Fig. 1.1. Schematic geometry of a large branch, showing nomenclature. Arrow indicates direction of flow (Caro *et al.*, 1969).

Work carried out by Anitschkow and colleagues ((Anitschkow, 1933), cited in (Weinberg, 2004)) was the first to draw attention to the non-uniform distribution of lipid deposition in the cholesterol fed-rabbit aorta. They showed that lesions occur downstream and to the sides of aortic branch ostia in an arrowhead pattern with the tip being oriented downstream, whilst regions upstream of the ostia were spared. In the 1960's, examination of lipid deposition in human autopsy tissue (Mitchell and Schwartz, 1965) suggested that the cholesterol-fed rabbit model of atherosclerosis was flawed since a totally different pattern of deposition was observed in which the downstream triangle region was highly resistant to disease.

The discrepancy could be partly accounted for following the observation that young humans (foetuses, neonates and infants) develop disease in the characteristic downstream arrowhead pattern (Fig. 1.2) (Sinzinger *et al.*, 1980) previously observed by Anitschkow; the size of lesion increasing as age increases. This led to the suggestion that age was a crucial factor in the location of lesions, and that if rabbits and humans of comparable ages were compared a similar pattern would be observed.

Spontaneous lipid deposition, detected by staining with oil red O in New Zealand White (NZW) rabbits was observed in a triangular pattern downstream of the intercostal branch ostia at weanling age; in mature rabbits the downstream triangle had the lowest distribution of disease - lesions generally occurred along axes either side of the triangle and at lateral and upstream margins of the ostium (Fig. 1.3) (Barnes and Weinberg, 1998). The same study also showed that surrounding the ostia of celiac branches, disease occurred downstream of branches in young rabbits (although the prevalence was low), but occasionally was found on the upstream lip of the flow divider. The young disease pattern was accentuated in old rabbits, but additionally there was a greater incidence of disease upstream of the branch.

As already reported by Anitschkow, a downstream triangle pattern of lipid deposition was seen in young cholesterol-fed rabbits by Ivey *et al* (Ivey *et al.*, 1995), with the tip of the triangle extending further downstream up to 6 months old. However, in mature

cholesterol-fed rabbits, lesions have been observed in different locations, with the downstream region being spared (Barnes and Weinberg, 1999).

To determine what causes the switch in disease pattern with age, studies looking at the transport properties of the aortic wall around branch points have been carried out. Albumin labelled with a fluorescent dye was introduced into the circulation of young and old rabbits fed a standard diet. Initial studies allowed the albumin to circulate for three hours (Sebkhi and Weinberg, 1994) to enable a quasi-steady state uptake to be reached, where the level of albumin in the arterial wall will be similar to that of native macromolecules. The aorta was fixed *in situ* and sections taken through the tissue and the fluorescence measured and quantified around the ostia. In young rabbits the net uptake by the intima-media was higher downstream of ostia than upstream, but as animals aged this difference decreased and then reversed. The average uptake of the tracer by upstream and downstream regions was higher shortly after the rabbits were weaned, than at later ages.

Later studies allowed fluorescent labelled albumin to circulate for only 10 minutes before fixing the tissue (Ewins *et al.*, 2002). This enables the influx alone to be measured as there is not enough time for efflux out of the wall to be significant, and shows how easily the macromolecule can travel into the wall. Again, following quantification of the fluorescence, it was shown that in young rabbits influx was greatest in a triangular region downstream of ostium, in a small patch displaced laterally from the ostium, and upstream of the branch along its longitudinal midline. Old rabbits had low influx downstream of the branch, except on the flow divider lip, and high influx upstream of the branch (away from the midline) and in a continuous streak at the lateral regions of the ostia. The mature pattern of influx was generally more uniform than for immature rabbits.

Four distinct patterns have been observed in various species around intercostal branch ostia that seem to show the progression of lesions with age (reviewed in Weinberg, 2002). A downstream arrowhead pattern seen in infancy (human, Fig. 1.2 (Sinzinger *et al.*, 1980) and rabbit, Fig 1.3 (Barnes and Weinberg, 1998)) develops, via a lateral

pattern (human, Fig. 1.4a (Sloop *et al.*, 1998), spontaneous (Barnes and Weinberg, 1998) and cholesterol-induced rabbits (Barnes and Weinberg, 1999)), into an upstream streak in adulthood (humans, Fig. 1.4b (Sloop *et al.*, 1998) and mature cholesterol-fed minipigs (Cornhill *et al.*, 1985)), before finally becoming a raised lesion (resembling a volcano) in old age (humans, Fig. 1.4c) (Mitchell and Schwartz, 1965)). A similar "volcano" distribution is also seen in low density lipoprotein (LDL) receptor/apolipoprotein E double knockout mice, which are known to develop fibroproliferative lesions. The lesion distribution changes with age, although in a non-significant manner. The raised volcano-like distribution becomes slightly larger and more upstream as the animals mature (Fig. 1.5 and 1.6) (McGillicuddy *et al.*, 2001).

The location of lesions has also been shown to change with age in White Carneau pigeons (Fig. 1.7). In hatchlings, lesions occurred at the right hand side of the celiac branch ostium, but they also occurred at the left side by five months old. As the birds aged, disease became more prevalent in these areas, and also spread to the upstream regions. However, there was not a definite switch from the downstream to upstream regions as seen in other species (Richards and Weinberg, 2000).

It is important when looking at lesion location to take note of strain of animal being observed as there are notable differences. Fluorescent labelled albumin transport studies have shown that the strain of animal has important repercussions on the age at which permeability switches from the upstream to downstream pattern. In NZW rabbits, the pattern changed at 6, 21 and 42 months in Interfauna, Murex and Highgate strains respectively (Staughton and Weinberg, 2004).

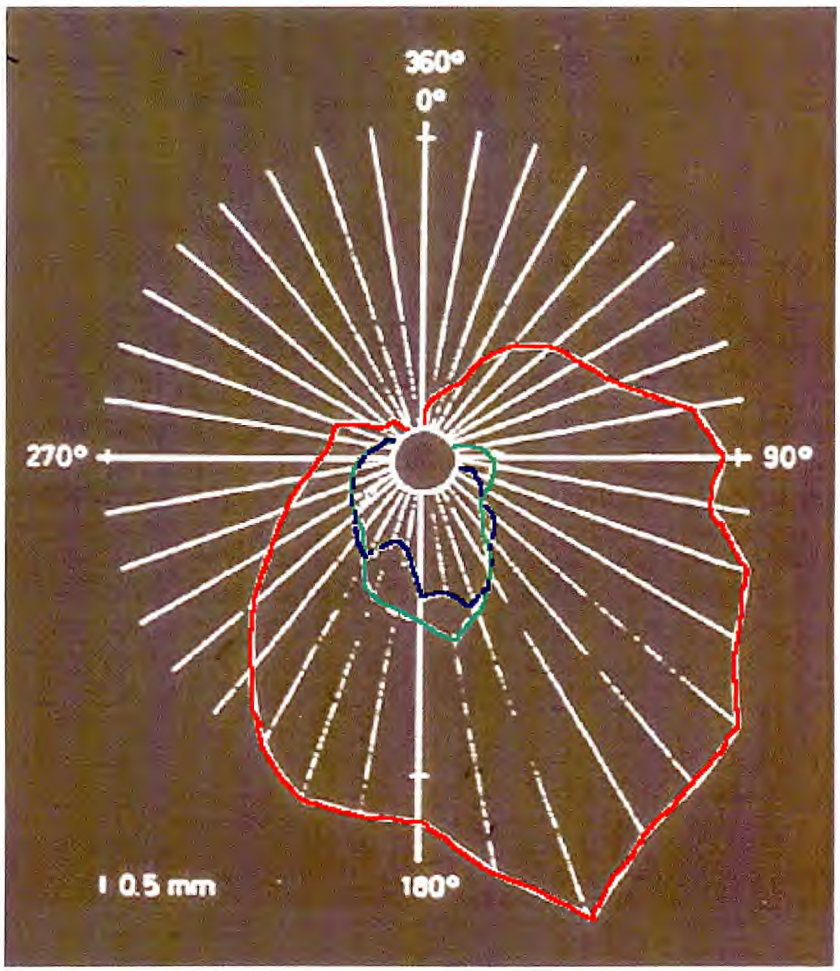

Fig. 1.2. Average lesion size around intercostal branch ostia (white circle) in young humans. Blood flow is from top to bottom. Blue = Fetus, Green = Neonate, Red = Infant. Adapted from (Sinzinger *et al.*, 1980).

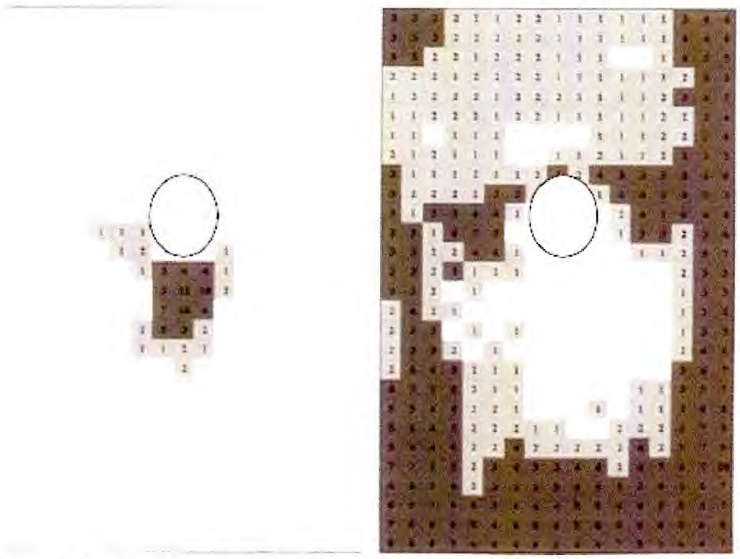

Fig. 1.3. Frequency of spontaneous disease in 6 normally-fed weanling young rabbits (left) and 10 aged (right) rabbits. Darker shading indicates higher frequency. (Barnes and Weinberg, 1998).

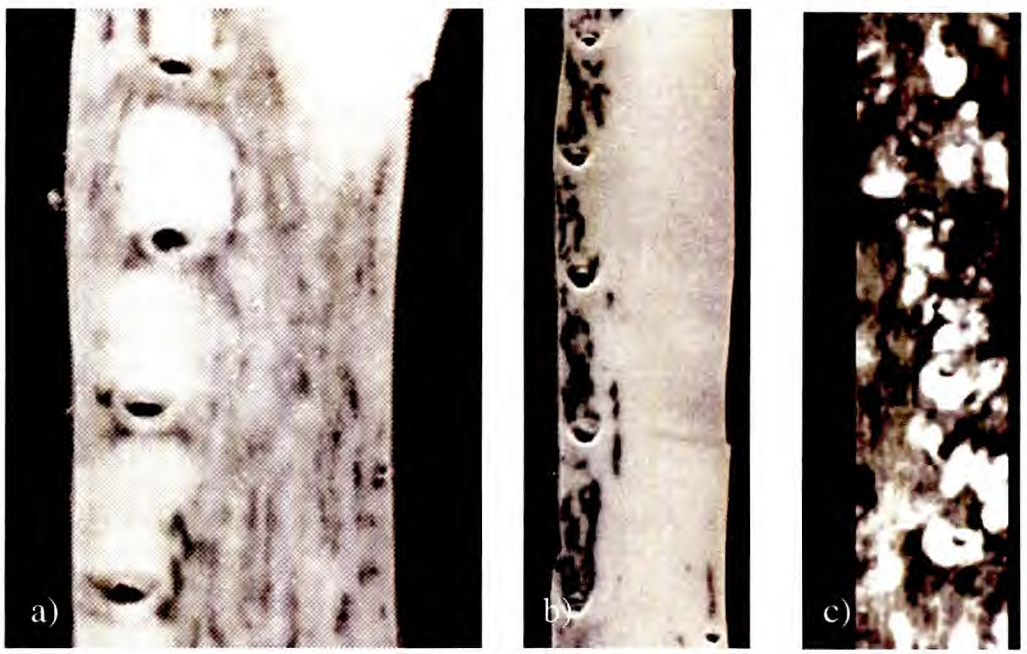

Fig. 1.4. a) Lateral disease pattern in a young adult, b) upstream streak disease pattern in an older human, c) volcano distribution in aged human. a) and b) (Sloop *et al.*, 1998), c) (Mitchell and Schwartz, 1965). In a) and b) the disease has darker staining. In c) the disease has lighter staining.

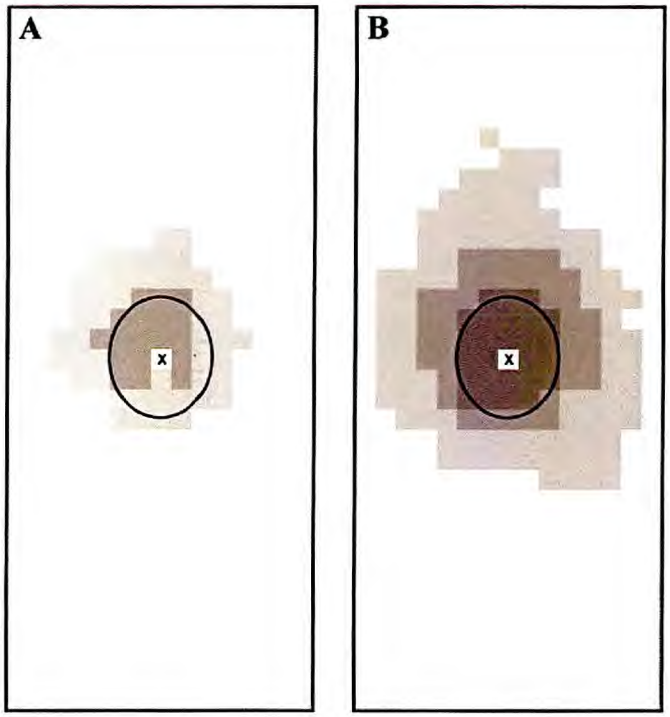

Fig. 1.5. Frequency of lipid staining around intercostal branch ostia in a) 5 young mice (9-15wks) and b) 6 aged mice (16-20wks). The maps represent a 0.7mm x 1.7mm area of aortic wall, viewed *en face*, with mean blood flow from top to bottom. The ostial centre is marked with a cross and the typical perimeter is approximated by an ellipse. Unshaded areas indicate a staining frequency <25%, and the 3 increasing levels of shading indicate frequencies of 25% to 49%, 50% to 74%, and 75% to 100% (McGillicuddy *et al.*, 2001).

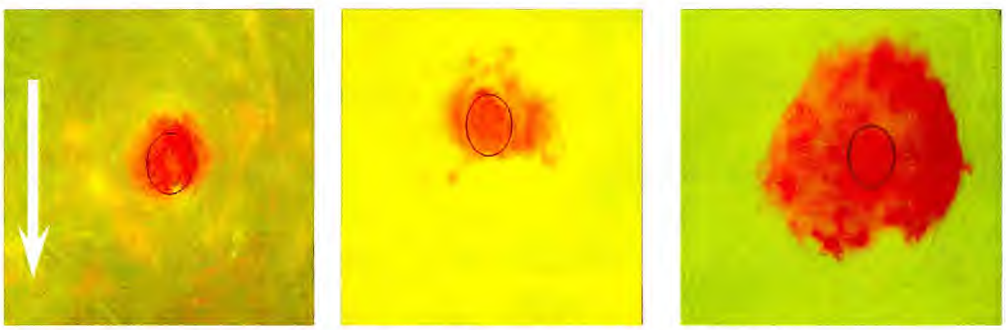

Fig. 1.6. Lipid deposition (red) around mouse aortic intercostal branch ostia stained with oil red O, viewed *en face*. Mean blood flow is indicated by the arrow and ostial perimeters are defined by an ellipse (McGillicuddy *et al.*, 2001).

Fig. 1.7. Maps showing the frequency of disease affecting the aortic wall near the branch ostium (black ellipse) of the celiac artery in White Carneau pigeons. Darker shading indicates increased disease prevalence. Mean blood flow is from top to bottom. Bar = 2mm (Richards and Weinberg, 2000).

1.8 Haemodynamics

Haemodynamics is the study of the relationship between pressure, viscous resistance to flow, and the volumetric flow rate in the cardiovascular system (Badeer, 2001). It is thought that the work of Rindfleisch, in 1872 (in Caro, 1982) first showed that there was a link between the distribution of atherosclerosis in arteries and "sites that experience the full stress and impact of the blood". It has been postulated that stresses associated with bends, bifurcations and T-junctions of arteries (Fig. 1.8) are responsible for the initiation and localization of atherosclerosis (Asakura and Karino, 1990). The flows near these structures, and in areas of non-planar curvature (e.g. in the aortic arch), are particularly difficult to measure accurately.

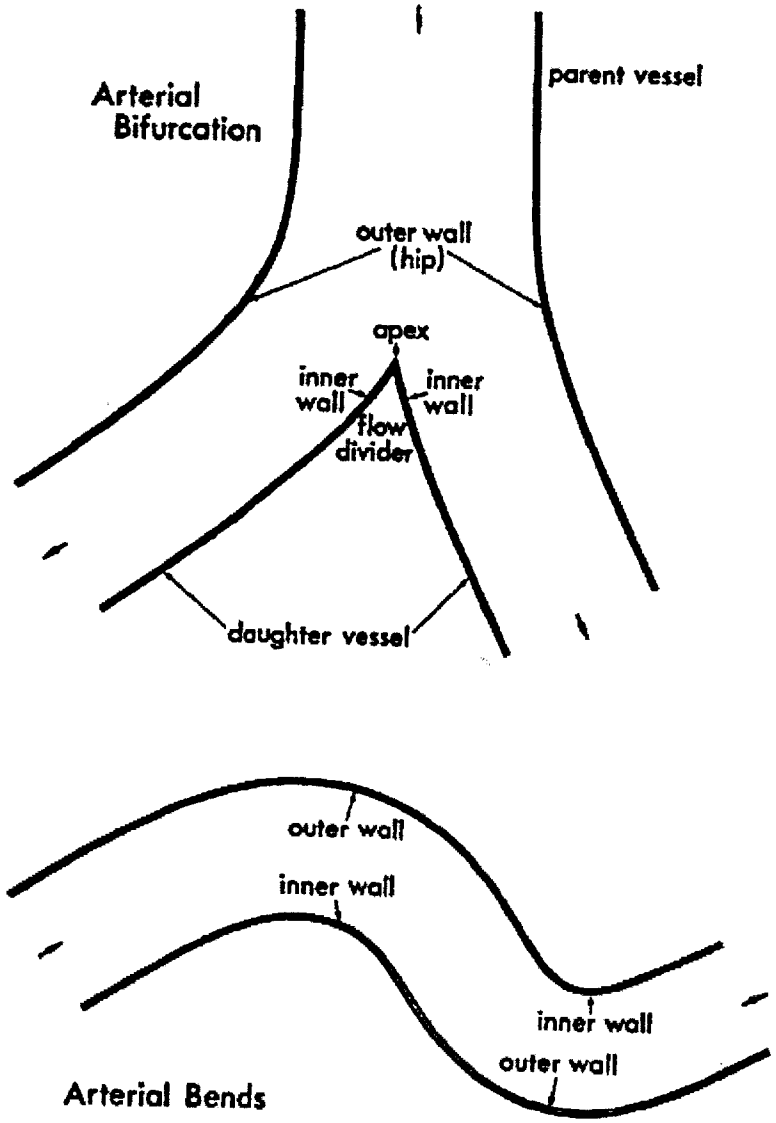

Fig. 1.8. Schematic drawings (two-dimensional representation) of an arterial bifurcation and arterial bends showing approximate anatomical locations of the inner (medial) and outer (lateral) walls used to describe locations of atherosclerotic lesions. Flow is from top to bottom of the bifurcation, and left to right of bends (Asakura and Karino, 1990).

Three different patterns of blood flow are found in blood vessels; laminar, turbulent and single-file flow. Laminar flow is found widely in arteries and in arterioles, venules and veins, and is considered further below. Turbulent flow occurs in the ventricles of the heart, in stenosed arteries and in the aortas of large species during diastole (since flow is less stable during deceleration). In contrast to laminar flow, which is smooth with

regular streamlines, turbulent flow has local, random fluctuations in the direction and magnitude of the velocity so that the streamlines are irregular and highly unsteady (Parker and Gibson, 2005). It requires more energy than streamline flow, and occurs in straight pipes when the Reynolds' number exceeds approximately 2000 (Badeer, 2001). The Reynolds' number (Re) is calculated as follows (eFunda, 2003):

$$\text{Reynolds' number} = \frac{\rho V D}{\mu}$$

ρ = fluid density

V = free stream fluid velocity

D = pipe diameter

μ = fluid viscosity (dynamic)

and can be considered as the ratio of inertial to viscous forces. Turbulent flow is not of importance at Reynolds numbers appropriate for the species studied in this thesis. Single-file flow is confined to the capillaries and shall not be discussed further (Levick, 2003).

Steady, laminar (or streamline) flow, in which an incompressible fluid moves as a series of layers, in a straight rigid tube of circular cross-section, will have a velocity profile that is parabolic when fully developed (so-called Poiseuille flow). Molecules immediately adjacent to the wall do not move at all (the no-slip condition) and those in the centre move fastest (Fig. 1.9). Once this state is reached, there will be no further change in the flow profile down a uniform unbranched tube.

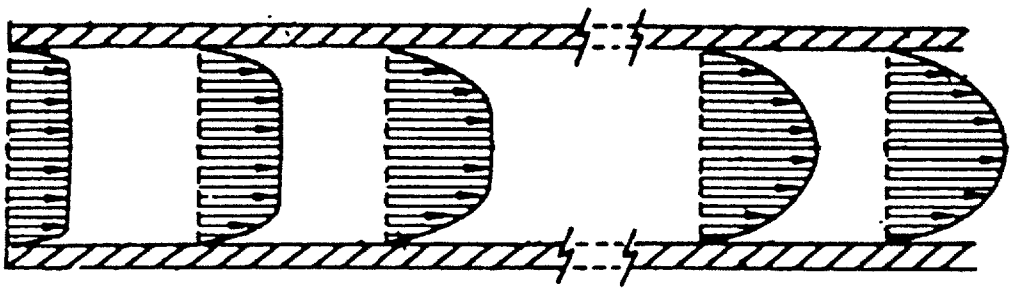

Fig. 1.9. Two-dimensional, steady parabolic flow down a straight rigid tube with a circular cross-section. Flow is from left to right. Arrows represent fluid velocity vectors (Adapted from Caro *et al* (1985)).

In the arterial system it is rare to find a uniformly straight, unbranched section of artery. At every bifurcation in the circulatory system the velocity profile of the blood is temporarily altered. For blood to change direction and enter a daughter branch there must be an acceleration of the fluid in the direction of curvature. For there to be acceleration, there must be a pressure gradient acting on the fluid in the direction of acceleration. As the fast-moving blood in the centre of the artery approaches the flow divider, a pressure gradient must be set up to deflect the blood into the branch. It has been postulated that the slower-moving fluid will be drawn into the branch near the wall and a new boundary layer will develop on the flow divider (Fig. 1.10) (Caro *et al.*, 1985).

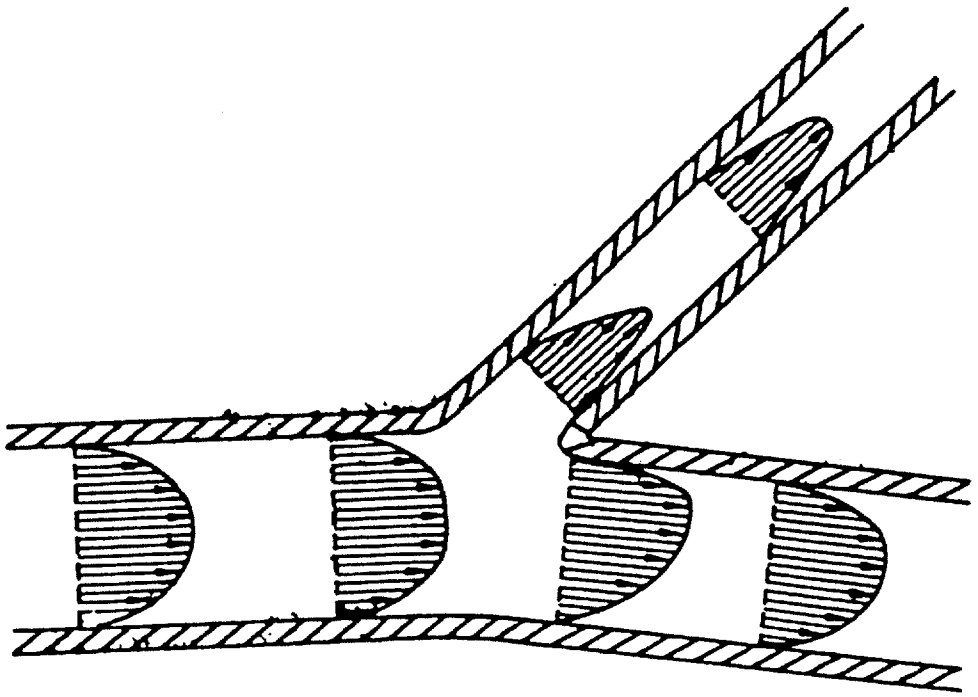

Fig. 1.10. Two-dimensional, steady parabolic flow down a branching tube (blood vessel). Faster moving fluid impinges on the flow divider while the slower moving fluid occurs on the opposite walls. Flow is from left to right. Arrows represent blood velocity vectors (Caro *et al.*, 1985).

Thus at branch points in large vessels i.e. the aorta and iliac arteries, the consensus view is that the medial sides (inner walls) (Fig. 1.8) of the daughter vessels will experience higher velocities and the lateral (outer) wall will experience lower velocities than those seen in the parent vessel. This has been shown in post-mortem human arteries made transparent, mounted at *in vivo* dimensions and perfused with microspheres to visualise the flow (Asakura and Karino, 1990). It has also been shown in studies that measure the elongation of EC (discussed later) in regions of higher shear stresses (Okano and Yoshida, 1993). The work presented later in this thesis will show that this is not always correct.

If the fluid velocity is large enough, an adverse pressure gradient may be established that can cause a region of flow separation and recirculation at the outer wall of the bifurcation (Caro *et al.*, 1985, Dewey, 2002) (Fig. 1.11).

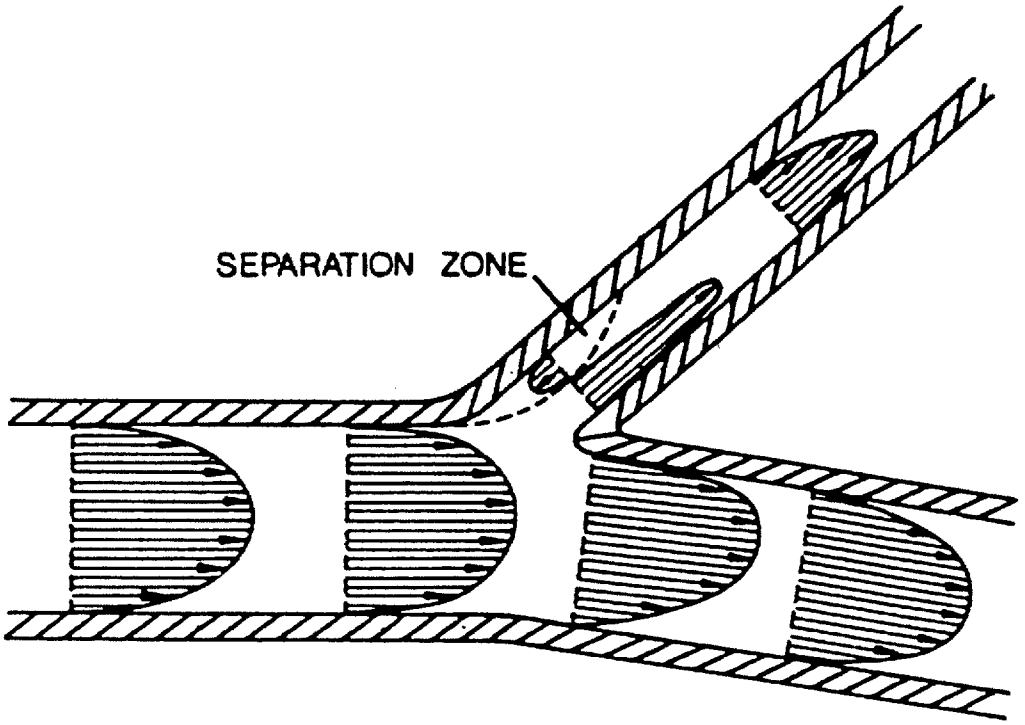

Fig. 1.11. Two-dimensional steady parabolic flow down a branching tube (blood vessel). If the fluid velocity is large enough, a region of flow separation may occur on the outer wall of the bifurcation. Flow is from left to right. Arrows represent blood velocity vectors (Caro *et al.*, 1985).

Even under these conditions, there would still be slower flow on the outer wall, than on the flow-divider.

If the flow were to be reversed in Fig. 1.8 and the blood from the daughter vessels were to flow into the parent vessel, as in the venous system, then higher velocities would initially occur nearer the walls and lower velocities in the centre of vessels, which is in effect the reverse of Poiseuille flow (LaBarbera, 1990).

1.9 What is shear stress?

Fluid shear stress (τ), measured in Pascals (Pa) or dynes/cm^2 (dyn/cm^2 = Pa x 10), is defined as the tractive force produced by a moving viscous fluid (blood) on a solid body (vessel wall, in particular the endothelium) constraining its motion (Dewey *et al.*, 1981). The magnitude of shear stress increases as the velocity and viscosity increase. It can be calculated using the equation:

$$\text{Shear stress} = \mu \frac{\delta v}{\delta z}$$

$\frac{\delta v}{\delta z}$ is the velocity gradient (s^{-1})

μ = fluid viscosity (gm/cm-s)

Reported values for shear stress vary greatly, depending on location e.g. arteries or veins, sampling method e.g. ultrasound, *in vivo/vitro* measurements, phase of cardiac cycle, or species. Values found in the literature show a large amount of variation, and perhaps it is this variation that is the underlying cause of the patchy nature of atherosclerosis. Average values in large human arteries have been reported as 2-20 dynes/cm^2, although it has been suggested that 30-100 dynes/cm^2 might be the average amount around branches in the vasculature ((Dewey Jr, 1979) cited in Eskin *et al.*, 1984). Stanton (1999) suggested a baseline value of 15-20 dynes/cm^2 which differs to Levesque & Nerem (1985) who suggest values range up to 100-200 dynes/cm^2 (although it is unclear which species this range refers to). Nerem & Seed (1983) suggest an average shear stress of 15 dynes/cm^2 for humans at rest. Exercise could account for the differences in shear stress, as when exercising the blood flows faster, thus increasing shear (Taylor *et al.*, 2002), therefore the overall activity of the subject may be a very important atherosclerotic factor. Other values reported are 18.7 ± 4.1 dynes/cm^2 (peak value in human carotid arteries) (Gnasso *et al.*, 1997), 8.0 ± 4.1 dynes/cm^2 (mean average WSS in human carotid arteries) (Oshinski *et al.*, 2006), and approximately 1.2 dynes/cm^2 (mean shear stress in the human abdominal aorta at the level of the diaphragm, predicted using finite element modelling) (Taylor *et al.*, 1998). Using an excised pressure fixed aorta made transparent and perfused with microspheres, Okano & Yoshida (1993) calculated shear stresses from velocity profiles. They found that the

shear stress on the leading edge of the flow divider was 132-237 dynes/cm^2 and those in the hips of the flow dividers were much lower (4-62 dynes/cm^2).

1.10 Effects of shear stress

Anomalies in plasma lipid concentration and lipid metabolism, such as those found in hypercholesterolaemia, have been seen to initiate, and help the progression of lesion formation, however this does not account for the distribution of lesions in the vasculature (Asakura and Karino, 1990). There must be another mechanism involved. Over 100 years ago it was recognised that when blood flows fast, blood vessels enlarge, and when it flows slower, they narrow (Thoma (1893) cited in (Masuda *et al.*, 2003)). It has been postulated that shear stress plays a key role in the initiation, formation and regression of atherosclerotic lesions, although the mechanisms for this are not yet fully known.

Many investigators predict that low shear stress regions have increased lipid deposition and/or develop atherosclerotic lesions (e.g. Asakura and Karino, 1990, Caro *et al.*, 1971, Gnasso *et al.*, 1997, Zarins *et al.*, 1983), however fewer implicate high shear regions (Fry, 1969). One theory is that in regions of lower shear stress blood is flowing slower over the arterial wall, and in particular the endothelium. This allows increased time for atherosclerosis causing particles i.e. LDL, to permeate across the endothelium and travel into the intima of the artery. Once in the intima, LDL can be oxidised and taken up by SMC and macrophages, which in turn become foam cells, one of the precursors for lesion development. It has been suggested that increased shear stress is actually atheroprotective as it activates the release of nitric oxide (NO) from the endothelium, having been converted from L-arginine through the action of endothelial nitric oxide synthase (eNOS). This has been shown in the carotid arteries of an eNOS-GFP (endothelial nitric oxide synthase - green fluorescent protein) transgenic mouse model having applied a shear stress modifying cast around the arteries (Cheng *et al.*, 2005). Application of the cast allows eNOS expression to be quantified in regions of increasing shear stresses (caused by decreasing the diameter of the cast). It was shown that as the shear stress increased, the fluorescence (caused by increased eNOS protein expression) also increased. Further evidence for the atheroprotective effects of NO is in smokers,

who have impaired eNOS production, and as such are more prone to developing atherosclerosis (Su *et al.*, 1998). Excessively high shear stress levels found in individuals with hypertension, atherosclerosis or Marfan's syndrome, are thought to lead to tears in the endothelium that can lead to potentially fatal conditions such as dissecting aortic aneurysms. However, it has been suggested that in healthy endothelium the stresses required to cause physical damage are beyond physiological levels (Levick, 2003).

In cholesterol-fed rabbits, early lesions develop at the flow divider of branching vessels, areas of high laminar shear stress (Cornhill and Roach, 1976). On the other hand, post-mortem studies of human subjects show a preferential development of lesions at areas of low shear stress, such as at the hips of bifurcations (Asakura and Karino, 1990, Caro *et al.*, 1969). This variation could be explained by age, because it is likely that animals used in the studies were young, whereas post-mortem tissue is likely to be from older humans.

Kratky and Roach (1987) reached the conclusion that shear stress around branch orifices of intercostal and lumbar arteries is very stable due to small amounts of flow, with few fluctuations over a 24 hour period. They suggested that flow into the celiac and mesenteric arteries is known to increase dramatically post-prandially, suggesting a less stable variation in shear stress. This again addresses the need for caution when studying the mechanisms behind lesion formation.

1.11 Methods for measuring blood flow and shear stress

It is very difficult to measure shear stresses *in vivo* under physiological conditions due to difficulties determining flow, and in particular boundary conditions, close to the arterial wall. Models can be used which give an accurate prediction of how flow develops around branches and flow dividers. The major problem that arises is how to maintain *in vivo* parameters and model distensible walls accurately. Therefore further work needs to be done to accurately determine the geometries of vessels so models can be developed, or methods need to be developed that view flow without having to remove the tissue from the body, indeed without having to open the body cavity at all. Models have been

developed that make the pressure fixed arterial wall transparent, allowing the flow to be observed directly either by injecting very small (0.08-0.3mm diameter) polystyrene microspheres (Asakura and Karino, 1990, Fukushima *et al.*, 1985), coloured dyes, bubbles of hydrogen, or aluminium particles (cited in Levesque *et al.*, 1986). However, it is not known how the procedure for making arteries transparent (alcohol dehydration followed by immersion in methyl salicylate (oil of wintergreen) containing ethanol) affects wall properties such as distensibility, and how this will change flow profiles. Intravascular Doppler velocimeters which use ultrasound to determine the time it takes the blood to travel a certain distance can be used to determine near-wall aortic velocity profiles (Uematsu et al., 1991, Lee et al., 2001).

Computational fluid dynamics (CFD) methods, which involve simulations within appropriate models (idealised or more-realistic), are frequently in use today for studying and analysing the flow in vessels. In very simple terms, CFD methods generally involve 3 stages: pre-processing, processing, and post-processing. In the pre-processing stage, a CFD mesh is generated over the domain of the geometry, i.e. the domain is discretized (divided) into smaller sub-domains, suitable for numerical evaluation. In the processing stage, assumptions are applied to the model (e.g. inflow, outflow, wall boundary conditions) and the blood flow field is computed by solving the Navier-Stokes equations. During post-processing, utilities are used for evaluating the wall shear stress and other flow parameters. CFD is playing an increasing role in furthering our understanding of flow in the arteries as it enables the study of different and separate flow parameters (e.g. Reynolds number, flow ratio, steady and unsteady flow, and compliance). CFD has until recently been constrained to only simple geometrical models, however with the development of medical modalities (e.g. ultrasound, magnetic resonance imaging (MRI), computed tomography (CT)) imaging of the arteries is now possible without the need for surgery. Algorithms are being developed to reconstruct and create appropriate CFD models of 3-dimensional anatomically correct arterial geometries (Xu et al., 1999, Starmans-Kool et al., 2002, Stone et al., 2003). This enables an improved evaluation of flow and wall shear stress within the vasculature.

All of the above techniques involve non-invasive imaging of the vessels and blood flow, making it possible to maintain *in vivo* geometries, but none of the techniques can look at the exact interface between the blood and the arterial wall. The endothelium is in constant contact with the blood from the day the blood vessels develop, and EC, their nuclei (ECn) and microfilaments (MFs) are all influenced by the flow of blood over their surface and can be used as biological flow sensors as they provide a time-averaged view of the near-wall flow fields.

1.12 Blood vessels and the endothelium

As discussed previously, atherosclerotic lesions are located predominantly within the large arteries of the vasculature, and as such the structure of the vessels may play an important role in whether a vessel is lesion resistant or susceptible. All blood vessels within the body, except capillaries, are made up of three main layers: the intima (inner layer), media (middle layer) and adventitia (outer layer) (Fig. 1.12).

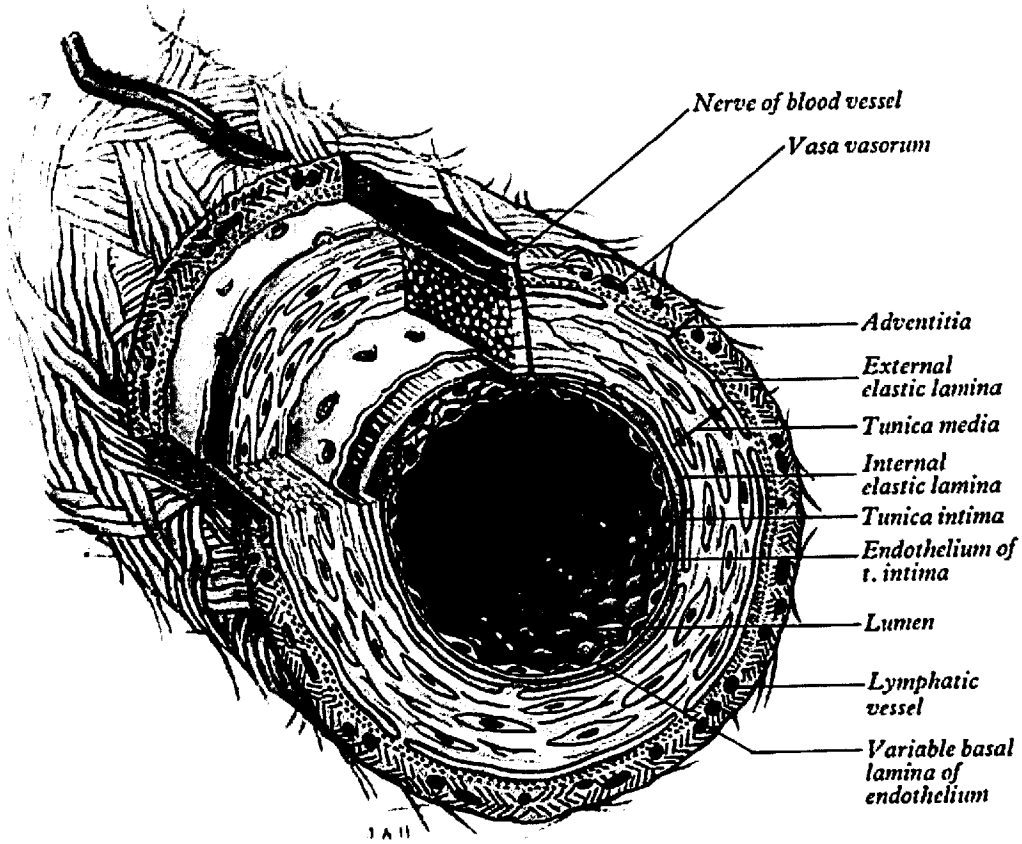

Fig. 1.12. Major features of large blood vessels (Williams *et al.*, 1989).

All vessels, including the capillaries, contain a lining made up of a single layer of EC resting on a thin layer of connective tissue. Other components e.g. smooth muscle, elastin, collagen will vary within the vessel wall depending on their location and whether they are an elastic (largest arteries), conduit (medium to small arteries), resistance (arterioles), exchange (capillaries) or capacitance (venules and veins) vessel (Table 1.1) (Levick, 2003). Blood vessels have been shown to adapt to their location and resulting shear stresses, presumably detected by EC, for example during saphenous vein grafts where a section of vein is removed and grafted in the place of an artery. Once exposed to the arterial flow and pressure the vein 'arterialises' (i.e. the wall thickens), atherosclerosis can develop and is the main pathology that can lead to stenosis and occlusion of the graft (Schachner et al., 2006). This problem is severe enough to warrant research into gene therapy, developing grafts resistant to atherosclerosis (Mann et al., 1995).

Table 1.1. Composition of the blood vessel wall (%). (Adapted from Levick, 2003)

Vessel Class	Vessel Type	Endothelium	Smooth Muscle	Elastic Tissue	Collagenous Tissue
Elastic / Conduit	Arteries	5	25	40	27
Resistance	Arterioles	10	60	10	20
Exchange	Capillaries	95	0	0	5
Capacitance	Venules / Veins	20	20	0	60

Although EC are often thought of as the barrier between the arterial wall and the flowing blood, this is actually untrue. On the luminal side of the EC is a thin layer of negatively charged biopolymers (Levick, 2003), approximately 500nm thick (Weinbaum et al., 2007), composed of glycoproteins, proteoglycans and glycosaminoglycans, known as the glycocalyx (Van Teeffelen *et al.*, 2007). The glycocalyx was traditionally thought of simply as a selective barrier between ECs and the blood, which retains plasma proteins within the circulation whilst allowing the passage of water and smaller solutes into the intercellular clefts (Levick, 2003). Its importance in atherosclerosis is now also becoming clear; if sites have a diminished glycocalyx they are more sensitive to further attack by atherogenic stimuli (Gouverneur *et al.*, 2006a), and the thickness of the glycocalyx has been shown to be less in athero-susceptible, lower shear stress sites, than

in regions of higher shear stress ((Wang et al., 1991) cited in Gouverneur et al., 2006a). This may be due to the ability of shear stress to stimulate the incorporation of hyaluronan in the glycocalyx (Gouverneur *et al.*, 2006b).

1.13 Effects of shear stress on endothelial cells

One of the most important concepts in lesion development and progression is the effect shear stress has on EC lining the artery walls. Shear stress is not just important during disease however. It is just as relevant during normal EC physiology, and without it the system would dysfunction (Dewey *et al.*, 1981).

In vivo, ECs are either ellipsoidal or polygonal in shape, depending on their location, and align themselves with their longitudinal axis in the direction of the time-averaged blood flow (Langille and Adamson, 1981, Nerem *et al.*, 1981), and after imposing a stenosis on a section of dog aorta have been shown *in vivo* to elongate in regions of higher shear stress (Levesque *et al.*, 1986). They are very dynamic and if misaligned experimentally will realign to the flow within a week (Flaherty *et al.*, 1972). Bovine aortic endothelial cells (BAEC) are commonly used for *in vitro* study, and have been shown to have a polygonal, 'cobblestone-like' shape in static culture. Steady laminar shear stress can be applied to a confluent monolayer of BAEC using equipment such as cone-and-plate viscometers, Couette flow devices (Dewey *et al.*, 1981), or parallel plate flow chambers (Levesque and Nerem, 1985). When these types of procedure are undertaken the EC start to elongate after four hours (Levesque and Nerem, 1985), before aligning themselves longitudinally to the flow, the effect being dependent on the level of shear stress and the time of exposure to the flow (Helmlinger *et al.*, 1991). McCue (McCue *et al.*, 2004) suggested that the species of origin of cultured endothelium, cell passage number, the type of substrate the cells are grown on, the media and sera used, and the state of confluence of the cultures (most important in their opinion), are all possible causes for variations in the time it takes for the endothelium to reorganise itself. *In vitro* cell culture would be a useful model except the nature of flow is different to that *in vivo*. In the body, the flow is pulsatile due to the pumping of the heart, and at times can be reversed (although the net flow is unidirectional). This has great importance to EC studies as, again in BAEC, it has been shown that when exposed to pulsatile, non-

reversing flow, 'cobblestone-like' cells elongate less rapidly than their steady flow controls, however, long-term they took on a more elongated shape (Helmlinger *et al.*, 1991, Zhao *et al.*, 1995). Exposing BAEC to low shear stress (approximately 3 dynes/cm^2) under pulsatile flow conditions for two-week periods resulted in hyperplasia and hypertrophy of the cells (Eskin *et al.*, 1984). Traub & Berk (Traub and Berk, 1998) suggested that there is a strong correlation between EC dysfunction, and areas of low mean shear stress and oscillatory flow with flow reversal (such as at branch points of the arterial tree). They suggested that steady laminar flow conditions (such as those found in straight sections of arteries) promote EC survival by preventing the migration of monocytes through the endothelium, and leading to anti-thrombotic effects through the production of thrombomodulin and NO. It also leads to the inhibition of SMC growth through the production of NO and transforming growth factor-β (TGF-β). Areas of flow reversal promote EC apoptosis leading to pro-thrombotic and pro-migratory effects, through the production of monocyte chemoattractant protein-1 (MCP-1) and vascular cell adhesion molecule-1 (VCAM-1), and pro-SMC growth through the production of angiotensin-II, platelet-derived growth factor and endothelin-1. Flow reversal could therefore also be seen as pro-atherosclerotic. This has also been suggested by Berceli (Berceli *et al.*, 1990) who reported increased uptake of lipoproteins at the lateral regions of the rabbit aorta-iliac bifurcation; sites that experience flow reversal. The accumulation of free lipids and esterified cholesterol soon follows (Traub and Berk, 1998).

It is thought that EC become more elongated under increased shear stress conditions so the least total force is experienced across their surface, by minimizing the width of the obstacle encountered by the fluid, and therefore reducing the pressure exerted on the cell (Hazel and Pedley, 2000). Cyclic circumferential strain also needs to be accounted for as it has been shown that *in vitro*, BAEC exposed to both shear stress and cyclic circumferential strain (hoop stretch) show significantly enhanced elongation and alignment along the direction of flow and perpendicular to the direction of strain, respectively (Zhao *et al.*, 1995). This effect was more enhanced when the stretch was 2-4%, although at mean shear stress levels greater than 3 dynes/cm^2, strain had little effect, suggesting that shear stress dominates strain.

When ECs are subjected to shear stress, responses are triggered that encompasses all aspects of cellular biochemistry ranging from electrophysiological modulation of membrane proteins and ion channels to activation of transcription factors within the nucleus, leading to activation of corresponding target genes or to changes in cellular morphology (Braddock *et al.*, 1998). Knowledge of the molecular mechanisms involved in the response of ECs to shear stress are very important in our understanding of the processes involved in the pathogenesis of arterial disease. Activation of various mechanosensors within the endothelium transduce physical stimuli into biochemical signals, that can lead to i.e. cell proliferation, apoptosis, migration, permeability or alignment (Li *et al.*, 2005). The transduction of shear stress is thought to be due to a combination of force transmission via elements of the cytoskeleton and transduction of the physical forces to biochemical signals at mechanosensor sites (Berk *et al.*, 1995). Integrins, vascular endothelial growth factor (VEGF) receptor-2 (Flk-1), ion channels, G-protein-coupled receptors (GPCRs) and trimeric G proteins, and adhesion molecules have all been suggested as being important mechanosensors that trigger phosphorylation cascades when flow is sensed. Activation of these, ultimately lead to the activation of mitogen-activated protein kinases (MAPK) (Li *et al.*, 2005) that are important for chemoattraction of monocytes, by monocyte chemotactic protein-1 (MCP-1), and the modulation of LDL permeability by changes in cell turnover (Chien, 2003). Integrins are transmembrane receptors on the abluminal side of ECs that link intracellular cytoskeletal proteins with the proteins in the extracellular matrix (ECM) (Schwartz, 2001), and are capable of transducing mechanical stimuli into biochemical signals (Ingber, 1998) bringing about the activation of the VEGF-receptor, Flk-1 (Wang *et al.*, 2002). Application of shear stress causes activation, and phosphorylation of Flk-1, which is a tyrosine kinase receptor on the luminal surface of ECs, enabling it to bind to adaptor molecules e.g. Shc that in turn activates Ras and its downstream molecules leading to the transcription activation of MCP-1 (Chien, 2003). The endothelial cell membrane permeability to K^+ ions (Alevriadou *et al.*, 1993), and also the influx of Ca^{2+} (Kanai *et al.*, 1995, Yamamoto *et al.*, 2000), have been shown to increase upon exposure to shear stress, and a sodium channel has been identified that mediates the activation of

extracellular signal-regulated kinase-1/2 (ERK-1/2) (Traub *et al.*, 1999). Through the activation of ion channels, cellular signalling and EC functions can be regulated.

1.14 Effect of shear stress on endothelial cell nuclei

An alternative method of visualizing flow is to look at the EC nuclei instead of the cells themselves. The advantage of this is that there are a lot of commercially available stains and dyes that stain nucleic acids within the ECn. The nuclei tend to align themselves, as with the cells, in the direction of flow. This has been shown by removing a section of dog aorta, reorienting it by 90 degrees, and then replacing it. When viewed 10 days later, the major axis of the nuclei completely realigned along the longitudinal axis of the blood flow (Flaherty *et al.*, 1972). It has been concluded that nuclei in low flow, and therefore low shear stress, areas have more rounded nuclei, and in high flow areas have more elliptical shapes, as with EC (Flaherty *et al.*, 1972, Malinauskas *et al.*, 1998). However, the nuclei only occupy 10% of the total endothelial surface (Cornhill *et al.*, 1980) therefore it is important to study the cells themselves as well in case shear stress has a different response in their nuclei.

Al-Musawi *et al* (Al-Musawi *et al.*, 2004) recently carried out a rabbit study to determine whether the change in lesion pattern is a function of age and reflects a change in the dependence of disease to flow, or whether it reflects a change in the flow pattern itself. Staining ECn enabled regions where the nuclei were elongated (regions of higher shear stress) to be observed The data provided evidence that highest shear stresses occur downstream of ostia in immature rabbits, but not at later ages, suggesting either that the ECn respond differently to the blood flow at later ages, or the blood flow itself actually changes with age.

1.15 Effects of shear stress on microfilaments

Changes in EC and nuclear alignment are accompanied by a change in cytoskeleton structure. The cytoskeleton is the "scaffolding" of the cell, found within the cytoplasm, which helps to maintain the cells shape. It is made up of three main types of filaments; actin microfilaments (MFs) or stress fibres, intermediate filaments, and microtubules. The function of the endothelial cytoskeleton is to act as a passive barrier to atherogenic

particles, enable migration of cells during wound repair, to maintain cell-cell and cell-substratum adhesion, and to enable cell signalling (Lee and Gotlieb, 2003). F-actin, within MFs, is found colocalizing with myosin, tropomyosin, α-actinin, and vinculin which suggests it has contractile properties (Colangelo *et al.*, 1994) which could be important in some of the aforementioned processes. In the thoracic aorta, away from branch ostia, actin MFs were localised in two regions of the EC; a prominent continuous band around the cell and in microfilament bundles, or 'stress fibres' in the central portion of cells (Kim *et al.*, 1989b). To demonstrate the role of the EC cytoskeleton in endothelial permeability, cytochalasins, enzymes that disturb microfilament structure by preventing the addition of G-actin to nucleation sites, can be added to a perfusate of isolated rabbit lung, causing a high permeability lung edema (Shasby *et al.*, 1982).

It has been suggested that MFs are formed and altered predominantly by blood flow (shear stress) triggering biochemical processes, due to the fact that they are not generally found in venous endothelium. Stress fibre-containing EC within the vascular system tend to be located at sites of higher shear stress, and experiments on cultured cells have been carried out to determine the effect of altered levels of shear stress (Franke *et al.*, 1984). Using rhodamine-labelled phalloidin, and antibodies to calf thymus myosin and chicken gizzard and pectoral muscle α-actinin, Franke *et al* observed the effects of applying a shear stress to the microfilaments within the endothelium. Phalloidin is part of the phallotoxin group, from the death cap mushroom (*Amanita phalloides*), that binds between F-actin subunits, locking adjacent subunits together, preventing their depolymerisation and subsequently poisoning the cell. After a 3-hour exposure to low shear stress (approximately 2 dynes/cm^2) the quantity and staining intensity of stress fibres had increased dramatically. Reorientation of the EC accompanied reorientation of the stress fibres. It should be noted that it has since been observed (Kim *et al.*, 1989b) that the orientation of stress fibres and the longitudinal axis of ECs does not always correspond; deviations of up to 30° have been seen. A possible explanation put forward to explain this were that the actin fibres can be oriented by extracellular proteins in the substratum in the presence of blood flow, whereas the endothelial cells have only been seen to be reoriented by substratum in the absence of flow. Another possible explanation is that only a small number of ECs (10 per rabbit) were measured by hand,

possibly not giving an accurate account of the cell length, and the method for measuring fibres was not described. It has been shown that there is a good correlation between angle of cell orientation and angle of stress fibre orientation ($r>0.9$) after 20min, 1hour and 6hours exposure to flow, and that the distribution of the angle of stress fibres becomes smaller with increasing exposure time (Sato and Ohashi, 2005). Texas Red-conjugated phalloidin has also been used as a fluorescent stain for actin filaments and enables good visualization of stress fibres (Birukov *et al.*, 2002).

In vivo findings (Langille *et al.*, 1991, Uematsu *et al.*, 1991) suggest that introducing a coarctation (narrowing) into rabbit aortas, causing an approximately two-fold increase in shear stress downstream of the coarctation, leads to an increase in microfilament size (after 48 hours), to what are now known as 'giant' stress fibres. This reversible process occurs through a series of interrelated events. Firstly, an increase in blood flow and shear causes the loss of many of the short stress fibres around the cell periphery. Two distinct bands of F-actin, possibly associated with adjacent cells, were seen to appear, either caused by physical separation of actin from the cell-cell junction, or simply due to a decreased staining intensity allowing two bands in a fixed position to be resolved. Following on from this is the formation of the giant stress fibres that are newly formed as opposed to being an extension of pre-existing microfilament bundles. The formation of giant stress fibres generally occurs near flow dividers where flow is fastest, suggesting a role in cell adhesion (Kim *et al.*, 1989b, Uematsu *et al.*, 1991). It has also been suggested that decreased shear stress in normo- and hyper-cholesterolemic beagles might attenuate the formation of bundles, regardless of the presence of plaques (Uematsu *et al.*, 1991).

Further evidence for the importance of flow on stress fibre formation was presented by (Yoshida and Sugimoto, 1996) who grafted a vein in a rabbit femoral artery and observed MF development and endothelial alignment. After transplantation the EC maintained a shape index that was intermediate between those of control arteries and veins for the 16 weeks of study, whereas the MFs increased in frequency and thickness from the start until they reached a point after 16 weeks where they were similar to controls.

1.16 Possible mechanisms for change in lesion location with age

Various mechanisms have been postulated for the variation with age in the pattern of macromolecule transport across the artery wall into the intima. It has been decided that acutely, the interaction of blood cells with the wall and the composition of the blood, are not entirely responsible for age-related variations in transport, as the same patterns are seen when a steady flow of physiological buffer is perfused through the vessels. The role of NO release was made evident when inhibitors were added to vessel perfusate, and the mature, but not immature, pattern is abolished suggesting that the change with age reflects an alteration in NO synthesis and function (Forster and Weinberg, 1997). Occlusion of intercostal arteries has shown that in mature rabbits, the uptake pattern of rhodamine-labeled albumin is also thought to be flow-dependent, whereas in immature rabbits, occlusion had no significant effect on uptake (Staughton *et al.*, 2001). Other possible reasons for a change with age are the increasing stiffness (compliance) of the arteries related to the inversion of the elastin to collagen ratio (Orlandi *et al.*, 2000), causing decreased reversal of flow during late systole/early diastole of the cardiac cycle, or the increased blood flow down the side branch that corresponds with an increase in body weight, without a corresponding increase in ostial diameter, as an animal ages (Al-Musawi *et al.*, 2004). A factor that should not be overlooked is blood pressure as both systolic and diastolic increase throughout (Pearson et al., 1997), possibly linked with the increased compliance already mentioned.

We are going to investigate whether differences in blood flow can account for the age- and species-dependent differences in lesion/permeability patterns by using EC morphology to determine flow patterns around intercostal branch ostia.

Chapter 2: Development of methods for endothelial nuclear staining

2.1 Introduction

The endothelium is the interface between the blood and the vessel wall, and is affected by the flow of blood over its luminal surface. As has been discussed previously, ECs and their nuclei align with the predominant direction of flow (Langille and Adamson, 1981, Nerem *et al.*, 1981) and elongate in regions of higher haemodynamic wall shear stress (Levesque *et al.*, 1986). To observe whether flow varies around branch points and between other locations in arteries, a method was developed to enable high-definition imaging of the elongation and orientation of ECn. Its development posed the following problems: 1) how to flatten the artery wall, 2) how to stain the endothelium without staining underlying SMCs, 3) how to observe the large numbers of cells within the endothelium, and 4) how to carry out image analysis of large numbers of cells.

2.1.1 Flattening the arterial wall

The initial problem encountered was that *in vivo* the artery is a curved tube and once removed from the body, after fixation at physiological pressure, retains this curved configuration. When cut longitudinally and opened for *en face* visualisation, the artery does not naturally lie flat. Previous investigators have tried to flatten the artery by cutting it open and pinning the tissue onto boards (cork or wax) (Kim et al., 1989b, Bugelski et al., 2000) or compressing it between glass slides (Truskey *et al.*, 1992), before fixing the tissue. However, these methods do not maintain *in vivo* arterial geometries because fixation is carried out at un-pressurised dimensions. An approach we attempted in preliminary experiments was to apply weights to a glass coverslip on top of the tissue, after fixation at pressure, to try and force it to lie flat. However, it was discovered that the pressure required exceeded that exerted by weights of practicable size. A method previously employed in our laboratory (Al-Musawi *et al.*, 2004) was to mount the tissue *en face* and place a cover slip over the tissue. Pressure was then applied by wrapping a piece of adhesive tape around the slide and coverslip. A 'window' (a small square) was then cut in the tape to enable the tissue to be visualised. Again, this did not generate enough downward pressure to flatten the tissue fully. Further problems visualising the endothelium were encountered due to the wall morphology. It has been shown that the intima itself is not a completely smooth surface and longitudinal and helical ridges are found along its length; they are thought to be

associated with fatty streaks (Back *et al.*, 1976). Furthermore, at branch points (the areas we were predominantly interested in), the remaining daughter branches, if not cut close to the parent vessel can push onto the wall affecting how flat the surface is. It was also very difficult to remove all adventitial fat from the outside of arteries causing an uneven surface when viewed *en face*.

Another method that has been used to visualise the endothelium of rats (Levesque *et al.*, 1979) and rabbits (Cornhill *et al.*, 1980) is vascular casting. This process involves perfusing vessels with a silver nitrate ($AgNO_3$) solution followed by liquid methacrylate resin at pressure. When the resin polymerises it solidifies, it was claimed, with minimal shrinkage (<1%); a review of quantitative measurements (Kratky et al., 1989) showed that casting materials can shrink from 0.2 – 20% from the original vessel luminal diameter. The surrounding tissue can then be removed by immersion in sodium hydroxide and the cast viewed using scanning electron microscopy (Reidy and Levesque, 1977). The main benefit of this technique is that the blood vessels need not be opened, fixed or dehydrated; thus *in vivo* geometries are maintained provided the resin is maintained at pressure as it sets (Levesque *et al.*, 1979). This is difficult to arrange. Furthermore, we wanted a light rather than electron microscopy technique, to enable larger areas to be observed.

2.1.2 Staining nuclei of endothelial cells without underlying smooth muscle cells

Due to the curvature of the wall, when microscopy techniques are used, the endothelium is not always in one focal plane, but multiple planes. This causes problems when trying to image the endothelium, as part of the image will contain the cells of interest whilst other parts will contain underlying tissue. The problems of wall curvature would not be such an issue if it were possible to stain the endothelium without interference from the underlying SMCs. Commercial nuclear stains are highly specific for nucleic acids (DNA and RNA) but are not specific to particular cell types. They stain nucleic acids within the nuclei of both EC and SMC making it very difficult to visualise the endothelium without interference from the nuclei of underlying SMC (Fig 2.1). To enable analysis of millions of cells it was necessary to develop image analysis

techniques that automatically measured parameters of the endothelial cells alone. SMC nuclei (SMCn) captured in the images would lead to inaccurate results.

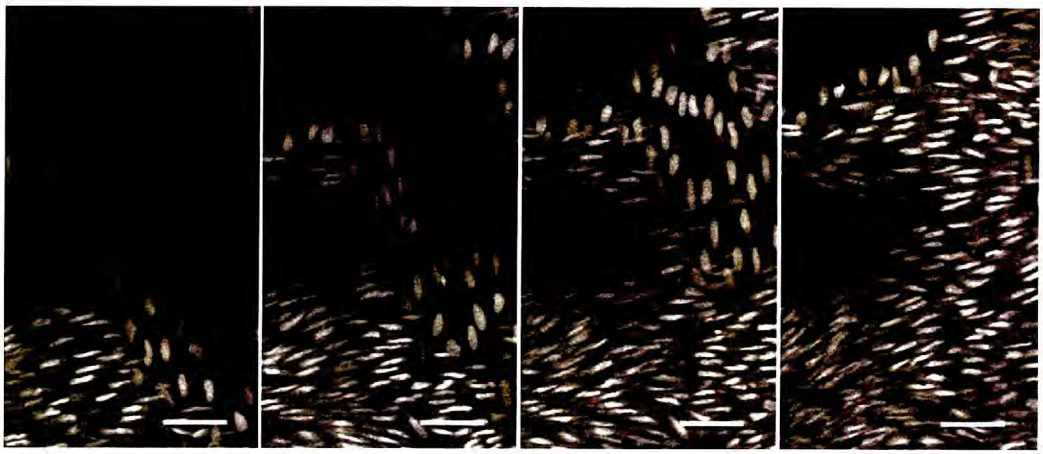

Fig. 2.1. Four optical slices taken from a confocal scan through a mouse arterial wall stained with propidium iodide. Note the occurrence and disappearance of endothelial cell nuclei (oriented from top to bottom) and underlying smooth muscle cell nuclei (oriented perpendicular to ECn). Scale Bars = 50μm.

In previous work from our group (Al-Musawi *et al.*, 2004), ECn were stained with Harris hematoxylin, a commonly used Alum Hematoxylin solution. Visualisation of underlying SMCn was largely prevented by making the tissue highly autofluorescent (by fixing with glutaraldehyde) and viewing it *en face* with an epifluorescence microscope; ECn were seen because the staining of their nuclei blocked autofluorescence from the underlying medial tissue, in which the SMC are present. Although this produced clear images of the ECn, there was a very uneven grey background where components of wall were stained (or autofluoresced) differently. This prevented automated image analysis, so ECn had to be measured manually; a very time consuming process not without its own problems such as the potential for different investigators to interpret edges of cells differently, errors due to repetitiveness of task etc. It was also possible to see some underlying SMC, presumably those nearer the inner layers of the media, in some areas, which had to be excluded.

2.1.3 Arterial Fixation

One of the complications that arises when studying arteries in relation to atherosclerosis is that in order to examine arterial cells it is normally necessary to remove the vessel from the body. This disrupts vessel geometry as physiological pressure, and tethering to other tissues, are removed. When elastic arteries are excised they contract by approximately one third (Stary *et al.*, 1992), potentially affecting observations of cells, and a further problem is that the cells are particularly susceptible to deterioration after death. Conditions such as temperature and fluid balance can modify the rate at which these alterations occur (Stary *et al.*, 1992). To try to overcome these problems, *in situ* fixation at physiological pressure was used. The following fixation methods were employed for all experiments described in this thesis unless otherwise stated.

2.2 Methods

2.2.1 Arterial fixation methods

All animal procedures were carried out in accordance with the Animals (Scientific Procedures) Act 1986, at either the University of Reading, UK, or Central Biomedical Services, Imperial College, UK. Male New Zealand White (NZW) rabbits (Interfauna strain, Harlan) and CD1xWild type mice (University of Reading strain) were maintained on standard laboratory diets.

2.2.2 Rabbit surgical procedures

Rabbits were injected with heparin (Sigma, ~2000 USP Units in 1.5ml Ringers, i.v.) which was allowed to circulate for 2 minutes, before euthanasia by injection of pentobarbitone (approximately 160mg/kg i.v.). Following thoracotomy and laparotomy along the ventral line, a retrograde cannula was inserted into the thoracic aorta at the level of the diaphragm and tied in place using surgical thread. The aorta was flushed with 50ml Ringers solution (9.0g NaCl, 0.2g $CaCl_2$, 0.2g KCl, 0.1g $NaHCO_3$ per litre) containing 1.5ml heparin (Sigma, ~2000 USP units), followed by perfusion with Karnovsky's fixative (4% glutaraldehyde plus 5% formaldehyde v/v) or 10% neutral buffered formalin (containing ~4% formaldehyde) (Sigma) for 30 minutes. To help maintain the vessel at physiological pressure and therefore maintain *in vivo* geometries, all solutions were released from a reservoir 100-120cm above the animal and the aortic

arch was clamped after one minute. Following fixation the thoracic aorta was excised and post-fixed in the same fixative for a minimum of 16 hours.

2.2.3 Mouse surgical procedures

Mice were euthanized by carbon dioxide inhalation. Following thoracotomy and laparatomy, and elevation of the ventral half of the ribcage, a cannula was inserted into the left ventricle and glued in place with cyanoacrylate (3M Vetbond, no.1469C). 1.5ml of a heparin solution (Sigma, ~2000 USP Units) was added to 5ml Ringers solution, and used to flush the arterial system of blood. This was followed by perfusion of either Karnovsky's fixative (n=7) or 10% neutral buffered formalin (n=2) (Sigma) for 30 minutes. As with rabbit fixations, all solutions were released from a reservoir 100-120cm above the animal, and thoracic aortas were excised before being post fixed for at least 16hours.

2.2.4 Nuclear staining development

The first task was to try to improve the rabbit hematoxylin staining method to produce high definition of the ECn without the underlying SMC, and with a more uniform background intensity.

2.2.4.1 *In vitro* hematoxylin staining

All haematoxylin staining procedures were carried out on a number of whole mount tissue preparations. For all the following methods, aortic rings were cut open longitudinally, opposite branch sites if these were present, and placed on glass slides with the endothelium facing upwards. A coverslip was placed over the surface and taped in place. The tissue was then examined *en face* under an epifluorescence microscope using filters for fluorescein. Images were taken using a low light CCD camera coupled to a software package, Maxim DL (Diffraction Limited, Canada)

2.2.4.1.1 Method One

The method of Al-Musawi *et al* was attempted first to confirm that the same level of ECn staining could be achieved. Their method involved submerging aortic rings (fixed

in Karnovsky's solution to increase autofluoresence) in Triton X-100 (Sigma, 0.2%, 1min), washing in phosphate buffered saline (PBS) (Sigma, 10.0 mmol/L phosphate buffer, 2.7 mmol/L KCl, 137.0 mmol/L NaCl, 15s), staining in Harris Hematoxylin (Sigma, 0.75%, 15s), de-staining in PBS (30s) and then repeating these steps.

2.2.4.1.2 Method Two

The previous method was repeated four times but using distilled water or, later, tap water after the first cycle to increase acidity.

2.2.4.1.3 Method Three

Method two was modified by the addition of ribonuclease (RNase) (Sigma, 0.01%, 10min, 37°C) followed by rinsing in PBS (15s) to the first cycle of staining. RNase was used to remove any RNA within the cytoplasm of the cells that may have been stained and therefore reduced contrast between cytoplasm and nuclei.

2.2.4.1.4 Method Four

Method two was adapted to include glacial acetic acid (5%), in the Harris hematoxylin. The stain and acid were mixed for 2 min prior to use.

2.2.4.1.5 Method Five

Method two was adapted by substituting Harris Hematoxylin with Gills hematoxylin no.1 (Sigma).

2.2.4.2 *In vitro* Acridine Orange

Aortic rings were placed in Triton X-100 (Sigma. 0.2%, 1 minute) to increase the permeability of the membranes, followed by rinsing in PBS (15 seconds), before being incubated in RNase (0.01%, 10 minutes, 37°C). Although it is suggested that Acridine

Orange (AO) is a cell permeable dye (Molecular Probes, 2004), Triton X-100 led to improved images. RNase was used to remove RNA from the cell, as above; when it was omitted, nuclei were still visible but "tails" were also visible on either side of the nuclei, thought to be due to the presence of RNA within the cytoplasm of the ECs. The aortic rings were then rinsed of RNase by placing in PBS (5 seconds) before being immersed in AO (Sigma; 6mg/ml (a saturated solution)) for 2.5 minutes, followed by a rinse in PBS to remove excess stain, and further destaining in PBS (1 hour). The aorta was then cut along its longitudinal axis opposite the branch sites before being mounted endothelium down in glass bottomed petri dishes for confocal microscopy.

2.2.4.3 *In vivo* Acridine Orange

1ml of AO (6mg/ml) was injected, via the marginal ear vein, into a conscious NZW rabbit and allowed to circulate for 10 minutes, followed by 1.5ml Heparin. The animal was then euthanized with 1ml pentobarbitone, and formalin fixation carried out for 30 minutes, as described previously. Following fixation the aorta was equilibrated with PBS (1 hour), defatted, incubated with RNase (10 minutes) and mounted, as before, for confocal microscopy.

2.2.4.4 *In vitro* Propidium Iodide

Aortic staining was carried out in the same manner as *in vitro* staining with acridine orange, the only difference being that the aortic ring was dipped in Propidium Iodide (PI) (Molecular Probes, 1.0mg/ml solution in water) as opposed to AO.

2.2.4.5 Perfusion with Propidium Iodide

An attempt was made to expose the vessel wall to stain for very brief periods, so that staining reached the endothelial cells but not the media. Following perfusion with 50ml Ringers solution, the aorta was fixed with formalin (30min), excised and then immersed in PBS (1hour). The aorta was placed in Triton X-100 (30 seconds) followed by PBS (15 seconds) and then cannulated at both ends (Fig 2.2). The system was initially flushed through with PBS to determine the flow rate (3.2ml/sec with clamp open – see diagram). 0.3ml PI was then introduced into the perfusion system via a syringe (to stain for approximately 1 millisecond) and 'pushed' through with PBS released from the

reservoir – see diagram. Aortic rings were then cut, placed in PBS (10mins) followed by RNase (10 minutes, 37°C) and finally in PBS (10mins) before being mounted as previously described for AO stained tissue.

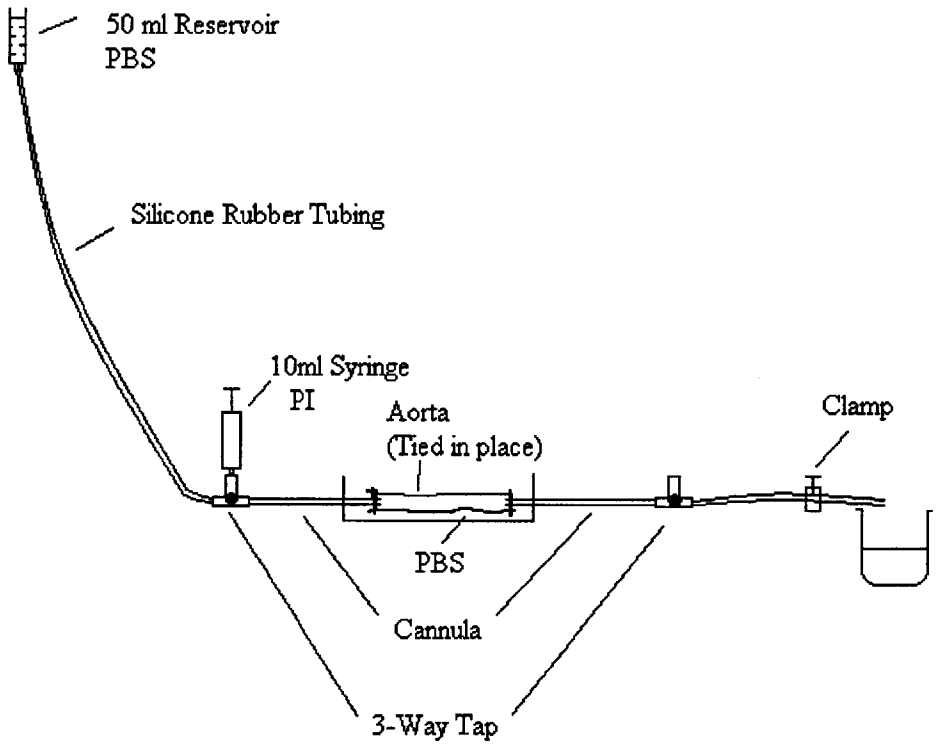

Fig. 2.2. Equipment used for *ex vivo* perfusion with propidium iodide (PI) for staining of rabbit aorta.

2.2.4.6 *In vivo* Propidium Iodide

1.5ml of PI (Molecular Probes, FluoroPure grade, 5mg/ml Ringers) was injected, as with *in vivo* AO staining, via the marginal ear vein and allowed to circulate for 10 minutes. Euthanization and the steps following this were the same as with AO staining and fixation.

2.2.5 Confocal microscopy

En face preparations were viewed with a Leica TCS NT inverted confocal microscope (Leica Microsystems, UK) using either a 20x or 63x immersion objective lens, with glycerol as an immersion fluid, in a temperature controlled unit (37°C, the temperature required to obtain the refractive index of glycerol for which the lens is designed), and at

a resolution of 2048pixels x 2048 pixels to allow changes in nuclear dimensions to be recorded accurately.

Acridine orange stained sections were excited at a wavelength of 488nm, and emission detected at 500-540nm using photo-multiplier tube 3 (PMT3), with the pinhole set to one Airy unit, and the beam expander set to 6.

Propidium iodide stained sections were excited at a wavelength of 543nm, and emission detected at 600-640nm using PMT 3 , also with the pinhole set at Airy 1, and the beam expander set to 6.

2.3 Results

2.3.1 Determining optimal staining techniques for light microscopy

2.3.1.1 *In vitro* hematoxylin staining

2.3.1.1.1 Method One

Stained ECn blocked the autofluorescence from underlying tissue, induced by the glutaraldehyde within Karnovsky's fixative, and appeared black. However, in all the sections stained there was an uneven background that prevented automated image analysis and smooth muscle cells were still visible underlying the EC.

2.3.1.1.2 Method Two

When method one was repeated four times, the outlines of the nuclei became clearer (Fig. 2.3). When PBS was replaced with distilled water after the first cycle of staining, the contrast of the nuclear outlines against the arterial wall was further improved and the background was more uniform (Fig. 2.4). This was improved still further when normal tap water was used (Fig. 2.5). In the majority of stained tissue the presence of SMCn was minimal, however where the endothelium was damaged and the SMCs were exposed to the stain, nuclei were still visible.

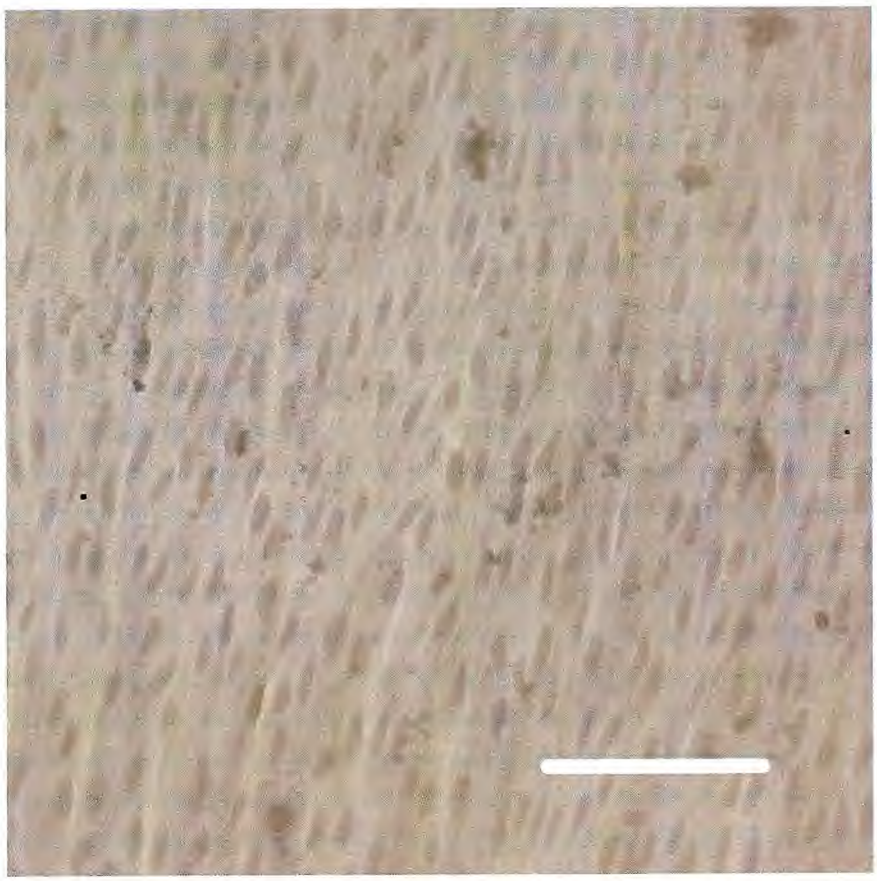

Fig. 2.3. Rabbit endothelium stained with Harris Hematoxylin. Method one repeated four times. Bar = 100μm.

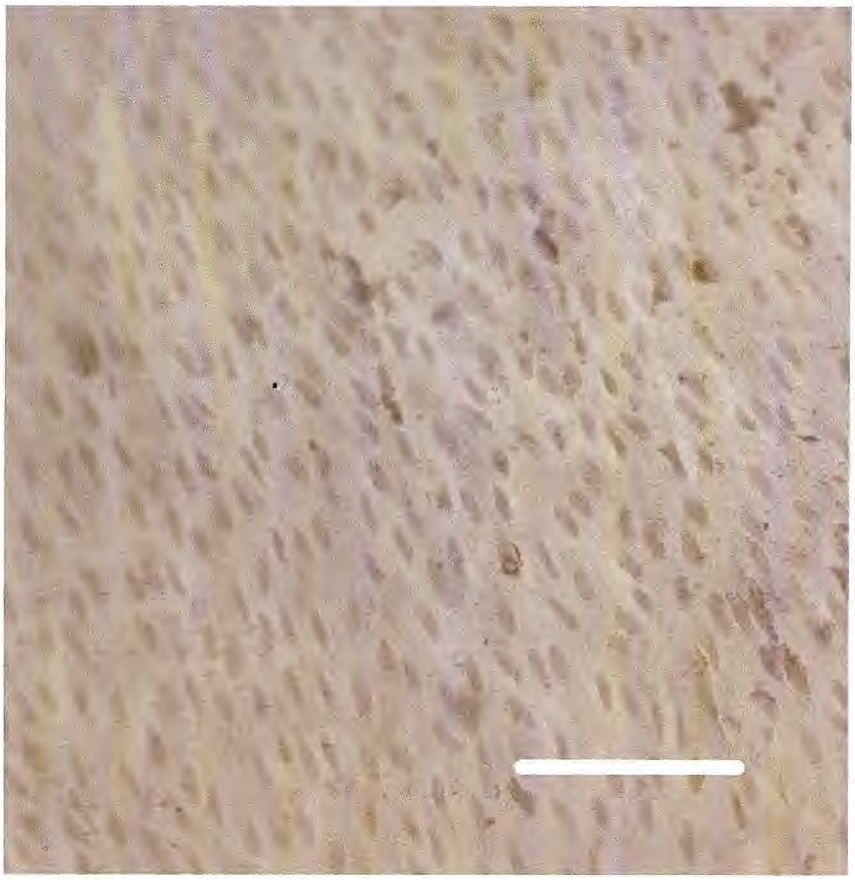

Fig. 2.4. Rabbit endothelium stained with Harris Hematoxylin and rinsed with distilled water. Bar = 100μm

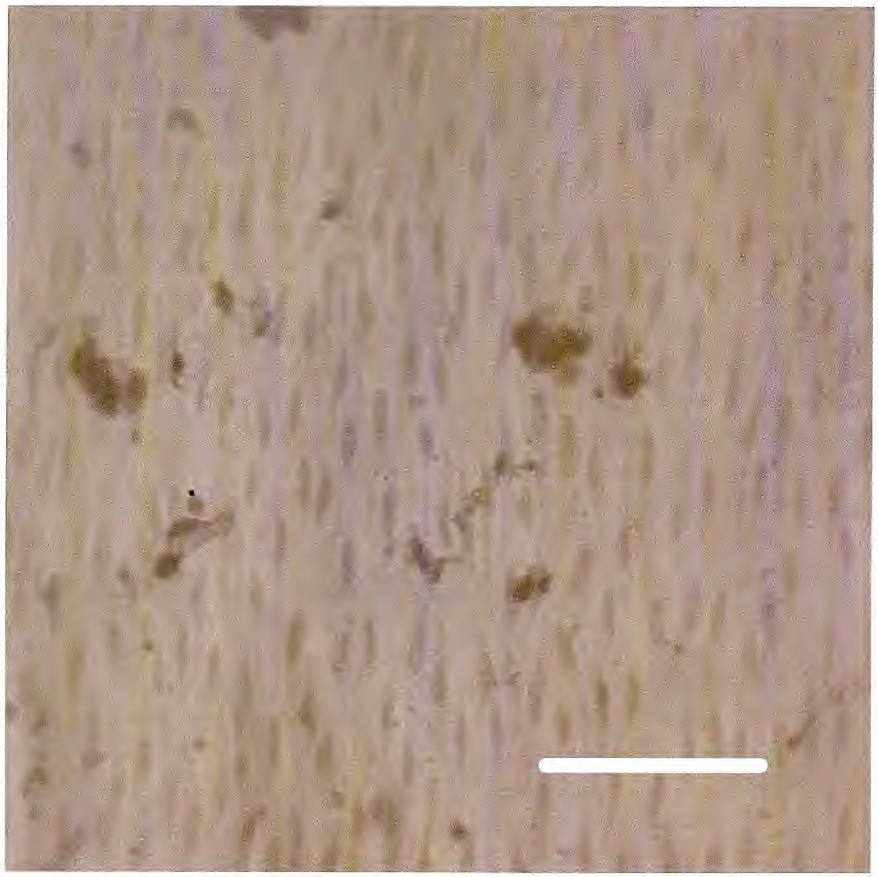

Fig. 2.5. Rabbit endothelium stained with Harris Hematoxylin and rinsed with tap water. Bar = 100μm

2.3.1.1.3 Method Three

Following the addition of RNase to the tissue, the background became much more uniform, however the endothelial nuclear staining was much fainter (Fig. 2.6). This could be because the time the tissue spent in RNase solution (10min) caused some of the hematoxylin to be removed from the nuclei. A few SMC nuclei were still visible in some regions of stained artery.

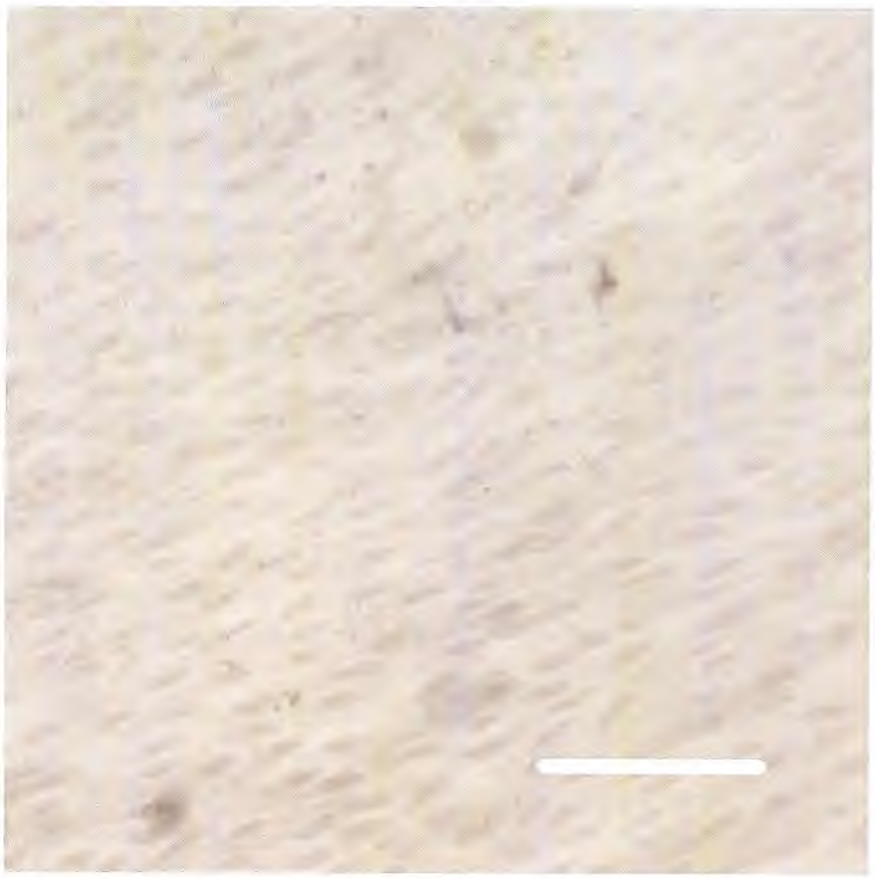

Fig. 2.6. Rabbit endothelium stained with Harris hematoxylin incubated with RNase. Bar = 100μm.

2.3.1.1.4 Method Four

The improvement seen after the addition of tap water (seen in method two) was thought to be caused by the acidity of the water. This led us to add glacial acetic acid. There was increased contrast between the stained ECn and background, but faint "tails" were visible at the edges of the nuclei (Fig. 2.7). The addition of acid also caused striations to be visible across the arterial wall, perhaps caused by staining of underlying SMC, or damage occurring to the endothelium itself.

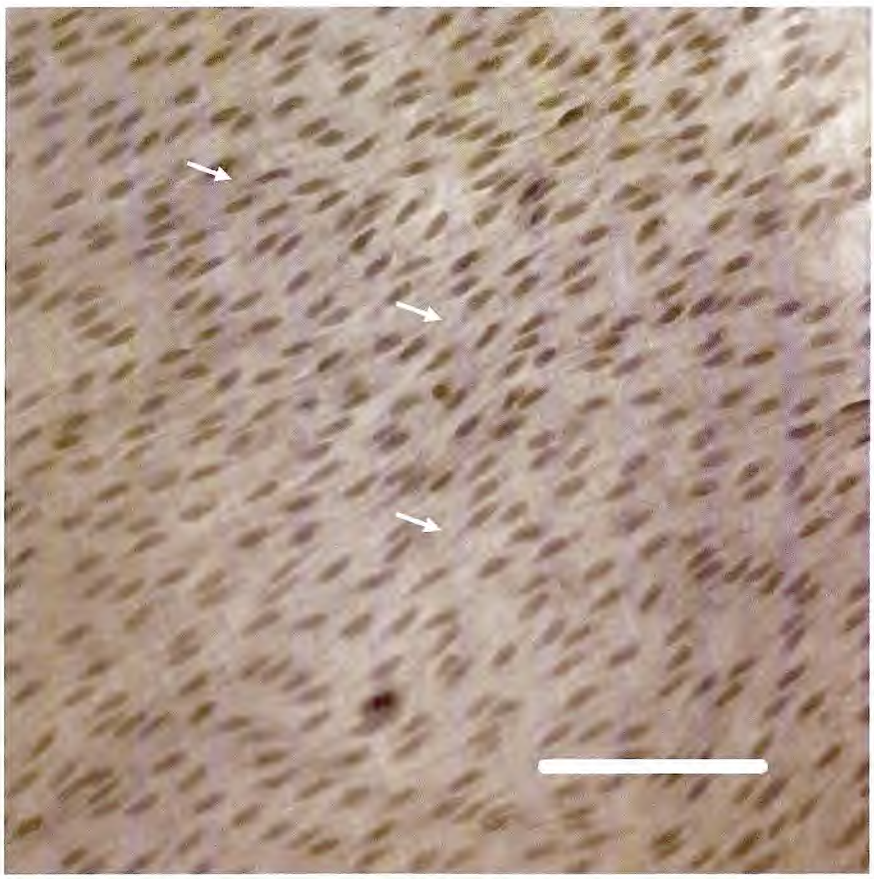

Fig. 2.7. Rabbit endothelium stained with Harris hematoxylin diluted in 5% Glacial acetic acid. Arrows indicate "tails" of nuclei. Bar = 100μm

2.3.1.1.5 Method Five

When Harris hematoxylin was substituted with Gills hematoxylin, staining was very similar to that found after addition of acetic acid (Fig. 2.8). EC nuclei were clearly visible along with nuclear "tails" again; however the background was more uniform than before, and as with the other methods, SMC nuclei were sparse.

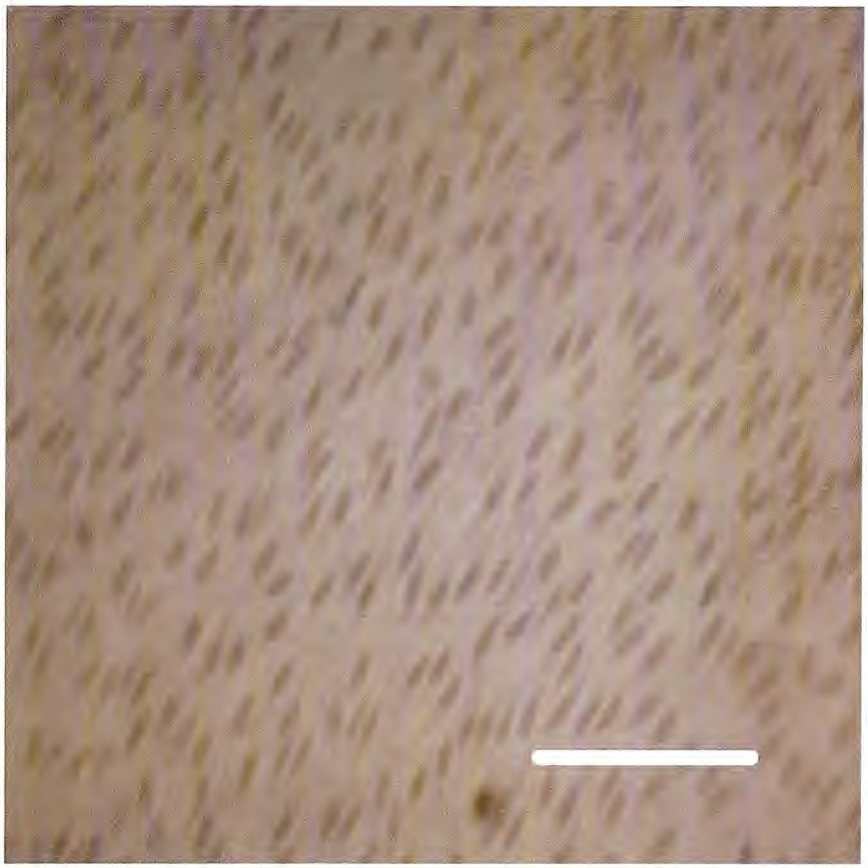

Fig. 2.8. Rabbit endothelium stained with Gill's hematoxylin. Bar = 100μm.

With all the hematoxylin techniques attempted, backgrounds remain too dark and variable to allow automated analysis of the images.

2.3.2 Determining optimal staining techniques for confocal images

2.3.2.1 Acridine orange

2.3.2.1.1 *In vitro* Acridine Orange

A major problem encountered when using AO *in vitro* was the amount of background fluorescence in the images (Fig. 2.9). This was caused by autofluorescence of the arterial wall, staining of RNA in the EC and SMC, and DNA staining in SMC nuclei. This was improved slightly by the use of RNase (Fig. 2.10) which reduced the amount of stain taken up by the endothelial cytoplasm. However, despite producing clearer images there was still too much background fluorescence for automated image analysis.

2.3.2.1.2 *In vivo* Acridine Orange

Using AO *in vivo* did not seem to improve the images, despite the addition of RNase before mounting the tissue (Fig. 2.11). This may have been due to the stain being diluted by the plasma before it had a chance to cross the EC membrane and diffuse into the nuclei.

2.3.2.2 Propidium iodide

2.3.2.2.1 *In vitro* Propidium Iodide

Early attempts at *in vitro* PI staining involved leaving the aortic ring in the stain for 30 seconds (as opposed to dipping) and not using RNase (Fig. 2.12). This produced a lot of background noise and the underlying SMC were visible, although not as clearly as with AO staining. The next step was to add RNase as it was thought that this would digest RNA in the cytoplasm (as mentioned previously). This appeared to 'clean-up' and improve the images. Nuclei had very sharp edges without excessive background noise (Fig. 2.13). However, SMCn were still visible underlying ECn.

2.3.2.2.2 Perfused Propidium Iodide

Vessels fixed *in vivo*, but stained *ex vivo*, by perfusing with PI produced very clear images (Fig. 2.14) but a number of SMC nuclei were visible, although their number varied across the tissue.

2.3.2.2.3 *In vivo* Propidium Iodide

In vivo staining with PI (Fig. 2.15) produced good definition of EC nuclei but also stained underlying SMC nuclei, therefore there was no advantage over the simpler *in vitro* procedure.

2.3.2 Staining Results - Images

The following images show the development of the staining technique. The direction of blood flow is unknown as at this time it was only necessary to determine whether the staining technique was working. All figures are single images and no image editing has been carried out.

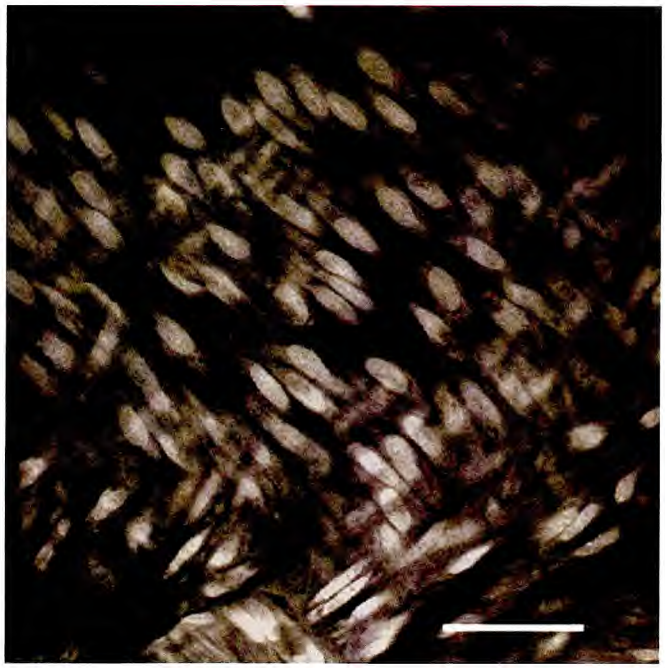

Fig. 2.9. Acridine orange staining of the endothelium of rabbit aorta. $\lambda_{excitation}$ 488nm, $\lambda_{emission}$ 500-540nm. Bar = 50μm.

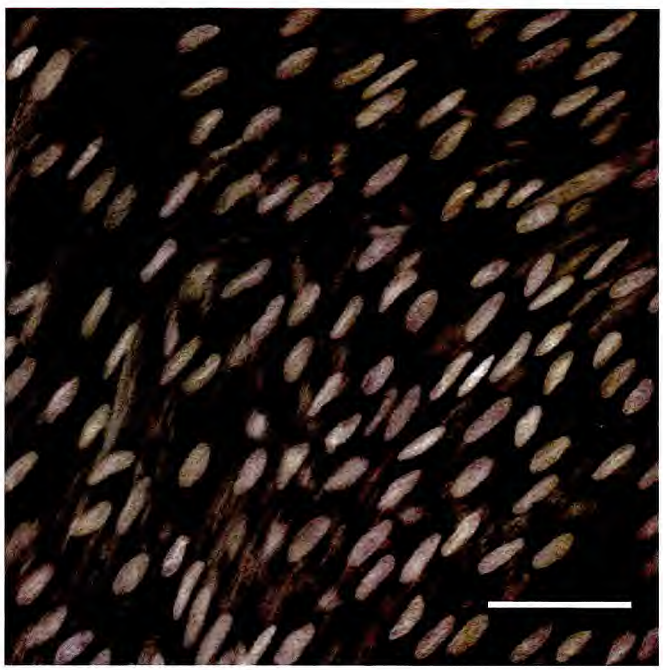

Fig. 2.10. Acridine orange staining of the endothelium of rabbit aorta treated with RNase before staining. $\lambda_{excitation}$ 488nm, $\lambda_{emission}$ 500-540nm Bar = 50μm.

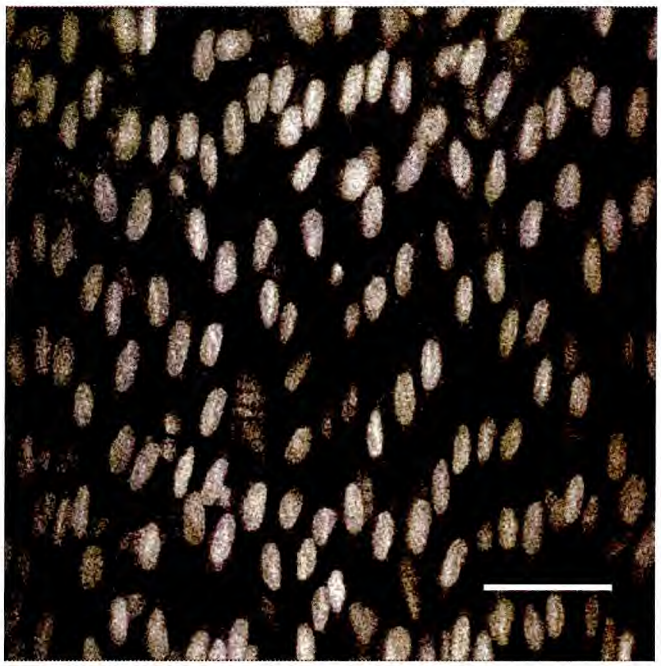

Figure 2.11. *In vivo* acridine orange staining of the endothelium of rabbit aorta treated post-staining with RNase. $\lambda_{excitation}$ 488nm, $\lambda_{emission}$ 500-540nm Bar = 50μm.

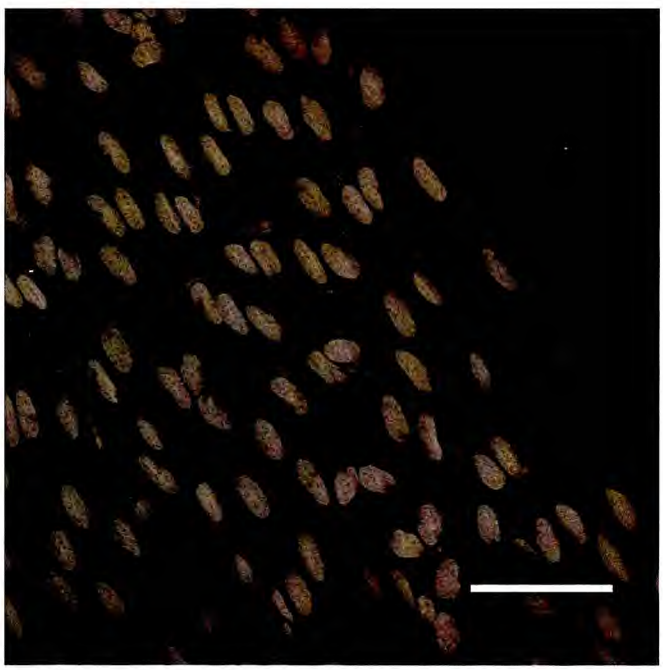

Figure 2.12. Propidium iodide staining of the endothelium of rabbit aorta. $\lambda_{excitation}$ 543nm, $\lambda_{emission}$ 600-640nm. Bar = 50μm.

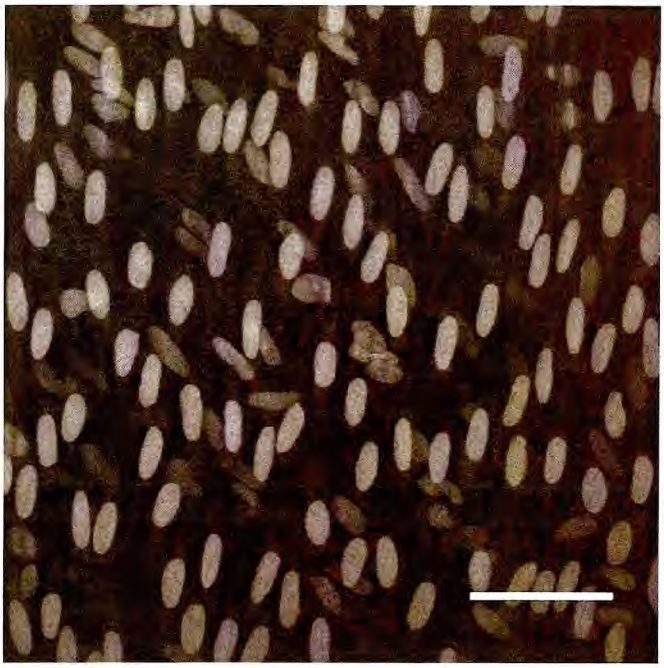

Figure 2.13. Propidium iodide staining of the endothelium of rabbit aorta treated with RNase before staining. $\lambda_{excitation}$ 543nm, $\lambda_{emission}$ 600-640nm. Bar = 50μm.

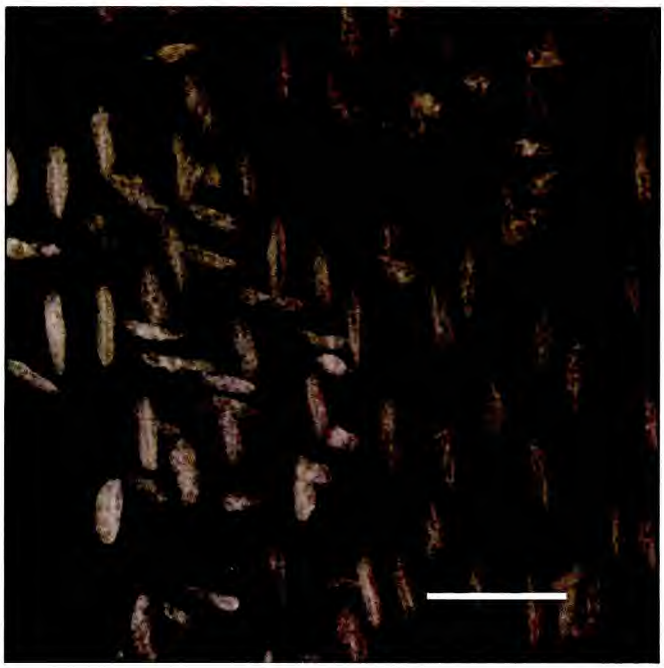

Figure 2.14. Perfused propidium iodide staining of the endothelium of rabbit aorta treated post-staining with RNase. $\lambda_{excitation}$ 543nm, $\lambda_{emission}$ 600-640nm. Bar = 50μm.

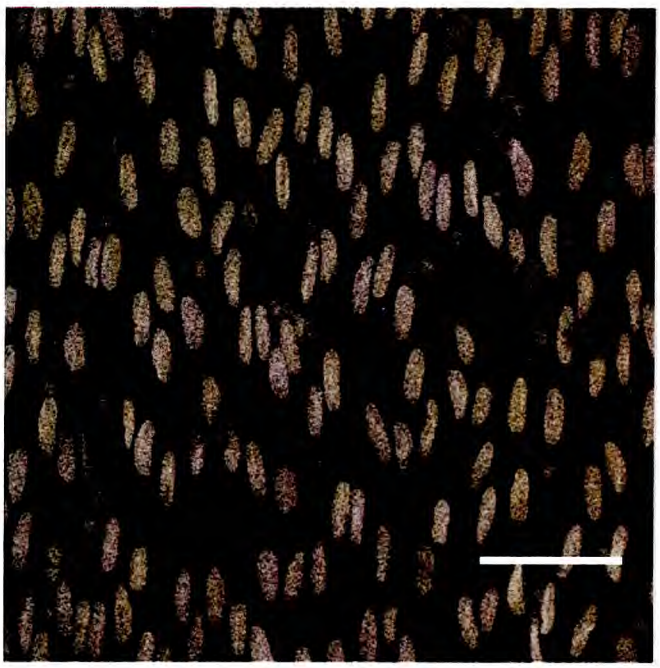

Figure 2.15. *In vivo* propidium iodide staining of the endothelium of rabbit aorta treated post-staining with RNase. $\lambda_{excitation}$ 543nm, $\lambda_{emission}$ 600-640nm. Bar = 50μm.

2.4 Discussion

Hematoxylin staining was improved by the addition of acid to Harris hematoxylin as it is a regressive stain and is differentiated by acids to remove excess dye (Sigma-Aldrich, 2003). Gills No.1 hematoxylin formulation is a progressive stain and selectively stains nuclear chromatin, and perhaps it is this selectivity that led to better definition nuclei. However, it was not possible to refine staining with hematoxylin to the point where automated image analysis could be undertaken.

Staining with acridine orange did enable visualisation of endothelial cell nuclei. Incubating the tissue with RNase prior to staining improved the definition of ECn, compared to not using RNAse, or to staining *in vivo* followed by RNase treatment. Treatment post-staining slightly alleviated the problems of SMCn being stained, however the amount of autofluorescence within the arterial wall increased, leading to images with a grainy appearance. Images would again only have enabled manual, not automated, measurement of ECn.

When viewing whole mount tissue by conventional epifluorescence or confocal microscopy, the use of propidium iodide in conjunction with prior ribonuclease incubation produced images of endothelial cell nuclei with sharply defined edges, without the presence of shadows or tails from the endothelial cells, and with minimal background staining. It was therefore concluded that images taken after such treatment could be thresholded and analysed semi-automatically as described elsewhere.

It was found that the *in vitro* PI staining method could be carried out on tissue viewed on either a confocal microscope or a standard fluorescent microscope system using filters for rhodamine. The benefits of using the confocal microscope system were that the wavelengths of emission could be finely adjusted to produce the clearest images with minimal background noise, and the depth the microscope viewed into the wall could be adjusted to focus on ECn rather than SMCn (if the section of tissue was flat). The benefits of the standard fluorescent microscope system were that photobleaching did not occur as rapidly, and they are less expensive to run.

In summary, staining with hematoxylin could be used as a rapid test to determine whether the endothelium is intact and that no cells are missing, but without manual measurements could not be used to determine parameters of nuclei. Staining the artery *in vitro* with propidium iodide, having first made the cells more permeable using Triton X-100 and treating the tissue in RNase, proved to be the most consistent method for staining EC nuclei with minimal background noise, and the sharpest definition of nuclear edges. This technique was therefore used for all subsequent endothelial cell nuclear staining. We have shown that it is very difficult to prevent staining of underlying SMC nuclei, due the curvature of the wall, so alternative methods (confocal microscope optical stacks, and the Endothelial Stick and Rip (EStAR) technique as discussed later) had to be developed to remove these from the image analysis.

Chapter 3: Changes in nuclear shape around intercostal branch ostia in mice, determined by confocal microscopy

3.1 Introduction

3.1.1 Mouse models of atherosclerosis

In the wild, mice tend to consume a low-fat diet and they have relatively high levels of high density lipoprotein (HDL) and relatively low levels of very low density lipoprotein (VLDL) and LDL (Getz and Reardon, 2006). Perhaps for the latter reason, they are highly resistant to the development of experimental atherosclerosis; lesions can only be induced by feeding a high fat diet with toxic additives (Lichtman *et al.*, 1999), or by inducing plasma cholesterol concentrations >300mg/dL (Getz and Reardon, 2006).

Alternative murine models of atherosclerosis have been obtained by gene knockouts: low density lipoprotein receptor ($LDLR^{-/-}$), apolipoprotein E ($ApoE^{-/-}$) and $LDLR^{-/-}$ /$ApoE^{-/-}$ double knockout mice are now commonly used models of hypercholesterolemia and atherosclerotic lesion development (Johnson and Jackson, 2001). LDL receptors are located on cell surfaces, and are responsible for the internalisation of lipoproteins. This enables cholesterol to be supplied to the cells, but also removes cholesterol-rich lipoprotein particles from the circulation, predominantly in the liver (Alberts *et al.*, 1994). Hence a deficiency in LDL-receptors causes an increase in circulating cholesterol. ApoE is a high affinity ligand for the chylomicron-remnant receptor that enables uptake by the liver of cholesterol-rich apo-E containing particles. Removing ApoE leads to the accumulation of atherogenic cholesterol-rich remnants in the circulation (Zhang *et al.*, 1992).

In $LDLR^{-/-}$/$ApoE^{-/-}$ mice, using a frequency mapping method, lipid deposits have been shown to completely surround the intercostal branch ostia (although deposits had twice the frequency upstream than downstream); there was no significant change in pattern with age (McGillicuddy *et al.*, 2001). Thus these double knockout mice develop raised lesions at these sites which are similar to the raised "volcano" lesions that are found surrounding equivalent ostia of aged humans ((Mitchell and Schwartz, 1965), cited in Weinberg, 2002). Interestingly, the same authors also discovered a chevron pattern of lipid deposition upstream of some ostia, but no explanation was provided for their presence.

Until recently, little was known about how shear stress values vary throughout the vasculature of mice, or how the endothelium responds to the applied shear. The widespread and increasing use of knockout mice as models of atherosclerosis makes this an important consideration. It has been shown *in vivo* that endothelial cell nuclei align with the predominant flow direction (Flaherty *et al.*, 1972) and elongate in response to increased shear stress levels in mice (Langille and Adamson, 1981), rabbits (Nerem *et al.*, 1981) and dogs (Levesque *et al.*, 1986). Recently, preliminary data have become available concerning overall shear levels (Weinberg and Ethier, 2007) predicting, using allometric arguments, that mice have a 20-fold-higher aortic wall shear stress than people. Other studies have used micro-CT and ultrasound methods (Suo *et al.*, 2007) combined with numerical modelling (Feintuch *et al.*, 2007) to develop CFD models of the mouse aorta, and these also found wall shear stress values in mice to be higher than those found in humans.

3.2 Mouse Hypothesis

We predict from the relatively uniform pattern of atherosclerosis around branches in knockout mice, that in wild-type mice there will be little spatial variation in shear stress surrounding the intercostal branch ostia. It is also predicted that there will be an age-related change in shear stress values caused by the stiffening of arteries that is seen in mice (Reddy *et al.*, 2003), rats (Cox, 1977), pigs (Greenwald *et al.*, 1982) and monkeys (Pissinatti *et al.*, 2000). The increase in aortic stiffness may also cause changes to the blood flow into and around intercostal branch ostia. It is also predicted that flow patterns will correlate with the chevron shaped pattern of disease seen in ApoE knockout mice by McGillicuddy (McGillicuddy *et al.*, 2001).

3.3 Methods

3.3.1 Animal Procedures

All animal procedures complied with the Animal (Scientific Procedures) Act 1986. Endothelial nuclei were examined in normal mice (University of Reading strain) aged 6-10 weeks (n=4) or 18-20 weeks (n=5) (i.e. 1.5-2.5, and 4.5-5 months). For comparison, and to check whether the new technique employed gives previously observed age-related changes in nuclear morphology of rabbit endothelium, male New Zealand White rabbits (Harlan Interfauna strain) aged 6 weeks (n=3), 17 weeks (n=3), 38 weeks (n=3) or ≥112 weeks (n=2) (i.e. approximately 1.5, 4, 9 and ≥24 months) were also examined. All animals were fed a standard laboratory diet without added fat.

3.3.2 Tissue Preparation

Aortas were fixed in either formalin or Karnovksy's fixative as previously described. Having remained in fixative for at least 16 hours, aortas were equilibrated in PBS for one hour. The adventitia of fixed aortas was removed by dissection and side branches were cut as close to their origin as possible so that the remaining stubs did not distort the main vessel when it was mounted for *en face* viewing. Mouse aortas were examined whole whereas the larger rabbit aortas were cut perpendicular to the longitudinal axis to produce rings each containing a pair of intercostal branches.

3.3.3 Nuclear Staining

Aortas and aortic rings were permeabilised with Triton X-100 (Sigma, 0.2%, 30 s), incubated in ribonuclease A (RNase) (Sigma, 0.01%, 10 min at 37 °C) to remove RNA but not DNA, and stained with propidium iodide (Molecular Probes, 1 mg/mL, ~0.5 s). They were then cut along the longitudinal axis opposite the branch sites before being mounted in PBS, luminal surface down, in cover-slip bottomed petri dishes.

The luminal surface around intercostal branch ostia was viewed *en face* with an inverted confocal microscope (TCS NT, Leica Microsystems) using a 20x immersion objective. Propidium iodide fluorescence was imaged using 543 nm excitation and 600-640 nm emission wavelengths. For most samples, wall autofluorescence was also imaged, using 488 nm excitation and 500-580 nm emission wavelengths. A stack of optical slices were

obtained, each 750μm x 750μm in area. This field of view allowed the whole mouse branch to be visualised. Control regions at least one branch diameter away from the ostia were also imaged. For the larger rabbit branches, regions 750μm x 750μm in areas upstream and downstream of the ostium were imaged separately.

3.3.4 Image processing and analysis

Images were initially processed using Photoshop (Version 7.0, Adobe Systems Incorporated). Individual slices from each stack were converted to grayscale images, and noise was reduced with a median filter (one-pixel radius). They were then binarised using a grey level of 70 (grey level range 0-255), and endothelial cell (EC) nuclei were selected manually. EC nuclei from every slice in a stack were copied onto a blank canvas to produce a montage of the endothelial surface in a single image, despite the irregular surface height in the original 3-dimensional data set (Fig. 3.1).

For quantitative analysis of nuclei around mouse ostia, montages were divided into eight regions of 200μm x 200μm (Fig. 3.1 inset). The region upstream of the branch frequently contained an arterial cushion (AC) (Fig. 3.2); nuclei covering this cushion were analysed separately. For the rabbits, analysis was restricted to single 600 x 600 μm areas upstream and downstream of the ostia, each offset approximately 75μm from the ostial lip to avoid regions of high curvature.

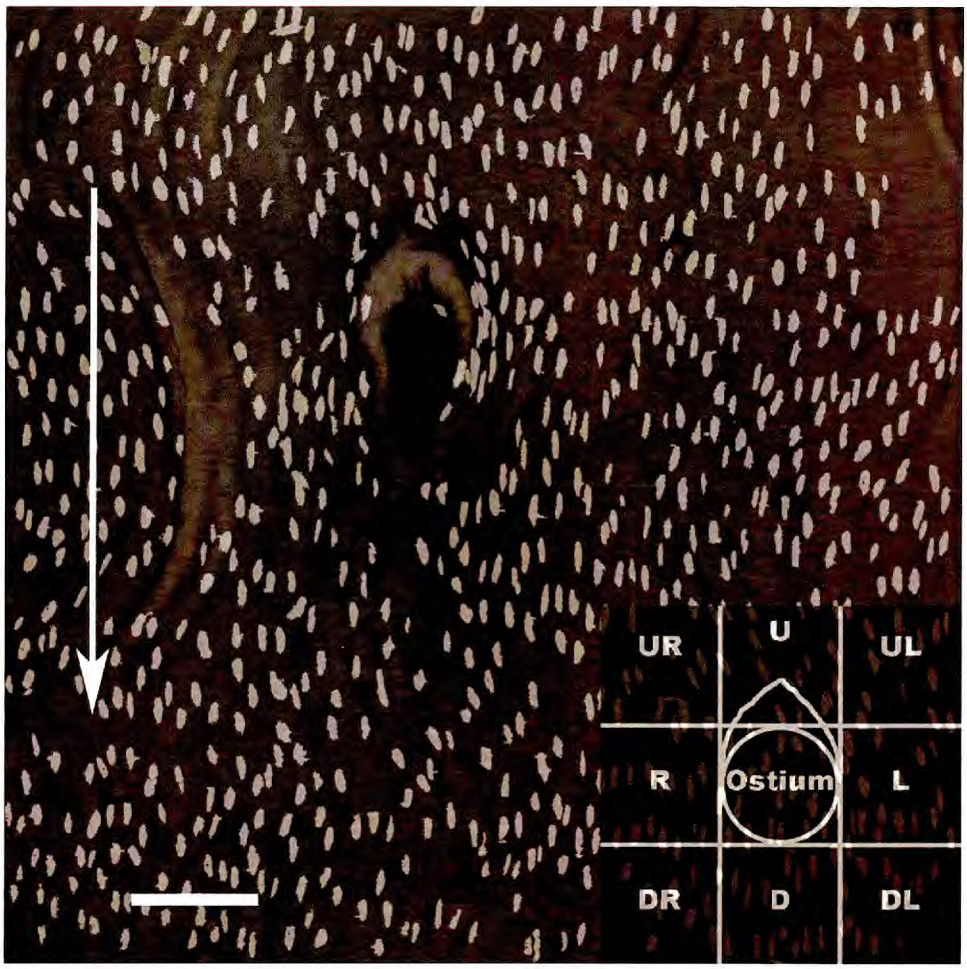

Fig. 3.1. *En face* montage of propidium iodide-stained endothelial nuclei around the origin of a mouse aortic branch. Arrow indicates direction of mean aortic blood flow. Scale bar = 100μm. Inset: regions for which mean nuclear shape and orientation were calculated ("UR", upstream anatomical right, etc.). Region "U" excludes the arterial cushion, which was analysed separately.

Fig. 3.2. *En face* view of confocal image stack showing tissue autofluorescence around the origin of a mouse aortic branch. A raised arterial cushion resembling the prow of a boat is present upstream of the ostium. Arrow indicates direction of mean aortic blood flow. Scale bar = 100μm.

All images were analysed in ImageTool (Version 3.00, UTHSCSA) using the "Analyze" command to obtain the length of the major axis ("length") and minor axis ("width"), the length-to-width (LW) ratio, and angle of orientation of each object in the image. Results tables were saved as text files to be transferred into the software package, Excel (2003, Microsoft Office). A large number of equations had to be written, columns added/removed etc. to enable analysis. These were automated using Macro codes developed using Excel's script language, Visual Basic (see Appendix C for Macro codes). ImageTool measured the angle of each object from the horizontal axis of the image to the major axis of the object (length of the nucleus) i.e. if a nucleus was aligned along the horizontal axis it would be assigned a value of zero degrees. Since we were interested in the angle of the nuclei with respect to the longitudinal axis of the aorta (which is from top to bottom of images), it was necessary to convert the data so that if a

nucleus were aligned along the longitudinal axis rather than the horizontal axis it would be assigned a value of zero degrees. This was done using an equation stating that:

IF (Angle>0) then (Angle*-1) +90
IF (Angle<0) then (Angle*-1) -90

Using these equations, nuclei with their upstream end leaning to the left of the longitudinal axis, as viewed on the screen, were assigned negative angles, and conversely, those with their upstream end leaning to the right were assigned positive angles (Fig. 3.3).

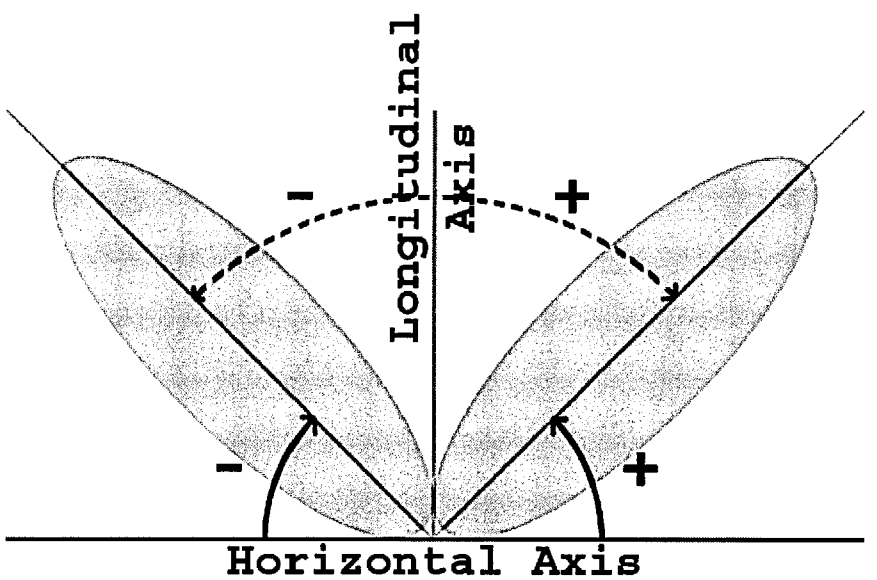

Fig. 3.3. Diagram showing the sign (+ or -) of the angle of endothelial cell nuclei measured by ImageTool from the horizontal axis to the major axis of the nuclei (solid arrows) and after angles were adjusted to measure from the longitudinal axis of the artery to the major axis (dashed arrow).

Orientations were normalised by averaging values for all nuclei around a branch, and subtracting this mean from all individual values. This procedure removed biases that would otherwise have been caused by inaccuracies in cutting or mounting the tissue, but would remove any overall non-axial orientation, for example arising from helical flows down the aorta.

When analysing images in ImageTool, the software could not distinguish between individual nuclei, pairs of nuclei very close together with their edges touching, or background noise. Thus, results contained data for these objects as well, which would produce inaccuracies. This was overcome by excluding objects that were too small or too large to be nuclei. A search through the literature for previously published parameters for endothelial cell nuclei was carried out (Table 3.1).

Table 3.1. Previously published parameters for endothelial cell nuclei.

Investigator	**Nuclear Length (μm)**	**Nuclear Width (μm)**	**Species**
(Flaherty *et al.*, 1972)	15	7	Dog
(He, 1998)	25	6	Frog (32-39D vessel)
	16	12	Frog (48-53D vessel)
	13	8	Hamster
(Hossler, 1998)	16	5	Duckling cast
Average	**17**	**8**	

Average nuclear length = 17μm = 46.42 pixels

Average nuclear width = 8μm = 21.85 pixels

By trial and error it was found that a 50% variation above and below the literature average encompassed changes in elongation caused by varying shear stresses but excluded most noise artefacts and multiple nuclei.

So,

A 50% variation above and below average nuclear length = 69.63 pixels and 23.21 pixels respectively.

A 50% variation above and below average nuclear width = 32.77 pixels and 10.92 pixels respectively.

Using these values it was then possible to calculate the area of an ellipse with a 50% variation around the average using an online ellipse calculator (Cleave Books, 2004) that used the equation:

Area = π x ((0.5 x ellipse's major axis) x (0.5 x ellipse's minor axis)).
Therefore,
Maximum and minimum area of ellipse = 1195.5 pixels^2 and 398.5 pixels^2

A macro code was written that filtered the data obtained in ImageTool to exclude any objects that had lengths, widths or areas outside this range, adjusted the angle of orientation to remove biases, and averaged each parameter for the regions of interest (Appendix C -Macro 1).

3.3.5 Analysis of arterial cushions

It was observed that immediately upstream of mice intercostal branches there was an arterial cushion (AC), raised above the luminal surface of the arterial wall, with a triangular shape resembling the bow of a boat, with the endothelial layer at the entrance to the branching intercostal artery representing the "deck" of the boat. The morphology of both the AC and its overlying endothelial cell nuclei were analysed.

3.3.6 Measurement of arterial cushions and branch ostia

Images of tissue autofluorescence, obtained using the confocal microscope by exciting tissue at 488nm and detecting emission at 500-580nm were opened in Photoshop and converted to grayscale images, and the Auto Levels function was applied. A median noise reduction filter (one pixel radius) was applied before the image was copied into a new blank canvas. The next image in the optical stack was then edited in the same way before being copied into the new canvas on top of the first. The top image was then made transparent (5%) so both layers could be seen. This process was repeated until every image in the stack had been added on top and made transparent enabling the whole artery wall including the branch and raised region to be visualised. All images were opened on the same computer, more importantly using the same size visual display unit (monitor), and the images were zoomed to 33.3% to enable the ostium and AC to fit

within the constraints of the display. Acetate transparencies were stuck over the screen and the outline of the ostium and raised region were traced. Acetates were photocopied without altering their size and photocopies were scanned, using a flatbed scanner.

Scanned images were opened in Photoshop before being converted into grayscale images, and median noise reduction (1 pixel radius), dust and scratches (1 pixel radius, threshold 0) and despeckle filters applied. When drawing outlines of the AC and ostia, the lines did not always meet exactly. This would have prevented object area analysis being performed accurately so any line breaks were filled in manually. To determine the area of the AC and branch ostia, edited images were opened in ImageTool and the "Find Objects" function performed at an intensity in the range of 1-255, and 0-250 (AC and branch ostium separately, and AC and branch ostium combined respectively (Fig. 3.4a,b). This enabled measurement of the area of the AC, branch ostium and the two combined. The AC entrance length (distance from the tip of the AC to the most proximal region of ostium), AC width, ostial length and ostial width were measured using the "measure tool" in Photoshop (Fig. 3.4c). All values were measured in pixels and therefore had to be converted into micrometers.

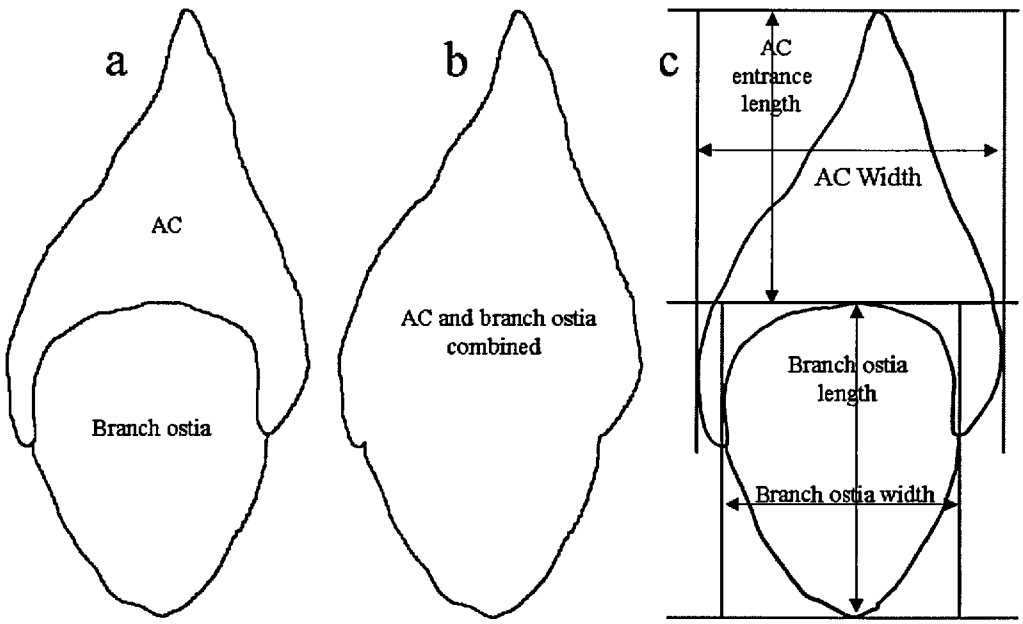

Figure 3.4a) outline of the area of the branch ostia and the arterial cushion (AC) when measured separately, b) outline of the area of the branch ostia and the AC when measured together, c) dimensions measured manually of the branch ostia and the AC.

3.3.7 Analysis of endothelial nuclei overlying arterial cushions

EC nuclei overlying the AC showed a great deal of variability in orientation compared to normal endothelium and were found in more focal planes due to the sloping of the AC into the intercostal ostium. This prevented the automated analysis of their shape that was possible in other regions. To determine nuclear morphology over the AC, images from optical stacks containing AC nuclei were opened on-screen. A transparency was placed over the screen, as when measuring AC dimensions, and nuclear outlines traced. The next image in the stack was opened and nuclei traced. This was continued until no more nuclei were visible. Using this method an accurate picture of the nuclei of the AC was produced. As with measurement of dimensions of AC, transparencies were scanned and images opened and edited in Photoshop.

3.3.8 Image analysis software

Initially V++ (Digital Optics) was used to measure nuclear morphology. However having analysed nuclei surrounding a large proportion of the branches, an inconsistency was discovered: having analysed two images twice by mistake, the output was slightly different the second time despite nothing having been changed within the image. Testing was carried out to determine where the fault lay.

3.3.8.1 V++ Validation - Test One

The nuclear image was printed and the major and minor axis (longest axis of the object, and object's widest point at 90° to the major axis respectively) were measured for a sample of the nuclei. It was found that the measurements by hand were approximately double those analysed by V++. It was thought this could be caused by one or more of the following, 1) the edge of the analysed nuclei had a ruffled appearance (i.e. the edge was not smooth) and when measuring by hand the axes may therefore have been slightly different from those measured by the software. This ruffled appearance was initially thought to be an artefact formed during the process of thresholding nuclei before selecting them from the optical slices produced during confocal imaging. However, images of nuclei found in the literature also appear to have a ruffled surface (Masuda *et al.*, 2003). 2) To derive the shape parameters, V++ takes measurements from the 2^{nd} moment of inertia of a perfect ellipse that it tries to fit to each object. This will

introduce inaccuracies as nuclei are rarely a perfect ellipse. 3) V++ assumes edges are perfectly smooth.

3.3.8.2 V++ Validation – Test Two

The next step to determine where the fault lay was to draw shapes of a known LW ratio and orientation (using Microsoft PowerPoint) and then analyse them. Squares and rectangles, with or without rounded corners, circles and ellipses were drawn (Fig. 3.5) for analysis with V++. Each image was analysed twice, and again, gave slightly differing results each time. The LW ratios were also wrong for some of the objects and the orientations were not accurate.

3.3.8.3 V++ Validation – Test Three

The images drawn in test 2 were used again, but this time were analysed after having been rotated (using Photoshop) by 5° and 90° (Fig. 3.5). As they were the same objects, only rotated, the LW ratio should have been the same; however they were different. Having decided V++ had produced inaccurate results a new software analysis tool was selected (ImageTool, UTHSCA) and validated.

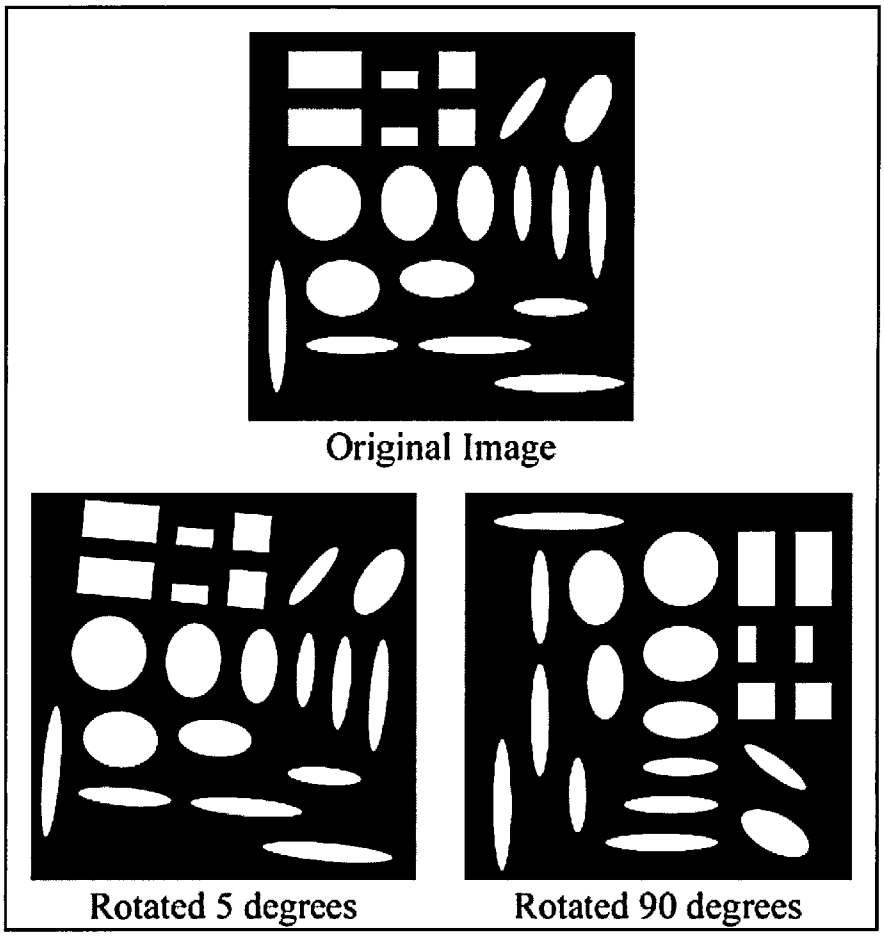

Fig. 3.5. Images used in V++ validation – Test 2 and 3. The original image was rotated by 5 and then 90 degrees clockwise before being analysed.

3.3.8.4 ImageTool Validation

Test three was carried out again on the images in Fig. 3.5 using ImageTool, and the results produced were much more accurate (with a few degrees error for orientation). Another image was drawn in PowerPoint containing replicates of the same size ellipse rotated by known angles (Fig 3.6), and the image was analysed in ImageTool. The results were accurate (again within a few degrees error). Finally, ellipses of known LW ratio and angle were drawn and analysed. Again, the results were accurate. It was found that inaccuracies occurred when analysing a circle, however that is reasonable as a circle does not have a definite major or minor axis, and it is highly unlikely that a nuclei will ever be a perfect circle.

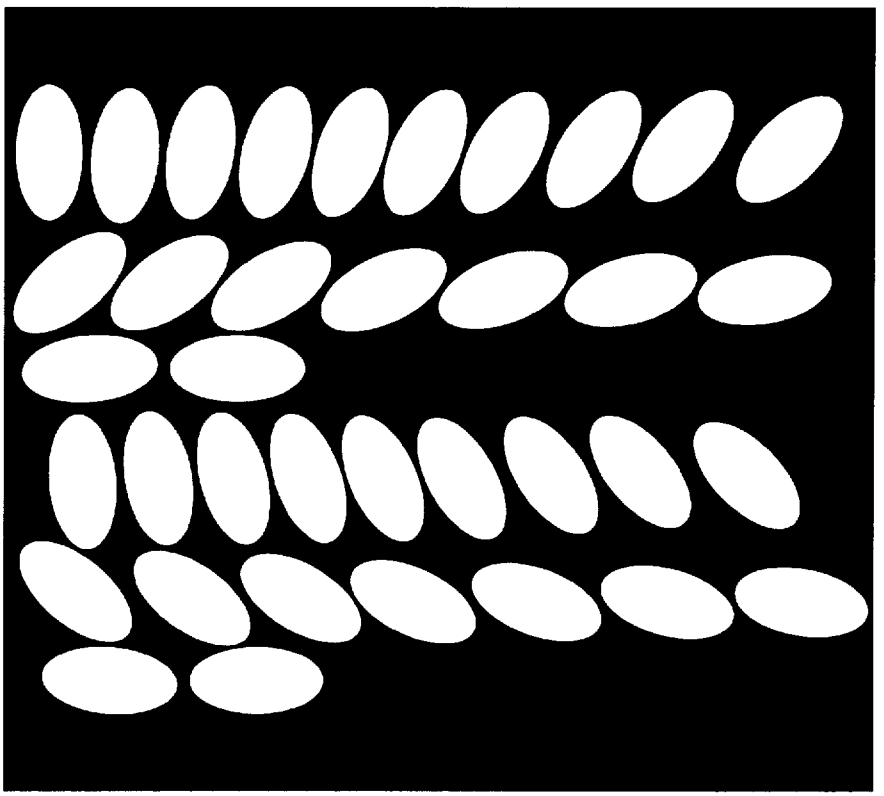

Fig. 3.6. Image used in ImageTool validation. Ellipse has a LW ratio of 2.0 and has been rotated by known angles.

3.3.9 Statistical Analysis

Data structure: two age groups were considered – 6-10 weeks and 18-20 weeks. In the young age group there were 4 mice and in the mature group there were 5 mice. Between 7-15 intercostal branches from the aorta of each mouse were examined (8-14 in young, 42 in total; 7-15 in mature, 57 in total). The branches were randomly selected from the 16 present in each animal. Eight main anatomical regions were examined around each branch (three upstream, three downstream and one at each lateral margin); for some analyses, a region corresponding to the intimal cushion and a control region (away from the branch) were also included. Within each of these anatomical regions, the morphology of around 30 nuclei were examined (except that numbers were sometimes smaller for the arterial cushion – see below). Morphological parameters included nuclear length-to-width ratio and the angle between the nuclear long axis and the longitudinal axis of the aortic segment. Because of the large sample size within each region, results for each parameter were aggregated before statistical analyses were

conducted: only the mean value (e.g. of length-to-width ratio or angle) for each region was used. Statistical tests were conducted to determine whether there was a significant effect on each parameter of age or region, and whether there was a significant interaction between effects of age and region (which would imply an effect of age on the anatomical pattern of that parameter).

The statistical test used was a general linear model univariate analysis of variance (SPSS Version 14.0) incorporating a nested design whereby mice were nested within age, and branches were in turn nested within mice. If this showed an overall significant result, the significance of differences between individual regions was determined using a post-hoc Tukey test, having first split the data by age. Effects of age on the dimensions of the branch and arterial cushion and effects of species were assessed using a Student's unpaired t-test. Data are presented as mean ± SEM. Results were deemed significant if $p<0.05$.

3.4 Results

3.4.1 Nuclear length:width ratios in mice

Mean nuclear LW ratios are shown for immature and mature mice in table 3.2 and figure 3.7. There were no overall significant changes in mean LW ratio with age (P=0.462), although there was a trend for mature mice to have more elongated nuclei in each of the 8 regions defined in figure 3.1. The mean nuclear LW ratios for immature (n = 297 regions), and mature (n = 426 regions) were 2.33 ± 0.02 and 2.49 ± 0.02 respectively (mature nuclei 6.9% more elongated) for the 8 regions. There was a highly significant effect of region (P<0.0005). The interaction between age and region approached significance (P=0.053) possibly providing evidence for a change in pattern of LW ratios with age.

When nuclei in non-branch regions were included in the analysis, the effect of age remained insignificant (P=0.418), the effect of region remained highly significant (P<0.0005), and the interaction between age and region remained insignificant (P=0.055). The mean nuclear LW ratios for immature and mature mice were 2.33 ± 0.02 and 2.49 ± 0.02 respectively (6.9% difference, n = 308 and 434 regions respectively) for the 8 regions and the nuclei in non-branch regions.

When nuclei over the arterial cushion were included in the analysis, the effect of age remained insignificant (P=0.442), the effect of region remained highly significant (P<0.0005), but the interaction between age and region became significant (P=0.030). The mean nuclear LW ratios for immature and mature mice were 2.27 ± 0.02 and 2.43 ± 0.02 respectively (a 7.0% difference, n = 333 and 475 regions respectively) for the 8 regions, including the nuclei overlying the AC.

When nuclei in both non-branch regions and over the AC were included, the effect of age remained insignificant (P=0.393), effect of region remained highly significant (P<0.0005) and the interaction between age and region was significant (P=0.026). The mean nuclear LW ratios for immature and mature mice were 2.27 ± 0.02 and 2.43 ± 0.02

respectively (7.0% difference, n = 344 and 483 regions respectively) for the 8 regions and the nuclei in non-branch regions and overlying the AC.

Nuclei in non-branch regions were 3.0% less elongated than nuclei in branch regions in immature mice. This was reversed in mature mice, where there was a 12.0% increase in LW ratio in non-branch regions when compared to branch regions.

The data were split by age to determine differences in nuclear parameters in immature and mature mice separately.

3.4.1.1 Immature nuclear length:width ratios

The effect of region was highly significant ($P<0.0005$) for immature mice, and including or excluding the nuclei over the AC and/or non-branch regions did not affect this. Mean values ranged from 2.23 ± 0.04 ("U", n = 38 branches) to 2.54 ± 0.04 ("R", n = 37 branches) for the 8 main regions (13.9% difference).

Nuclei in the lateral regions ("L" and "R") were significantly more elongated ($P<0.0005$) than nuclei in all other regions but were not different from each other ($P=1.000$). Nuclei overlying the AC were significantly less elongated than nuclei in all other regions ($P<0.0005$).

3.4.1.2 Mature nuclear length:width ratios

The effect of region was highly significant ($P<0.0005$) for mature mice, and including or excluding the nuclei over the AC and/or non-branch regions did not affect this. Mean values ranged from 2.31 ± 0.05 ("D", n = 55 branches) to 2.64 ± 0.06 ("L", n = 56 branches) for the 8 main regions (14.3% difference).

Nuclei in the lateral regions ("L" and "R") were significantly more elongated ($P<0.0005$) than nuclei in all other regions except nuclei in the upstream left ("UL") and non-branch regions ($P>0.1$). The LW ratio of nuclei in the region downstream ("D") of the branch ostia was significantly higher than nuclei overlying the AC ($P<0.0005$), but lower than all other regions ($P<0.05$), with the exception of the upstream ("U") region

(P>0.05). Nuclei overlying the arterial cushion were significantly less elongated than nuclei in all other regions (P<0.0005), whilst nuclei in the non-branch region were significantly more elongated (P<0.05) than all other regions, with the exception of lateral regions as previously mentioned.

Table 3.2. Mice nuclear length:width ratios where n equals the number of branches

Region	Immature		Mature	
	Mean	SEM	Mean	SEM
UR	2.28	0.05	2.46	0.06
U	2.23	0.04	2.42	0.06
UL	2.29	0.04	2.52	0.05
R	2.54	0.04	2.62	0.06
L	2.52	0.04	2.64	0.06
DR	2.25	0.04	2.45	0.06
D	2.26	0.04	2.31	0.05
DL	2.25	0.04	2.48	0.05
Arterial cushion	1.78	0.04	1.88	0.02
Non-branch	2.26	0.06	2.79	0.12
Total (excl. AC + non-branch)	2.33	0.02	2.49	0.02
Total (incl. AC)	2.27	0.02	2.43	0.02
Total (incl. non-branch)	2.33	0.02	2.49	0.02
Total (incl.AC + non-branch)	2.27	0.02	2.43	0.02

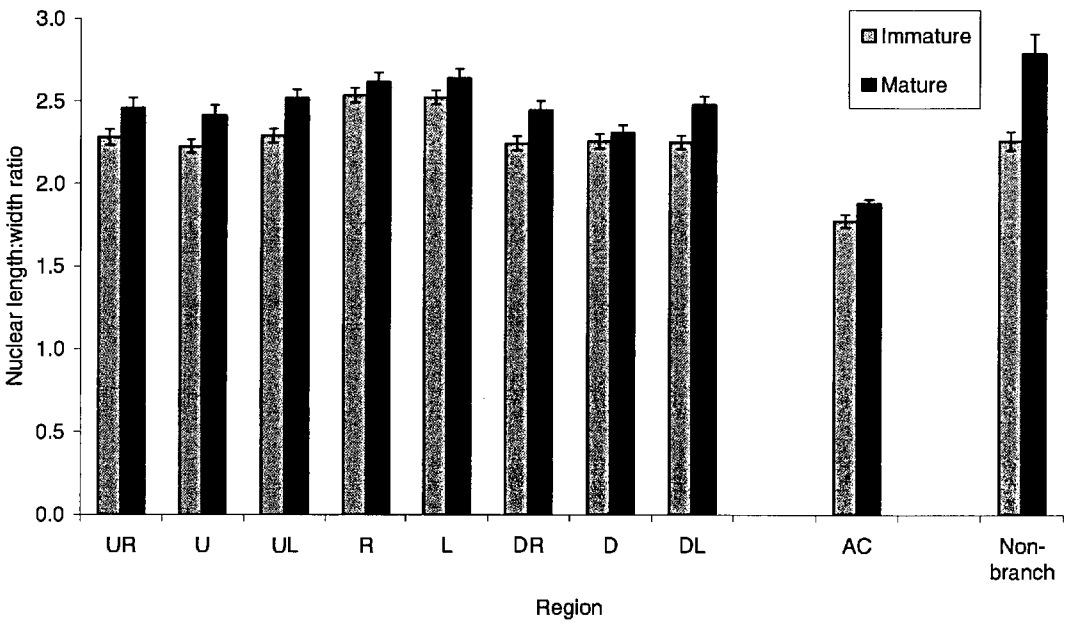

Fig. 3.7. Mice nuclear LW ratios in the 8 regions defined in Fig. 3.1, over the arterial cushion and in non-branch regions. Bars show means ± SEM (n = number of branches).

3.4.2 Nuclear orientations in mice

Normalised mean nuclear orientations are shown for immature and mature mice in Table 3.3 and Fig. 3.8. When the 8 main regions were analysed it was found that there was no overall significant change in mean orientation with age (P=0.345), however there was a highly significant effect of region (P<0.0005). There was no significant interaction between age and region (P=0.096) suggesting there was no change in the pattern of nuclear orientation with age. When nuclei overlying the AC were included in the analysis, the effect of region remained significant (P<0.0005) and the effect of age and the age*region interaction remained non-significant (P=0.552 and 0.145 respectively).

Lines illustrating the angle of orientation of nuclei in each of the 8 main regions surrounding the branch ostia (excluding the nuclei on the AC) are shown for immature and mature mice in Fig. 3.9. Each line is orientated by the angle of the mean for the nuclei within each region. It is presumed that the blood flow is from top to bottom over each region that surrounds the branch ostia, but this is only an assumption, hence the lack of direction to the lines. The nuclei deviate from the longitudinal axis by very small amounts.

Nuclei in non-branch regions were not included in the analysis; since they were normalised to give an average value of zero degrees, nothing could be gained from such an analysis.

The mean nuclear orientation for all mice was 0 degrees, as the values had been normalised. The minimum and maximum orientations for the main 8 regions in immature mice were -3.01 ± 1.21° ("D", n = 33 branches) and 5.09 ± 1.27° ("UR", n = 38 branches) respectively. The minimum and maximum orientations for mature mice were -2.48 ± 1.02° ("DR", n = 51 branches) and 2.27 ± 0.84° ("R", n = 51 branches) respectively. The orientations of nuclei over the AC were 6.89 ± 1.69° (n = 36 branches) and 4.50 ± 1.67° (n = 49 branches) for immature and mature mice respectively.

3.4.2.1 Immature nuclear orientation

The effect of region on nuclear orientations in immature mice was highly significant ($P<0.0005$) when looking at the 8 main regions with or without nuclei over the AC, although as mentioned previously, deviations away from the longitudinal axis were small.

Nuclei in region "UR" were oriented to the anatomical left of the longitudinal axis to a greater extent ($P<0.05$) than regions "UL", "D" and "DR", and the orientation of nuclei overlying the AC were significantly different to those in regions "UL", "D", "DR", "DL", "R" and "L".

3.4.2.2 Mature nuclear orientation

The effect of region on nuclear orientations in mature mice was highly significant ($P<0.005$) when looking at the 8 main regions with or without nuclei over the AC.

Nuclear orientations in region "R" were significantly different ($P<0.05$) to those found in regions "UL" and "DR", and nuclei over the AC were significantly different ($P<0.05$) to those in regions "U", "UL", "D", "DR" and "L".

Table 3.3. Mice nuclear orientation (degrees) (normalised by a constant so the mean equals 0°) where n equals the number of branches.

Region	Immature		Mature	
	Mean	SEM	Mean	SEM
UR	5.09	1.27	2.19	0.97
U	1.57	1.11	-0.36	0.97
UL	-1.60	1.27	-2.42	0.84
R	-0.53	0.87	2.27	0.84
L	0.49	0.89	-0.26	0.86
DR	-2.80	1.60	-2.48	1.02
D	-3.01	1.21	-0.35	0.87
DL	0.15	1.38	1.54	0.84
AC	6.89	1.69	4.50	1.67
Total (excl. AC + non-branch)	0.00	0.45	0.00	0.33
Total (incl. AC)	0.74	0.45	0.46	0.34

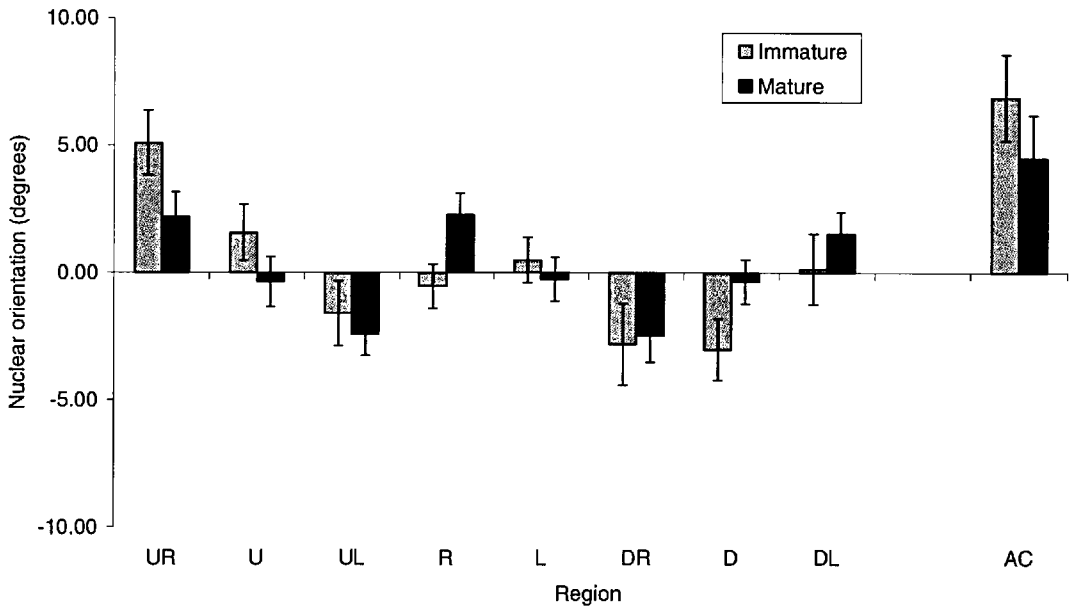

Fig. 3.8. Mice nuclear orientations in the 8 regions defined in figure 3.1, and over the arterial cushion. An angle of zero degrees indicates nucleus is aligned along the longitudinal axis of the artery. Bars show means ± SEM (n = number of branches).

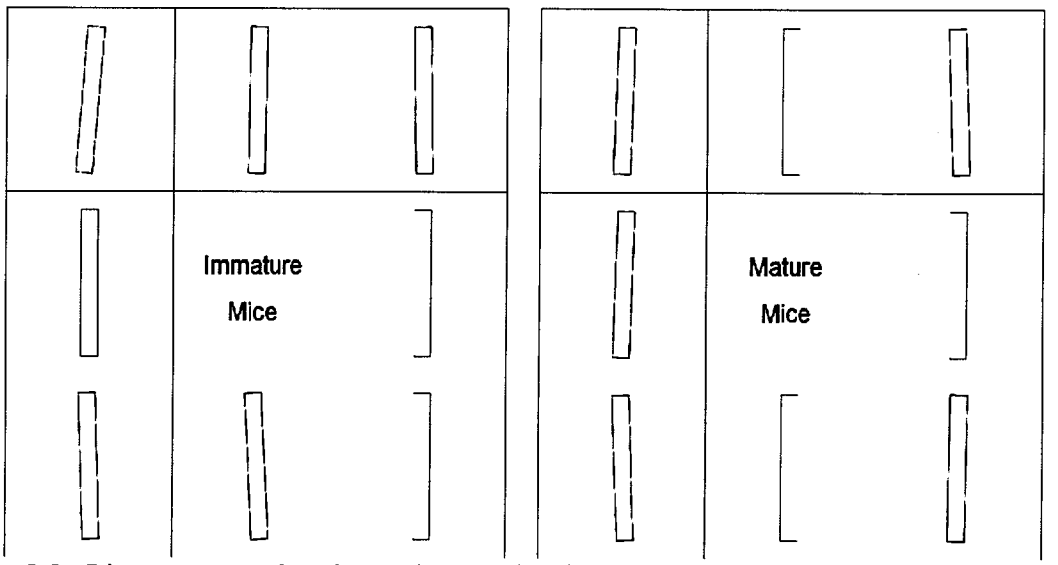

Fig. 3.9. Lines representing the nuclear angle of orientation surrounding branch ostia of immature and mature mice. Time-averaged blood flow is from top to bottom. The ostium is located in the central square in each image. Each square equates to a region measuring 200μm*200μm.

3.4.3 Nuclear lengths in mice

Mean nuclear lengths are shown for immature and mature mice in Table 4 and Fig. 3.10. There were no overall significant changes in mean length with age (P=0.269), although there was a trend for mature mice to have longer nuclei in each of the 8 regions defined in Fig. 3.1. There was a highly significant effect of region (P<0.0005) but there was no significant interaction between age and region (P=0.752). Data for nuclear lengths in non-branch regions or nuclei over the AC are not available.

The mean nuclear lengths for immature and mature mice were 17.03 ± 0.10 μm and 18.08 ± 0.08 μm respectively (nuclei in mature rabbits were 6.2% longer, n = 297 and 426 regions respectively) for the 8 regions in Fig. 3.1(inset).

3.4.3.1 Immature nuclear length

The effect of region was highly significant ($P<0.0005$) for immature mice. Values ranged from 16.30 ± 0.27 μm ("U", n = 38 branches) to 18.01 ± 0.26 ("L", n = 38 branches), a 10.5% increase.

Nuclei in the "R" region were significantly longer than those in regions "U", "UR", "DR" and "DL" ($P<0.05$), and nuclei in the "L" region were significantly longer than in all other regions ($P<0.005$) (except "R"). Nuclei in "U" were significantly shorter than nuclei in "UL" ($P<0.05$).

3.4.3.2 Mature nuclear length

The effect of region was also highly significant ($P<0.0005$) for mature mice. Values ranged from 17.45 ± 0.21 μm ("U", n = 52 branches) to 19.08 ± 0.19 ("L", n = 56 branches), a 9.3% increase in length.

Nuclei in "R" region were significantly longer ($P<0.01$) than those in all regions except "L" and "UL", however the difference was approaching significance for "UL" ($P=0.062$). Nuclei in "L" were significantly longer ($P<0.005$) than those in all other regions except "R". Nuclei in "D" were significantly shorter than nuclei in the "UL" regions ($P<0.05$).

Table 3.4. Mice nuclear length (μm), where n equals the number of branches.

Region	Immature		Mature	
	Mean	SEM	Mean	SEM
UR	16.68	0.30	17.87	0.23
U	16.30	0.27	17.45	0.21
UL	17.05	0.29	18.11	0.22
R	17.65	0.28	18.65	0.22
L	18.01	0.26	19.08	0.19
DR	16.78	0.28	17.90	0.21
D	16.92	0.22	17.54	0.18
DL	16.84	0.25	17.98	0.21
Total	17.03	0.10	18.08	0.08

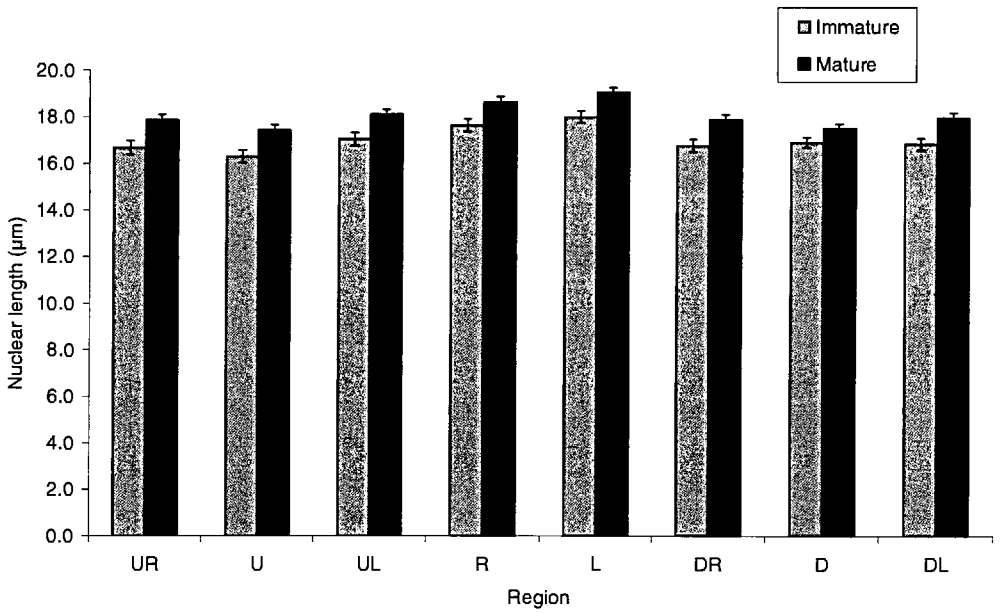

Fig. 3.10. Mice nuclear lengths (µm) in the 8 regions defined in Fig. 3.1. Bars show means ± SEM (n = number of branches).

3.4.4 Nuclear widths in mice

Mean nuclear widths are shown for immature and mature mice in Table 3.5 and Fig. 3.11. There were no overall significant changes in mean width with age (P=0.919), but there was a highly significant effect of region (P<0.0005) and interaction between age and region (P<0.05) possibly providing evidence for a change in pattern with age. Data for nuclear widths in non-branch regions or nuclei over the AC are not available

Mean nuclear widths for immature and mature mice were 7.54 ± 0.03 and 7.59 ± 0.03 respectively (a difference of 0.7%, n = 297 and 426 regions respectively) for the 8 regions in Fig. 3.1(inset).

3.4.4.1 Immature nuclear width

The effect of region on nuclear width was highly significant (P<0.0005) in immature mice. Widths ranged from 7.17 ± 0.08 µm ("R", n = 37 branches) to 7.71 ± 0.10 µm ("DL", n = 39 branches), an increase of 7.5%.

Nuclei in region "R" were significantly thinner (P<0.05) than any other region except "L" (P=0.533). There were no significant differences between any other regions.

3.4.4.2 Mature nuclear width

The effect of region on nuclear width was highly significant (P<0.0005) in mature mice. Values ranged from 7.43 ± 0.10 μm ("R", n = 51 branches) to 7.90 ± 0.09 ("D", n = 55 branches), an increase of 6.3%.

Nuclei downstream of the branch ("D") were significantly wider than nuclei in any other region (P<0.05).

Table 3.5. Mice nuclear widths (μm) for the 8 regions defined in Fig.3.1 where n equals the number of branches.

Region	Immature		Mature	
	Mean	SEM	Mean	SEM
UR	7.54	0.09	7.59	0.10
U	7.52	0.09	7.56	0.11
UL	7.67	0.11	7.49	0.09
R	7.17	0.08	7.43	0.10
L	7.38	0.10	7.57	0.10
DR	7.66	0.08	7.62	0.10
D	7.70	0.11	7.90	0.09
DL	7.71	0.10	7.55	0.08
Total	7.54	0.03	7.59	0.03

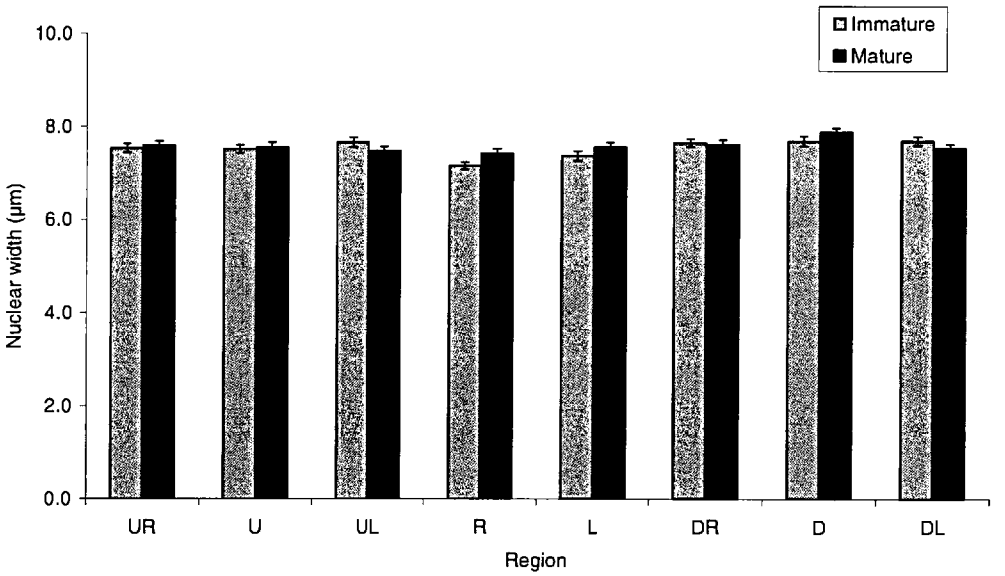

Fig. 3.11. Mice nuclear widths in the 8 regions defined in Fig. 3.1. Bars show means ± SEM (n = number of branches).

3.4.5 Dimensions of ostia and arterial cushions

Average lengths, widths and areas of branch ostia and arterial cushions in immature and mature mice are shown in Table 3.6. The arterial cushion resembled the bow of a boat extending upstream from the ostium (Fig. 3.2). The shape of the AC and branch ostia could be analysed for 74% of the branches (n = 29 immature, n = 45 mature) studied. The dimensions of the arterial cushion were unaffected by age (entrance length, $P>0.5$; width, $P>0.6$; area, $P>0.8$). The branch length was 9.6% more elongated in mature mice (196.11 ± 5.74µm) than in immature mice (178.93 ± 4.57µm; $P<0.05$). The branch width was 1.4% wider in immature (117.75 ± 4.65µm) than mature (119.44 ± 7.23µm) mice. The branch area in immature mice was $197x10^3 \pm 10x10^3$ pixels^2 and was larger in mature mice ($217x10^3 \pm 17x103$ pixels^2) (a 10.2% difference). Neither the width or the area were significantly different between ages ($P>0.8$, and >0.3 respectively).

Table 3.6. Dimensions of mouse arterial cushions and branch ostia where n equals the number of mice.

		Immature		Mature	
		Mean	SEM	Mean	SEM
Arterial cushion	Entrance Length (μm)	88.09	8.62	81.89	5.71
	Width (μm)	138.45	5.72	142.81	5.97
	Area (pixels^2)	137 x 10^3	13 x 10^3	140 x 10^3	10 x 10^3
Branch Ostium	Length (μm)	178.93	4.57	196.11	5.74
	Width (μm)	117.75	4.65	119.44	7.23
	Area (pixels^2)	197 x 10^3	10 x 10^3	217 x 10^3	17 x 10^3

3.4.6 Summary of main mouse results

- There were no significant differences between immature and mature mice for endothelial nuclear LW ratio, length, width or nuclear orientation
- There was a significant effect of region for all nuclear parameters analysed
- There was no significant interaction between age and region for nuclear LW ratio, length or nuclear orientation (suggesting no change in pattern with age) when looking at the 8 main regions surrounding branch ostia
- There was a significant interaction between age and region for nuclear widths
- Nuclei overlying the arterial cushion were less elongated than those found in other regions
- Nuclei in regions located to the sides of branch ostia were more elongated than those up- and downstream of the branch
- In immature mice, there was a trend for nuclei upstream of the branch to be less elongated than in all other regions
- In mature mice, there was a trend for nuclei downstream of the branch to be less elongated than in all other regions
- Dimensions of the arterial cushion were unaffected by age
- The area of the branch ostia were unaffected by age

3.4.7 Nuclear length:width ratios in rabbits

Nuclear length:width ratios are shown in Table 3.7 for immature (n=6) and mature (n=5) rabbits. LW ratios were greater downstream of the branch than upstream in immature rabbits: the ratio of the mean upstream value to the mean downstream value was 0.87 for the youngest age group (Fig. 3.12) (values <1 indicate greater nuclear elongation downstream and values >1 indicate greater elongation upstream). This difference increased in the second age group (ratio = 0.90), disappeared in the third (ratio = 1.00) and reversed in the oldest group (ratio = 1.03). (Statistical analyses were not carried out due to small number of branches studied). Nuclei in control regions showed a consistent elongation with age.

The ratios of the mean upstream LW ratio to the mean downstream values, for immature and mature rabbits plotted by their weights are shown in Fig. 3.13. As before, values <1 indicate greater nuclear elongation downstream and values >1 indicate greater elongation upstream. At a weight of approximately 3.3kg the ratio was approaching 1, suggesting there was no change between the upstream and downstream nuclear LW ratios.

Table 3.7. Rabbit nuclear LW ratio data for validation of mouse confocal technique where n equals the number of branches.

Region	Immature				Mature			
	1.5 months		4.3 months		9.5 months		≥24 months	
	Mean	SEM	Mean	SEM	Mean	SEM	Mean	SEM
Upstream	2.32	0.06	2.38	0.07	3.10	0.08	3.28	0.11
Downstream	2.68	0.08	2.65	0.04	3.09	0.06	3.19	0.10
Control	2.60	0.06	2.96	0.11	3.14	0.09	3.25	0.17
LW Upstream / LW Downstream	0.87		0.90		1.00		1.03	

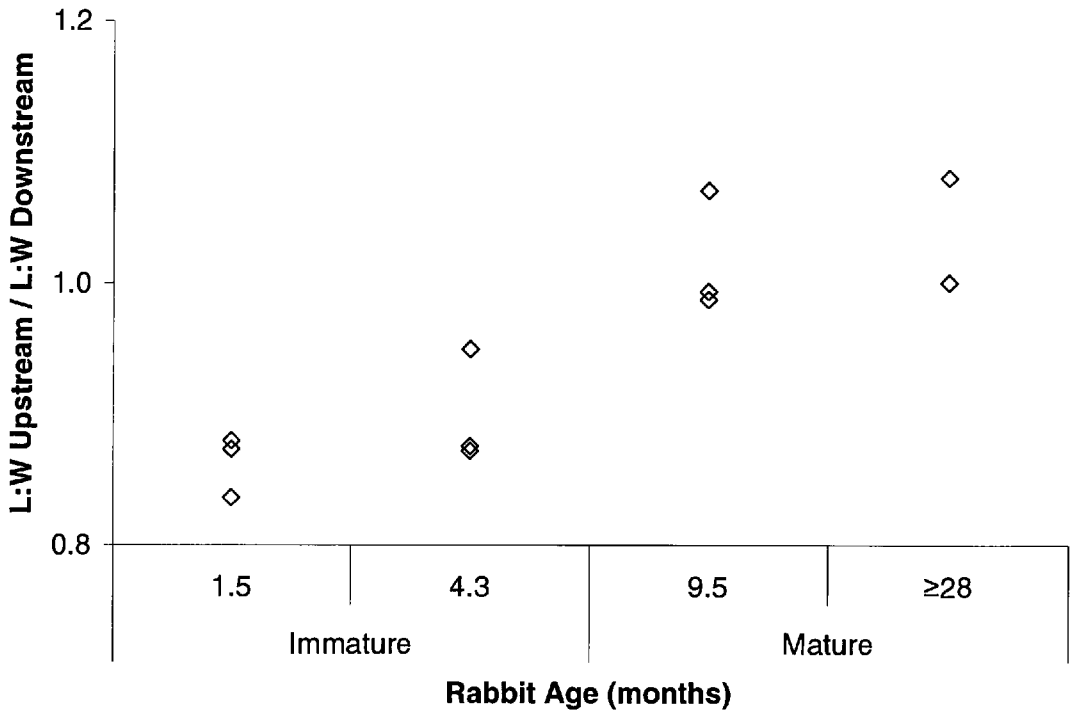

Figure 3.12. Changes with age in the pattern of endothelial nuclear length-to-width (LW) ratios upstream and downstream of rabbit aortic intercostal branch ostia. The upstream LW ratio has been divided by the downstream LW ratio so values <1 indicate greater nuclear elongation downstream and values >1 indicate greater elongation upstream. Each point indicates the data for a single rabbit (24 branches in total, 5-8 in each age group).

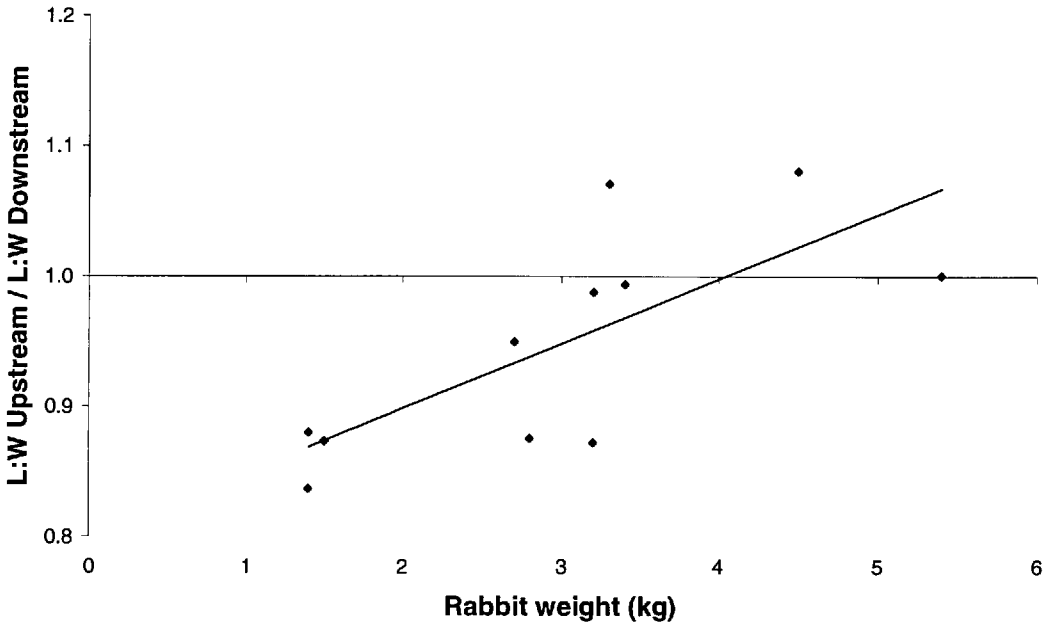

Figure 3.13. Changes with body weight in the pattern of endothelial nuclear length-to-width (LW) ratios upstream and downstream of rabbit aortic intercostal branch ostia. The upstream LW ratio has been divided by the downstream LW ratio so values <1 indicate greater nuclear elongation downstream and values >1 indicate greater elongation upstream. Each point indicates the data for a single rabbit. The trend line is linear.

When all branch values for each species were averaged, LW ratios for mice (2.42 ± 0.01) were lower than those for rabbits (2.87 ± 0.06).

3.5 Discussion

3.5.1 Mouse nuclear morphology

A previous study of rabbit endothelial cell nuclei morphology by our group (Al-Musawi *et al.*, 2004) found greater nuclear elongation downstream than upstream of branch ostia in immature aortas (< 4months), but observed the opposite trend in animals aged 10-11months. The small study of rabbits here, conducted to determine whether our confocal technique for measuring endothelial cell elongation gave comparable results,

showed the same trend (Fig. 3.12). As the age of animal increased, nuclei went from being more elongated downstream, to being more elongated upstream, the change occurring after 4 months. This shows that any changes in nuclear patterns in mice can be attributed to genuine differences around the branch mouth, rather than problems with the technique.

If the age of rabbit is substituted by its body weight and a linear trend line added (Fig. 3.13), then it appears that there is greater nuclear elongation downstream of the branch up to a weight of approximately 4kg, and then the pattern reverses as weight increases further. Growth charts for various breeds of rabbits (not including NZW) (Larzul and de Rochambeau, 2004) show that rabbits reach a weight of 4kg by 13 - 26weeks (3.3 - 6.5 months) depending on the strain, therefore the ratio of LW ratios plotted against age or weight are showing roughly the same result.

The pattern of nuclear elongation, used as an indicator of shear stress, observed in immature mice (and in mature mice with the exception of nuclei within the "UL" regions) appears to be consistent with what we would expect if blood near the aortic wall is diverted away from the longitudinal axis of the artery, around the branch ostium. This would cause the streamlines to become closer together as they reach the lateral regions ("L" and "R"), causing the increased shear stress values we have seen. The cause for this deflection of blood is thought to be the AC, as microscopical techniques show that it protrudes slightly from the artery wall at its proximal margin (Gorgas and Bock, 1975). Wagenvoort (1954) devised a model that included a structure similar to an AC and showed that blood was diverted around the cushion and branch ostia. This streamline theory is reflected in the nuclear orientation: opposite regions ("UR" vs. "UL", "R" vs. "L", "DR" vs. "DL") have opposite sign angles (i.e. positive vs. negative) (See Fig. 3.9). It should be noted that although there are significant differences between orientations, the largest mean deviation from the longitudinal axis was only 5.09° ("UR") in immature mice and -2.48° in mature (nuclei over the AC excluded). This is very different to the values previously found in rabbits where mean orientations in lateral regions were in the range of 10-20° (Al-Musawi *et al.*, 2004). The alignment of the nuclei near the branch mouth is very different as well. In rabbits, the long axis of the

nuclei deviates from the aortic axis towards the ostium, whereas in mice the long axis deviates away from the ostium. Other work in our group (Kazakidi et al., 2006) suggests that this difference may reflect the lower Reynolds number (ratio of inertia to viscosity) for flow in the mouse aorta.

There was a trend for nuclei in the upstream region in immature mice to be less elongated than nuclei in all other regions, however nuclei in the downstream region of mature mice were significantly less elongated. This pattern is similar to that seen in rabbits, whereby nuclei are more elongated downstream in young, and less elongated in mature. Nuclei were 1.3% more elongated downstream than upstream in immature mice, and 4.5% more elongated upstream than downstream in mature. However, our data for rabbits showed that nuclei were 13.6% more elongated downstream than upstream in immature, but only 1.6% more elongated upstream than downstream in mature.

Nuclei within the non-branch (control) regions of immature mice did not differ in the amount of elongation, when compared to the branch regions (except for those in the lateral regions that were significantly more elongated). This was opposite to the nuclear elongation in mature mice; nuclei in non-branch regions were significantly more elongated than nuclei in all other regions, except for those lateral to the ostia. The fact that mature mice have increased LW ratios (shear stresses) away from the branch could explain why the nuclear orientation near the branch changed to a lesser extent than in immature mice: the faster flowing blood may reduce the amount it is diverted around the AC, thus decreasing the changes in the angle of nuclear orientation.

The mean length of nuclei differed between ages by 6.3%, whereas the width only varied by 0.7%. The small degree of variation in nuclear widths perhaps suggests that the LW ratio mainly reflects changes in nuclear length.

Despite the mean LW ratios being lower in mice than those previously reported (Al-Musawi *et al.*, 2004), comparison of the overall difference in LW ratios within each species shows very little difference. Mean rabbit LW ratios for branch regions ranged

from 2.51 to 2.85 in immature, and 2.67 to 3.05 in mature; a 13.5% and 14.2% difference respectively. Our data for branch regions show that LW ratios range from 2.23 to 2.54 in immature mice and from 2.31 to 2.64 in mature mice; a 13.9% and 14.3% difference. Nuclear data from rabbits (Al-Musawi *et al.*, 2004) suggests that immature rabbits develop lesions in regions of relatively higher shear stress (regions of greater nuclear elongation), and that a change to lower nuclear elongation with age lowers the prevalence of disease. Our mice data appears to show the opposite pattern. Although not significant, McGillicuddy *et al* (2001) showed that there was a greater prevalence of disease upstream of the branch at earlier ages, but this trend decreases with age. Immature mice have LW ratios downstream that are higher than those upstream of the branch, whereas in mature mice there is greater nuclear elongation upstream than downstream, and the prevalence of disease decreases. Lesions have also been shown to cover a larger area around the branch ostia in mature mice than in immature (McGillicuddy *et al.*, 2001). This may be caused by the change in shear stress gradients between non-branch regions and branch regions. In immature mice, LW ratios did not change very much between non-branch and branch regions (3% difference), however in mature mice, nuclei in non-branch regions were 12% higher than in the periostial regions.

3.5.2 Nuclei of arterial cushions

From the lower LW ratios it can be inferred that the shear stress affecting the nuclei within the AC appears to much lower than that affecting the rest of the branch or the arterial wall. This again could be due to the AC being raised up from the arterial wall at its proximal margin, perhaps causing a region of flow separation over the AC, thus resulting in lower shear stress values. However, the lower LW ratios could potentially be due to foreshortening of the nuclei. At regions of arterial wall curvature, and in particular over the AC that slopes into the branch ostia, nuclei are not being viewed directly *en face* to their local orientation, but at an angle. This might lead to errors in nuclear analysis due to the nuclei appearing shorter than they actually are. A way to avoid this would have been to adjust the angle of the microscope stage, or the tissue on the slide, so it corresponded to the angle of the slope but this would not be the most practical solution. An alternative method would have been to produce a 3-dimensional

(3D) image of the arterial wall, and develop image analysis techniques that measure the 3D nuclear morphology.

We have seen that the surface of the AC is covered in a layer of ECs which extend into the endothelial layer of the rest of the aorta, and at the entrance to the "boat" the ECs are packed tightly together, and are orientated as though being channelled into the ostia. Both features have been seen previously (Gorgas and Bock, 1975). This "channelling" could have led to the results for the orientation of nuclei on the AC being flawed. Nuclei on the AC appear to be aligned in various directions, some leaning to the left and some to the right. When analysed, the sign of the angles would tend to cancel each other out making the mean orientation approximately zero. This does not appear to be the case. Arterial cushion nuclei were oriented at 6.89 ± 1.69 ° and 4.50 ± 1.67 ° in immature and mature mice respectively. This suggests either that the AC is itself orientated to the anatomical left of the longitudinal axis or that the nuclei are being affected by a spiralling of blood flow down the aorta. Without analysis of whole aortas to remove the need to normalise the angles, it is unclear which of these theories is correct.

Although no rigorous analysis was been carried out, it was observed that over the AC the intensity of the propidium iodide stain was much brighter than within the surrounding nuclei (Fig. 3.14). This was also seen in EStAR preparations of whole mice aortas stained with PI (Fig. 4.9) (discussed later). Since the tissue had been incubated in RNase the stain was only picking up DNA within the nuclei. The increase in intensity could be due to an increase in the amount of DNA present, as regions of disturbed flow have been shown to cause increased cell replication and more rapid cell turnover (Chuang *et al.*, 1990, Lin *et al.*, 1990).

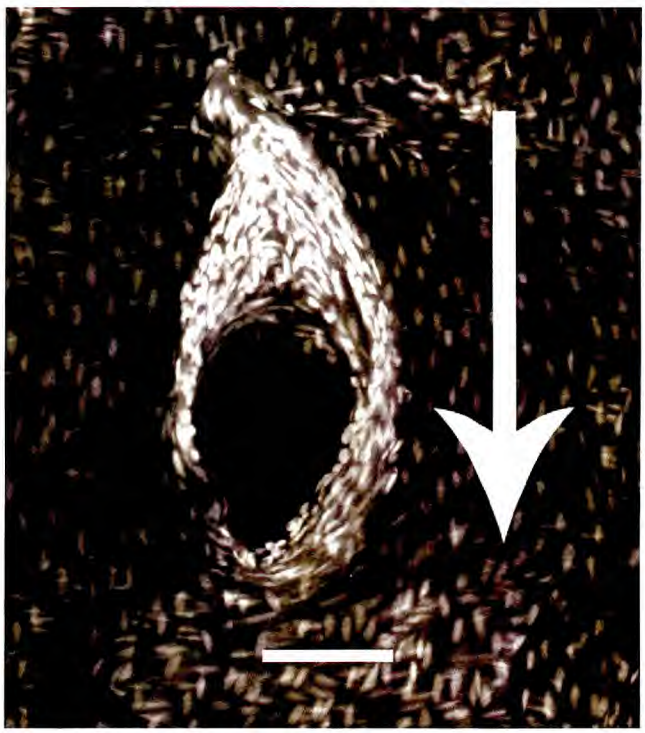

Fig. 3.14. Resulting image from a compressed confocal stack of propidium iodide stained images of a mouse ostium. Brightly stained region in upstream region of branch, possibly suggesting increased cell turnover. Scale bar = 100μm. Blood flow is from top to bottom (arrow).

3.5.3 Morphology of arterial cushions

Initially it was thought that the AC we were seeing was an area where the remainder of the intercostal artery was impinging onto the ostium from below; an artefact from the mounting procedure. Due to the uniformity of the raised region, and the fact that it has been seen previously using different types of microscopy and sectioning techniques (Gorgas and Bock, 1975, Hesse and Bock, 1980, Heidger et al., 1983), and that they have also been seen during our EStAR preparation, it is felt that this can be discarded. Furthermore, histology has shown that the cushion has a distinct histological structure, linked to the normal aortic intima and media (Gorgas and Bock, 1975). It is not known how far the AC protrudes into the lumen, and as such it is unknown how much influence it will have on the flow of blood into the branches. Using image analysis software that enables reconstruction of the confocal stacks in 3D would allow the AC to be measured,

however in this study there was too much reflectance from the coverslip used to mount the tissue, preventing any measurements from being taken.

The shape of the arterial cushion may be related to a disease pattern observed by McGillicuddy *et al* (2001) in $LDLR^{-/-}/ApoE^{-/-}$ double knockout mice (Fig. 3.15). In this paper it was reported that "a crescentic or triangular region of apparent sparing occurred immediately upstream from the ostium and was surrounded by a line or larger patch of stain". This correlates very well with the shape of AC we have seen using confocal microscopy. It is not certain whether the pattern they saw was due to increased lipid deposition caused by flow being disturbed at the edge of the AC, or whether the lipid stain located at this region was masked by the presence of the AC overlying it.

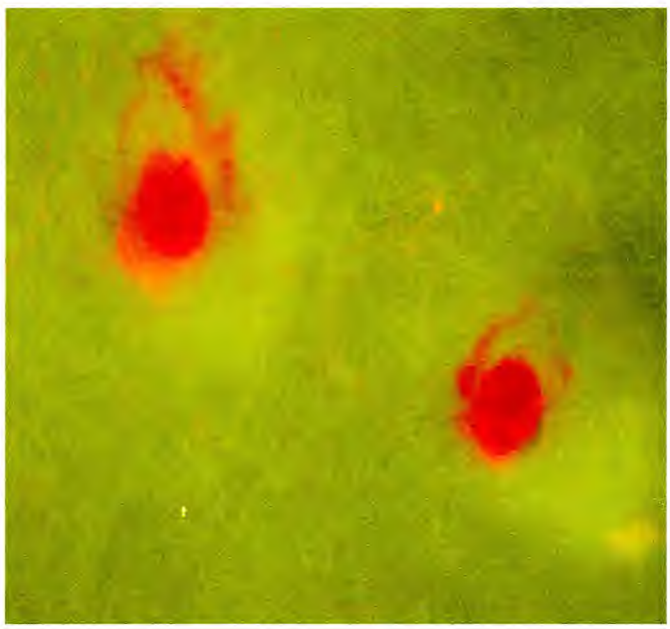

Fig. 3.15. *En face* image of the aortic wall from a mouse stained with oil red O showing the chevron pattern of lipid deposition upstream from two intercostal ostia. Blood flow is from top to bottom.

There seem to be various theories put forward for the presence of the cushion. During sectioning of the AC, Gorgas and Böck (Gorgas and Bock, 1975) discovered a cavity formed within the aortic wall, from which the intercostal artery originates. They suggest that the initial course of intercostal arteries is a retrograde one when compared to the direction of aortic blood flow. Grooves found within the AC were predicted to channel

the blood stream into the cavity so it is able to "turn around" the flow into the initial segment of the intercostal artery in the reverse direction.

Studies looking at mice (Gorgas and Bock, 1975) and rats (Hesse and Bock, 1980) have provided evidence that ACs change shape depending on the amount of distension of the arteries. During our studies, fixation was carried out at physiological pressure and for the same time period for each mouse, however, each mouse may have been slightly over or under their exact physiological pressure, causing changes to the size of AC. Increased pressure would cause the artery to distend more leading to a flattened AC profile, whereas decreasing pressure may enable it to rise up. If the pressure does affect the size of the AC, as previously suggested (Gorgas and Bock, 1975), then it is highly likely that during the phases of the cardiac cycle the AC will change its shape. This would tie in with another theory in which the AC are thought to act as sphincters. In systole, when the heart is contracting, blood pressure will be raised and blood will be flowing in a forward direction, the AC will be flattened and oxygenated blood can flow freely into the intercostal branches. During diastole, when the heart is relaxing the pressure will decrease and the AC will increase in size, closing the "valve" over the ostia. This will prevent blood flowing back out of the branches whilst the parent vessels may be experiencing reversal of flow.

The Wagenvoort model that has previously been mentioned also showed that blood was drawn into the side branch from central portions of the aortic blood stream, and Fourman & Moffat (1961) have provided an explanation as to why this might occur. When blood flows through a small artery, red blood cells (RBC) are found in the central (axial) stream where the blood is moving fastest. They suggested that the increased velocity blood causes a region of lower pressure at the peripheral regions reducing the number of RBCs. If a branch left the artery at right-angles it is thought that it would sample blood predominantly from the cell-poor peripheral zones, so-called "plasma skimming" (Fourman and Moffat, 1961). It is thought that the consequences of this are that blood within the side branches have about 25 percent lower haematocrit than that in the larger vessels (Ezeilo, 2005). Fourman and Moffat (1961) suggest that the AC are acting to reduce plasma-skimming, and are in fact encouraging blood sampling from the

oxygenated RBC-enriched axial stream. A process they termed "cell-skimming". They carried out experiments on immature and mature female, and mature male rats to determine whether the size of AC increased the haemoglobin (Hb) concentration in the blood in the branches of mesenteric (male rats) and uterine (female) arteries. Their results showed that in mesenteric arteries, the Hb concentration was lower in the branch than in the main trunk, and this was attributed to plasma-skimming. In female rats, where uterine arteries were studied, young animals had a greater concentration of Hb in the trunk than in the branch (plasma-skimming) whereas the adult animals had greater Hb in the branch (cell-skimming). They attributed this difference to the size of the AC. In young rats, ACs were very flat and did not project far into the lumen, whereas in older animals the AC projected towards the centre of the lumen to sample the axial stream. It should be noted that in their study, animals were not fixed at pressure therefore results they obtained for size differences may not be wholly accurate. A consequence of cell-skimming and thus increasing the haematocrit content in the side branches is that the viscosity of blood will be increased (or at least maintained at levels similar to the parent artery). This may cause an increase in shear stress, determined using the equation for calculating shear stress (viscosity x velocity gradient).

Work has also been carried out looking at AC in the uterine arterial bed of rats and pigs (Heidger *et al.*, 1983). Utilizing scanning electron microscopy of vascular casts, the AC in rats was shown to vary in the amount of contraction or relaxation and this was dependent on the stage of estrous cycle, pregnancy and pharmacologic vasoconstriction. Interestingly, the number and size of cushions were consistently greater in non-pregnant sows compared to pregnant sows.

Chapter 4: Development of the EStAR technique for producing monolayers of endothelium

4.1 Introduction

The method previously used to determine ECn morphology using confocal microscopy was deemed too time consuming to use further. A new technique was required that enabled imaging of the endothelium without the problems of uneven aortic wall surfaces and the associated problems with underlying SMC. Previous groups have shown that it is possible to prepare monolayers of endothelium (Häutchen preparations) from monkeys (Skantze *et al.*, 1998), dogs (Smith et al., 1996), mice (Guzman *et al.*, 2002), rats (Senis *et al.*, 1996), rabbits (Hirsch *et al.*, 1980) and humans (Lupinetti et al., 1993). Such monolayers can be examined using a normal microscope, without the problems occurring when using whole mounts and confocal microscopy.

The most detailed method for producing Häutchens has been given by Hirsch *et al*, (Hirsch *et al.*, 1980) and images from their papers show good endothelial layers (ELs); therefore an attempt was made to replicate this method. Using their method, the resulting ELs were found to be highly inconsistent, frequently containing areas with missing cells or with SMC that overlay ECs. Modifications were made to the technique (as detailed below), which was subsequently renamed the "EStAR" (Endothelial Stick and Rip) technique, resulting in the production of complete ELs from rabbit and mice thoracic aortas. Using rabbit tissue it was possible to produce ELs containing pairs of intercostal ostia, and in mouse tissue it was possible to produce ELs containing ostia in the thoracic aorta, and the aortic arch. To our knowledge we are the first to produce Häutchens containing multiple ostia.

4.2 Methods

4.2.1 Tissue preparation for Endothelial Stick and Rip technique

Thoracic aortas from rabbits, mice, and pigs were removed from fixative and equilibrated in PBS for at least one hour to remove any fixative for safer handling. Under a dissecting microscope, fine forceps and ophthalmic scissors were used to physically remove adventitial fat from the aortas. Sketches were drawn of aortas to document the location of intercostal branches. The intercostal arteries were cut short so that only stubs remained attached to the thoracic aorta.

Segments of rabbit and pig aorta containing intercostal branch ostia were dehydrated by immersion in a graded series of ethanol (30%, 50%, 70%, 95% ethanol in water and twice at 100%) (Fisher Scientific, Analytical Reagent Grade) for 20 minutes each, before being placed into 100% ethanol for at least 16 hours. Whole aortas of mice were cut open longitudinally and pressed flat between two glass slides held together with a metal clip before being dehydrated in ethanol as described. Glass microscope slides (Menzel-Glaser, pre-cleaned) were prepared by wiping the surface with paper towel to remove any dust particles that could get trapped under the EL and lead to the surface being uneven. Strips of double-sided adhesive tape (3M, Scotch pressure sensitive), whilst still attached to backing paper, were pressed onto the slides and a finger nail was run over the paper to remove any trapped air bubbles.

Aortas were removed from 100% ethanol and, before all the alcohol could evaporate, aortic rings containing pairs of intercostal branches (rabbits) or single branches (pigs) were cut perpendicular to the longitudinal axis. The rings were cut longitudinally along their ventral side, opened out and pressed, endothelial surface down, onto the tape (after the backing paper had been removed). Whole mouse aortas were pressed, endothelial surface down onto the tape. The backing paper was then used to press the tissue flat onto the tape, ensuring no air bubbles were present (particularly around ostia) as these prevent the endothelium adhering. Removed backing paper was used as opposed to any other form of paper as it does not stick to the tape; this would damage the tape and endothelium. Inverting the slide and pressing down onto paper towel enabled visualisation of any air bubbles, whilst also allowing any excess ethanol to be blotted away from edge of the EL before it had a chance to seep under the tape, decreasing adhesiveness. Downward pressure was maintained onto the slide for at least three minutes, either manually or with a weight, to ensure the endothelium was stuck, before the slide was placed correct side up and the backing paper removed. Sections were then left to dry in air for five minutes to enable any excess alcohol within the tissue to fully evaporate. The tissue was then completely immersed in glycerol (10% in water, Sigma), ensuring the edges were also immersed, for 8-10minutes to rehydrate the tissue. The intima and media were then peeled away using fine forceps, starting in one corner and

peeling across the tape. If resistance was met, another corner was tried. In rare cases where there was still resistance, tissue was left under glycerol for a further five minutes.

On rare occasions, particularly around branch points, some SMC remained on the EL. These could easily be removed using fine forceps under a dissecting microscope. A more common problem was that of glycerol or air bubbles becoming trapped in the branch mouth leading to the tissue rising up slightly and causing problems with microscopic imaging. This was alleviated slightly by cutting the intercostal arteries as close as possible to the main thoracic aorta, without actually damaging the aortic wall itself. This also seemed to lessen the problem of SMC remaining on the EL.

Before developing the EStAR technique, the method of Hirsch *et al* (1980) was used which, although it did sometimes produce good endothelium, was highly inconsistent and frequently left SMC on the tape. The two main differences were the omission of Hirsch's use of acetone and a freezing step that will be discussed in more detail. Hirsch *et al* suggested immersion in acetone for 5-10seconds after removal from ethanol, before sticking to tape. It is thought that this was to speed up the evaporation and enable better adhesion to the tape. With the tape we now have available it was felt that this step was not necessary as the ethanol evaporated on its own and enabled good adhesion. In fact, acetone was found if anything to decrease the ease of stripping of intima and media so this step was removed. Hirsch *et al* also suggested spraying the underside of the slide with dichlorodifluoromethane after immersion in glycerol, before peeling. They suggested that this increases cohesion of the tape adhesive and its adhesion to its plastic base. In early experiments, after glycerol immersion, we tried cooling the underside of the slide with 100% tetrafluoroethane (Cryospray 134, Bright) for a few seconds but this was a very irreproducible way of cooling and yielded inconsistent EStARs. It was more consistent to cool the slide by placing it (for 1.5min) on a metal block within a Cryostat cooled to -40°C. Once cooled the slide was left at room temperature (1min) to start thawing. The intima and media were then peeled away as previously mentioned. As with the addition of acetone, this also led to inconsistent and irreproducible results, possibly due to inconsistent thawing of glycerol due, for example, to variable room temperature. Results were again more reproducible if this step was omitted.

Using our technique it was possible to produce rabbit EStARs up to 1cm in length, encompassing the whole width of the arteries, completely devoid of SMCs, and containing pairs of intercostal branch ostia. Having produced EStARs of individual segments, the whole length of the artery could be joined together during image processing. EStARs of mice aortas including the aortic arch and the thoracic aorta, and small sections of pig thoracic aortas including individual branch ostia were also produced.

4.2.2 EStAR nuclear staining and image analysis

EStAR preparations were stained using the technique previously described for ECn. Briefly, glycerol was rinsed from the EL with water, followed by PBS. The ELs were immersed in 0.2% Triton X-100 (Sigma, 30s), followed by PBS (15s), before being incubated in RNase (Sigma, 10min, 37°C). Following the incubation period, ELs were rinsed in PBS, and a drop of PI was added before being rapidly rinsed away, again with PBS. The stained EL was then flooded with water, excess water was dabbed away and the EL was mounted under a coverslip in Fluorsave (Calbiochem) mounting medium.

Slides were viewed using an Axioplan epifluorescence microscope (Zeiss) and PI was excited at a wavelength of 546nm, through a rhodamine filter. Images were taken using a low light CCD camera with a Kodak KF1600 chip, coupled to the software package Maxim DL (Diffraction Limited, Canada), at 200x magnification using a 20x objective lens (NA 0.45), using an exposure time of 3.0 seconds, and were saved in Tagged-Image File Format (TIFF). Since the area of the ELs was larger than the field of view, images of the endothelium were taken in a grid-like pattern, ensuring each image overlapped slightly with its neighbours, and their location was noted.

Individual images were opened in Adobe Photoshop (Version 7.0, Adobe Systems Incorporated) and the pixel intensity levels were manually adjusted using the "levels" command so the range of pixel intensity values was 2 to 4. This converts all pixels with an intensity less than 2 to black (pixel value 0), and all pixels with an intensity greater

than 4 to white (pixel value 255). Any other pixels within the image are automatically adjusted proportionately to increase the tonal range.

A median noise reduction filter (set to two pixel radius) was applied, and the image converted from 16-bit/channel to 8-bit/channel pixel depth. Each image was then copied to a new image destined to become the final montage, made semi-transparent so the previous image could be seen underneath, and the nuclei towards the edges aligned with the previous image. This process was continued until all the images for each pair of intercostal branches were aligned and in the final montage image.

Any remaining SMCs or areas of damage were removed from the montage image manually using the eraser tool. Contrast in the images was improved (Fig. 4.1a, b), again using the "levels" command, by setting the range of pixels between the minimum and maximum value within the image so anything above or below this range was converted to white and black respectively. This was followed by a Sharpen filter (Sharpen More) (Fig. 4.1c) that increases the contrast of adjacent pixels, and a high-pass filter (10-pixel radius) (Fig. 4.1d) that retains details at edge of objects whilst suppressing the rest of image, thus effectively flattening the intensity profile. This was necessary because a variation in the brightness of the microscope's mercury bulb and other optical factors caused an uneven distribution of pixel intensities across the field of view. Another median noise filter (2 pixel radius) (Fig. 4.1e) was then applied.

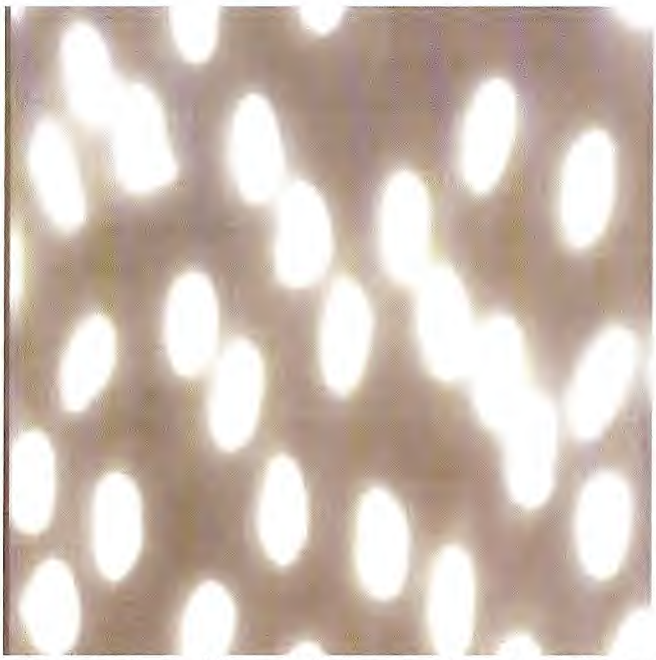

Fig. 4.1a. Section of original propidium iodide stained montage image showing endothelial cell nuclei. The image is 100μm x 100μm.

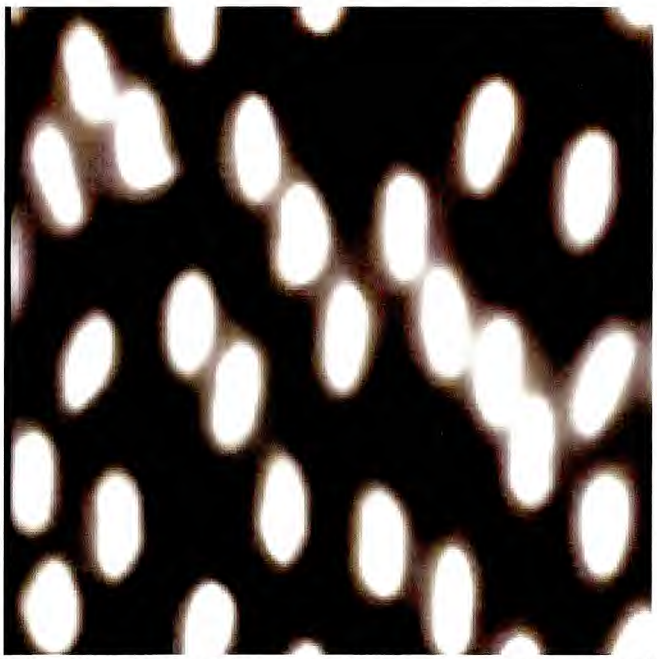

Fig. 4.1b. Figure 4.1a after contrast has been improved using the levels command.

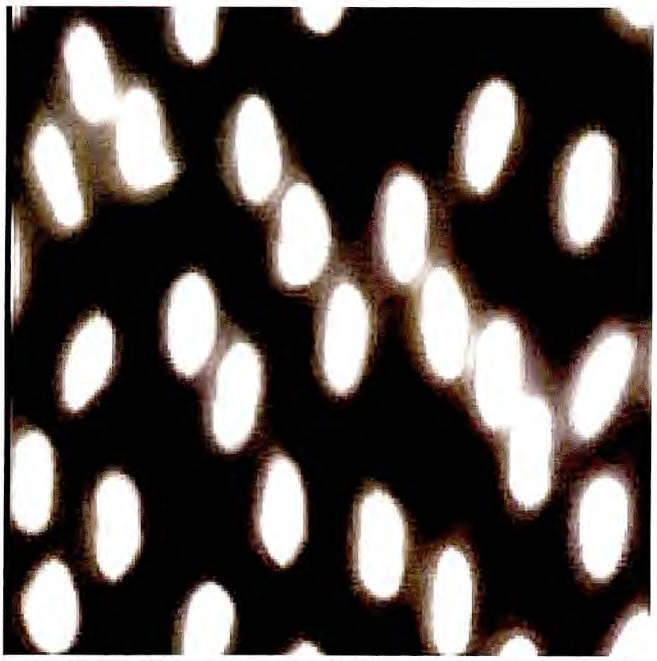

Fig. 4.1c. Figure 4.1b after a "Sharpen more" filter has been applied.

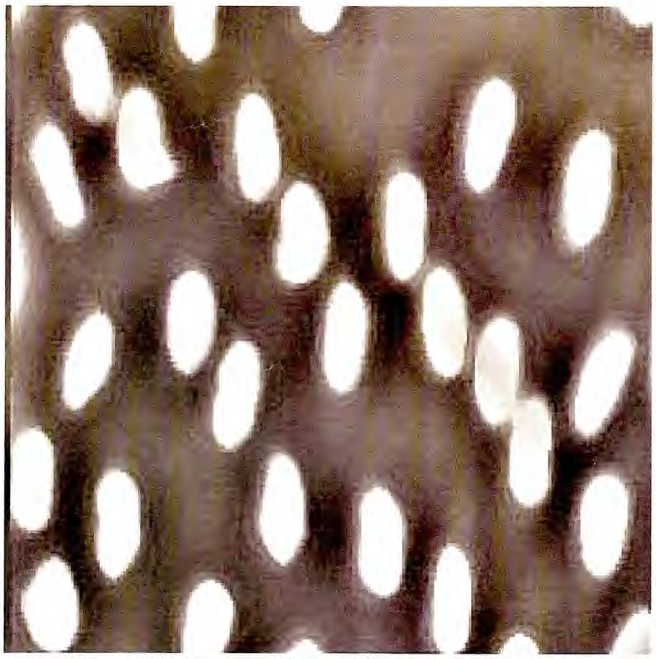

Fig. 4.1d. Figure 4.1c after a high pass filter (10 pixel radius) has been applied.

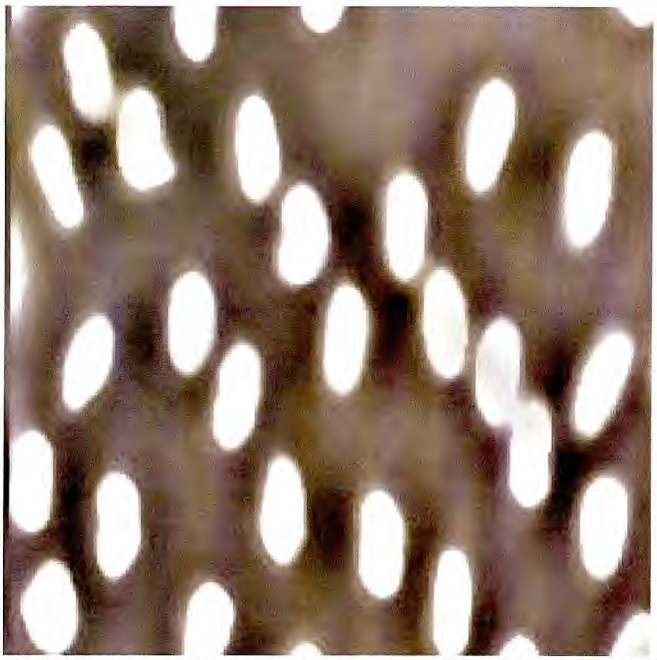

Fig. 4.1e. Figure 4.1d after a median noise reduction filter (2 pixel radius) has been applied.

The canvas size (dimensions of the final image) was always adjusted so the height and width was a multiple of 1000μm. This enabled the filtered montage images to then be subdivided into regions measuring 1000μm x 1000μm to be analysed in the image analysis software package, ImageTool (Version 3.0, The University of Texas Health Science Centre in San Antonio (UTHSCSA)).

Cropped images were opened in ImageTool and thresholded to convert grayscale images into binary (black and white) ones using the "Find Objects" command. This was done by converting all pixels with an intensity within the range 135-255 (i.e. nuclei) to black, and everything else (non-nuclei) white. This level was determined by trial and error: it was the optimum threshold level at which nuclei were detected at their actual dimensions, without picking up too much background staining or eroding the edges of the nuclei (Fig. 4.2). Once thresholded, images were analysed using the "Analyze" command to produce tables containing parameters for every black object within each image. Objects included artefacts such as background image noise that had to be removed. These were filtered out as described below. Parameters included area,

perimeter, major axis length (length), minor axis length (width), angle of orientation, elongation (length-to-width ratio) and coordinates for the centre of mass of each object.

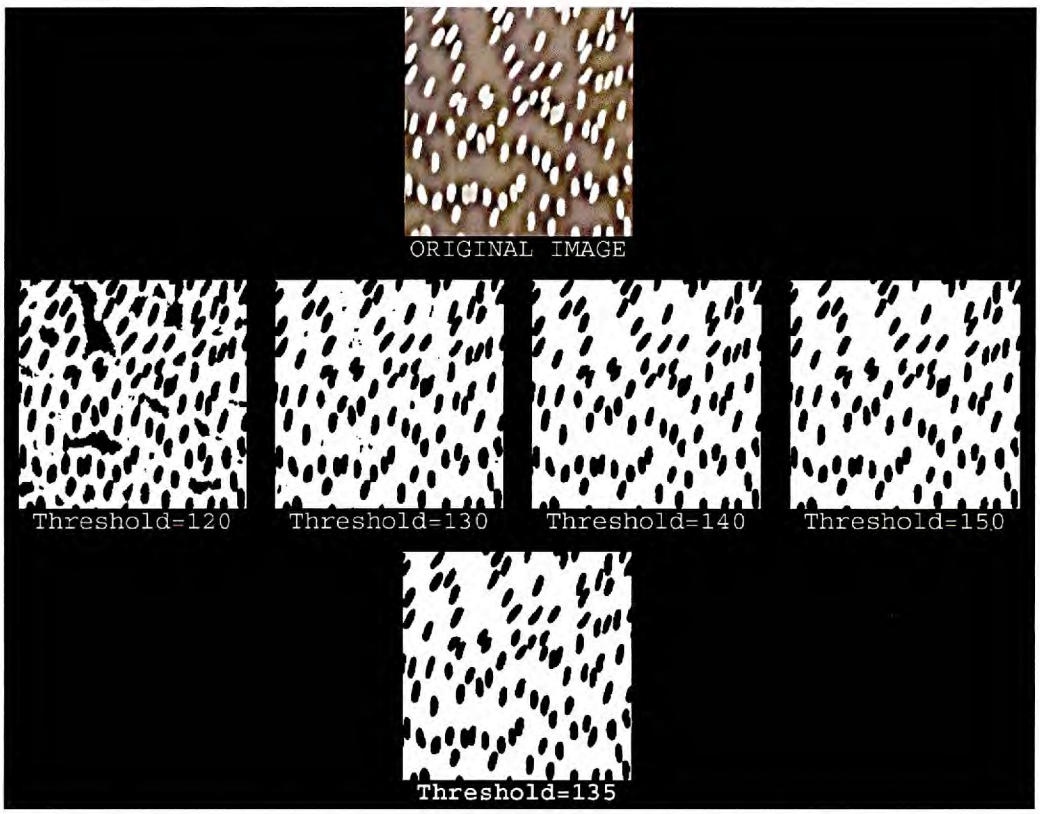

Fig. 4.2. Examples of various levels of image thresholding. Note the artefacts in threshold levels 120 and 130. Images with threshold levels 140 and 150 contain objects that have had their edges eroded and are therefore smaller than those in the original image. Images with threshold levels at 135 had few artefacts and the edges of objects were not eroded, and this level was therefore chosen.

Results tables were saved as text files, transferred to Excel (2003, Microsoft Office) and analysed to filter out data for pairs of nuclei counted as a single object because their edges touched, and background noise. The method for filtering objects was the same as that used during analysis of mice confocal nuclear images, with the slight difference that EStAR image objects were filtered using their area and perimeter as opposed to their area, length and width. Using the average nuclear length and widths (17μm and 8μm respectively) for ECn found in the literature (Table 3.1) it was possible to calculate the

average area and perimeter of an ellipse using an online ellipse calculator (Cleave Books, 2004).

It calculated the area using the equation:
Area = π x ((0.5 x ellipse's major axis) x (0.5 x ellipse's minor axis)).
The perimeter of an ellipse cannot be found easily, so the online calculator uses an approximation formula by Ramanujan (1914).

The "classification" function in ImageTool allows colour coding of objects according to dimensions entered by the user. Various percentage variations in area and perimeter were entered and the "yield" of nuclei observed. It was found that a 50% variation above and below the literature average encompassed changes in elongation caused by varying shear stresses but excluded most noise artefacts and multiple nuclei. Thus the area and perimeter were calculated (see below).

Average nuclear length = 17μm = 37.74 image pixels
Average nuclear width = 8μm = 17.76 image pixels

A 50% variation above and below average nuclear length = 56.61 pixels and 18.87 pixels respectively.
A 50% variation above and below average nuclear width = 26.64 pixels and 8.88 pixels respectively.
(These values differ to mice confocal images due to a different microscope setup and therefore a different micrometer to pixel conversion).

Therefore,
Maximum and minimum area of ellipse = **1184.45** pixels^2 and **131.61** pixels^2 respectively.
Maximum and minimum perimeter of ellipse = **135.04** pixels and **45.01** pixels respectively.

These assumptions may not be perfect as nuclear size variations between animals and within an individual aorta could be greater than 50%. However, paired nuclei and background noise that would have interfered with the analysis were largely removed (Fig. 4.3). Again using the "classification" function and colour coding nuclei, it was possible to manually count the number of paired nuclei included in the analysis of regions of 1000 μm x 1000 μm. Nuclei from 14 separate regions from EStARs produced from different rabbits and branches were counted and it was determined that only about 3.6 ± 0.8 % (mean ± SEM) of objects analysed were paired nuclei.

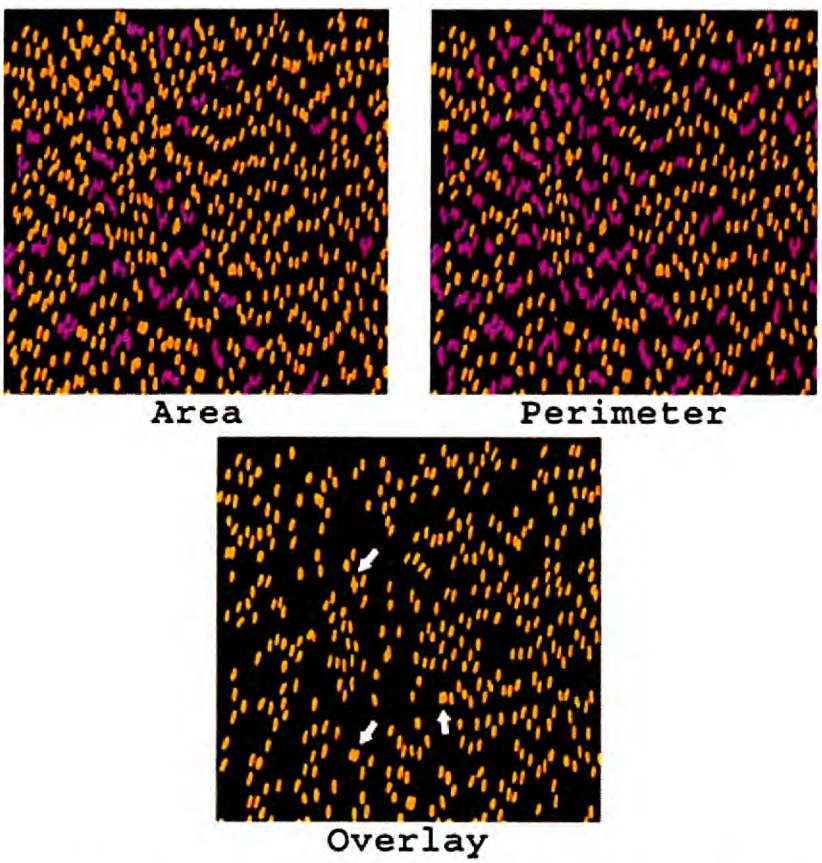

Fig. 4.3. Images obtained using the "classification" function in ImageTool. Area image) red and purple objects indicate nuclei excluded from analysis due to their area not being within the range 131.61 - 1184.45 pixels^2. Perimeter image) red and purple objects indicate nuclei excluded from analysis due to their perimeter not being within the range 45.01 – 135.04 pixels. Overlay image) the objects that will be included in the analysis. Objects were excluded due to their area and perimeter not being with the range specified. White arrows indicate paired nuclei that were not excluded.

The range of values for the perimeter and area were then included in the macro code (Appendix C - Macro 2) to exclude objects outside of these ranges. The equations below were also included in the macro code to convert the data so that if a nucleus were aligned along the longitudinal axis rather than the horizontal axis it would equal zero degrees (Fig. 3.3).

IF (Angle>0) then (Angle*-1) +90
IF (Angle<0) then (Angle*-1) -90

Since it is unclear exactly how much variation in morphology there is from one nucleus to the next and, more importantly, how the nuclear morphology changes across regions of the arterial wall, the data from the 1000μm x 1000μm images were further divided into regions measuring 100μm x 100μm. This was to prevent local effects being removed by averaging results from too large an area. This was again included in the Macro code to enable replication across all worksheets. Nuclei were filtered by their Cartesian coordinates. Data were then averaged within each 100μm x 100μm region. Using the coordinates, results were presented in a grid formation, akin to the original 1000μm x 1000μm image. The Excel cells that correspond to the 1000μm x 1000μm image were then manually pasted into a new worksheet for each parameter of interest, to produce maps that were spatially accurate and could therefore be overlaid onto the original montage image.

4.2.3 Nuclear Counting

To test whether there were variations in cell density, a macro was developed (Appendix C – Macro 3) to count the number of nuclei within the images. As before, there was a problem in that ImageTool could not distinguish single nuclei from groups of touching nuclei and would count the latter as one object. This was overcome by making the assumption that there is a linear increase in perimeters i.e. one nuclei equals 1x perimeter (45-135 pixels), two nuclei equals 2x perimeter (135-225 pixels), three nuclei equals 3x perimeter (225-315 pixels) and four nuclei equals 4x perimeter (315-405 pixels). The macro was then able to distinguish which objects contained one, two, three or four nuclei. Using the objects' Cartesian coordinates as before, images/results were

automatically divided into 250μm x 250μm regions (due to time constraints it was not possible to carry out nuclear counting for 100μm x 100μm regions) and arranged in their correct spatial location to be pasted into a new sheet containing data from the whole EL. Using the perimeters for 1, 2, 3 and 4 nuclei, combined with the classification function in ImageTool to colour code the nuclei within the different ranges, nuclei appeared to be counted accurately (Fig. 4.4). To further validate the technique, nuclei within 34 regions (1000μm x 1000μm) from different branches were also analysed using the macro, but also counted manually; the automated technique under-counted by 6.6 ± 11.9 cells (mean ± SD). The average number of cells per image, determined by a manual count, was 145.8 ± 22.6 (mean ± SD).

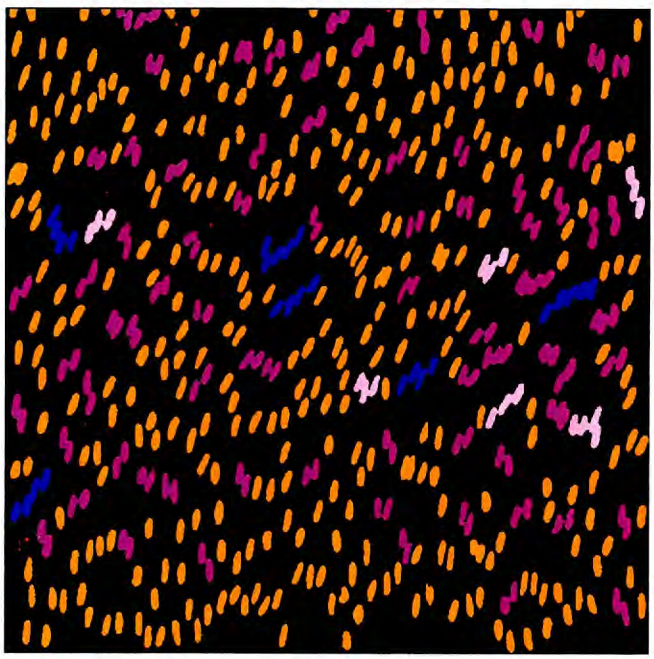

Fig. 4.4. Image showing how perimeter is used to determine the number of endothelial cell nuclei within an object. Nuclei are colour coded by the distance around their perimeter. Red = Excluded from analysis, Orange = 45-135 pixels = 1x perimeter, Purple = 135-225 pixels = 2 x perimeter, Pink = 225-315 pixels = 3 x perimeter, Blue = 315-405 pixels = 4 x perimeter.

4.2.4 Colouring of data within maps

Data were displayed as colour maps i.e. the data contained within the spatially accurate Excel maps were coloured according to their values. The easiest, most reliable and replicable way to do this was to write a further macro (Appendix C- Macros 4-10) that automatically scans through the data and colours each Excel cell depending on its value. At first, conditional formatting in Excel was attempted; however the function only allows three ranges of values to be defined per worksheet. The parameters we are looking at vary greatly in their values e.g. nuclear LW ratio values are in the range of 1-3, whereas nuclear area values are in the range 400-600. To enable spatial changes in parameters to be easily observed, eight ranges of values were defined for each parameter. This meant different Macro codes had to be written for each parameter to enable the colours to best represent the range of values presented (Fig. 4.5). The ranges of values assigned to each colour were usually determined by a trial and error approach.

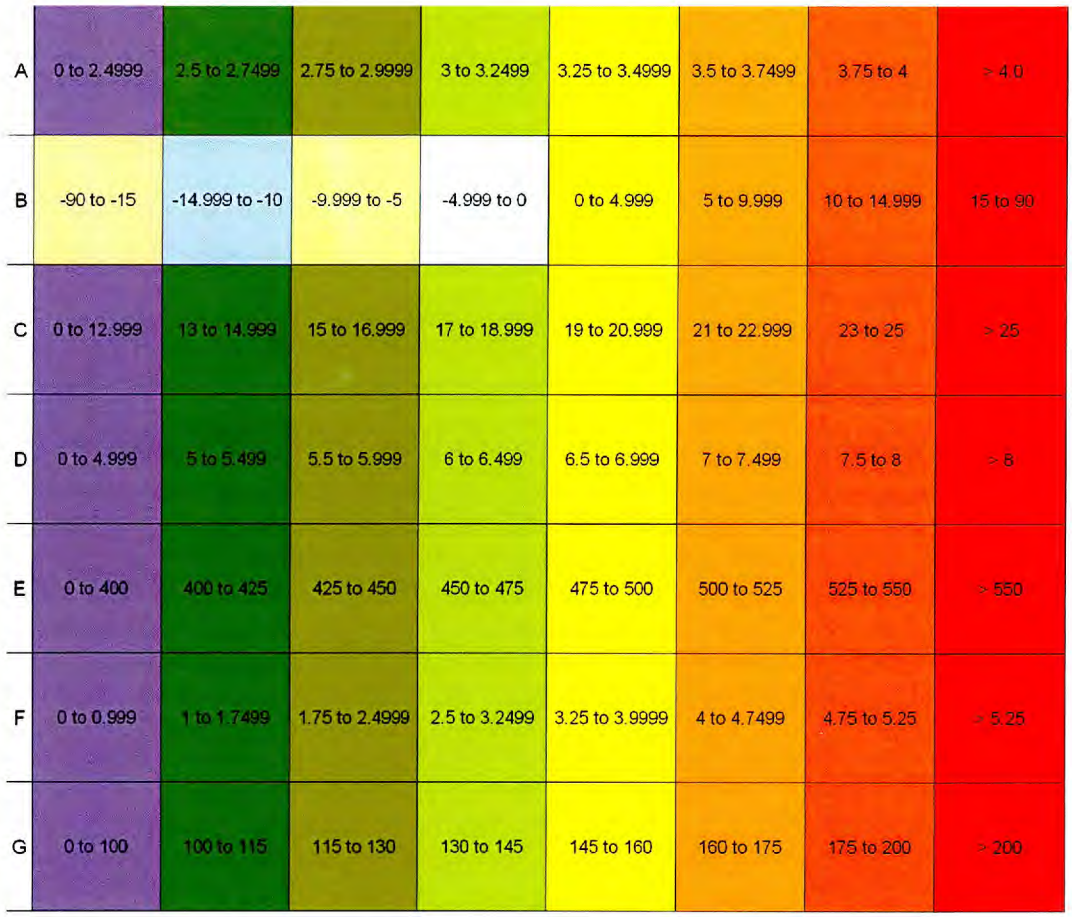

Fig. 4.5. Key to colour maps. Numbers show the range of values that will be coloured by each colour (in rabbits unless indicated otherwise).

A = Nuclear length:width ratio; B = Nuclear orientation (°); C = Nuclear length (μm); D = Nuclear width (μm); E = Nuclear area (pixels^2); F = Nuclear length:width ratio in mice and pigs; G = Number of nuclei.

4.2.5 Removing data from colour maps for nuclei at the edges of endothelial layers and branch ostia

Having produced colour maps for individual branches containing data for nuclear L/W ratios, angle of orientation etc it was possible to see that in regions at the edge of the maps, next to areas where damage to the EStAR was found, and in regions immediately adjacent to branch ostia, there were results that appeared slightly erratic, and did not follow the general trend. It was thought that this was caused by nuclei whose shape had been distorted but still maintained the correct area and perimeter for a nucleus, and thus did not get filtered out. This distortion could have been due to a few factors. 1) During

the process of manually erasing regions containing damage (in photoshop) some nuclei were not erased fully i.e. the tip of some nuclei were erased causing a lower LW ratio, 2) again during the erasing process some nuclei that should have been erased due to damage were missed, 3) when the tissue was initially stuck to the tape to produce the EStAR there may have been some movement at the edge of the EL causing nuclei to become slightly stretched, or their orientation to be altered slightly.

Distorted nuclei affected the average values in 100μm x 100μm regions so it was decided that these regions bordering the edge of the EL or the borders of branch ostia should be removed from the colour maps and subsequent analysis. Due to the large number of sheets to be analysed, doing this manually would have been extremely time consuming so a macro (Appendix C – Macro 11) was produced to automate this process. The only way to do this was to write a formula containing an IF statement that multiplied the values in the region of interest by the value in each region surrounding it. If the region next to it was empty, then the value would be returned as zero and an "X" was placed in the region (Fig. 4.6). If the value was not returned as zero then the cell was left as it was e.g. IF RC x RC[-1] = 0, then "X", IF RC x RC[-1] not = 0, then RC*1. All regions containing "X" were then removed from the maps.

R[-1]C[-1] Region 2	R[-1]C Region 3	R[-1]C[1] Region 4
RC[-1] Region 1	RC Region of interest	RC[1] Region 5
R[1]C[-1] Region 8	R[1]C Region 7	R[1]C[1] Region 6

Fig. 4.6. Formulae used to determine the region of interest and the regions surrounding it. R and C denote row and column respectively. If any of the Excel cells next to the region of interest were blank then an X would be placed in the region for deletion.

This method was repeated for LW, length, width, angle, and area data. Due to the nature of the EStAR technique it was impossible to align the longitudinal axis at exactly zero degrees for every EL. To overcome this potential spatial bias, all orientations were normalised. This was done by calculating the average angle of all the nuclei within the orientation map for each EL and producing a new, adjusted map with the mean angle being zero.

4.2.6 Determining the centre of branch ostia

The different colour maps had to be aligned so that averaging could be carried out across different animals. The ideal method would have been to align all the arteries by the first pair of ostia in each artery and somehow stretch the images so all further ostia from that point onwards were also aligned, enabling each artery to be analysed as a whole (Cornhill et al., 1985). However, the number of branches and the spacing and angle between pairs of branch ostia were different, ostia were different sizes, and on occasion ostia were damaged or missing. Instead it was decided that it would be more accurate to

find the centre of each ostium and use this as the centre point for the regions analysed around that ostium. All branches could then be superimposed using the centre as a point of reference.

Montage images containing branch ostia were opened in Photoshop and were cropped to produce a region measuring 1000μm x 1000μm surrounding each ostia. Using the eraser tool, the region thought to be the branch ostium was carefully erased so it became white. The cropped region, containing the erased ostium, was then opened in ImageTool and using the "find objects" command and a pixel intensity range of 254-255 pixels, the white region of the ostium was selected. The objects within the image were then analysed and the resulting data produced coordinates for the centre of mass of each object. This value was noted down for each ostium. The cropped image was re-opened in Photoshop and slices made visible (slices divide an image into separate areas, and are usually used during the design of web pages). Using the X and Y coordinates noted down for the ostium it was possible to set the dimensions of the slices so the point where the slices met corresponded to the centre of the branch ostia. At this point a black mark, measuring 30 pixels diameter, was placed. The cropped region, now containing a black mark at the centre of the ostium, was pasted back into the original montage image. Two images were produced in Photoshop of an x-axis and y-axis, both containing letters corresponding to cell coordinates in an Excel spreadsheet, in 100μm x 100μm boxes. The axis images were superimposed over the montage image, and made opaque. The point where the black mark was found, and the corresponding Excel coordinates were noted down.

4.2.7 Defining regions for analysis of results

It was not possible to analyse every region in each EStAR image. Since the focus of our research is on changes in blood flow surrounding branch ostia we predominantly need to look at the results for these regions. Once coordinates for the Excel cell (Excell) at the centre of each ostium had been defined it was possible to start to define regions. In maps containing just an individual branch, a region of 65 x 65 Excells (6500μm x 6500μm) was defined centred on the Excell containing the ostium (Fig. 5.1). In maps containing pairs of ostia, a 65 x 65 Excell region centred on one branch would also

overlap the other, leading to partly duplicated data. To prevent this, the distance (number of Excells) between the centres of each pair of ostia in the horizontal direction (not accounting for angle between branches) was counted (Table 4.1) for every map. To enable the region sizes to be standardised across all rabbits, the smallest number of Excel cells between ostia was determined (=12), and this number was divided by two (=6). Thus, the data were analysed for a region measuring 39 x 65 Excells (3900μm x 6500μm) for each ostium within a pair (Fig. 5.2). This hopefully also reduced any effects of flow caused by the other branch.

Table 4.1. Horizontal distance (Excel cells and micrometers) between pairs of branch ostium and the average distance per rabbit. I1-4 and M1-4 are immature and mature rabbits respectively. Value in bold denotes the smallest horizontal distance between branch pairs.

Rabbit	Branches	Horizontal distance		Average distance per rabbit	
		Excel Cells	Micrometers	Micrometers	SEM
I1	A+B	20	2000	1950.0	209.4
	C+D	22	2200		
	E+F	26	2600		
	G+H	22	2200		
	I+J	15	1500		
	K+L	**12**	1200		
I2	A+B	22	2200	2020.0	251.8
	C+D	27	2700		
	E+F	23	2300		
	G+H	16	1600		
	I+J	13	1300		
I3	B+C	22	2200	2325.0	103.1
	D+E	25	2500		
	F+G	25	2500		
	H+I	21	2100		
I4	C+D	17	1700	1900.0	200.0
	E+F	21	2100		
M1	C+D	18	1800	2250.0	263.0
	E+F	28	2800		
	G+H	26	2600		
	I+J	18	1800		
M2	B+C	25	2500	2114.3	151.9
	D+E	20	2000		
	F+G	24	2400		
	H+I	26	2600		
	J+K	18	1800		
	L+M	20	2000		
	N+O	15	1500		
M3	D+E	23	2300	2300.0	248.3
	F+G	30	3000		
	H+I	20	2000		
	J+K	19	1900		
M4	E+F	15	1500	1600.0	100.0
	G+H	17	1700		

4.3 Results

Using the EStAR technique, combined with propidium iodide staining, endothelial cell nuclei from the arterial walls of rabbits, mice and pigs could be viewed in very clear detail without the presence of underlying SMC nuclei (Fig. 4.7). We were able to produce EStARs of pairs of intercostal branch ostia in rabbits (Fig. 4.8), whole aortas in mice (Fig. 4.9), and single branch ostium in pigs (Fig. 4.10).

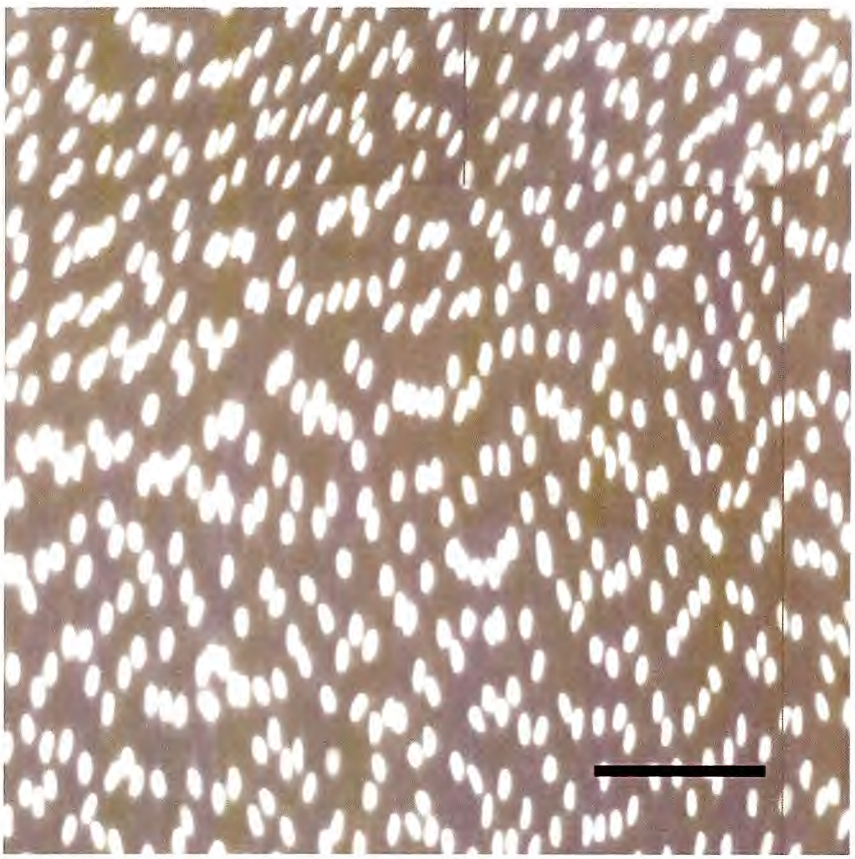

Fig. 4.7. *En face* view of endothelial cell nuclei stained with propidium iodide on an endothelial stick and rip (EStAR) preparation. Blood flow is from top to bottom. Scale bar = 100μm.

Fig. 4.8. *En face* view of endothelial cell nuclei surrounding a pair of rabbit intercostal branch ostium stained with propidium iodide on an endothelial stick and rip (EStAR) preparation. Blood flow is from top to bottom. Scale bar = 500μm.

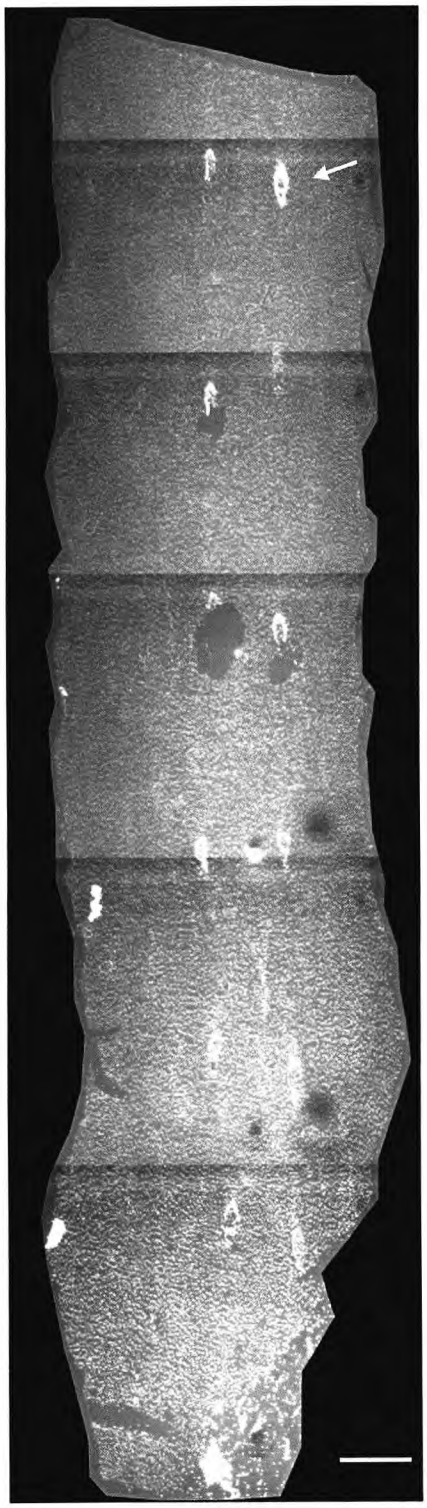

Fig. 4.9. *En face* view of endothelial cell nuclei in a mouse aorta stained with propidium iodide on an endothelial stick and rip (EStAR) preparation. Blood flow is from top to bottom. Arrow indicates an arterial cushion surrounding a branch ostium. Scale bar = 200μm.

Fig. 4.10. *En face* view of endothelial cell nuclei surrounding a pig intercostal branch ostium stained with propidium iodide on an endothelial stick and rip (EStAR) preparation. Blood flow is from top to bottom. Scale bar = 500μm

Production of EStARs has enabled quantitative data to be collected for endothelial nuclear parameters, and subsequently colour maps have been produced mapping the changes in nuclear dimensions around intercostal branch ostia (see next chapter).

4.4 Discussion

The EStAR technique has proved to be a reliable and rapid method for the production of endothelial monolayers from the thoracic aortas of rabbits of different ages. It has also been possible to produce EStARs from the thoracic aortas of mice and pigs and there is the potential also to produce EStARs from human aortas. Of the three species looked at, EStARs of rabbit aortas proved the easiest to produce, whilst pigs proved most difficult. Rabbit aortas had a luminal diameter that was large enough to get one blade of the ophthalmic scissors inside the lumen to cut open the artery longitudinally, without damaging the endothelium on the opposite wall. Pig aortas also had a large lumen, however the thickness of the wall caused the biggest problem. Due to the wall thickness, during the dehydration step a lot of alcohol became absorbed into the tissue.

When attempting to stick the endothelium onto the tape by applying pressure to the artery, the alcohol kept leaking out rather than evaporating, preventing adhesion. With more time it is felt the timings could be adjusted to improve EStAR production in pig aortas.

The main problem encountered with mice aortas was due to their small lumen diameter: it was very difficult to get a blade of the ophthalmic scissors into the lumen to cut down the wall to enable the artery to be opened longitudinally. This could also have caused damage to the endothelium as the point of the scissors may scrape along the wall. With practice, it is felt that mouse EStARs will be produced reliably, with little damage to the endothelium.

One of the main purposes of developing the EStAR technique was to remove SMC nuclei from the analysis of ECn. Occasionally SMCn still remained on the endothelial surface and, if these were not noticed and peeled away with forceps, they could have affected the final results. Having produced montage images, these could be easily erased in Adobe Photoshop. However if they were not removed manually, the Macro codes were designed to exclude them from subsequent analysis, and hence the EStAR technique fulfilled our aim.

Due to the size of montage images and the large number of pixels it was not possible to analyse whole montages in one go, hence the need to subdivide into smaller regions before analysis. With hindsight, it would have been more efficient to make the canvas for every image exactly the same dimensions. This would have made it possible to write an automated procedure that sub-divided the image, carried out all the filtering procedures, and finally saved the individual filtered images to enable analysis in ImageTool. Though this would have required enormous file sizes and the time taken to process each image would have been large, it may have been more efficient. Another benefit of identical canvas sizes would have been when it came to producing the colour maps, a further Macro code could have been written that enabled the maps to be produced without manual input.

Chapter 5: Assessing near wall blood-flow around intercostal branch ostia in the thoracic aorta from endothelial nuclear shape, as determined by fluorescence microscopy of EStAR preparations.

5.1 Introduction

Previous work (Al-Musawi *et al.*, 2004) has shown that there is a change in the pattern of endothelial nuclear elongation around intercostal branch ostia with age; immature rabbits have more elongated nuclei downstream than upstream of the ostia, whereas mature rabbits have more elongated nuclei upstream than downstream. Using the EStAR technique, the morphology of the nuclei surrounding branch ostia in immature and mature rabbits will be determined, and it is predicted that we will be able to confirm the change in the pattern of elongation previously seen. It will also be possible to determine the alignment of the nuclei with respect to the longitudinal axis of the arteries, and use this as an indicator of the direction of blood flow. Again, this has previously been done (Al-Musawi *et al.*, 2004). However, since our technique is semi-automated, it will be possible to observe more rabbits and branches, and to look at nuclei within smaller areas, giving more detailed and accurate maps of nuclear morphology.

It is predicted that there will be local changes in blood flow direction, due to blood being drawn into the intercostal branches from the regions immediately upstream and at the sides of the ostia, but there may be an overriding spiralling of the blood flow down the length of the arteries, indicating secondary flows.

It is also predicted that changes in nuclear orientation will be greater in rabbits than in mice arteries. The ratio between branch and aortic diameters are approximately equal (~0.1 – 0.15) for dogs (Caro, 1978, Nichols and O'Rourke, 1998) and rabbits (Cornhill and Roach, 1976), and from this it is presumed the ratio in mice would be similar. Therefore such differences would probably not be caused by the size of branch, but are more likely to be due to the differences in Reynolds numbers between mice and rabbits. Blood flow in rabbit aortas has higher Reynolds numbers, suggesting increased inertia, than in mice aortas (cited in (Weinberg and Ethier, 2007). A CFD model of an intercostal artery branching off the thoracic aorta perpendicularly, with a diameters ratio of 0.1, has shown that under steady flow conditions increasing Reynolds number caused fluid to enter the branch from areas of slower velocities, closer to the aortic wall, thus affecting more strongly the wall shear stress around the ostium, decreasing it at the sides and increasing it upstream and downstream. Wall shear stress patterns found at higher

Reynolds values correlated well with lesion patterns observed in mature rabbits. For the lowest values of Reynolds number and flow division ratio the wall shear stress pattern correlated well with the lesion pattern seen in mice (Kazakidi et al., 2006).

No previous data have been found concerning how nuclear lengths, widths and areas change in the periostial regions. Studies of human aortas (Repin *et al.*, 1984) have shown that the mean cell density in young arteries is greater than in old, and this change should be evident in the rabbit aortas studied here. Nuclear lengths and widths are analysed to determine whether changes in one or both of them underlie the changes observed in LW ratios, and nuclear areas are also analysed in an exploratory fashion to determine whether they are also related to LW ratios.

EStAR preparations of mice and pig aortas shall also be carried out to a) see whether it is possible using this technique to obtain nuclear shape data in these species, and b) if this is possible, to see whether the nuclear shape is different between species.

5.2 Methods

5.2.1 Rabbit aortas

Thoracic aortas of male New Zealand White rabbits (Harlan Interfauna strain) were fixed at physiological pressure with 10% neutral buffered formalin (Sigma) as previously described. Rabbits were aged 6-7 weeks (n=4), 44 weeks (n=1), 50 weeks (n=2) and 88 weeks (n=1) (i.e. approximately 1.5, 11, 12.5 and 22 months). Based on the characteristics of semen, it has been shown that male NZW rabbits have reached sexual maturity by six months old (Macari and Machado, 1978). Rabbits were therefore classed as immature (I1-4) if less than 6 months old, and rabbits older than this were counted as mature (M1-4). The rabbits used in our experiments fell clearly within these groups, and did not include any period of transition between the two ages (Table 5.1). All rabbits were fed a standard laboratory diet without supplementary fat.

Table 5.1. Details of immature and mature rabbits used in EStAR technique experiments to determine patterns of endothelial cell nuclei around intercostal branch ostia.

Age group	Rabbit	Age (weeks)	Age (months)	Body weight (kg)	Number of branches used
Immature	I1	6	1.5	1.0	12
	I2	6	1.5	1.4	11
	I3	6	1.5	1.6	9
	I4	7	1.5	1.4	4
Mature	M1	44	11	4.1	10
	M2	50	12.5	3.8	15
	M3	50	12.5	4.0	9
	M4	88	22	4.5	4

All aortas underwent EStAR preparation, staining with propidium iodide, and imaging at 200x magnification using a rhodamine filter, as previously described.

5.2.2 Mouse aortas

Thoracic aortas of three mice (one each of Wild-type (WT), eNOS-GFP, and Balb/c) were fixed at physiological pressure with 10% neutral buffered formalin before being excised and stored in formalin. The eNOS-GFP mouse is a transgenic mouse model in which an eNOS-GFP fusion protein is expressed that can be used to study vascular reactions in which eNOS is involved (van Haperen *et al.*, 2003). Both WT and eNOS-GFP mice were aged 29 weeks (7.25 months). The age of the Balb/c mouse was unknown but it weighed 24.2g at the time of fixation.

All aortas underwent EStAR preparation, staining with PI, and imaging at 200x magnification using a rhodamine filter as previously described.

5.2.3 Pig aortas

Thoracic aortas from two Babraham pigs aged 3.5 months (reared at the University of Bristol, UK) were excised and flushed with PBS to remove any blood. Aortas were placed in 10% neutral buffered formalin but not fixed at physiological pressure due to the large volumes of fixative that would have been required. Whilst still *in situ* the aortas were measured as it was thought that once excised they could be stretched back to

their original length before fixation. This proved unsuccessful, but EStARs were still attempted to determine whether it would be possible in future to use the technique to determine ECn parameters in this species.

EStARs were stained with PI and imaged at 200x magnification using a rhodamine filter as previously described.

5.2.4 Data processing and statistical analysis

Statistical tests were conducted on data from rabbits. Data structure: as with mice (Chapter 3), two age groups were considered – 6-7 weeks and 44-88 weeks. There were 4 rabbits in each age group. Between 4-15 intercostal branches from the aorta of each rabbit were examined (4-12 in young, 36 in total; 4-15 in mature, 38 in total). The branches were randomly selected from the 16 present in each animal. The number and distribution of anatomical regions examined around each branch was more complex than in mice and is described below. Within each of these anatomical regions, the morphology of around 15 nuclei were examined. As with mice, the morphological parameters again included nuclear length-to-width ratio and the angle between the nuclear long axis and the longitudinal axis of the aortic segment. Because of the large sample size within each region, results for each parameter were aggregated before statistical analyses were conducted: only the mean value (e.g. of length-to-width ratio or angle) for each region was used. Statistical tests were conducted to determine whether there was a significant effect on each parameter of age or region, and whether there was a significant interaction between effects of age and region (which would imply an effect of age on the anatomical pattern of that parameter).

The statistical test used was a general linear model univariate analysis of variance (SPSS Version 14.0) incorporating a nested design whereby rabbits were nested within age, and branches were in turn nested within rabbits. If this showed an overall significant result, the significance of differences between individual regions was determined using a post-hoc Tukey test, having first split the data by age. Data are presented as mean ± SEM. Results were deemed significant if $P<0.05$.

Anatomical regions examined: Due to the large number of 100μm x 100μm regions ("sub-regions") to be analysed (at least 2500 per branch), it was not possible to compare every one due to computer memory constraints. To overcome this, the sub-regions were averaged before analysis to give fewer 500μm x 500μm regions ("main regions") (Fig. 5.1 & 5.2). However, to observe changes in ECn parameters close to the branch ostium at greater spatial resolution, the sub-regions in main regions "U1", "U2", "D1", "D2", "R1", "L1", "U1R1", "U1L1", "D1R1" and "D1L1" were analysed without such averaging. These sub-regions are labelled "U2R1s", "U2s", "U2L1s", "U1R1s", "U1s", "U1L1s", "R1s", "L1s", "D1R1s", "D1s", "D1L1s", "D2R1s", "D2s" and "D2L1s". ("U", "D", "R", "L" and "s" denote upstream, downstream, right, left and sub-region, respectively). Main regions were also grouped into three "zones" (Zone A, Zone B and Zone C) according to their distance from the ostium (0-1mm, 1-2mm, and 2-3mm respectively – (see Fig. 5.1 and 5.2).

Due to time constraints, fewer regions were analysed for cell density than for other nuclear parameters (Fig. 5.3). This allowed smaller regions to be analysed: each main region measured 250μm * 250μm, not 500μm * 500μm as for other parameters, but were not sub-divided into smaller sub-regions. Additionally, main-regions were grouped into two rather than three zones (Zone A* and Zone B*) depending on their distance (0-0.5mm and 0.5-0.75mm, respectively) from the ostium.

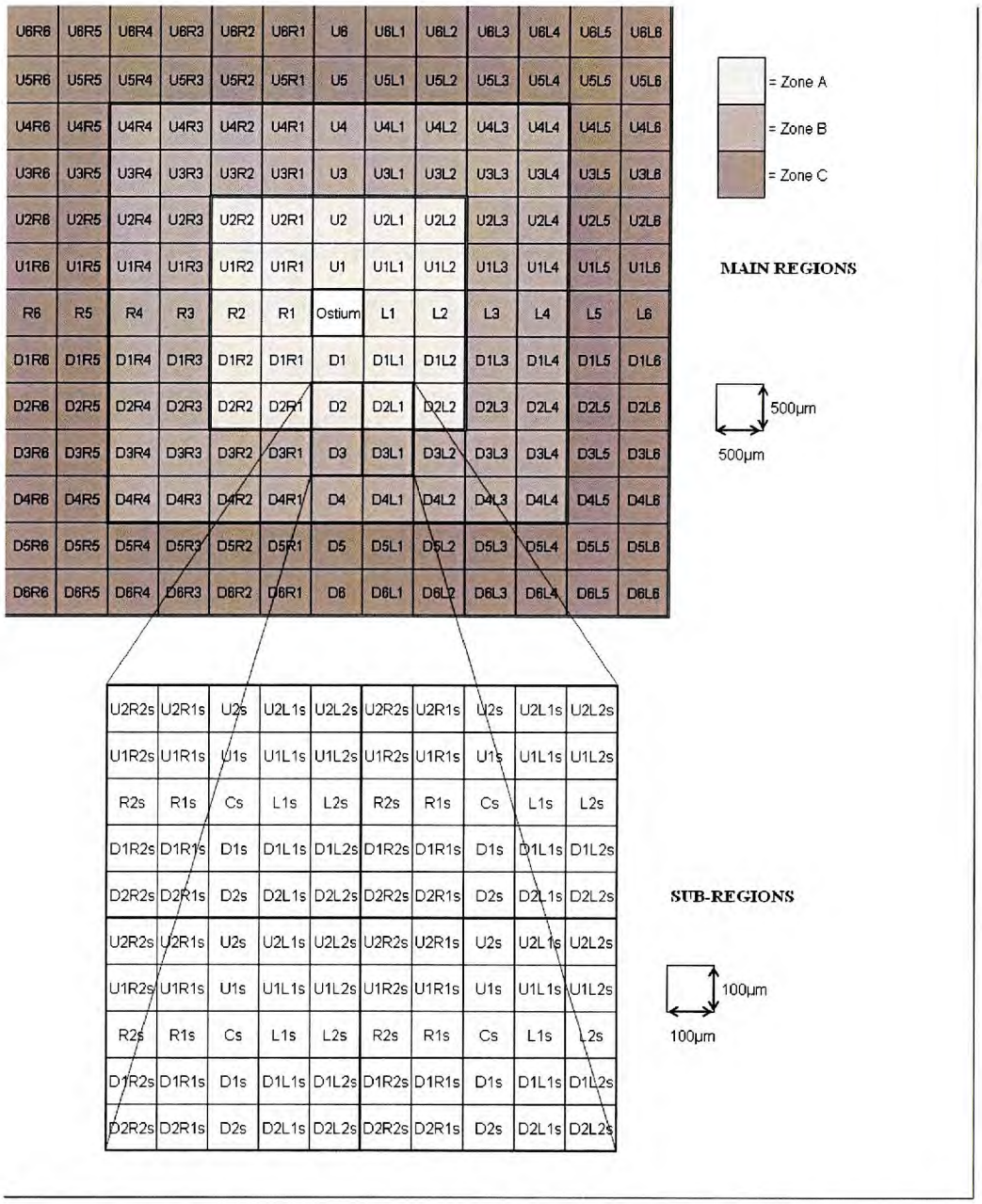

Fig. 5.1. Regions analysed surrounding branch ostium. "Zone A", "Zone B", and "Zone C" contain nuclei 0-1000µm, 1-2mm, and 2-3mm away from branch ostia respectively. Each "main-region" square is 500µm*500µm, and can be sub-divided into "sub-regions" measuring 100µm*100µm. "U", "D", "R", "L" and "s" denote upstream, downstream, right, left and sub-region, respectively.

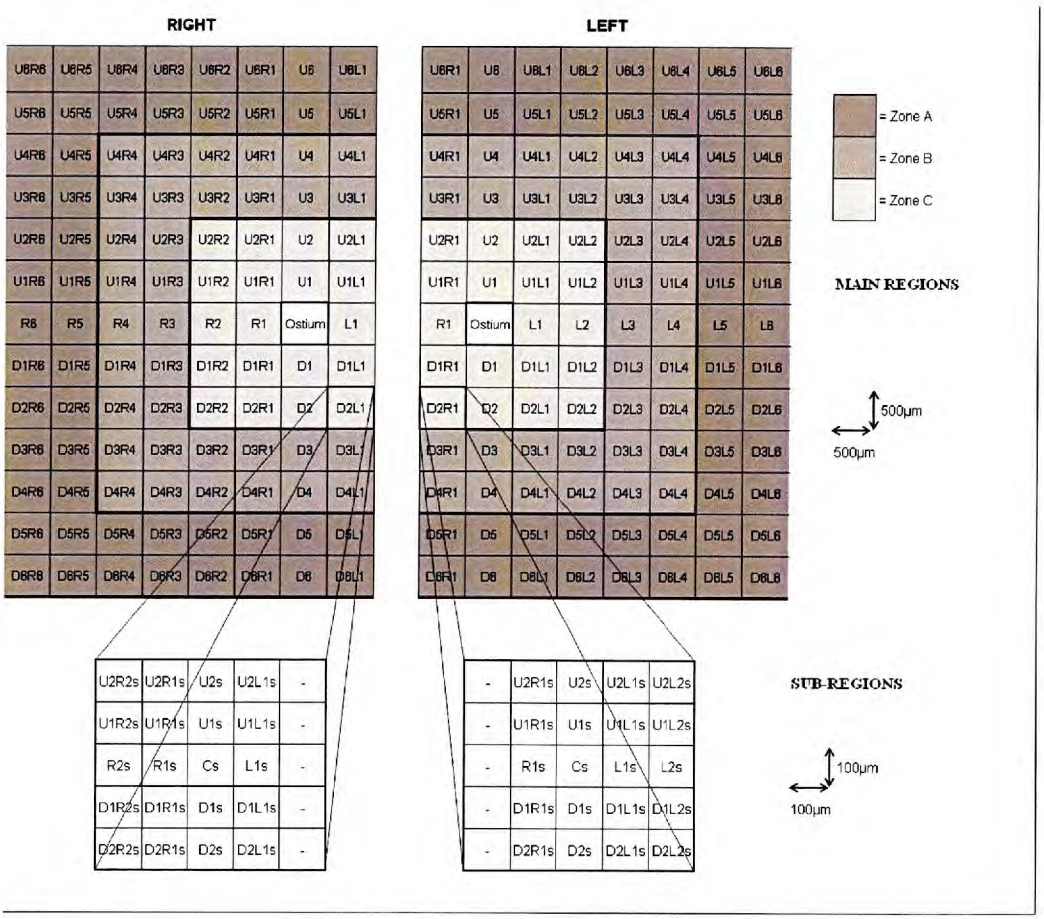

Fig. 5.2. Regions analysed for left and right branches separately. "Zone A", "Zone B", and "Zone C" contain nuclei 0-1mm, 1-2mm and 2-3mm away from branch ostia respectively. Each "main-region" square is 500µm * 500µm, and can be sub-divided into "sub-regions" measuring 100µm * 100µm. "U", "D", "R", "L" and "s" denote upstream, downstream, right, left and sub-region, respectively.

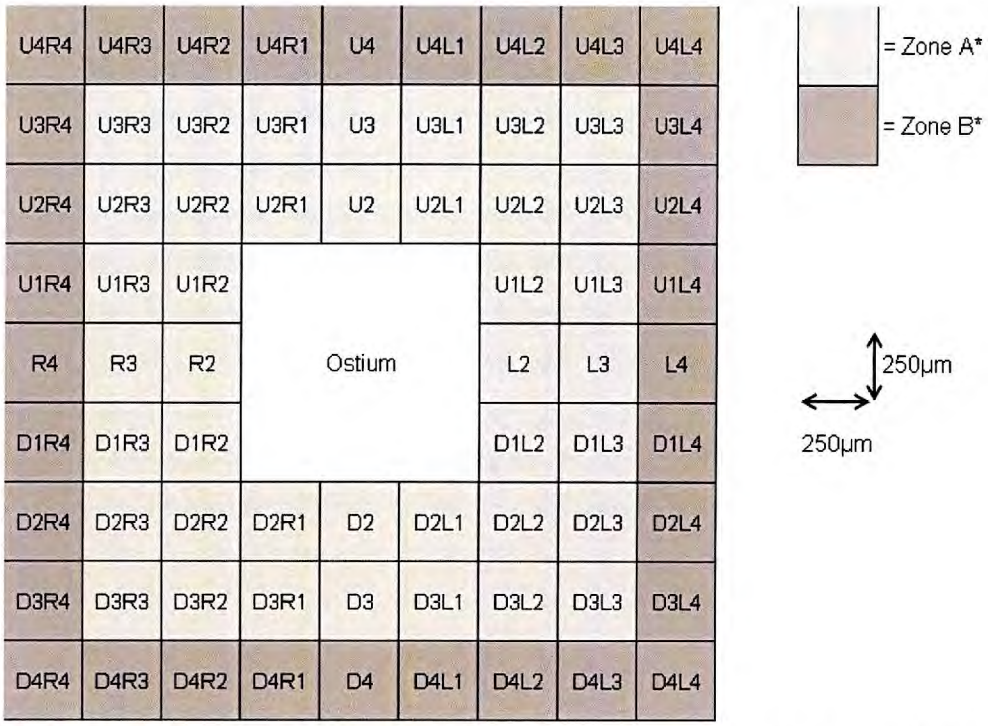

Fig. 5.3. Regions analysed surrounding branch ostia for nuclear density analysis. "Zone A*" and "Zone B*" contain nuclei 0-0.5mm and 0.5-0.75mm away from branch ostia respectively. "U", "D", "R", and "L" denote upstream, downstream, right and left, respectively.

Additional tests not conducted on mice (Chapter 3) were carried out. To see whether different areas of the aortas experienced different flow patterns, branches were analysed depending on their location within the aorta; they were subdivided into branches within upper or lower portions of the descending thoracic aorta, and left hand or right hand branches. Upper and lower portions included regions around branches 1 to 6 and 7 to 12 respectively, branch 1 being the first intercostal branch ostium after the aortic arch. Branches lower down the artery than number 12 were recovered in one mature rabbit (they were missing from other arteries due to being below the level of cannulation, or EStAR preparations were not carried out due to time constraints), but they were ignored in subsequent analysis.

Differences between branches in different portions of the artery i.e. upper and lower, or left and right branch ostia were determined using a one-way ANOVA. To determine comparisons between individual regions within the area defined as "Zone A" in figure

5.1 and 5.2, Tukey post-hoc tests were performed after first splitting the data so that immature and mature rabbits were analysed separately. All data are presented as mean ± SEM.

Statistical analysis was not carried out for mice or pig aortas due to the small number of EStARs produced.

5.3 Results from rabbit aortas

Results are displayed in colour maps, tables (to present mean values and standard errors, as SEMs cannot be shown in the maps) and graphs (to highlight important changes in morphology). All colour maps show the average data for endothelial cell nuclei from the regions described in Fig. 5.1 for immature (left) and mature (right) rabbits (unless otherwise marked). All maps are spatially accurate i.e. they could be overlaid onto the original images, and represent the data for endothelial cell nuclei in the thoracic aorta surrounding branch ostia (marked with a star), with mean aortic blood flow from top to bottom. The white square underneath the star equates to a region 500μm*500μm. Data are not available for this region due to damage caused during the EStAR preparation, and slight inaccuracies determining the exact centre of the branch ostia when aligning images. Average values per region are indicated in each individual square, and correspond with the colour of the square (for key, see Fig. 4.5). "Low" resolution colour maps show data averaged per 500μm * 500μm regions, and "high" resolution maps show data averaged per 100μm * 100μm sub-region.

5.3.1 Rabbit nuclear length:width ratios

Nuclear LW ratios for 36 immature (I) and 38 mature (M) branches for the regions defined in Fig. 5.1 (zones A-C) are shown in Fig. 5.4. There were highly significant differences in mean LW ratio between ages and regions and a highly significant interaction between age and region (age*region) (all $P<0.005$). Mean LW ratios for individual rabbits are shown in Table 5.2. Nuclei of immature rabbits had mean LW ratios of 2.46 ± 0.00 (n = 3263 regions), whereas the nuclei of mature rabbits were 34.6% more elongated, having an average LW ratio of 3.31 ± 0.01 (n = 3539 regions). LW ratios in rabbit M4, the oldest rabbit by a margin of at least 38 weeks, were

approximately 25% higher than the mean LW ratio for the nuclei of the other three mature rabbits. In subsequent analyses, to determine the changes in pattern of nuclear elongation surrounding branch ostia, exclusion of the data from this rabbit did not affect the statistical significance of differences: therefore the data were included in the analysis.

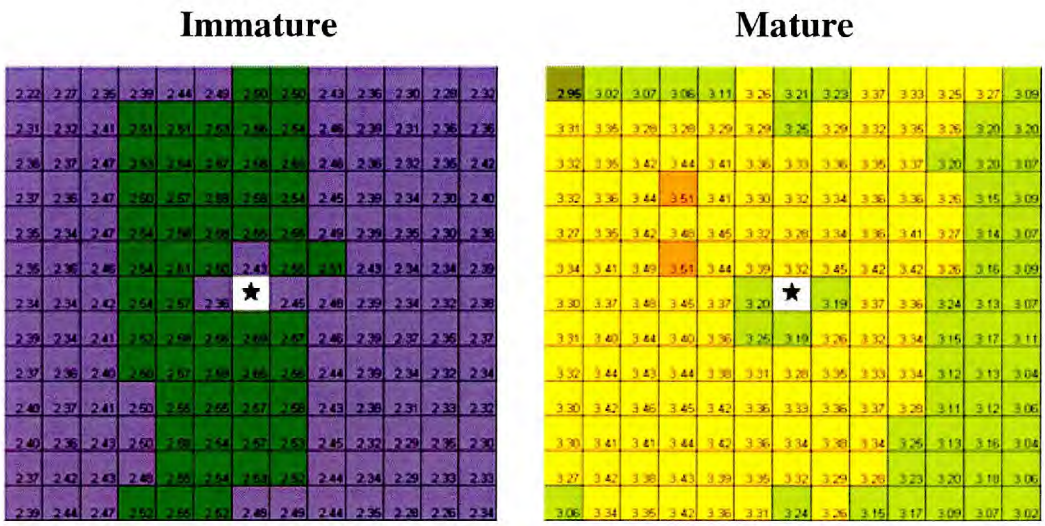

Fig. 5.4. Length:width ratios of rabbit endothelial cell nuclei for all branch ostia. Each square represents the average data for a 500μm * 500μm region. Total area of each map is 42.25mm^2. n = 4 immature rabbits, n = 4 mature rabbits. Data represent averages for all 36 immature and 38 mature branches.

Table 5.2. Mean endothelial cell nuclear length:width ratios for all zones (see fig. 5.1) in individual rabbits, where n equals the number of regions.

Age Group	Rabbit	LW ratio	
		Mean	SEM
Immature	I1	2.48	0.01
	I2	2.43	0.01
	I3	2.44	0.01
	I4	2.67	0.01
	All immature	2.46	0.00
Mature	M1	3.50	0.01
	M2	3.03	0.01
	M3	3.32	0.01
	M4	4.11	0.02
	All mature	3.31	0.01

5.3.1.1 "Zone A" (500μm * 500μm regions)

LW ratios for "Zone A" regions (within 1000μm of branch ostia) are shown in Fig. 5.5. There was a significant effect of age (mean LW ratios 2.54 ± 0.01 and 3.32 ± 0.02 for immature (n = 677 regions) and mature (n = 741 regions) rabbits respectively, a 30.7% difference), region and the age*region interaction (all $P<0.005$).

In immature rabbits, the mean LW ratios for nuclei upstream of the branch ostia were generally lower (2.43 ± 0.03, "U1", n = 36 branches) than for those downstream, the greatest nuclear elongation being in regions "D1" and "D2" (2.69 ± 0.04, n = 34 branches, and 2.65 ± 0.03, n = 34 branches, respectively): the ratio of the mean upstream value ("U1") to the mean downstream ("D1") value was 0.90 (values <1 indicate greater nuclear elongation downstream and values >1 indicate greater elongation upstream). Nuclei at the lateral regions ("R1" and "L1") were lower than for all other regions in zone A, a result that differs from the findings of (Al-Musawi *et al.*, 2004), who found the lowest LW ratios in the "UL" region. The LW ratios ranged from 2.36 ± 0.03 ("R1", n = 36 branches) to 2.69 ± 0.04 ("D1", n = 34 branches); a 14.0% difference.

Mature rabbits had a different pattern of nuclear elongation, in Zone A, to immature rabbits. Nuclei had LW ratios in downstream and lateral regions, located next to the branch ostia ("R1", "L1", "D1", "D1R1" and "D1L1"), that were approximately equal to each other but were lower than all other zone A regions. Values ranged from 3.19 ± 0.07 ("L1" and "D1", both n = 34 brances) to 3.45 ± 0.08 ("U2R2", n = 21 branches) and 3.45 ± 0.07 ("U1L1", n = 38 branches), a difference of 8.2%. The ratio of the mean upstream value ("U1", 3.32 ± 0.07, n = 38 branches) to the mean downstream value ("D1", 3.19 ± 0.07, n = 38 branches) was 1.04.

The significance of differences between individual regions within Zone A for immature and mature rabbits, obtained using the Tukey test, is shown in Fig. 5.6.

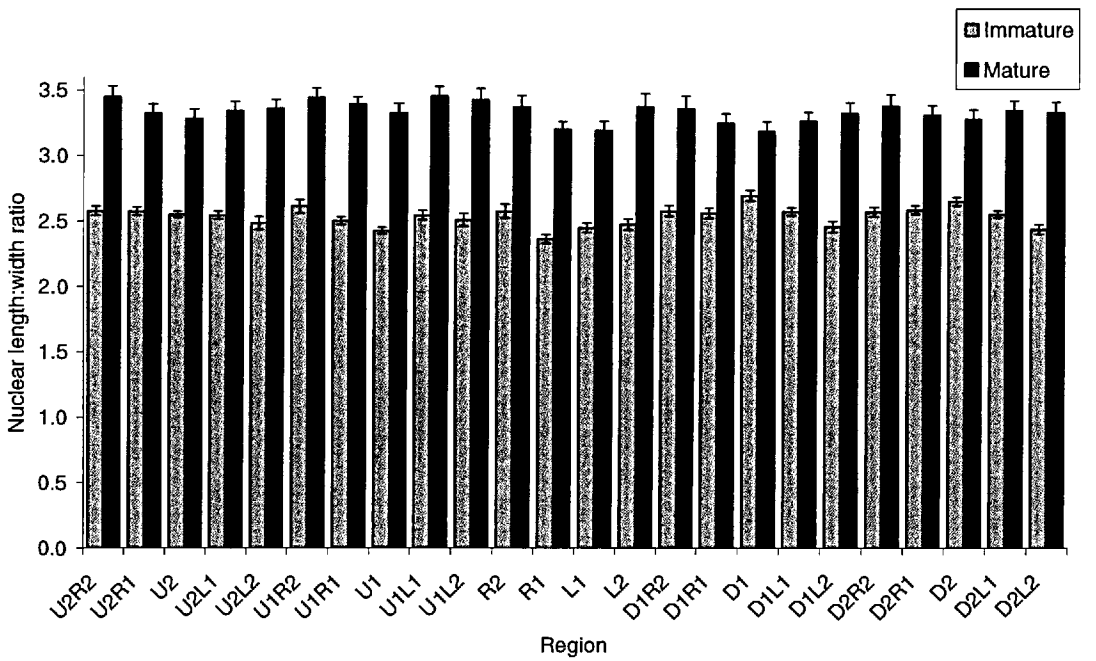

Fig. 5.5. Nuclear LW ratios in immature and mature rabbits for regions surrounding branch ostia (Zone A) defined in Fig. 5.1. Bars show means ± SEM (n = number of branches).

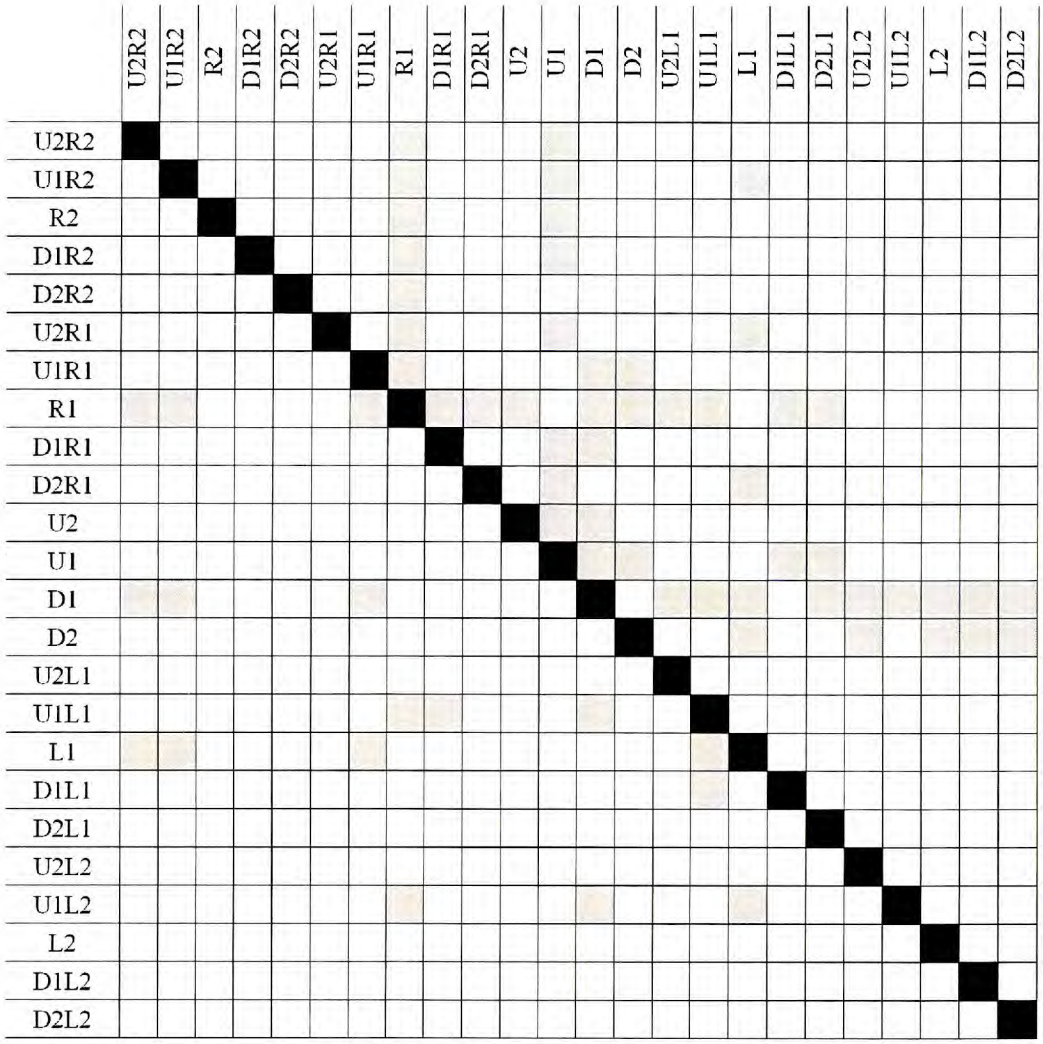

Fig. 5.6. Significant differences in nuclear LW ratios between 500μm * 500μm regions within Zone A as determined by the Tukey test for multiple comparisons. Squares shaded in grey depict significant differences ($P<0.05$) between regions. Squares to the right of the black diagonal line indicate differences in immature rabbits. Squares to the left indicate differences in mature rabbits.

5.3.1.2 "Zone A" (100μm * 100μm sub-regions)

The data was split so the regions nearest the branch ostia ("U2R1", "U2", "U2L1", "U1R1", "U1", "U1L1", "R1", "L1", "D1R1", "D1", "D1L1", "D2R1", "D2", "D2L1") were analysed individually, using nuclear morphologies averaged per 100μm * 100μm sub-region rather than 500μm * 500μm (Fig. 5.7, Table 5.3a, b and 5.4a,b). Data were examined for effects of age or region, or any interaction between age and region. There was a significant effect of age ($P<0.05$) for all regions, and a significant effect of region

($P<0.01$) for sub-regions within main regions "U1R1", "U1", "U1L1", "R1", "L1", "D1R1", "D1", and "D1L1". There was a significant change with age in pattern (age*region interaction) for the regions "L1", "D1R1", "D1", "D1L1" and "D2L1" ($P<0.01$). In immature rabbits, nuclei closest to the branch ostia were least elongated, and in a small region offset approximately 200μm distal to the ostia, the nuclei were more elongated. In mature rabbits, there was a different pattern; the most rounded nuclei were found in a triangular region, extending approximately 800μm downstream of the ostia, but nuclei were more elongated upstream and to the sides of the branch.

The ratio of the mean LW ratio immediately upstream (sub-region "D2s" in main-region "U1") to the mean LW ratio immediately downstream of the ostia (sub-region "U2s" in main-region "D1) was 0.89 in immature rabbits, and 0.95 in mature rabbits. In the regions 100μm from the branch ostia, the ratio for the LW ratios upstream (sub-region "D1s" in main region "U1") to downstream (sub-region "U1s" in main region "D1"), was 0.88 in immature rabbits and 1.02 in mature rabbits.

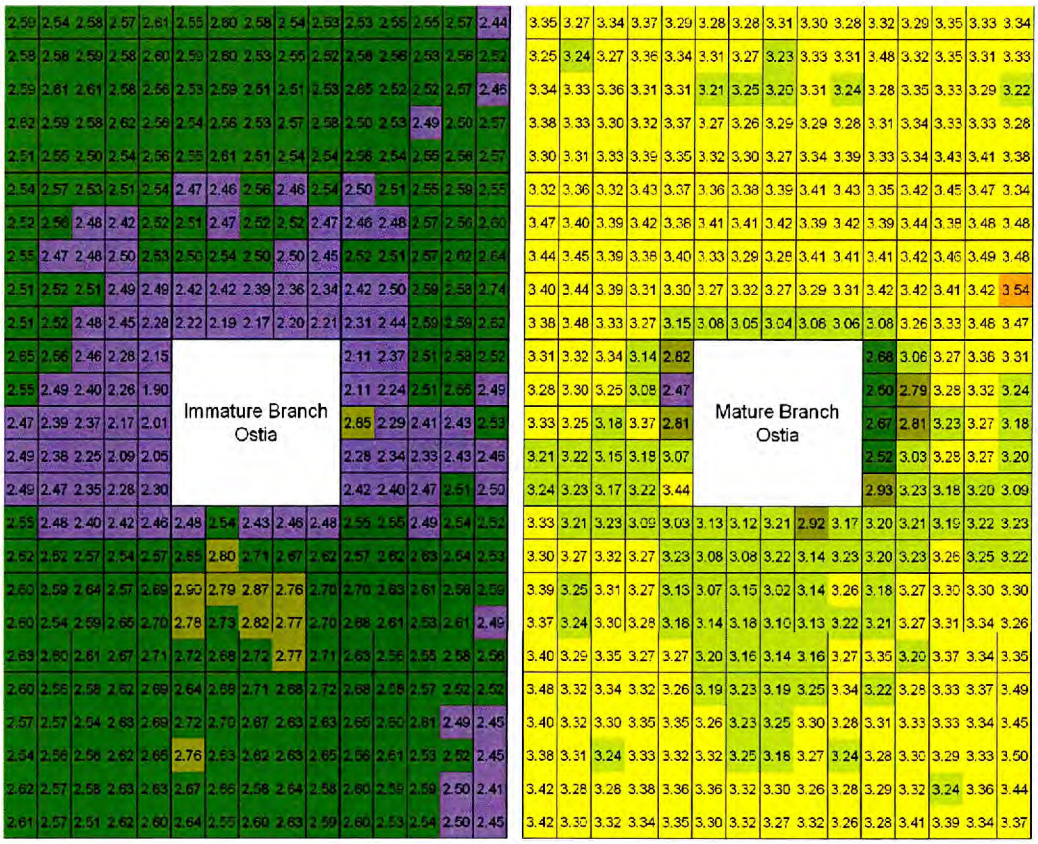

Fig. 5.7. Colour maps of length:width ratios of rabbit endothelial cell nuclei for all branch ostia. Each square represents the average data for a 100μm*100μm region. Total area of each map is 3.75mm^2. n = 4 immature rabbits, n = 4 mature rabbits. Data represent averages for all 36 immature and 38 mature branches.

Table 5.3a. Immature rabbit endothelial cell nuclear LW ratios for sub-regions (100μm * 100μm) within upstream and lateral main-regions in "Zone A", where n equals the number of branches.

Immature	U2R1		U2		U2L1		U1R1		U1		U1L1		R1		L1	
Sub-Region	Mean	SEM	Mean	SEM	Mean	SEM	Mean	SEM	Mean	SEM	Mean	SEM	Mean	SEM	Mean	SEM
U2R2s	2.59	0.06	2.55	0.05	2.53	0.04	2.54	0.05	2.47	0.04	2.50	0.05	2.65	0.10	2.11	0.13
U2R1s	2.54	0.05	2.60	0.04	2.55	0.05	2.57	0.04	2.46	0.04	2.51	0.04	2.56	0.05	2.37	0.08
U2s	2.58	0.06	2.58	0.04	2.55	0.05	2.53	0.04	2.56	0.04	2.55	0.06	2.46	0.05	2.51	0.07
U2L1s	2.57	0.05	2.54	0.04	2.57	0.05	2.51	0.04	2.46	0.03	2.59	0.04	2.28	0.07	2.58	0.06
U2L2s	2.61	0.04	2.53	0.05	2.44	0.06	2.54	0.04	2.54	0.05	2.55	0.07	2.15	0.07	2.52	0.08
U1R2s	2.58	0.07	2.59	0.03	2.56	0.05	2.52	0.06	2.51	0.04	2.46	0.03	2.55	0.06	2.11	0.10
U1R1s	2.58	0.04	2.60	0.03	2.56	0.04	2.56	0.04	2.47	0.04	2.48	0.04	2.49	0.06	2.24	0.12
U1s	2.59	0.06	2.53	0.03	2.53	0.04	2.48	0.04	2.52	0.04	2.57	0.05	2.40	0.07	2.51	0.08
U1L1s	2.58	0.05	2.55	0.04	2.56	0.05	2.42	0.04	2.52	0.04	2.56	0.06	2.26	0.09	2.55	0.07
U1L2s	2.60	0.03	2.52	0.05	2.52	0.08	2.52	0.05	2.47	0.04	2.60	0.07	1.90	0.16	2.49	0.07
R2s	2.59	0.06	2.53	0.04	2.65	0.06	2.55	0.07	2.50	0.06	2.52	0.05	2.47	0.06	2.85	0.46
R1s	2.61	0.05	2.59	0.04	2.52	0.04	2.47	0.04	2.54	0.04	2.51	0.05	2.39	0.05	2.29	0.10
Cs	2.61	0.05	2.51	0.03	2.52	0.04	2.48	0.04	2.50	0.04	2.57	0.06	2.37	0.07	2.41	0.07
L1s	2.58	0.04	2.51	0.03	2.57	0.05	2.50	0.04	2.50	0.04	2.62	0.07	2.17	0.09	2.43	0.05
L2s	2.56	0.03	2.53	0.04	2.46	0.07	2.53	0.04	2.45	0.04	2.64	0.08	2.01	0.16	2.53	0.07
D1R2s	2.62	0.06	2.54	0.04	2.50	0.04	2.51	0.08	2.42	0.05	2.42	0.05	2.49	0.06	2.28	0.14
D1R1s	2.59	0.04	2.56	0.05	2.53	0.05	2.52	0.04	2.42	0.04	2.50	0.05	2.38	0.04	2.34	0.08
D1s	2.58	0.05	2.53	0.04	2.49	0.04	2.51	0.05	2.39	0.04	2.59	0.07	2.25	0.06	2.33	0.06
D1L1s	2.62	0.05	2.57	0.03	2.50	0.05	2.49	0.05	2.36	0.05	2.58	0.07	2.09	0.06	2.43	0.05
D1L2s	2.56	0.03	2.58	0.05	2.57	0.08	2.49	0.05	2.34	0.06	2.74	0.06	2.05	0.14	2.46	0.05
D2R2s	2.51	0.06	2.55	0.04	2.56	0.04	2.51	0.09	2.22	0.06	2.31	0.07	2.49	0.05	2.42	0.08
D2R1s	2.55	0.04	2.61	0.04	2.54	0.05	2.52	0.05	2.19	0.07	2.44	0.08	2.47	0.04	2.40	0.06
D2s	2.50	0.04	2.51	0.04	2.55	0.04	2.48	0.05	2.17	0.06	2.59	0.06	2.35	0.06	2.47	0.05
D2L1s	2.54	0.04	2.54	0.04	2.56	0.05	2.45	0.06	2.20	0.06	2.59	0.06	2.28	0.06	2.51	0.04
D2L2s	2.56	0.05	2.54	0.04	2.57	0.05	2.28	0.05	2.21	0.06	2.62	0.06	2.30	0.09	2.50	0.05

Table 5.3b. Immature rabbit endothelial cell nuclear LW ratios for sub-regions (100μm * 100μm) within downstream main-regions in "Zone A", where n equals the number of branches.

Immature	D1R1		D1		D1L1		D2R1		D2		D2L1	
Sub-Region	Mean	SEM	Mean	SEM	Mean	SEM	Mean	SEM	Mean	SEM	Mean	SEM
U2R2s	2.55	0.05	2.48	0.09	2.55	0.07	2.60	0.06	2.64	0.06	2.68	0.05
U2R1s	2.48	0.05	2.54	0.07	2.55	0.05	2.56	0.04	2.68	0.05	2.58	0.05
U2s	2.40	0.04	2.43	0.07	2.49	0.05	2.58	0.05	2.71	0.04	2.57	0.04
U2L1s	2.42	0.06	2.46	0.08	2.54	0.05	2.62	0.06	2.68	0.06	2.52	0.04
U2L2s	2.46	0.07	2.48	0.06	2.52	0.05	2.69	0.06	2.72	0.06	2.52	0.06
U1R2s	2.62	0.06	2.65	0.08	2.57	0.06	2.57	0.05	2.72	0.06	2.65	0.06
U1R1s	2.52	0.05	2.80	0.08	2.62	0.05	2.57	0.04	2.70	0.05	2.60	0.04
U1s	2.57	0.06	2.71	0.07	2.63	0.04	2.54	0.05	2.67	0.05	2.61	0.04
U1L1s	2.54	0.06	2.67	0.06	2.54	0.05	2.63	0.06	2.63	0.05	2.49	0.04
U1L2s	2.57	0.06	2.62	0.07	2.53	0.05	2.69	0.06	2.63	0.05	2.45	0.07
R2s	2.60	0.07	2.90	0.16	2.70	0.06	2.54	0.04	2.76	0.07	2.56	0.06
R1s	2.59	0.05	2.79	0.07	2.63	0.04	2.56	0.03	2.63	0.05	2.61	0.05
Cs	2.64	0.05	2.87	0.08	2.61	0.05	2.56	0.05	2.62	0.05	2.53	0.04
L1s	2.57	0.06	2.76	0.06	2.56	0.04	2.62	0.06	2.63	0.05	2.52	0.04
L2s	2.69	0.07	2.70	0.07	2.59	0.05	2.65	0.05	2.65	0.05	2.45	0.06
D1R2s	2.60	0.06	2.78	0.08	2.68	0.06	2.62	0.06	2.67	0.05	2.60	0.04
D1R1s	2.54	0.05	2.73	0.07	2.61	0.04	2.57	0.03	2.66	0.05	2.59	0.03
D1s	2.59	0.05	2.82	0.06	2.53	0.04	2.58	0.04	2.58	0.04	2.59	0.05
D1L1s	2.65	0.06	2.77	0.07	2.61	0.03	2.63	0.05	2.64	0.05	2.50	0.05
D1L2s	2.70	0.07	2.70	0.05	2.49	0.09	2.63	0.05	2.58	0.04	2.41	0.06
D2R2s	2.63	0.05	2.72	0.07	2.63	0.05	2.61	0.04	2.64	0.05	2.60	0.06
D2R1s	2.60	0.04	2.68	0.05	2.56	0.05	2.57	0.04	2.55	0.04	2.53	0.04
D2s	2.61	0.05	2.72	0.04	2.55	0.05	2.51	0.03	2.60	0.05	2.54	0.05
D2L1s	2.67	0.05	2.77	0.05	2.58	0.03	2.62	0.04	2.63	0.04	2.50	0.04
D2L2s	2.71	0.07	2.71	0.06	2.56	0.06	2.60	0.04	2.59	0.04	2.45	0.07

Table 5.4a. Mature rabbit endothelial cell nuclear LW ratios for sub-regions (100μm * 100μm) within upstream and lateral main-regions in "Zone A", where n equals the number of branches.

Mature	U2R1		U2		U2L1		U1R1		U1		U1L1		R1		L1	
Sub-Region	Mean	SEM	Mean	SEM	Mean	SEM	Mean	SEM	Mean	SEM	Mean	SEM	Mean	SEM	Mean	SEM
U2R2s	3.35	0.11	3.28	0.08	3.32	0.07	3.32	0.07	3.36	0.09	3.35	0.10	3.31	0.09	2.68	0.16
U2R1s	3.27	0.07	3.28	0.07	3.29	0.08	3.36	0.08	3.38	0.10	3.42	0.09	3.32	0.08	3.06	0.10
U2s	3.34	0.08	3.31	0.07	3.35	0.08	3.32	0.08	3.39	0.09	3.45	0.09	3.34	0.11	3.27	0.08
U2L1s	3.37	0.08	3.30	0.07	3.33	0.06	3.43	0.10	3.41	0.10	3.47	0.09	3.14	0.11	3.38	0.08
U2L2s	3.29	0.09	3.28	0.07	3.34	0.12	3.37	0.08	3.43	0.11	3.34	0.09	2.82	0.10	3.31	0.08
U1R2s	3.25	0.11	3.31	0.10	3.48	0.19	3.47	0.09	3.41	0.10	3.39	0.09	3.28	0.11	2.50	0.19
U1R1s	3.24	0.07	3.27	0.08	3.32	0.07	3.40	0.09	3.41	0.09	3.44	0.09	3.30	0.07	2.79	0.17
U1s	3.27	0.08	3.23	0.08	3.35	0.08	3.39	0.07	3.42	0.10	3.38	0.08	3.25	0.11	3.28	0.08
U1L1s	3.36	0.09	3.33	0.08	3.31	0.06	3.42	0.08	3.39	0.10	3.48	0.09	3.08	0.14	3.32	0.07
U1L2s	3.34	0.09	3.31	0.08	3.33	0.10	3.38	0.09	3.42	0.10	3.48	0.11	2.47	0.14	3.24	0.10
R2s	3.34	0.10	3.21	0.08	3.28	0.09	3.44	0.09	3.33	0.08	3.41	0.09	3.33	0.11	2.67	0.41
R1s	3.33	0.08	3.25	0.09	3.35	0.07	3.45	0.08	3.29	0.09	3.42	0.09	3.25	0.07	2.81	0.19
Cs	3.36	0.10	3.20	0.08	3.33	0.07	3.39	0.08	3.28	0.09	3.46	0.08	3.18	0.12	3.23	0.08
L1s	3.31	0.09	3.31	0.09	3.29	0.08	3.38	0.09	3.41	0.10	3.49	0.07	3.37	0.24	3.27	0.07
L2s	3.31	0.09	3.24	0.07	3.22	0.08	3.40	0.08	3.41	0.10	3.48	0.11	2.81	0.15	3.18	0.10
D1R2s	3.38	0.09	3.27	0.09	3.31	0.08	3.40	0.08	3.27	0.08	3.42	0.08	3.21	0.11	2.52	0.15
D1R1s	3.33	0.08	3.26	0.09	3.34	0.08	3.44	0.07	3.32	0.09	3.42	0.08	3.22	0.08	3.03	0.13
D1s	3.30	0.09	3.29	0.09	3.33	0.08	3.39	0.08	3.27	0.09	3.41	0.07	3.15	0.09	3.28	0.08
D1L1s	3.32	0.09	3.29	0.08	3.33	0.09	3.31	0.07	3.29	0.10	3.42	0.07	3.18	0.10	3.27	0.09
D1L2s	3.37	0.09	3.28	0.09	3.28	0.10	3.30	0.08	3.31	0.09	3.54	0.11	3.07	0.30	3.20	0.12
D2R2s	3.30	0.08	3.32	0.09	3.33	0.10	3.38	0.09	3.08	0.10	3.08	0.09	3.24	0.13	2.93	0.14
D2R1s	3.31	0.08	3.30	0.09	3.34	0.10	3.48	0.07	3.05	0.12	3.26	0.08	3.23	0.09	3.23	0.09
D2s	3.33	0.10	3.27	0.08	3.43	0.10	3.33	0.09	3.04	0.14	3.33	0.07	3.17	0.09	3.18	0.08
D2L1s	3.39	0.10	3.34	0.09	3.41	0.09	3.27	0.06	3.08	0.14	3.48	0.07	3.22	0.11	3.20	0.08
D2L2s	3.35	0.08	3.39	0.10	3.38	0.10	3.15	0.08	3.06	0.11	3.47	0.11	3.44	0.23	3.09	0.11

Table 5.4b. Mature rabbit endothelial cell nuclear LW ratios for sub-regions (100μm * 100μm) within downstream main-regions in "Zone A", where n equals the number of branches.

Mature	D1R1		D1		D1L1		D2R1		D2		D2L1	
Sub-Region	Mean	SEM	Mean	SEM	Mean	SEM	Mean	SEM	Mean	SEM	Mean	SEM
U2R2s	3.33	0.12	3.13	0.12	3.20	0.12	3.48	0.13	3.19	0.08	3.22	0.08
U2R1s	3.21	0.07	3.12	0.15	3.21	0.09	3.32	0.08	3.23	0.09	3.28	0.07
U2s	3.23	0.08	3.21	0.20	3.19	0.07	3.34	0.08	3.19	0.08	3.33	0.07
U2L1s	3.09	0.08	2.92	0.16	3.22	0.08	3.32	0.08	3.25	0.09	3.37	0.09
U2L2s	3.03	0.10	3.17	0.09	3.23	0.09	3.26	0.08	3.34	0.10	3.49	0.16
U1R2s	3.30	0.13	3.08	0.10	3.20	0.09	3.40	0.12	3.26	0.08	3.31	0.08
U1R1s	3.27	0.08	3.08	0.10	3.23	0.09	3.32	0.08	3.23	0.08	3.33	0.08
U1s	3.32	0.09	3.22	0.11	3.26	0.07	3.30	0.08	3.25	0.09	3.33	0.07
U1L1s	3.27	0.08	3.14	0.10	3.25	0.07	3.35	0.09	3.30	0.09	3.34	0.07
U1L2s	3.23	0.11	3.23	0.09	3.22	0.09	3.35	0.08	3.28	0.10	3.45	0.13
R2s	3.39	0.12	3.07	0.09	3.18	0.10	3.38	0.11	3.32	0.07	3.28	0.08
R1s	3.25	0.09	3.15	0.09	3.27	0.09	3.31	0.09	3.25	0.08	3.30	0.08
Cs	3.31	0.08	3.02	0.08	3.30	0.07	3.24	0.08	3.18	0.09	3.29	0.08
L1s	3.27	0.08	3.14	0.09	3.30	0.07	3.33	0.08	3.27	0.09	3.33	0.08
L2s	3.13	0.09	3.26	0.09	3.30	0.09	3.32	0.07	3.24	0.08	3.50	0.12
D1R2s	3.37	0.14	3.14	0.09	3.21	0.07	3.42	0.12	3.36	0.07	3.29	0.07
D1R1s	3.24	0.09	3.18	0.08	3.27	0.07	3.28	0.09	3.32	0.08	3.32	0.07
D1s	3.30	0.08	3.10	0.09	3.31	0.09	3.28	0.08	3.30	0.09	3.24	0.07
D1L1s	3.28	0.08	3.13	0.08	3.34	0.08	3.38	0.09	3.26	0.09	3.36	0.09
D1L2s	3.18	0.08	3.22	0.08	3.26	0.10	3.36	0.07	3.28	0.07	3.44	0.11
D2R2s	3.40	0.13	3.20	0.09	3.35	0.10	3.42	0.13	3.30	0.07	3.28	0.07
D2R1s	3.29	0.09	3.16	0.09	3.20	0.07	3.30	0.09	3.32	0.07	3.41	0.09
D2s	3.35	0.08	3.14	0.09	3.37	0.08	3.32	0.09	3.27	0.09	3.39	0.09
D2L1s	3.27	0.07	3.16	0.08	3.34	0.08	3.34	0.09	3.32	0.09	3.34	0.09
D2L2s	3.27	0.09	3.27	0.07	3.35	0.12	3.35	0.08	3.26	0.08	3.37	0.11

Tukey tests were performed on nuclear morphologies in "Zone A" – that is, within 500μm of the branch ostia (main regions "U1R1", "U1", "U1L1", "R1", "L1", "D1R1", "D1", "D1L1") - to observe where differences in nuclear elongation existed between the sub-regions within each of these main regions (Appendix B.1a-h).

5.3.1.3 "Zone B" (500μm * 500μm regions)

LW ratios of nuclei within "Zone B" i.e. nuclei 1mm-2mm from branch ostia, defined in Fig. 5.1, are shown in Table 5.5. There were highly significant effects of age and region, and the pattern of nuclear elongation changed with age ($P<0.005$). The mean LW ratio in immature rabbits was 2.48 ± 0.01 (n = 1163 regions), and in mature rabbits the nuclei were 35.5% more elongated (3.36 ± 0.01, n = 1355 regions). Values ranged from 2.29 ± 0.04 ("D4L4", n = 14 branches) to 2.59 ± 0.03 ("U3R1", n = 36 branches) in immature rabbits, a difference of 13.1%, and in mature rabbits, values ranged from

3.11 ± 0.07 ("D3L4", n = 18 branches) to 3.51 ± 0.09 ("U3R3", n = 21 branches) and 3.51 ± 0.08 ("U1R3", n = 21 branches), a difference of 12.9%.

Table 5.5. Rabbit endothelial cell nuclear LW ratios for "Zone B" regions, where n equals the number of branches.

Region	Immature		Mature	
	Mean	SEM	Mean	SEM
U4R4	2.47	0.05	3.42	0.10
U4R3	2.53	0.05	3.44	0.09
U4R2	2.54	0.04	3.41	0.09
U4R1	2.57	0.03	3.36	0.06
U4	2.58	0.03	3.33	0.06
U4L1	2.55	0.03	3.36	0.07
U4L2	2.46	0.04	3.35	0.08
U4L3	2.36	0.04	3.37	0.07
U4L4	2.32	0.05	3.20	0.08
U3R4	2.47	0.05	3.44	0.09
U3R3	2.50	0.04	3.51	0.09
U3R2	2.57	0.04	3.41	0.10
U3R1	2.59	0.03	3.30	0.06
U3	2.58	0.03	3.32	0.07
U3L1	2.54	0.03	3.34	0.07
U3L2	2.45	0.05	3.36	0.07
U3L3	2.39	0.04	3.36	0.07
U3L4	2.34	0.04	3.26	0.07
U2R4	2.47	0.05	3.42	0.09
U2R3	2.54	0.04	3.48	0.09
U2L3	2.39	0.05	3.41	0.08
U2L4	2.35	0.05	3.27	0.08
U1R4	2.46	0.05	3.49	0.08
U1R3	2.54	0.05	3.51	0.08
U1L3	2.43	0.04	3.42	0.09
U1L4	2.34	0.05	3.26	0.08
R4	2.42	0.05	3.48	0.08
R3	2.54	0.05	3.45	0.10
L3	2.39	0.04	3.36	0.10
L4	2.34	0.06	3.24	0.08
D1R4	2.41	0.06	3.44	0.08
D1R3	2.52	0.04	3.40	0.10
D1L3	2.39	0.04	3.34	0.09
D1L4	2.37	0.06	3.15	0.06
D2R4	2.40	0.05	3.43	0.08
D2R3	2.50	0.05	3.44	0.09
D2L3	2.39	0.04	3.34	0.09
D2L4	2.34	0.06	3.12	0.07
D3R4	2.41	0.04	3.46	0.08
D3R3	2.50	0.05	3.45	0.10
D3R2	2.55	0.04	3.42	0.10

D3R1	2.55	0.02	3.36	0.08
D3	2.57	0.03	3.33	0.07
D3L1	2.58	0.03	3.36	0.07
D3L2	2.43	0.05	3.37	0.08
D3L3	2.38	0.04	3.28	0.08
D3L4	2.31	0.05	3.11	0.07
D4R4	2.43	0.05	3.41	0.10
D4R3	2.50	0.06	3.44	0.09
D4R2	2.58	0.04	3.42	0.11
D4R1	2.54	0.03	3.36	0.08
D4	2.57	0.03	3.34	0.06
D4L1	2.53	0.03	3.38	0.06
D4L2	2.45	0.06	3.34	0.07
D4L3	2.32	0.04	3.25	0.07
D4L4	2.29	0.04	3.13	0.06
Total mean	**2.48**	**0.01**	**3.36**	**0.01**

5.3.1.4 "Zone C" (500μm * 500μm regions)

Nuclear LW ratios in the regions within "Zone C" (2-4mm from branch ostia) defined in Fig. 5.1 are shown in Table 5.6. There were highly significant effects of age and region, and the pattern of nuclear elongation changed with age ($P<0.005$). The mean LW ratios were 2.41 ± 0.01 and 3.26 ± 0.01 in immature (n = 1423 regions) and mature (n = 1443 regions) rabbits respectively; LW ratios in mature rabbits were 35.3% more elongated. Values ranged from 2.22 ± 0.05 ("U6R6", n = 9 branches) to 2.56 ± 0.03 ("U5", n = 33 branches) in immature rabbits, a difference of 15.3%, and in mature rabbits, values ranged from 2.95 ± 0.17 ("U6R6", n = 4 branches) to 3.44 ± 0.09 ("D2R5", n = 19 branches), a difference of 16.6%.

Table 5.6. Rabbit endothelial cell nuclear LW ratios for immature and mature rabbits in "Zone C", where n equals the number of branches.

Region	Immature		Mature	
	Mean	SEM	Mean	SEM
U6R6	2.22	0.05	2.95	0.17
U6R5	2.27	0.06	3.02	0.11
U6R4	2.35	0.07	3.07	0.12
U6R3	2.39	0.06	3.06	0.12
U6R2	2.44	0.06	3.11	0.13
U6R1	2.49	0.04	3.26	0.10
U6	2.50	0.04	3.21	0.10
U6L1	2.50	0.04	3.23	0.10
U6L2	2.43	0.05	3.37	0.11
U6L3	2.36	0.04	3.33	0.10
U6L4	2.30	0.04	3.25	0.13
U6L5	2.28	0.04	3.27	0.12
U6L6	2.32	0.03	3.09	0.14
U5R6	2.31	0.04	3.31	0.10
U5R5	2.32	0.03	3.35	0.11
U5R4	2.41	0.04	3.28	0.08
U5R3	2.51	0.05	3.28	0.08
U5R2	2.51	0.05	3.29	0.08
U5R1	2.53	0.04	3.29	0.06
U5	2.56	0.03	3.25	0.06
U5L1	2.54	0.04	3.29	0.06
U5L2	2.46	0.04	3.32	0.08
U5L3	2.39	0.04	3.35	0.08
U5L4	2.31	0.04	3.26	0.08
U5L5	2.36	0.05	3.20	0.07
U5L6	2.36	0.05	3.20	0.10
U4R6	2.36	0.04	3.32	0.13
U4R5	2.37	0.04	3.35	0.09
U4L5	2.35	0.04	3.20	0.08
U4L6	2.42	0.06	3.07	0.09
U3R6	2.37	0.04	3.32	0.09
U3R5	2.36	0.03	3.36	0.07
U3L5	2.30	0.04	3.15	0.08
U3L6	2.40	0.05	3.09	0.10
U2R6	2.35	0.04	3.27	0.07
U2R5	2.34	0.04	3.35	0.07
U2L5	2.30	0.03	3.14	0.08
U2L6	2.38	0.05	3.07	0.10
U1R6	2.35	0.04	3.34	0.09
U1R5	2.36	0.04	3.41	0.07
U1L5	2.34	0.03	3.16	0.07
U1L6	2.39	0.03	3.09	0.10
R6	2.34	0.03	3.30	0.09
R5	2.34	0.03	3.37	0.07
L5	2.32	0.04	3.13	0.07
L6	2.38	0.03	3.07	0.10

D1R6	2.39	0.03	3.31	0.09
D1R5	2.34	0.04	3.40	0.09
D1L5	2.35	0.04	3.17	0.07
D1L6	2.37	0.04	3.11	0.09
D2R6	2.37	0.04	3.32	0.09
D2R5	2.36	0.05	3.44	0.09
D2L5	2.32	0.04	3.13	0.06
D2L6	2.34	0.03	3.04	0.10
D3R6	2.40	0.04	3.30	0.09
D3R5	2.37	0.04	3.42	0.10
D3L5	2.33	0.05	3.12	0.07
D3L6	2.32	0.04	3.06	0.09
D4R6	2.40	0.04	3.30	0.09
D4R5	2.36	0.05	3.41	0.09
D4L5	2.35	0.04	3.16	0.06
D4L6	2.30	0.05	3.04	0.09
D5R6	2.37	0.06	3.27	0.10
D5R5	2.42	0.06	3.42	0.08
D5R4	2.43	0.06	3.38	0.11
D5R3	2.48	0.06	3.43	0.10
D5R2	2.55	0.06	3.39	0.10
D5R1	2.54	0.03	3.35	0.07
D5	2.53	0.03	3.32	0.07
D5L1	2.52	0.03	3.29	0.06
D5L2	2.44	0.06	3.28	0.09
D5L3	2.34	0.04	3.23	0.07
D5L4	2.29	0.05	3.20	0.07
D5L5	2.33	0.04	3.18	0.07
D5L6	2.33	0.04	3.06	0.10
D6R6	2.39	0.05	3.06	0.12
D6R5	2.44	0.05	3.34	0.10
D6R4	2.47	0.06	3.35	0.12
D6R3	2.52	0.08	3.42	0.11
D6R2	2.55	0.08	3.36	0.08
D6R1	2.52	0.04	3.31	0.06
D6	2.48	0.04	3.24	0.06
D6L1	2.49	0.04	3.26	0.07
D6L2	2.44	0.07	3.15	0.08
D6L3	2.35	0.07	3.17	0.08
D6L4	2.28	0.06	3.09	0.06
D6L5	2.26	0.03	3.07	0.05
D6L6	2.34	0.03	3.02	0.06
Total mean	**2.41**	**0.01**	**3.26**	**0.01**

5.3.1.5 Nuclear LW ratios along the longitudinal midline through the branch ostium

LW ratios of nuclei along the longitudinal midline, from upstream ("U6" to "U1") to downstream ("D1" to "D6") are shown in Fig. 5.8. Data for nuclei within "U1", "U2", "D1" and "D2" are shown split into their constitutive sub-regions along the midline, to show how the pattern of nuclear elongation changes close to the ostia.

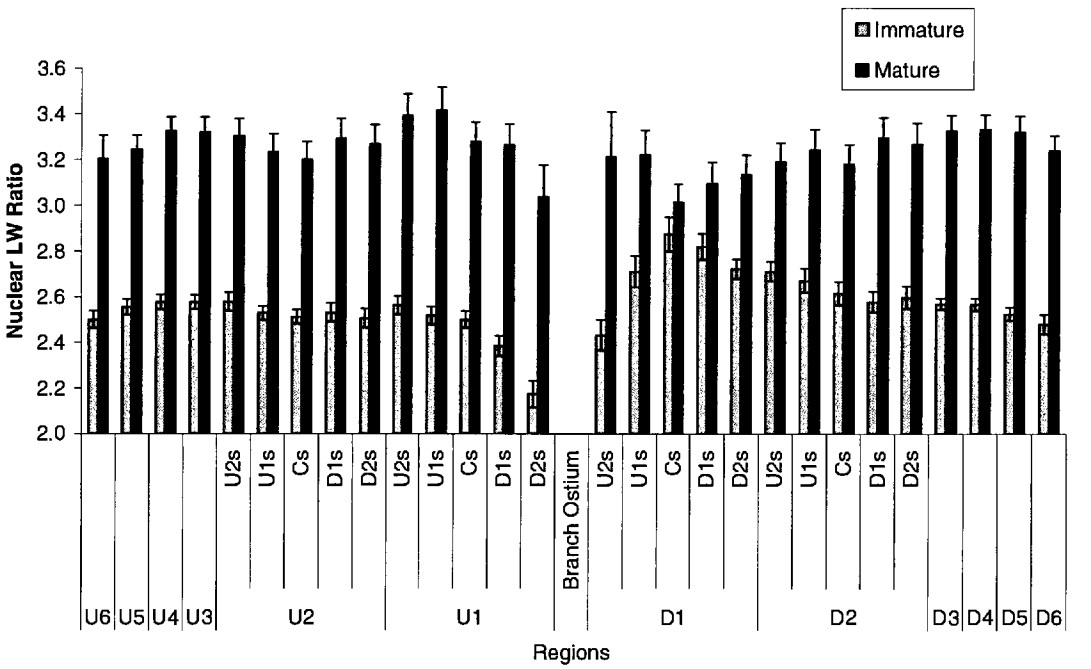

Fig. 5.8. Mean nuclear LW ratios along the longitudinal midline through the branch ostia from upstream to downstream, for immature and mature rabbits. The branch ostia falls between regions "U1" and "D1". Data for regions closest to the ostia have been sub-divided into their constitutive sub-regions to show changes over a small area (100μm). Region names are described in Fig. 5.1. Bars show means ± SEM (n = number of branches).

5.3.1.6 Nuclear LW ratios around ostia in different parts of the descending thoracic aorta (500μm * 500μm regions)

When the morphology of the nuclei within Zones A-C was analysed as a function of the location of the branch ostium i.e. when branches within the upper or lower portion of the artery, and branch ostia on the left hand or right hand side of a branch pair, were analysed separately, the differences between immature and mature rabbits, regions and

the interaction between age and region were still significant ($P<0.05$). LW ratios for immature rabbits in the upper and lower portion of the artery were 2.51 ± 0.01 and 2.40 ± 0.00 respectively (4.4% difference, $P<0.01$, n = 1854 and 1409 regions respectively), and for mature rabbits were 3.47 ± 0.01 and 3.30 ± 0.01 respectively (4.9% difference, $P<0.01$, n = 1378 and 1755 regions respectively). Nuclear LW ratios for left and right branch ostia for immature rabbits were 2.48 ± 0.01 and 2.44 ± 0.01 respectively (1.6% difference, $P<0.01$, n = 1635 and 1460 respectively), and for mature rabbits were 3.33 ± 0.01 and 3.24 ± 0.01 respectively (2.7% difference, $P<0.01$, n = 1535 and 1475 respectively). Data for nuclei within individual regions in "Zone A" for the upper and lower portion of the artery and right and left portions of the artery are shown in Tables 5.7 and 5.8 respectively.

Nuclear LW ratios for immature and mature rabbits, in regions "Zone A", "Zone B", and "Zone C", separated into the means for ostia from the upper and lower portions of the artery, and branch ostia on the left and right hand side of artery, are shown in Table 5.9. Colour maps showing mean variations in LW ratio around the branch ostia at low resolution (averages per 500μm * 500μm regions) for different branch ostia locations are shown in Figures 5.9-5.12.

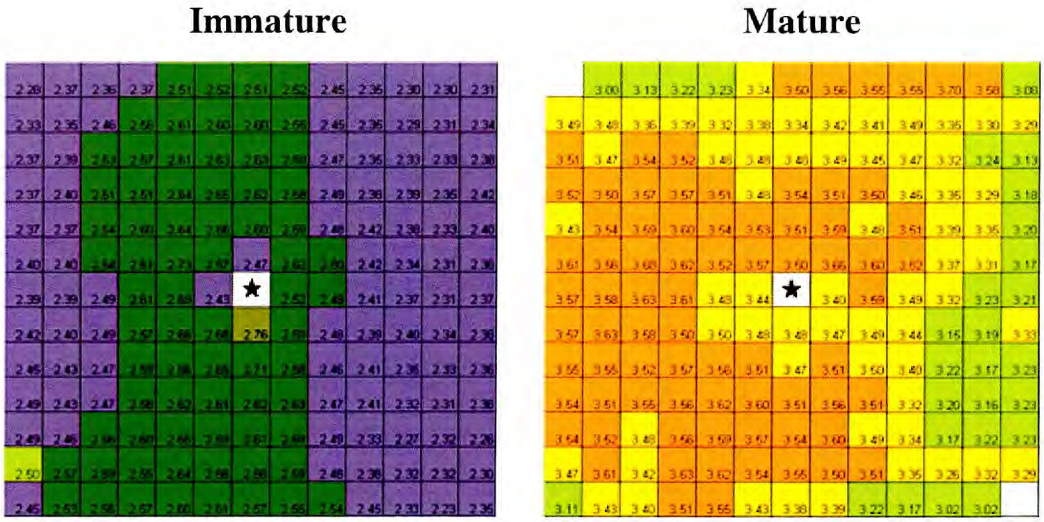

Fig. 5.9. Length:width ratios of rabbit endothelial cell nuclei in the upper descending thoracic aorta. Values are averages for branches 1 to 6 (branch 1 being the first branch downstream from the aortic arch). Each square represents the average data for a 500μm*500μm region. Total area of map is 42.25mm^2. n = 4 immature rabbits, n = 4 mature rabbits. Data represent averages for 21 immature and 14 mature branches.

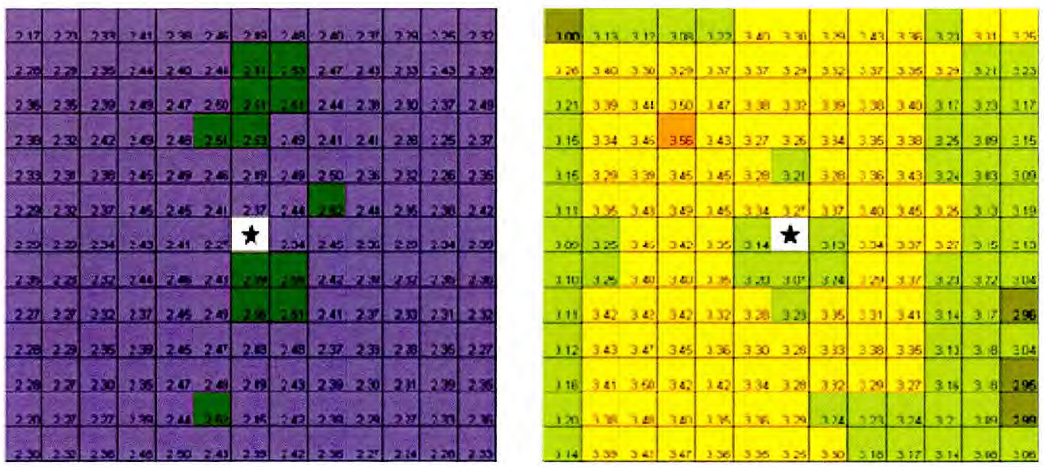

Fig. 5.10. Length:width ratios of rabbit endothelial cell nuclei in the lower descending thoracic aorta. Values are averages for branches 7 to 12. Each square represents the average data for a 500μm * 500μm region. Total area of map is 42.25mm^2. n = 4 immature rabbits, n = 4 mature rabbits. Data represent averages for 15 immature and 20 mature branches.

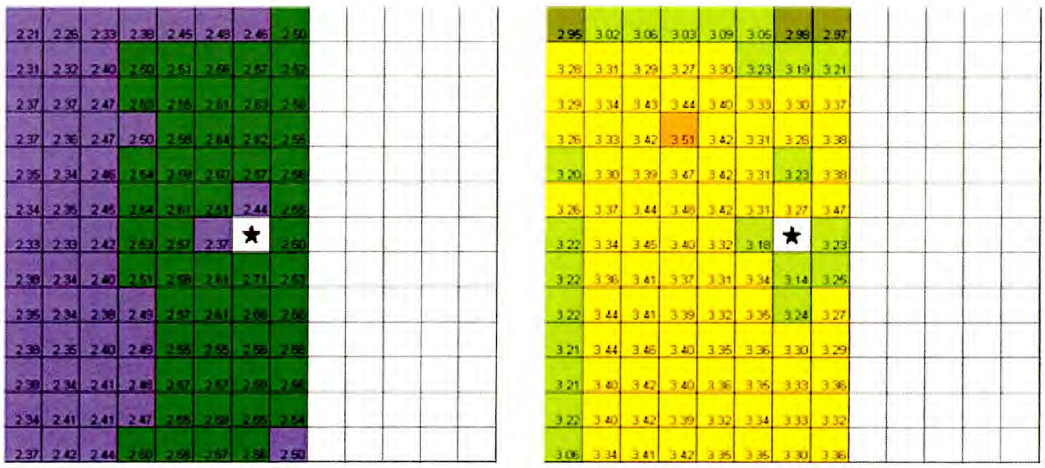

Fig. 5.11. Length:width ratios of rabbit endothelial cell nuclei for branches on the anatomical right hand side of the aorta. (The map has been truncated to avoid affects of flow around ostia on the left hand side). Each square represents the average data for a 500μm*500μm region. Total area of map is 26.0mm^2. n = 4 immature rabbits, n = 4 mature rabbits. Data represent averages for 17 immature and 17 mature branches.

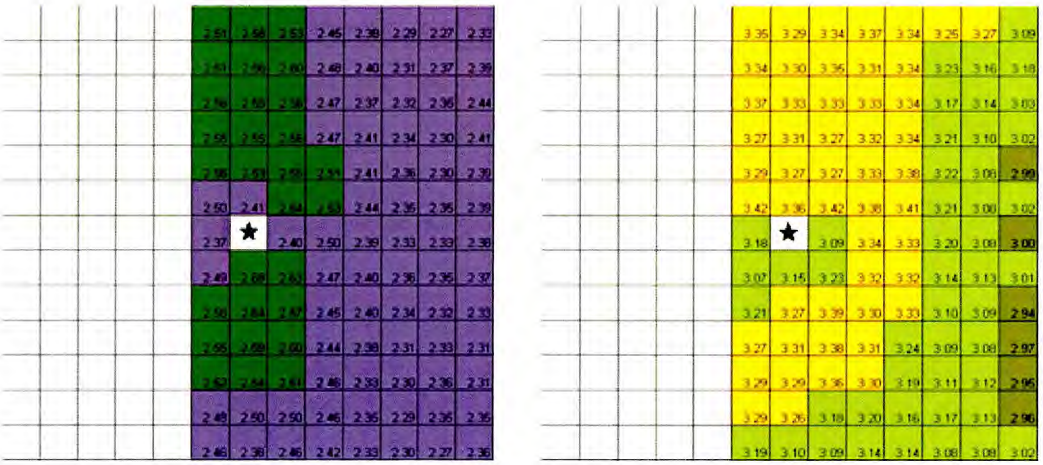

Fig. 5.12. Length:width ratios of rabbit endothelial cell nuclei for branches on the anatomical left hand side of the aorta. (The map has been truncated to avoid affects of flow around ostia on the right hand side). Each square represents the average data for a 500μm * 500μm region. Total area of map is 26.0mm^2. n = 4 immature rabbits, n=4 mature rabbits. Data represent averages for 18 immature and 17 mature branches.

Table 5.7. Nuclear LW ratio for branch ostia within upper and lower portions of the descending thoracic aorta, where n equals the number of branches.

	UPPER				LOWER			
Region	Immature		Mature		Immature		Mature	
	Mean	SEM	Mean	SEM	Mean	SEM	Mean	SEM
U2R2	2.64	0.04	3.54	0.12	2.49	0.05	3.45	0.13
U2R1	2.66	0.04	3.53	0.11	2.46	0.04	3.28	0.10
U2	2.60	0.03	3.51	0.12	2.49	0.03	3.21	0.09
U2L1	2.59	0.04	3.59	0.09	2.49	0.04	3.28	0.10
U2L2	2.48	0.07	3.48	0.08	2.50	0.08	3.36	0.09
U1R2	2.73	0.06	3.52	0.11	2.45	0.06	3.45	0.10
U1R1	2.57	0.03	3.57	0.11	2.41	0.04	3.34	0.06
U1	2.47	0.03	3.50	0.13	2.37	0.04	3.27	0.10
U1L1	2.62	0.04	3.66	0.10	2.44	0.05	3.37	0.11
U1L2	2.50	0.07	3.60	0.12	2.52	0.07	3.40	0.11
R2	2.69	0.06	3.48	0.12	2.41	0.06	3.35	0.12
R1	2.43	0.04	3.44	0.10	2.27	0.05	3.14	0.06
L1	2.52	0.05	3.40	0.08	2.34	0.04	3.13	0.10
L2	2.49	0.06	3.59	0.16	2.45	0.06	3.34	0.08
D1R2	2.66	0.05	3.50	0.17	2.46	0.04	3.35	0.11
D1R1	2.65	0.05	3.48	0.12	2.43	0.04	3.20	0.08
D1	2.76	0.05	3.48	0.13	2.59	0.06	3.07	0.07
D1L1	2.59	0.04	3.47	0.08	2.55	0.04	3.24	0.09
D1L2	2.48	0.06	3.49	0.15	2.42	0.07	3.29	0.06
D2R2	2.66	0.03	3.56	0.15	2.45	0.04	3.32	0.09
D2R1	2.65	0.04	3.51	0.13	2.49	0.04	3.28	0.09
D2	2.71	0.03	3.47	0.14	2.56	0.07	3.23	0.08
D2L1	2.58	0.04	3.51	0.11	2.51	0.04	3.35	0.10
D2L2	2.46	0.05	3.50	0.11	2.41	0.06	3.31	0.09
Total mean	**2.59**	**0.01**	**3.51**	**0.02**	**2.45**	**0.01**	**3.27**	**0.02**

Table 5.8. Nuclear LW ratio for branch ostia on the anatomical right and left of the descending thoracic aorta, where n equals the number of branches.

	RIGHT				LEFT			
Region	Immature		Mature		Immature		Mature	
	Mean	SEM	Mean	SEM	Mean	SEM	Mean	SEM
U2R2	-	-	-	-	2.59	0.04	3.42	0.10
U2R1	2.56	0.04	3.29	0.10	2.60	0.05	3.31	0.13
U2	2.53	0.03	3.27	0.10	2.57	0.04	3.23	0.12
U2L1	2.55	0.04	3.27	0.10	2.56	0.05	3.38	0.12
U2L2	2.51	0.05	3.33	0.08	-	-	-	-
U1R2	-	-	-	-	2.61	0.06	3.42	0.08
U1R1	2.50	0.03	3.42	0.10	2.51	0.05	3.31	0.07
U1	2.41	0.04	3.36	0.12	2.44	0.03	3.27	0.11
U1L1	2.54	0.06	3.42	0.11	2.55	0.05	3.47	0.12
U1L2	2.53	0.05	3.38	0.10	-	-	-	-
R2	-	-	-	-	2.57	0.06	3.32	0.10
R1	2.37	0.04	3.18	0.11	2.37	0.05	3.18	0.07
L1	2.40	0.05	3.09	0.11	2.50	0.05	3.23	0.10
L2	2.50	0.04	3.34	0.12	-	-	-	-
D1R2	-	-	-	-	2.58	0.04	3.31	0.11
D1R1	2.49	0.06	3.07	0.08	2.61	0.05	3.34	0.13
D1	2.68	0.06	3.15	0.11	2.71	0.05	3.14	0.11
D1L1	2.63	0.05	3.23	0.09	2.53	0.03	3.25	0.12
D1L2	2.47	0.04	3.32	0.10	-	-	-	-
D2R2	-	-	-	-	2.57	0.04	3.32	0.10
D2R1	2.56	0.06	3.21	0.09	2.61	0.04	3.35	0.13
D2	2.64	0.06	3.27	0.11	2.66	0.04	3.24	0.12
D2L1	2.57	0.05	3.39	0.12	2.56	0.03	3.27	0.11
D2L2	2.45	0.04	3.30	0.09	-	-	-	-
Total mean	**2.52**	**0.01**	**3.28**	**0.02**	**2.56**	**0.01**	**3.30**	**0.02**

Table 5.9. Rabbit endothelial cell nuclear LW ratios for all regions, results separated by location of the branch ostia, where n equals the number of regions.

Location of branch ostia	Region	Immature		Mature	
		Mean	SEM	Mean	SEM
Upper branch ostia	Zone A-C	2.51	0.01	3.47	0.01
	Zone A	2.59	0.01	3.51	0.02
	Zone B	2.53	0.01	3.50	0.02
	Zone C	2.45	0.01	3.41	0.01
Lower branch ostia	Zone A-C	2.40	0.00	3.30	0.01
	Zone A	2.45	0.01	3.27	0.02
	Zone B	2.42	0.01	3.36	0.01
	Zone C	2.36	0.01	3.27	0.01
Right branch ostia	Zone A-C	2.44	0.01	3.24	0.01
	Zone A	2.52	0.01	3.28	0.02
	Zone B	2.45	0.01	3.28	0.02
	Zone C	2.40	0.01	3.17	0.01
Left branch ostia	Zone A-C	2.48	0.01	3.33	0.01
	Zone A	2.56	0.01	3.30	0.02
	Zone B	2.52	0.01	3.39	0.02
	Zone C	2.42	0.01	3.30	0.02

The overall mean ("Zones A-C") LW ratio for nuclei surrounding ostia in the upper portion of the artery was higher, for both immature (4.4% difference) and mature (4.9% difference) rabbits, than nuclei in the lower portion of the arteries (both $P<0.01$). Nuclei surrounding ostia on the left side of the artery were consistently more elongated than those on the right, in both immature (1.6% difference) and mature (2.8% difference) rabbits (both $P<0.01$).

5.3.2 Rabbit normalised nuclear orientation

A constant was subtracted from all endothelial cell nuclear orientations to make the mean angle zero for each EStAR preparation, as previously described, enabling changes in the pattern with age, but not changes in the mean angle (such as the helicity caused by spiral flows down the aorta) (Flaherty *et al.*, 1972) to be determined. An angle of 0° indicates nuclei are aligned parallel to the longitudinal axis of the aorta, whereas positive and negative angles indicate the proximal tip of the nuclei is leaning to the anatomical left and right of the longitudinal axis respectively.

Normalised nuclear orientations for 36 immature (I) and 38 mature (M) branches, for the regions defined in Fig. 5.1 (Zones A-C), are shown in Fig. 5.13. There was no significant effect of age on mean orientation ($P=0.07$), but there was a highly significant effect of region and the interaction between age and region (both $P<0.005$).

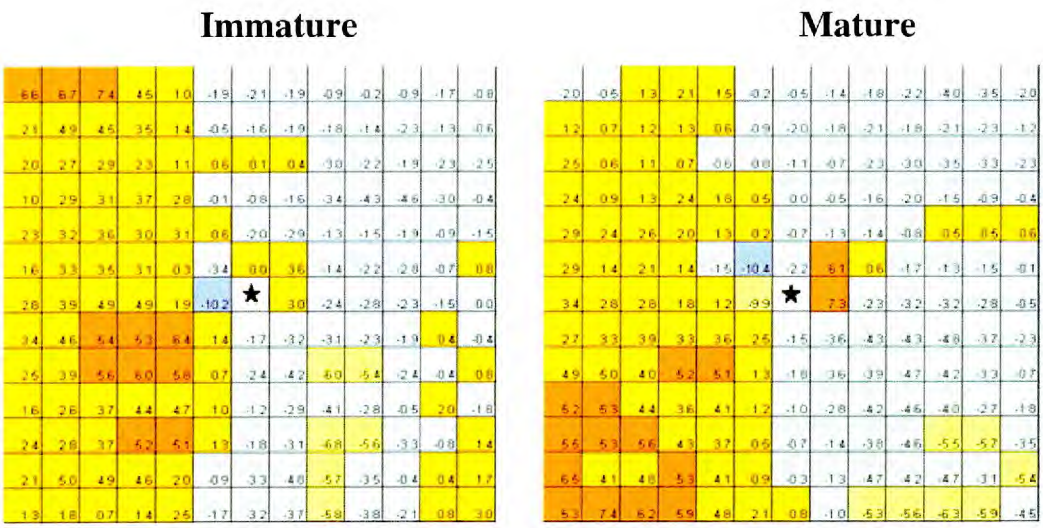

Fig. 5.13. Normalised angle of orientation of rabbit endothelial cell nuclei for all branch ostia. Each square represents the average data for a 500μm * 500μm region. Total area of map is 42.25mm^2. n = 4 immature rabbits, n = 4 mature rabbits. Data represent averages for 36 immature and 38 mature branches.

5.3.2.1 "Zone A" (500μm * 500μm regions)

Normalised orientations for nuclei within "Zone A" are shown in Fig. 5.14. There was no significant effect of age ($P<0.05$) (mean orientations -0.96 ± 0.30° and -0.95 ± 0.27° for immature (n = 677 regions) and mature (n = 741 regions) rabbits respectively), however there were significant effects of region and for the age*region interaction (both $P<0.005$).

In immature rabbits, nuclei in the regions immediately adjacent to the branch had positive angles in the upstream, upper left, left, and lower right regions. The opposite was true for nuclei in the upper right, right, lower left, and downstream regions in which the angles were negative. For the other regions in "Zone A", nuclei in general had positive angles if on the anatomical right, and negative angles on the anatomical left. Angles ranged from -10.23 ± 1.61° ("R1", n = 36 branches) to 6.39 ± 1.34 ("D1R2", n = 19 branches). In mature rabbits, regions immediately adjacent to the branch contained nuclei with positive angles in the upper left, left and lower right regions. Nuclei within upstream, upper right, right, downstream and lower left regions had negative angles.

Values ranged from -10.42 ± 1.09° ("U1R1", n = 38 branches) to 7.25 ± 1.86° ("L1", n = 38 branches).

Significant differences between individual regions for immature and mature rabbits are shown in Fig. 5.15.

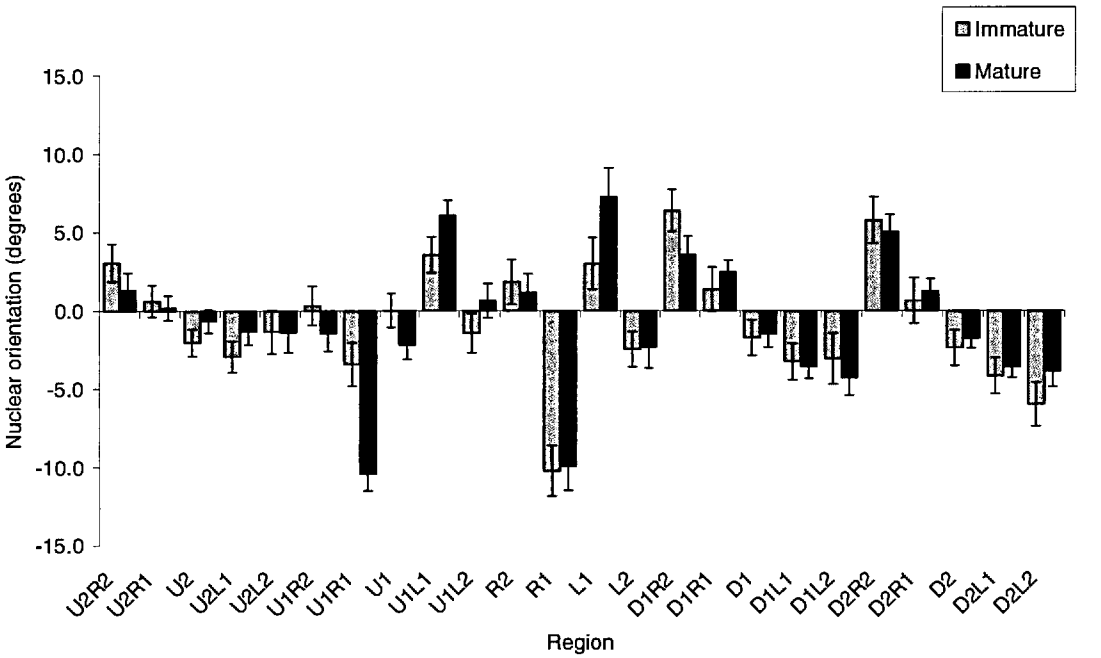

Fig. 5.14. Normalised nuclear orientations for regions in "Zone A" surrounding branch ostia, defined in Fig. 5.1, in immature and mature rabbits. Positive angles indicate that the proximal tip of the nucleus is inclined towards the anatomical left, negative angles indicate inclination towards the anatomical right. Bars show means ± SEM (n = number of branches).

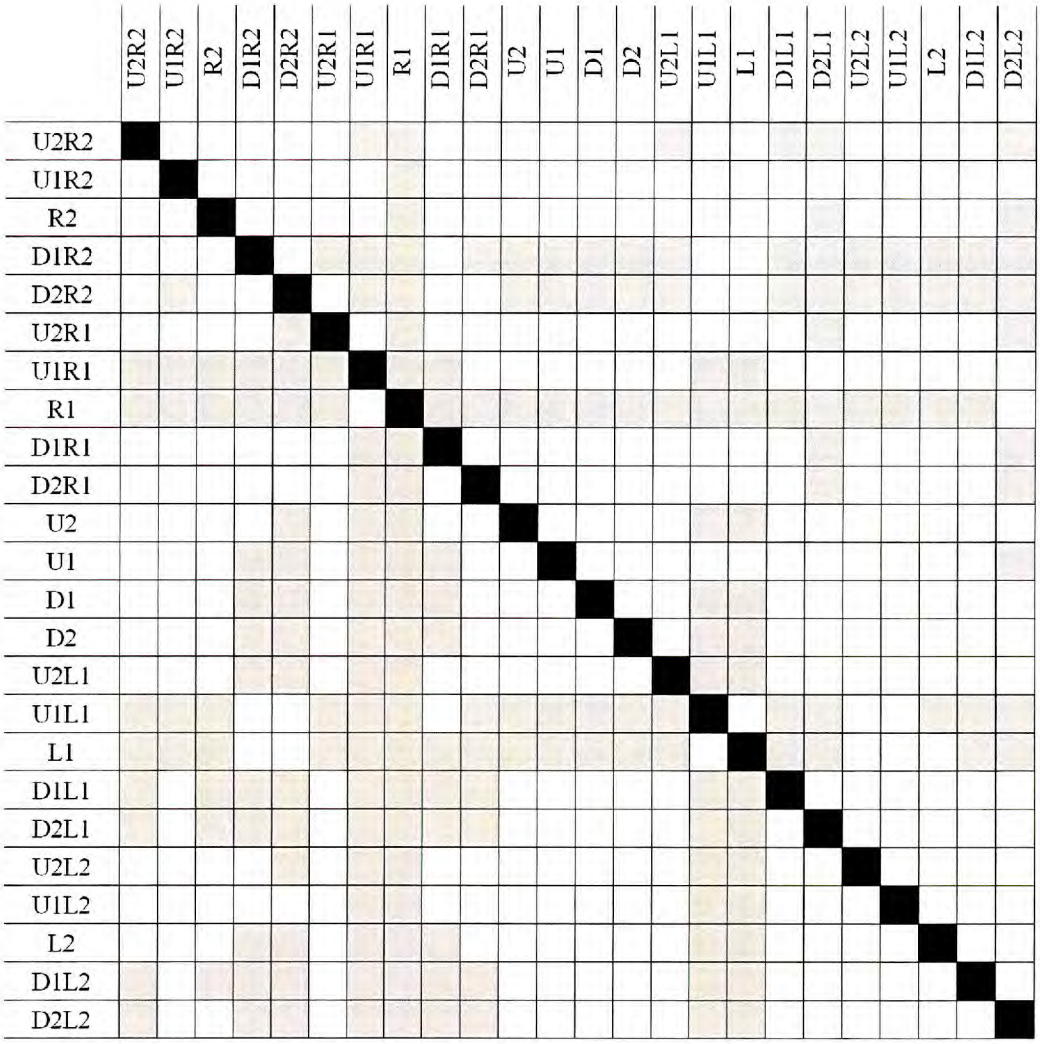

Fig. 5.15. Significant differences in normalised nuclear orientation between 500μm * 500μm regions within Zone A as determined by the Tukey test for multiple comparisons. Squares shaded in grey depict significant differences ($P<0.05$) between regions. Squares to the right of the black diagonal line indicate differences in immature rabbits. Squares to the left indicate differences in mature rabbits.

5.3.2.2 "Zone A" (100μm * 100μm sub-regions)

As with nuclear LW ratios, the normalised nuclear orientation data were split so that the 100μm * 100μm sub-regions in each of the 500μm * 500μm main regions nearest the branch ostia ("U2R1", "U2", "U2L1", "U1R1", "U1", "U1L1", "R1", "L1", "D1R1", "D1", "D1L1", "D2R1", "D2", "D2L1") were analysed individually rather than being combined (Fig. 5.16, Table 5.10a,b and 5.11a,b). Significant changes with age in orientation occurred within regions "U1R1", "R1", and "U2" (all $P<0.05$). There were

significant effects of sub-region for nuclei within main regions "U1R1", "R1", "D1R1", "U1", "D1", "D2", "U1L1", "L1", and "D1L1" (all $P<0.01$). There was a significant interaction between age and region in "U1R1", "R1", "U1", "D1" (all $P<0.01$), "L1" and "D1L1" (both $P<0.05$).

Figs. 5.17 and 5.18 present the mean normalised nuclear orientations, for immature and mature rabbits, in each 100μm * 100μm region as lines surrounding the branch ostium. Each line is parallel to the orientation of endothelial cell nuclei in that sub-region. However, unlike a vector, no arrowhead is placed on the line; since flows near the ostium may be complex, it is unsafe to make an assumption about the direction of the mean flow.

For both immature and mature rabbits, it can be seen that in the more upstream lateral regions, close to the branch ostium, nuclei are aligned with their distal ends oriented towards the branch, the angle increasing as the distance from the branch decreases. In the lateral regions, the angles seem greater in mature than immature rabbits, especially on the anatomical right of the branch (also seen in Fig. 5.19). In the downstream lateral regions, angles are smaller and are almost aligned with the (normalised) aortic axis. On the anatomical right of the colour maps, the nuclei tend to have positive angles; whereas the opposite is true for the anatomical left (nuclei largely have negative angles). The change in normalised orientation in the upper lateral regions appears to be greater than those found by Al-Musawi (2004); this could reflect the different sampling sizes used. In upstream regions, nuclei are also aligned with their distal ends oriented towards the centre of the ostium, and nuclei closest to the longitudinal axis angles approaching 0°. The size of the area with largely reoriented nuclei appears to extend further upstream in mature rabbits than in immature.

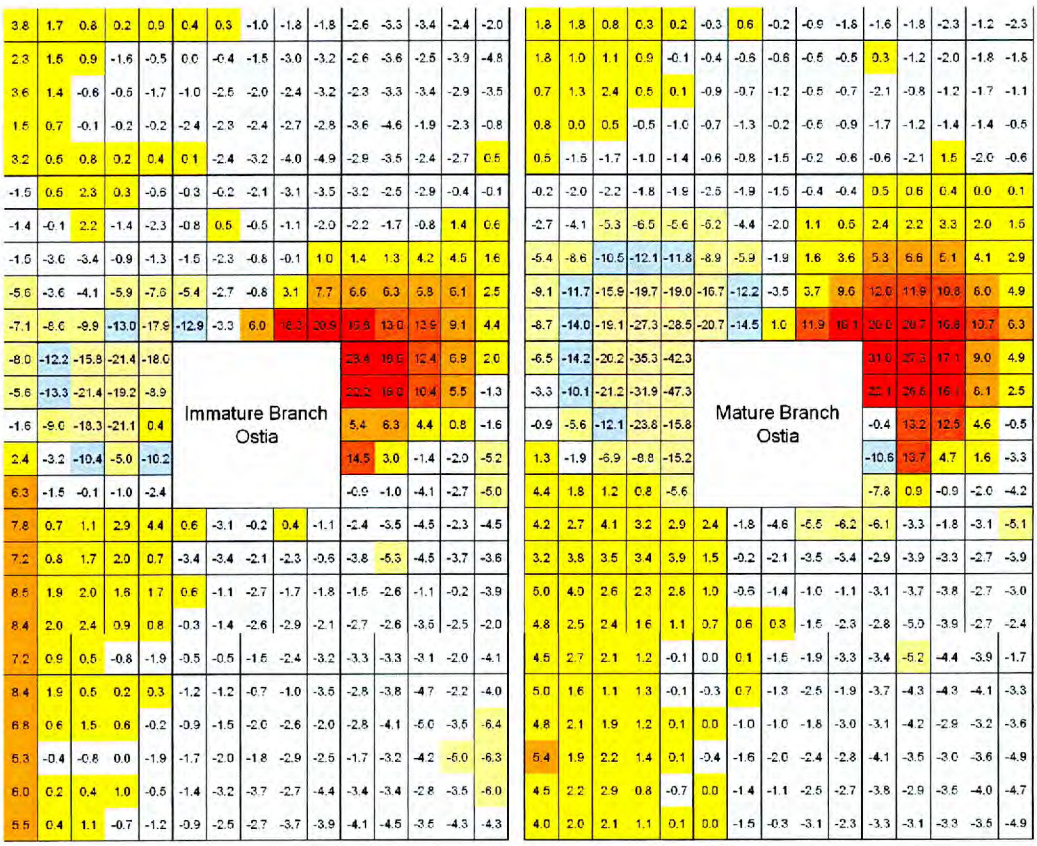

Fig. 5.16. Normalised angle of orientation of rabbit endothelial cell nuclei averaged for all branch ostia. Each square represents the average data for a 100μm * 100μm region. Total area of map is 3.75mm^2. n = 4 immature rabbits, n = 4 mature rabbits. Data represent averages for 36 immature and 38 mature branches.

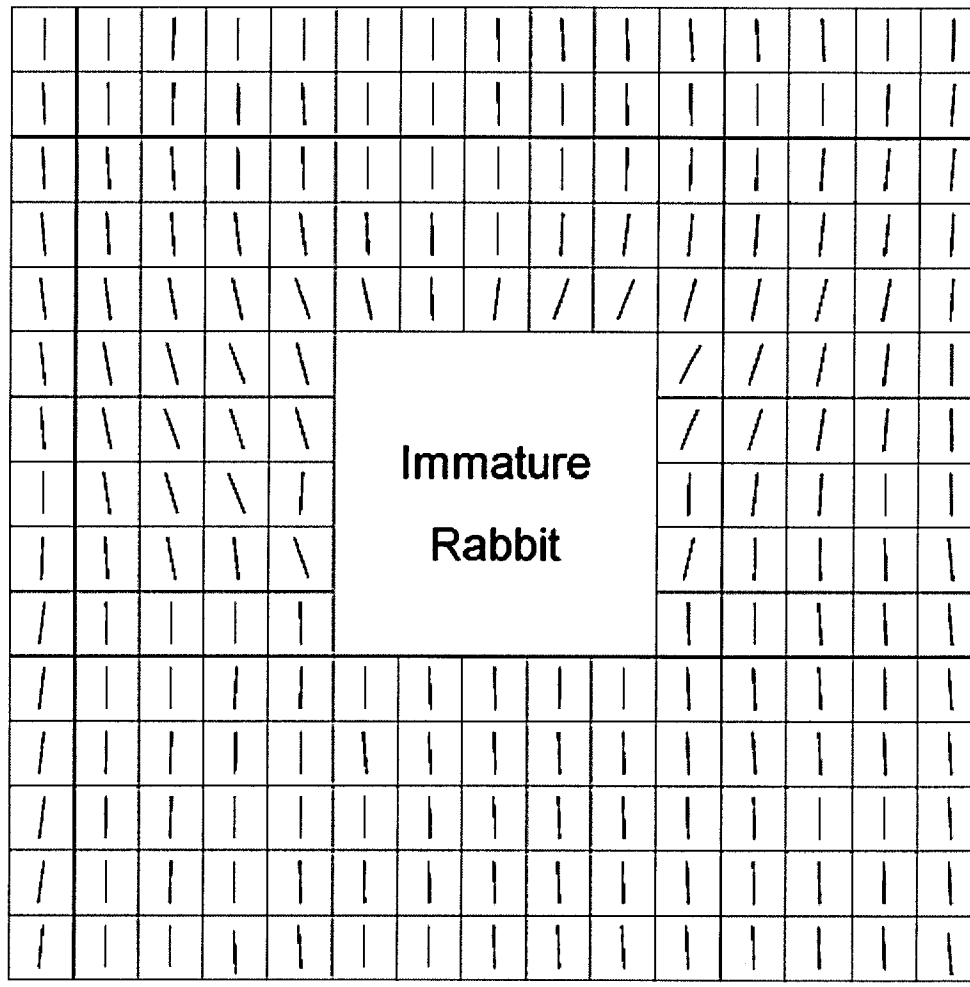

Fig. 5.17. Direction indicators depicting mean normalised angle of orientation of nuclei in 100μm * 100μm regions (individual squares) surrounding branch ostia (central square) of immature rabbits (n = 36 branches, 4 rabbits). Total area of map = 2.25mm^2. Mean aortic blood flow is from top to bottom.

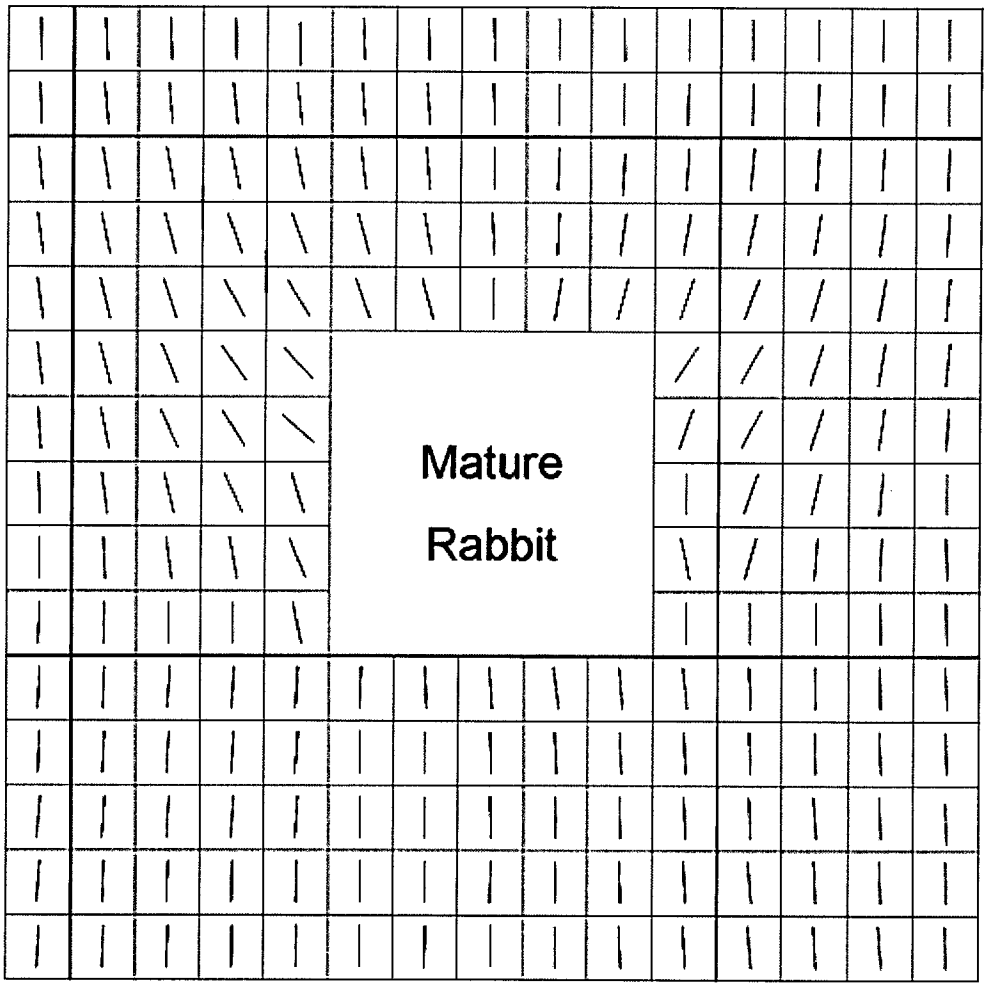

Fig. 5.18. Direction indicators depicting mean normalised angle of orientation of nuclei in 100μm * 100μm regions (individual squares) surrounding branch ostia (central square) of mature rabbits (n = 38 branches, 4 rabbits). Total area of map = 2.25mm^2. Mean aortic blood flow is from top to bottom.

Table 5.10a. Immature rabbit endothelial cell nuclear normalised orientations for sub-regions (100μm * 100μm) within upstream and lateral main-regions in "Zone A", where n equals the number of branches.

Immature	U2R1		U2		U2L1		U1R1		U1		U1L1		R1		L1	
Sub-Region	Mean	SEM	Mean	SEM	Mean	SEM	Mean	SEM	Mean	SEM	Mean	SEM	Mean	SEM	Mean	SEM
U2R2s	3.78	1.58	0.44	1.65	-2.61	1.57	-1.52	1.58	-0.32	1.70	-3.23	1.69	-7.96	2.54	28.44	5.18
U2R1s	1.65	1.78	0.29	1.57	-3.26	1.73	0.52	1.55	-0.15	1.86	-2.54	1.63	-12.20	1.83	18.59	2.63
U2s	0.82	1.95	-0.97	1.61	-3.43	1.67	2.33	1.79	-2.09	1.63	-2.90	1.56	-15.80	2.18	12.37	2.35
U2L1s	0.23	1.66	-1.78	1.52	-2.42	1.93	0.30	1.73	-3.13	1.65	-0.41	1.38	-21.36	2.69	6.91	1.32
U2L2s	0.91	1.54	-1.83	1.62	-1.96	2.54	-0.61	1.73	-3.55	1.79	-0.09	2.07	-17.97	3.76	1.97	1.81
U1R2s	2.28	1.52	-0.02	1.33	-2.62	1.68	-1.35	1.94	-0.83	1.73	-2.24	1.60	-5.60	1.93	22.15	13.73
U1R1s	1.53	1.49	-0.41	1.31	-3.57	1.59	-0.09	1.74	0.48	1.76	-1.69	1.90	-13.25	1.99	15.99	4.59
U1s	0.89	1.68	-1.51	1.40	-2.52	1.43	2.23	2.53	-0.49	1.47	-0.76	2.05	-21.41	2.83	10.35	2.22
U1L1s	-1.58	1.62	-3.00	1.52	-3.88	1.26	-1.41	1.83	-1.10	1.56	1.38	2.08	-19.21	6.01	5.53	1.64
U1L2s	-0.47	1.34	-3.15	1.64	-4.76	2.35	-2.29	1.87	-1.98	1.81	0.60	2.88	-8.92	11.83	-1.34	1.43
R2s	3.60	1.90	-1.00	1.38	-2.35	1.58	-1.51	2.05	-1.47	1.95	1.36	1.77	-1.59	2.50	5.44	17.82
R1s	1.38	1.84	-2.47	1.25	-3.28	1.57	-2.99	1.64	-2.34	1.63	1.28	1.77	-9.00	2.23	6.27	5.57
Cs	-0.62	1.79	-2.01	1.34	-3.42	1.58	-3.38	1.69	-0.81	1.77	4.18	1.63	-18.32	2.31	4.39	2.08
L1s	-0.54	1.58	-2.36	1.30	-2.86	1.32	-0.87	1.80	-0.12	1.54	4.48	1.67	-21.12	4.31	0.83	2.21
L2s	-1.75	1.49	-3.17	1.66	-3.49	1.73	-1.26	2.08	1.01	1.66	1.64	2.48	0.40	13.27	-1.63	2.20
D1R2s	1.51	2.12	-2.44	1.43	-3.62	1.31	-5.62	2.16	-5.39	2.24	6.57	1.71	2.36	1.82	14.46	6.88
D1R1s	0.66	1.41	-2.29	1.13	-4.56	1.47	-3.59	1.46	-2.68	1.75	6.32	2.42	-3.18	2.16	2.97	3.90
D1s	-0.15	1.39	-2.43	1.47	-1.90	1.24	-4.09	1.85	-0.79	1.50	6.85	1.61	-10.43	2.71	-1.39	2.48
D1L1s	-0.23	1.54	-2.69	1.48	-2.27	1.26	-5.94	2.61	3.14	1.66	6.15	1.48	-5.04	4.28	-1.96	2.21
D1L2s	-0.20	1.38	-2.78	1.42	-0.82	1.52	-7.61	2.20	7.73	2.22	2.54	1.50	-10.20	10.71	-5.19	2.68
D2R2s	3.23	1.71	0.11	1.54	-2.92	1.34	-7.06	2.03	-12.91	2.63	16.78	2.75	6.31	1.73	-0.91	2.09
D2R1s	0.46	1.38	-2.36	1.53	-3.50	1.54	-8.58	1.50	-3.30	2.97	12.99	1.78	-1.53	2.05	-1.01	1.98
D2s	0.77	1.60	-3.19	1.61	-2.45	1.37	-9.86	2.44	5.97	3.12	13.92	1.88	-0.13	2.25	-4.13	2.06
D2L1s	0.21	1.41	-4.01	1.82	-2.71	1.37	-13.03	3.24	18.28	3.62	9.08	1.36	-1.01	3.32	-2.74	1.94
D2L2s	0.36	1.60	-4.86	1.43	0.46	1.74	-17.85	3.46	20.92	3.07	4.43	1.50	-2.36	2.61	-5.02	2.33

Table 5.10b. Immature rabbit endothelial cell nuclear normalised orientations for sub-regions (100μm * 100μm) within downstream main-regions in "Zone A", where n equals the number of branches.

Immature	D1R1		D1		D1L1		D2R1		D2		D2L1	
Sub-Region	Mean	SEM	Mean	SEM	Mean	SEM	Mean	SEM	Mean	SEM	Mean	SEM
U2R2s	7.84	1.64	0.61	2.59	-2.37	1.82	8.35	2.15	-1.20	1.57	-2.76	1.34
U2R1s	0.70	1.97	-3.08	1.85	-3.54	1.72	1.88	1.91	-1.19	1.77	-3.78	1.12
U2s	1.12	1.82	-0.23	2.19	-4.50	1.73	0.50	2.05	-0.74	1.40	-4.75	1.21
U2L1s	2.93	2.05	0.37	2.01	-2.31	2.08	0.18	1.72	-1.00	1.58	-2.19	1.35
U2L2s	4.39	2.34	-1.07	1.88	-4.54	2.02	0.27	1.70	-3.46	1.62	-3.98	2.02
U1R2s	7.23	1.56	-3.39	1.75	-3.76	1.63	6.77	2.62	-0.95	1.60	-2.81	1.52
U1R1s	0.84	1.59	-3.42	1.40	-5.33	1.25	0.65	2.12	-1.48	1.48	-4.07	1.24
U1s	1.69	1.43	-2.07	1.73	-4.52	1.48	1.52	1.89	-2.01	1.47	-4.98	1.31
U1L1s	1.99	1.65	-2.31	1.60	-3.73	1.58	0.57	1.70	-2.64	1.34	-3.53	1.44
U1L2s	0.68	1.80	-0.64	2.10	-3.57	1.21	-0.17	1.61	-1.95	1.45	-6.39	1.65
R2s	8.49	1.33	0.62	1.55	-1.55	1.41	5.33	1.99	-1.75	1.60	-1.72	1.37
R1s	1.88	1.60	-1.08	1.24	-2.64	1.57	-0.42	1.98	-2.02	1.52	-3.16	1.42
Cs	2.02	1.65	-2.66	1.45	-1.13	1.37	-0.76	2.03	-1.82	1.50	-4.17	1.38
L1s	1.64	1.52	-1.70	1.59	-0.21	1.25	-0.02	1.98	-2.85	1.35	-5.00	1.47
L2s	1.66	1.62	-1.75	1.37	-3.90	1.42	-1.91	1.49	-2.48	1.45	-6.26	1.76
D1R2s	8.40	1.68	-0.27	1.80	-2.73	1.32	5.99	1.67	-1.43	1.46	-3.37	1.46
D1R1s	2.05	1.78	-1.36	1.34	-2.56	1.38	0.23	1.57	-3.18	1.41	-3.43	1.65
D1s	2.39	1.59	-2.59	1.48	-3.50	1.36	0.39	1.71	-3.72	1.62	-2.81	1.34
D1L1s	0.91	1.47	-2.87	1.52	-2.48	1.51	1.03	1.73	-2.71	1.74	-3.51	1.54
D1L2s	0.78	1.55	-2.13	1.62	-2.05	1.70	-0.50	1.67	-4.39	1.38	-6.04	1.92
D2R2s	7.24	1.79	-0.46	1.54	-3.33	1.32	5.46	1.69	-0.92	1.52	-4.12	1.65
D2R1s	0.87	1.88	-0.46	1.50	-3.30	1.12	0.43	1.59	-2.46	1.55	-4.50	1.61
D2s	0.54	1.74	-1.54	1.22	-3.14	1.56	1.12	1.64	-2.69	1.45	-3.48	1.48
D2L1s	-0.80	1.86	-2.42	1.36	-1.96	1.55	-0.74	1.49	-3.68	1.41	-4.34	1.45
D2L2s	-1.85	1.89	-3.24	1.40	-4.12	2.08	-1.23	1.52	-3.93	1.47	-4.27	1.70

Table 5.11a. Mature rabbit endothelial cell nuclear normalised orientations for sub-regions (100μm * 100μm) within upstream and lateral main-regions in "Zone A", where n equals the number of branches.

Mature	U2R1		U2		U2L1		U1R1		U1		U1L1		R1		L1	
Sub-Region	Mean	SEM	Mean	SEM	Mean	SEM	Mean	SEM	Mean	SEM	Mean	SEM	Mean	SEM	Mean	SEM
U2R2s	1.85	1.25	-0.31	1.03	-1.56	1.12	-0.21	1.34	-2.49	1.17	0.50	1.00	-6.48	2.14	31.05	5.10
U2R1s	1.76	1.00	0.62	0.89	-1.83	1.03	-2.02	1.03	-1.93	1.08	0.63	1.03	-14.17	1.94	27.30	2.41
U2s	0.80	0.90	-0.24	0.95	-2.26	1.01	-2.18	1.16	-1.51	0.96	0.37	1.03	-20.16	3.86	17.08	2.32
U2L1s	0.33	0.90	-0.90	1.00	-1.17	0.88	-1.78	1.05	-0.36	1.00	0.03	0.91	-35.33	3.11	8.99	1.98
U2L2s	0.18	1.01	-1.78	0.95	-2.30	1.46	-1.92	1.07	-0.41	1.00	0.13	1.47	-42.32	3.79	4.85	2.60
U1R2s	1.80	1.00	-0.43	0.98	0.34	1.31	-2.66	0.92	-5.20	1.39	2.40	1.09	-3.31	2.15	22.14	16.10
U1R1s	0.99	1.05	-0.62	1.02	-1.18	1.04	-4.06	1.10	-4.38	1.18	2.21	1.06	-10.11	2.07	26.85	3.59
U1s	1.13	0.89	-0.56	1.10	-1.98	1.21	-5.30	1.21	-2.00	1.10	3.29	1.05	-21.19	4.15	16.08	2.61
U1L1s	0.87	1.09	-0.49	1.09	-1.84	0.97	-6.51	1.42	1.07	1.17	2.00	1.04	-31.87	5.82	8.13	1.80
U1L2s	-0.15	1.04	-0.49	0.89	-1.76	1.29	-5.62	1.27	0.53	1.14	1.51	1.52	-47.26	6.61	2.48	2.44
R2s	0.73	1.33	-0.94	0.91	-2.09	1.06	-5.44	1.35	-8.92	1.40	5.30	1.45	-0.92	1.98	-0.37	26.35
R1s	1.34	1.04	-0.72	1.03	-0.76	1.03	-8.63	1.33	-5.90	1.25	6.56	1.23	-5.63	1.77	13.22	5.71
Cs	2.40	1.99	-1.24	0.99	-1.24	1.03	-10.53	1.41	-1.87	1.48	5.09	1.24	-12.13	3.53	12.48	2.60
L1s	0.49	0.87	-0.51	1.07	-1.67	1.00	-12.11	1.61	1.57	1.37	4.05	1.21	-23.83	5.31	4.56	1.57
L2s	0.08	0.95	-0.74	0.96	-1.09	1.65	-11.76	1.30	3.64	1.25	2.88	1.79	-15.84	8.75	-0.46	2.09
D1R2s	0.85	1.22	-0.69	1.01	-1.74	1.15	-9.11	1.46	-16.71	2.04	11.96	1.49	1.33	1.92	-10.62	21.43
D1R1s	0.00	1.00	-1.28	1.06	-1.16	0.93	-11.75	1.67	-12.16	2.05	11.93	1.46	-1.88	1.40	13.70	3.86
D1s	0.47	0.90	-0.18	0.93	-1.40	1.07	-15.89	1.85	-3.49	1.54	10.83	1.47	-6.85	2.51	4.66	1.73
D1L1s	-0.52	0.90	-0.46	1.08	-1.43	1.17	-19.68	1.99	3.74	1.49	7.96	1.25	-8.79	3.40	1.60	1.88
D1L2s	-0.98	1.04	-0.89	1.14	-0.54	1.49	-19.01	1.79	9.64	1.51	4.86	1.29	-15.19	16.14	-3.25	2.22
D2R2s	0.49	1.00	-0.56	1.07	-0.62	1.15	-8.70	1.96	-20.73	1.92	19.97	2.08	4.42	1.84	-7.78	6.98
D2R1s	-1.45	1.01	-0.77	1.07	-2.14	1.45	-14.02	1.63	-14.51	1.63	20.65	1.72	1.76	1.26	0.91	2.22
D2s	-1.68	0.87	-1.54	1.02	1.49	2.38	-19.07	2.41	0.98	3.51	16.80	1.43	1.20	1.40	-0.93	1.52
D2L1s	-1.02	1.09	-0.19	0.96	-1.97	1.07	-27.34	2.64	11.91	2.97	10.67	1.30	0.79	1.44	-2.01	1.77
D2L2s	-1.35	1.15	-0.56	0.92	-0.55	1.49	-28.50	3.42	16.13	2.23	6.25	1.64	-5.57	7.49	-4.15	2.48

Table 5.11b. Mature rabbit endothelial cell nuclear normalised orientations for sub-regions (100μm * 100μm) within downstream main-regions in "Zone A", where n equals the number of branches.

Mature	D1R1		D1		D1L1		D2R1		D2		D2L1	
Sub-Region	Mean	SEM	Mean	SEM	Mean	SEM	Mean	SEM	Mean	SEM	Mean	SEM
U2R2s	4.21	1.66	2.44	1.69	-6.10	1.39	4.96	1.17	-0.31	1.01	-3.65	0.90
U2R1s	2.74	1.03	-1.76	2.10	-3.28	1.01	1.64	1.01	0.67	0.91	-4.31	0.75
U2s	4.12	1.07	-4.63	1.81	-1.77	1.37	1.08	1.12	-1.29	0.88	-4.29	1.01
U2L1s	3.21	1.17	-5.51	2.30	-3.05	1.45	1.29	0.90	-2.47	0.81	-4.05	0.92
U2L2s	2.88	1.36	-6.25	1.33	-5.08	1.23	-0.12	1.04	-1.92	1.02	-3.35	1.41
U1R2s	3.17	1.81	1.55	1.23	-2.93	0.95	4.85	1.13	0.00	0.90	-3.13	0.90
U1R1s	3.75	0.96	-0.22	1.27	-3.88	1.23	2.07	1.25	-1.01	0.90	-4.16	0.84
U1s	3.49	0.98	-2.14	1.56	-3.33	1.09	1.88	1.00	-1.01	0.79	-2.87	0.89
U1L1s	3.37	0.97	-3.50	1.11	-2.66	0.93	1.22	0.95	-1.81	0.78	-3.17	0.86
U1L2s	3.94	1.06	-3.44	1.07	-3.85	1.58	0.06	0.91	-2.98	0.85	-3.61	1.35
R2s	5.00	1.41	1.02	1.22	-3.06	0.88	5.43	1.15	-0.37	0.84	-4.06	0.80
R1s	3.97	1.01	-0.56	1.28	-3.67	0.98	1.88	1.08	-1.59	0.88	-3.52	0.73
Cs	2.59	0.86	-1.38	1.11	-3.77	0.86	2.25	0.97	-2.05	0.72	-2.99	0.77
L1s	2.32	0.96	-1.02	1.08	-2.72	0.87	1.38	0.86	-2.36	0.64	-3.59	0.77
L2s	2.78	1.14	-1.14	1.16	-3.04	1.23	0.06	0.82	-2.78	0.67	-4.91	1.19
D1R2s	4.79	1.16	0.75	1.12	-2.83	0.91	4.46	1.22	0.05	0.79	-3.81	0.98
D1R1s	2.53	0.90	0.58	1.22	-4.98	0.78	2.19	0.88	-1.40	0.83	-2.90	0.85
D1s	2.38	0.75	0.33	1.22	-3.89	0.89	2.94	0.92	-1.09	0.64	-3.46	0.82
D1L1s	1.59	0.81	-1.50	1.10	-2.67	0.90	0.81	0.70	-2.52	0.74	-4.05	0.90
D1L2s	1.06	0.85	-2.29	1.05	-2.38	1.05	-0.70	0.91	-2.73	0.75	-4.69	1.31
D2R2s	4.48	1.14	-0.03	0.89	-3.36	0.79	3.98	1.17	0.04	0.88	-3.33	0.84
D2R1s	2.72	0.95	0.09	0.96	-5.23	1.55	2.01	0.95	-1.50	0.88	-3.12	0.97
D2s	2.11	0.94	-1.52	0.98	-4.41	0.94	2.09	0.87	-0.25	0.92	-3.29	0.84
D2L1s	1.22	0.94	-1.85	0.90	-3.87	0.92	1.06	0.84	-3.14	0.84	-3.51	0.82
D2L2s	-0.10	1.09	-3.33	0.86	-1.73	1.15	0.06	0.89	-2.28	0.86	-4.90	1.25

Tukey tests were performed on normalised nuclear orientations for sub-regions in "Zone A" (main regions "U1R1", "U1", "U1L1", "R1", "L1", "D1R1", "D1", "D1L1") to observe where changes in normalised nuclear orientation existed between the sub-regions within each of these main regions (Appendix B.2a-g).

5.3.2.3 "Zone B" (500μm * 500μm regions)

The orientations of nuclei within "Zone B" are shown in Table 5.12. There was a highly significant effect of region ($P<0.005$), but no significant effect of age ($P=0.24$) or interaction between age and region ($P=0.88$). The mean angles of orientation were 0.19 ± 0.22° and -0.24 ± 0.16° for immature and mature rabbits respectively (n = 1163 and 1355 regions respectively). Nuclear angles ranged from -6.80 ± 1.72° ("D4L2", n = 17 branches) to 6.01 ± 1.02° ("D2R3", n = 19 branches) in immature rabbits, and from

-5.49 ± 1.62° ("D4L4", n = 18 branches) to 5.63 ± 1.17° ("D4R4", n = 20 branches) in mature rabbits.

Table 5.12. Rabbit endothelial cell nuclear normalised orientations for regions in "Zone B", where n equals the number of branches.

Region	Immature		Mature	
	Mean	SEM	Mean	SEM
U4R4	2.92	1.33	1.12	1.32
U4R3	2.29	1.54	0.67	1.26
U4R2	1.13	1.65	-0.58	1.31
U4R1	0.57	1.31	-0.80	0.68
U4	0.13	1.20	-1.14	0.70
U4L1	0.40	1.13	-0.71	0.73
U4L2	-2.95	1.42	-2.27	1.02
U4L3	-2.23	1.33	-2.96	1.28
U4L4	-1.87	2.10	-3.48	1.46
U3R4	3.08	1.09	1.28	1.12
U3R3	3.72	1.21	2.40	1.09
U3R2	2.79	1.53	1.75	1.10
U3R1	-0.06	1.46	0.47	0.71
U3	-0.75	1.40	-0.05	0.60
U3L1	-1.63	1.33	-0.46	0.74
U3L2	-3.35	1.55	-1.64	1.33
U3L3	-4.29	1.64	-2.03	1.16
U3L4	-4.60	1.71	-1.47	1.26
U2R4	3.59	1.23	2.62	1.18
U2R3	3.03	1.22	2.02	1.11
U2L3	-1.52	1.40	-0.77	1.29
U2L4	-1.86	1.58	0.46	1.00
U1R4	3.51	1.22	2.10	1.39
U1R3	3.08	1.02	1.35	1.30
U1L3	-2.22	1.37	-1.75	1.21
U1L4	-2.81	1.83	-1.28	1.21
R4	4.90	1.37	2.75	1.36
R3	4.88	1.36	1.80	1.34
L3	-2.83	1.53	-3.16	1.22
L4	-2.26	2.38	-3.23	1.43
D1R4	5.44	1.48	3.92	1.40
D1R3	5.31	1.35	3.28	1.23
D1L3	-2.32	1.62	-4.35	1.18
D1L4	-1.95	1.99	-4.81	1.29
D2R4	5.58	1.01	4.03	1.35
D2R3	6.01	1.02	5.20	1.27
D2L3	-5.45	1.92	-4.71	1.28
D2L4	-2.45	2.56	-4.25	1.57
D3R4	3.73	1.47	4.39	1.74
D3R3	4.38	1.22	3.63	1.56
D3R2	4.68	1.27	4.11	1.24

D3R1	0.96	1.24	1.16	0.78
D3	-1.21	1.27	-0.95	0.66
D3L1	-2.94	1.34	-2.77	0.72
D3L2	-4.12	1.58	-4.15	1.09
D3L3	-2.76	1.93	-4.56	1.44
D3L4	-0.54	2.26	-3.96	1.55
D4R4	3.70	1.71	5.63	1.17
D4R3	5.24	1.58	4.32	1.23
D4R2	5.10	1.43	3.67	1.25
D4R1	1.35	1.42	0.45	0.80
D4	-1.80	1.27	-0.68	0.82
D4L1	-3.12	1.30	-1.39	0.87
D4L2	-6.80	1.72	-3.83	1.37
D4L3	-5.58	2.05	-4.59	1.52
D4L4	-3.25	2.39	-5.49	1.62
Total mean	**0.19**	**0.22**	**-0.24**	**0.16**

5.3.2.4 "Zone C" (500μm * 500μm regions)

The normalised orientations of nuclei within "Zone C" are shown in Table 5.13. Nuclear orientations were just significantly different between ages (P=0.05), and there were highly significant differences between regions, and a significant interaction between age and region (both P<0.005). The mean orientations were 0.33 ± 0.21° (n = 1423 regions) and 0.31 ± 0.16° (n = 1443 regions) for immature and mature rabbits respectively. Angles were between -5.80 ± 2.50° ("D6L2", n = 11 branches) and 7.39 ± 1.86° ("U6R4", n = 11 branches) in immature rabbits, and between -6.27 ± 1.42° ("D6L4", n = 11 branches) and 7.35 ± 1.51° ("D6R5", n = 15 branches) in mature rabbits.

Table 5.13. Rabbit endothelial cell nuclear normalised orientations for regions in "Zone C", where n equals the number of branches.

Region	Immature		Mature	
	Mean	SEM	Mean	SEM
U6R6	6.62	2.56	-1.96	1.53
U6R5	6.66	2.25	-0.51	1.45
U6R4	7.39	1.86	1.35	1.46
U6R3	4.45	1.77	2.08	1.79
U6R2	0.98	1.20	1.45	1.96
U6R1	-1.91	1.25	-0.18	1.05
U6	-2.12	1.41	-0.53	0.86
U6L1	-1.91	1.36	-1.44	0.98
U6L2	-0.86	1.43	-1.84	0.82
U6L3	-0.21	1.89	-2.23	1.28
U6L4	-0.87	1.79	-3.95	1.50
U6L5	-1.70	2.41	-3.53	1.46
U6L6	-0.80	3.51	-2.03	1.88
U5R6	2.06	1.37	1.16	1.85
U5R5	4.89	1.08	0.71	1.08
U5R4	4.47	1.22	1.17	1.01
U5R3	3.51	1.17	1.32	1.07
U5R2	1.39	1.33	0.61	1.05
U5R1	-0.45	1.23	-0.86	0.83
U5	-1.60	1.13	-2.03	0.61
U5L1	-1.95	1.05	-1.82	0.69
U5L2	-1.84	1.46	-2.09	1.12
U5L3	-1.37	1.64	-1.83	1.39
U5L4	-2.30	1.87	-2.14	1.68
U5L5	-1.30	2.38	-2.27	1.37
U5L6	-0.58	3.39	-1.21	1.77
U4R6	1.96	1.52	2.52	2.29
U4R5	2.70	1.12	0.61	1.44
U4L5	-2.30	2.11	-3.29	1.61
U4L6	-2.45	2.82	-2.26	2.00
U3R6	0.99	1.56	2.35	1.56
U3R5	2.95	1.01	0.94	1.44
U3L5	-2.99	1.82	-0.91	1.24
U3L6	-0.41	2.65	-0.35	1.59
U2R6	2.25	1.36	2.94	1.54
U2R5	3.21	1.15	2.36	1.10
U2L5	-0.91	2.28	0.55	1.10
U2L6	-1.54	3.01	0.58	1.29
U1R6	1.61	1.57	2.90	1.40
U1R5	3.33	1.30	1.40	1.24
U1L5	-0.66	2.10	-1.50	1.40
U1L6	0.78	2.74	-0.11	1.28
R6	2.76	1.56	3.37	1.39
R5	3.88	1.48	2.81	1.38
L5	-1.50	2.63	-2.83	1.66
L6	-0.02	3.12	-0.54	1.68

D1R6	3.44	1.57	2.75	1.59
D1R5	4.59	1.42	3.25	1.39
D1L5	0.36	2.15	-3.73	1.44
D1L6	-0.43	2.54	-2.30	1.55
D2R6	2.50	1.58	4.87	1.46
D2R5	3.94	1.36	4.97	1.36
D2L5	-0.37	2.79	-3.26	1.55
D2L6	0.76	3.41	-0.72	1.43
D3R6	1.62	1.58	5.18	1.62
D3R5	2.58	1.71	5.35	1.46
D3L5	2.01	2.87	-2.68	1.48
D3L6	-1.82	2.94	-1.76	1.60
D4R6	2.44	1.82	5.49	1.40
D4R5	2.83	1.63	5.27	1.22
D4L5	-0.83	2.83	-5.69	1.87
D4L6	1.38	2.90	-3.53	2.11
D5R6	2.13	1.72	6.51	1.80
D5R5	4.96	1.98	4.11	1.46
D5R4	4.88	1.69	4.76	1.41
D5R3	4.56	1.51	5.34	1.43
D5R2	2.01	1.73	4.07	1.07
D5R1	-0.89	1.51	0.89	0.89
D5	-3.30	1.32	-0.35	0.94
D5L1	-4.76	1.31	-1.30	0.90
D5L2	-5.75	1.29	-4.70	1.06
D5L3	-3.55	2.05	-4.21	1.11
D5L4	-0.42	2.44	-4.69	1.34
D5L5	0.40	2.63	-3.13	1.57
D5L6	1.71	3.37	-5.43	2.44
D6R6	1.26	2.51	5.31	1.99
D6R5	1.80	2.04	7.35	1.51
D6R4	0.74	1.66	6.24	1.43
D6R3	1.44	1.74	5.95	1.24
D6R2	2.50	1.50	4.80	1.16
D6R1	-1.70	1.65	2.12	1.10
D6	-3.15	1.73	0.83	0.99
D6L1	-3.68	1.58	-0.96	1.08
D6L2	-5.80	2.50	-5.32	1.57
D6L3	-3.84	3.20	-5.57	1.22
D6L4	-2.13	2.94	-6.27	1.42
D6L5	0.79	3.61	-5.86	1.84
D6L6	3.00	5.50	-4.49	2.29
Total mean	**0.33**	**0.21**	**0.31**	**0.16**

5.3.2.5 Normalised nuclear orientations along the lateral centreline through the branch ostium

Normalised nuclear orientations along the lateral centreline through the branch ostia from the anatomical right ("R6" to "R1") to the anatomical left ("L1" to "L6") of the aorta are shown in Fig. 5.19. Data for nuclei in "R1" and "L1" are shown split into their constitutive sub-regions along the midline, but offset proximally by 100μm to try and remove variation caused by the population of nuclei immediately upstream of the flow divider (as described in Al-Musawi *et al*, 2004).

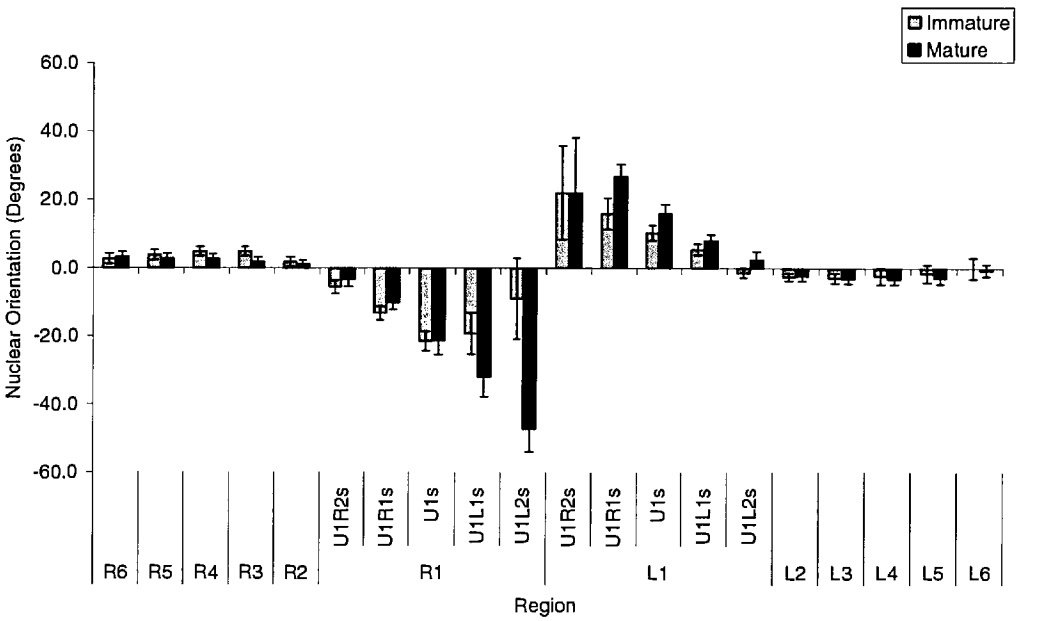

Fig. 5.19. Normalised angle of nuclear orientation along the lateral centreline through the branch ostia from the anatomical right to the anatomical left, for immature and mature rabbits. The branch ostia falls between regions "R1" and "L1". Data for main regions closest to the ostia have been shown sub-divided into the constitutive sub-regions found along the centreline (but offset proximally by 100μm) to show changes at higher resolution. Region names are as described in Fig. 5.1. Bars show means ± SEM (n = number of branches).

5.3.2.6 Normalised nuclear orientations around ostia in different parts of the descending thoracic aorta (500μm * 500μm regions)

Mean normalised nuclear orientations for ostia within the upper portion and lower portion of the descending thoracic aorta, and ostia from the left and right hand side of the vessel are shown in Table 5.14. Data are further subdivided according to Zone.

Data for nuclei within individual regions in "Zone A" for the upper and lower portion of the artery and right and left portions of the descending thoracic aorta are shown in Tables 5.15 and 5.16 respectively. Colour maps showing mean variations in nuclear orientation around the branch ostia at low resolution (averages per 500μm * 500μm regions) for different branch ostial locations are shown in Figs 5.20-5.23.

Table 5.14. Rabbit endothelial cell nuclear normalised orientations for all regions, results separated by location of the branch ostia, where n equals the number of regions.

Location of branch ostia	Region	Immature		Mature	
		Mean	SEM	Mean	SEM
Upper branch ostia	Zone A-C	0.31	0.17	0.03	0.17
	Zone A	0.74	0.35	-1.84	0.39
	Zone B	0.76	0.29	-0.32	0.24
	Zone C	-0.32	0.26	1.38	0.28
Lower branch ostia	Zone A-C	-0.37	0.22	-0.23	0.15
	Zone A	-3.46	0.49	-0.41	0.39
	Zone B	-0.61	0.34	0.04	0.22
	Zone C	1.11	0.32	-0.38	0.21
Right branch ostia	Zone A-C	-2.23	0.20	-2.60	0.15
	Zone A	-3.46	0.41	-2.31	0.39
	Zone B	-2.59	0.30	-2.73	0.24
	Zone C	-1.29	0.34	-2.63	0.22
Left branch ostia	Zone A-C	2.15	0.17	2.25	0.16
	Zone A	1.38	0.42	0.82	0.42
	Zone B	3.09	0.27	2.41	0.24
	Zone C	1.75	0.24	2.82	0.23

5.3.2.6.1 Nuclear orientation for branch ostia within the upper and lower portion of artery

Normalised nuclear orientations averaged for all zones for immature rabbits were 0.31 ± 0.17° and -0.37 ± 0.22° (n = 1854 and 1409 regions respectively) for ostia in the upper and lower portion of the artery, respectively ($P<0.005$), and for mature rabbits were 0.03 ± 0.17° and -0.23 ± 0.15 (n = 1378 and 1755 regions) respectively ($P = 0.25$).

Normalised orientations in regions surrounding branch ostia in the upper portion of the aorta (Fig. 5.20) were not significantly affected by age ($P=0.66$). However, there was an effect of region and a significant interaction between age and region (both $P<0.005$). In regions surrounding branch ostia in the lower portion (Fig. 5.21) there was a significant effect of age ($P<0.05$) and region and interaction between age and region (both $P<0.005$).

5.3.2.6.2 Normalised nuclear orientations for branch ostia from the left hand and right hand side of the artery

Normalised nuclear orientations for left and right branch ostia for immature rabbits were 2.15 ± 0.17° and -2.23 ± 0.20° (n = 1635 and 1460 regions) respectively ($P<0.005$), and for mature rabbits were 2.25 ± 0.16° and -2.60 ± 0.15° (n = 1535 and 1475 regions) respectively ($P<0.005$).

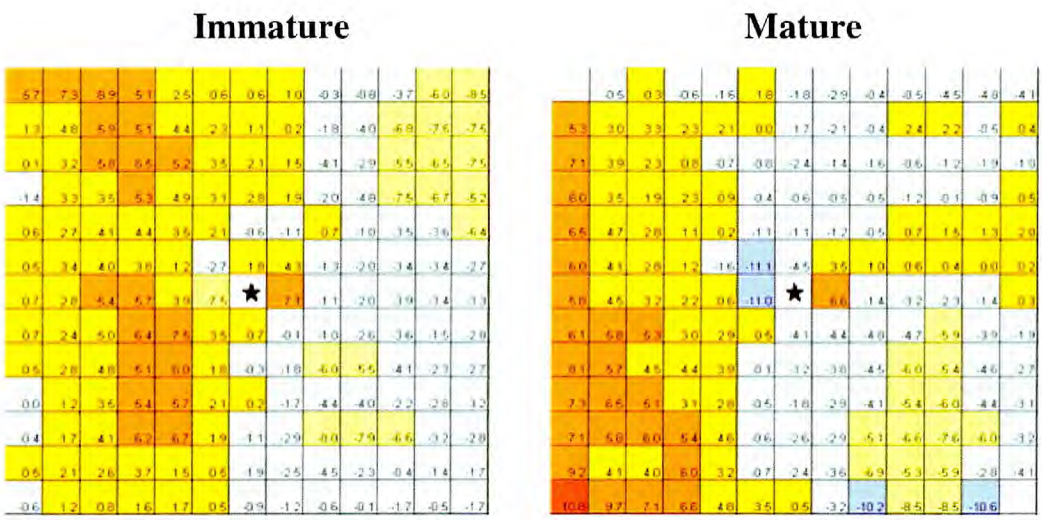

Fig. 5.20. Normalised angle of orientation of rabbit endothelial cell nuclei in the upper descending thoracic aorta. Values are averages for branches 1 to 6 (branch 1 being the first branch downstream from the aortic arch). Each square represents the average data for a 500μm*500μm region. Total area of map is 42.25mm^2. n = 4 immature rabbits, n = 4 mature rabbits. Data represent averages for 21 immature and 14 mature branches.

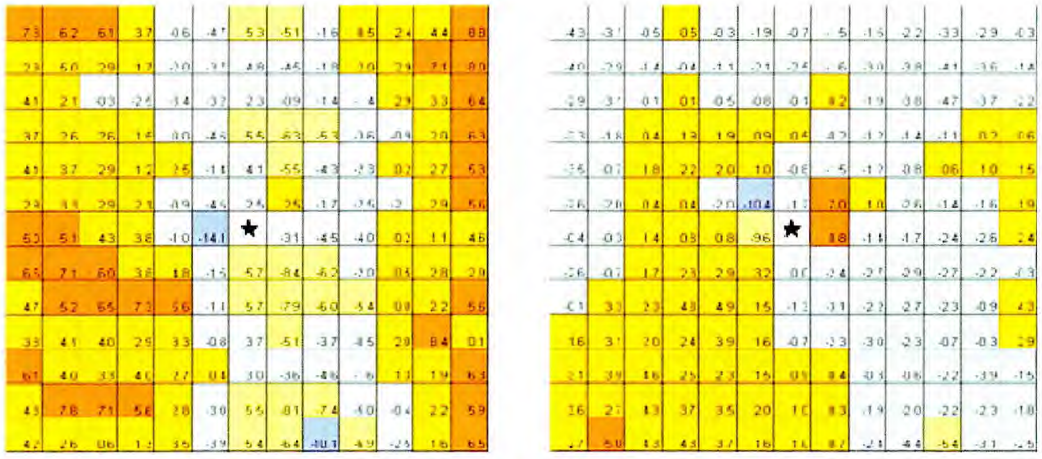

Fig. 5.21. Normalised angle of orientation of rabbit endothelial cell nuclei in the lower descending thoracic aorta. Values are averages for branches 7 to 12. Each square represents the average data for a 500μm * 500μm region. Total area of map is 42.25mm^2. n = 4 immature rabbits, n = 4 mature rabbits. Data represent averages for 15 immature and 20 mature branches.

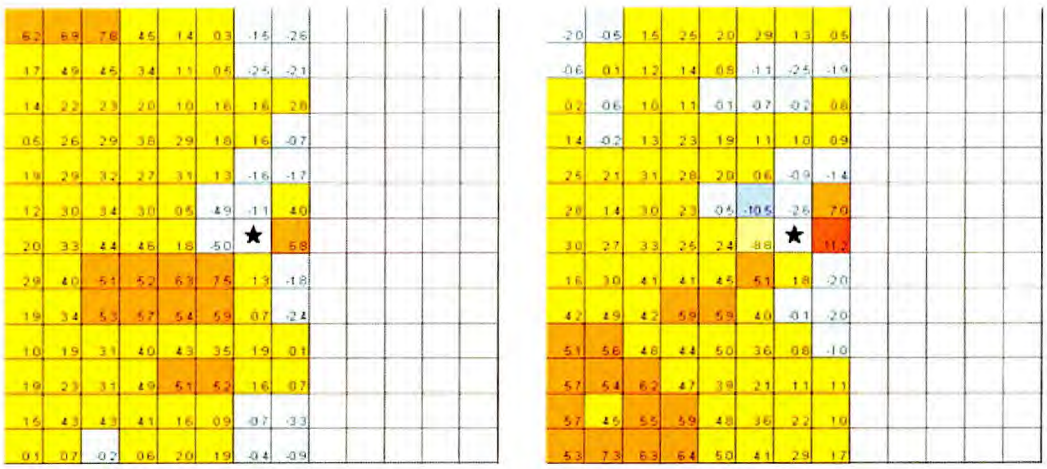

Fig. 5.22. Normalised angle of orientation of rabbit endothelial cell nuclei for branches on the anatomical right hand side of the aorta. (The map has been truncated to avoid affects of flow around ostia on the left hand side). Each square represents the average data for a 500μm*500μm region. Total area of map is 26.0mm^2. n = 4 immature rabbits, n = 4 mature rabbits. Data represent averages for 17 immature and 17 mature branches.

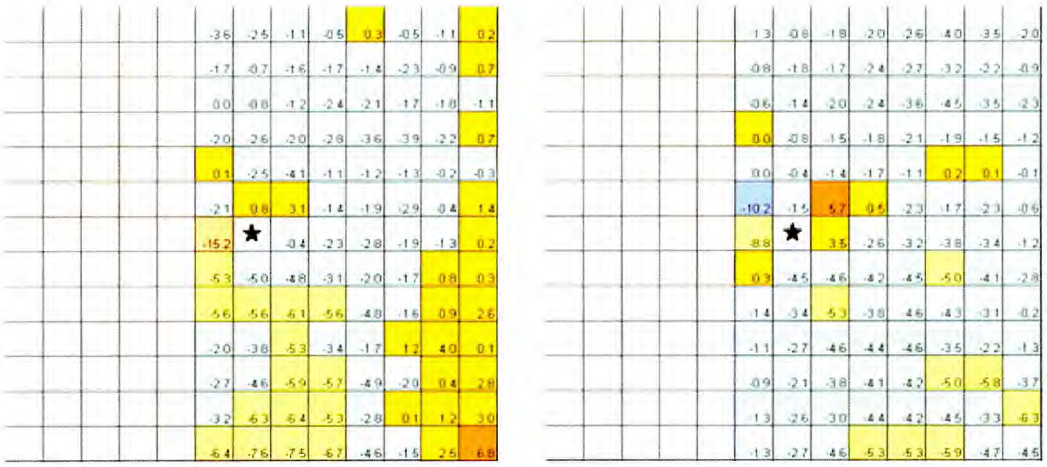

Fig. 5.23. Normalised angle of orientation of rabbit endothelial cell nuclei for branches on the anatomical left hand side of the aorta. (The map has been truncated to avoid affects of flow around ostia on the right hand side). Each square represents the average data for a 500μm * 500μm region. Total area of map is 26.0mm^2. n = 4 immature rabbits, n = 4 mature rabbits. Data represent averages for 18 immature and 17 mature branches.

Table 5.15. Normalised nuclear orientation for branch ostia within upper and lower portion of the descending thoracic aorta, where n equals the number of branches.

	UPPER				LOWER			
Region	Immature		Mature		Immature		Mature	
	Mean	SEM	Mean	SEM	Mean	SEM	Mean	SEM
U2R2	3.47	1.53	0.20	1.58	2.53	2.05	1.98	1.83
U2R1	2.05	1.22	-1.14	0.82	-1.39	1.60	0.99	1.35
U2	-0.58	1.05	-1.06	0.33	-4.05	1.29	-0.82	1.32
U2L1	-1.13	1.10	-1.23	1.16	-5.46	1.64	-1.48	1.38
U2L2	0.71	1.49	-0.50	1.27	-4.29	2.23	-1.18	2.38
U1R2	1.23	1.58	-1.60	1.73	-0.93	2.08	-1.97	1.85
U1R1	-2.66	2.04	-11.07	1.86	-4.48	1.78	-10.38	1.60
U1	1.84	1.35	-4.48	1.54	-2.53	1.52	-1.19	1.28
U1L1	4.33	1.39	3.50	0.94	2.50	1.98	6.99	1.47
U1L2	-1.27	1.51	1.03	1.28	-1.67	2.32	1.03	1.96
R2	3.93	1.52	0.56	1.54	-1.01	2.44	0.83	2.07
R1	-7.50	2.04	-11.04	2.60	-14.06	2.34	-9.60	2.04
L1	7.09	1.74	6.59	3.10	-3.12	2.50	8.81	2.66
L2	-1.12	1.48	-1.43	1.36	-4.53	1.59	-1.41	2.28
D1R2	7.51	1.17	2.93	1.32	4.84	2.77	2.89	2.02
D1R1	3.45	1.55	0.54	1.13	-1.52	2.48	3.19	1.03
D1	0.72	1.19	-4.10	1.38	-5.66	1.81	-0.01	1.01
D1L1	-0.06	1.14	-4.39	1.15	-8.37	1.65	-2.44	1.11
D1L2	-1.05	1.50	-4.78	1.03	-6.21	3.28	-2.70	1.79
D2R2	5.95	1.84	3.89	1.12	5.56	2.63	4.86	1.77
D2R1	1.81	1.62	-0.11	1.19	-1.05	2.68	1.49	1.09
D2	-0.27	1.44	-3.16	0.90	-5.73	1.54	-1.29	0.81
D2L1	-1.81	1.33	-3.82	0.91	-7.94	1.68	-3.07	0.98
D2L2	-5.96	1.58	-4.50	1.09	-6.00	2.93	-2.21	1.54
Total Mean	**0.74**	**0.35**	**-1.84**	**0.39**	**-3.46**	**0.49**	**-0.41**	**0.39**

Table 5.16. Normalised nuclear orientation for branch ostia within anatomical right and left of the descending thoracic aorta, where n equals the number of branches.

	RIGHT				LEFT			
Region	Immature		Mature		Immature		Mature	
	Mean	SEM	Mean	SEM	Mean	SEM	Mean	SEM
U2R2	-	-	-	-	3.15	1.27	2.01	1.29
U2R1	0.05	1.44	-0.03	1.25	1.28	1.49	0.59	1.26
U2	-2.54	1.30	-0.42	1.13	-1.58	1.22	-0.92	1.19
U2L1	-4.13	1.63	-1.41	1.45	-1.70	1.22	-1.39	1.13
U2L2	-1.08	1.43	-1.72	1.52	-	-	-	-
U1R2	-	-	-	-	0.52	1.31	-0.47	1.28
U1R1	-2.11	2.29	-10.22	1.03	-4.88	1.74	-10.50	2.12
U1	0.84	1.61	-1.53	1.57	-1.10	1.44	-2.64	1.27
U1L1	3.07	1.57	5.73	1.63	4.00	1.80	7.00	1.29
U1L2	-1.41	1.32	0.47	1.23	-	-	-	-
R2	-	-	-	-	1.77	1.51	2.38	1.26
R1	-15.21	1.80	-8.84	2.05	-4.99	2.13	-8.78	2.48
L1	-0.37	2.28	3.46	3.19	6.79	2.25	11.24	2.11
L2	-2.29	1.20	-2.62	1.63	-	-	-	-
D1R2	-	-	-	-	6.35	1.41	4.53	1.33
D1R1	-5.25	1.50	0.25	1.01	7.49	1.24	5.11	1.03
D1	-4.97	1.19	-4.45	1.20	1.32	1.68	1.77	1.06
D1L1	-4.76	1.36	-4.58	1.16	-1.80	1.93	-2.04	1.16
D1L2	-3.07	1.73	-4.15	1.33	-	-	-	-
D2R2	-	-	-	-	5.43	1.54	5.87	1.22
D2R1	-5.62	1.44	-1.44	1.01	5.89	1.64	3.98	1.12
D2	-5.59	1.18	-3.37	0.94	0.65	1.74	-0.07	0.82
D2L1	-6.14	1.16	-5.30	1.07	-2.43	1.96	-1.99	0.84
D2L2	-5.63	1.44	-3.76	1.17	-	-	-	-
Total Mean	**-3.46**	**0.41**	**-2.31**	**0.39**	**1.38**	**0.42**	**0.82**	**0.42**

5.3.3 Rabbit endothelial nuclear length

Endothelial nuclear lengths for immature and mature rabbits for the 500μm * 500μm regions defined in Fig.5.1 (Zones A-C) are shown in Fig. 5.24. There were highly significant differences in mean length between ages and regions and a highly significant interaction between age and region (age*region) (all $P<0.005$). Mean lengths for individual rabbits are shown in Table 5.17. The mean lengths of nuclei were 16.68 ± 0.02μm (n = 3263 regions) and 19.06 ± 0.02μm (n = 3539 regions) in immature and mature rabbits respectively; a difference of 14.3%.

Immature **Mature**

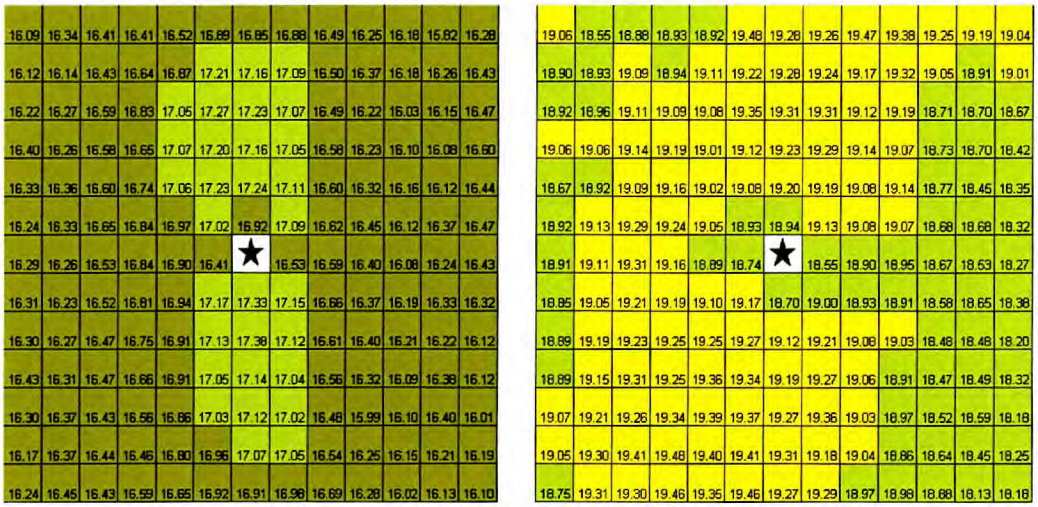

Fig. 5.24. Length (μm) of rabbit endothelial cell nuclei for all the branch ostia. Each square represents the average data for a 500μm * 500μm region. Total area of the map is 42.25mm^2. n = 4 immature rabbits, n = 4 mature rabbits. Data represent average for 36 immature and 38 mature branches.

Table 5.17. Mean rabbit endothelial nuclear length (μm), where n equals the number of regions.

Age Group	Rabbit	Length (μm)	
		Mean	SEM
Immature	I1	16.94	0.02
	I2	15.90	0.02
	I3	17.16	0.04
	I4	16.91	0.05
	All immature	16.68	0.02
Mature	M1	19.38	0.03
	M2	18.49	0.02
	M3	19.20	0.03
	M4	20.49	0.06
	All mature	19.06	0.02

5.3.3.1 "Zone A" (500μm * 500μm regions)

Mean lengths for nuclei in "Zone A" are shown in Fig. 5.25. There was a highly significant effect of age and region and a highly significant interaction between age and region (all $P<0.005$).

In immature rabbits, the maximum mean length of nuclei (17.38 ± 0.13μm, "D2", n = 34 branches) was lower than the minimum length of nuclei (18.55 ± 0.14, "L1", n = 38 branches) in mature rabbits. In immature rabbits, nuclei were generally longer downstream of the branch ostia than upstream: the ratio of the mean length upstream (16.92 ± 0.15μm, "U1", n = 36 branches) to the mean length downstream (17.33 ± 0.14, "D1", n = 34 branches) was 0.98. Nuclei in the lateral regions ("R1" and "L1") and immediately upstream of the ostia ("U1") were the shortest. Nuclei in mature rabbits were generally lower in the immediate branch vicinity, with very little variation between upstream and downstream regions: the ratio of the mean length upstream (18.94 ± 0.15μm, "U1", n = 38 branches) to the mean length downstream (18.70 ± 0.15, "D1", n = 38 branches) was 1.01. The shortest nuclei were found in the lateral regions ("R1" and "L1") and in the region immediately downstream of the ostia ("D1"). The significance of differences between individual regions for immature and mature rabbits, obtained using the Tukey test, are shown in Fig 5.26.

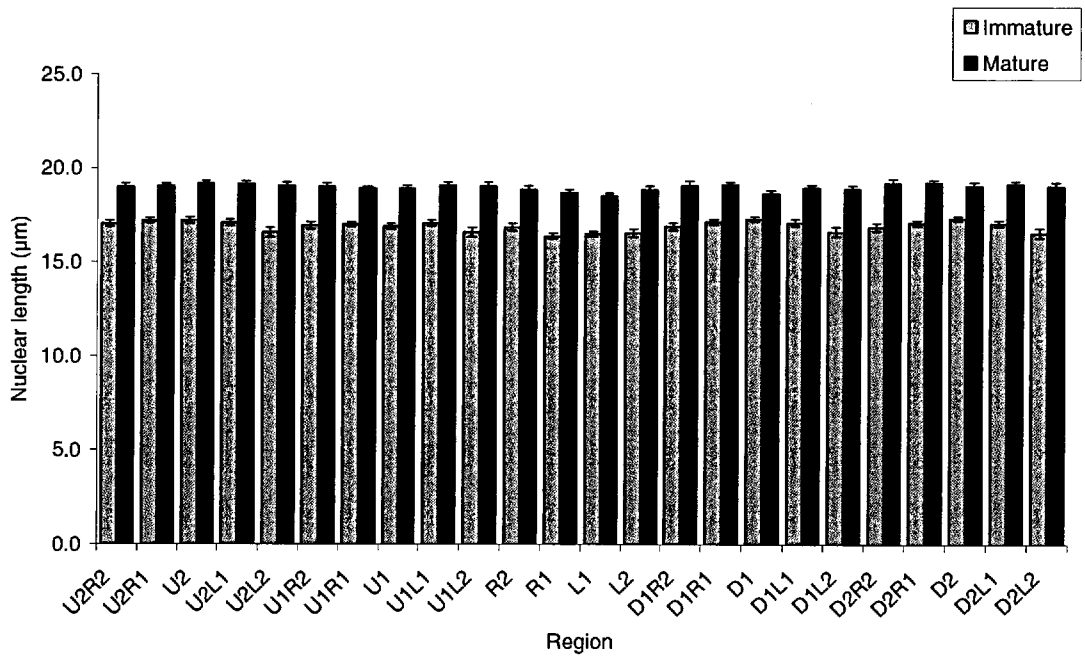

Fig. 5.25. Endothelial nuclear lengths (μm) for regions surrounding branch ostia, defined in Fig. 5.1, in immature and mature rabbits. Bars show means ± SEM (n = number of branches).

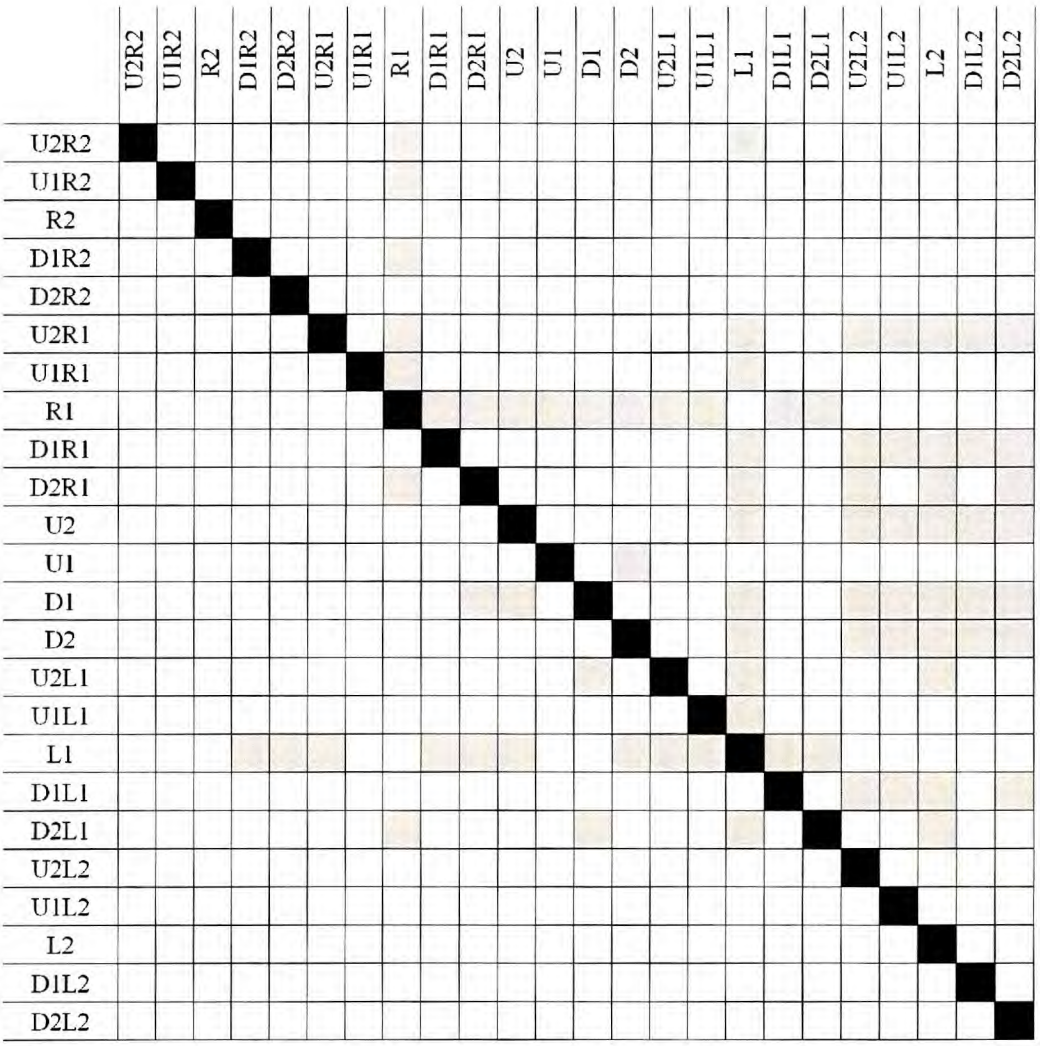

Fig. 5.26. Significant differences in nuclear length between 500μm * 500μm regions within Zone A, determined by the Tukey test for multiple comparisons. Squares shaded in grey depict significant differences ($P<0.05$). Squares to the right of the black diagonal line indicate differences in immature rabbits. Squares to the left indicate differences in mature rabbits.

5.3.3.2 "Zone A" (100μm * 100μm sub-regions)

Nuclear lengths in the main regions nearest the branch ostia ("U2R1", "U2", "U2L1", "U1R1", "U1", "U1L1", "R1", "L1", "D1R1", "D1", "D1L1", "D2R1", "D2", "D2L1") were also analysed at higher resolution, using data for individual 100μm * 100μm sub-regions (Fig. 5.27, Tables 5.18a,b and 5.19a,b). There were significant changes with age within all regions analysed ($P<0.05$), and significant effects of sub-region for nuclei within "U1R1", "R1", "D1R1", "U1", "D1", "U1L1", "L1", "D1L1" (all $P<0.005$) and

"D2L1" (P<0.05). There was a significant change with age in pattern (age*region interaction) for the main regions "D1R1", "U1", "D1", "L1" (all P<0.005), "D2R1", "D1L1" and "D2L1" (all P<0.01). In immature and mature rabbits, the shortest nuclei were located in a strip running along the lateral axis at the level of the branch ostia, but in addition, nuclei in mature rabbits were also shorter than the average in a region extending slightly downstream of the ostia.

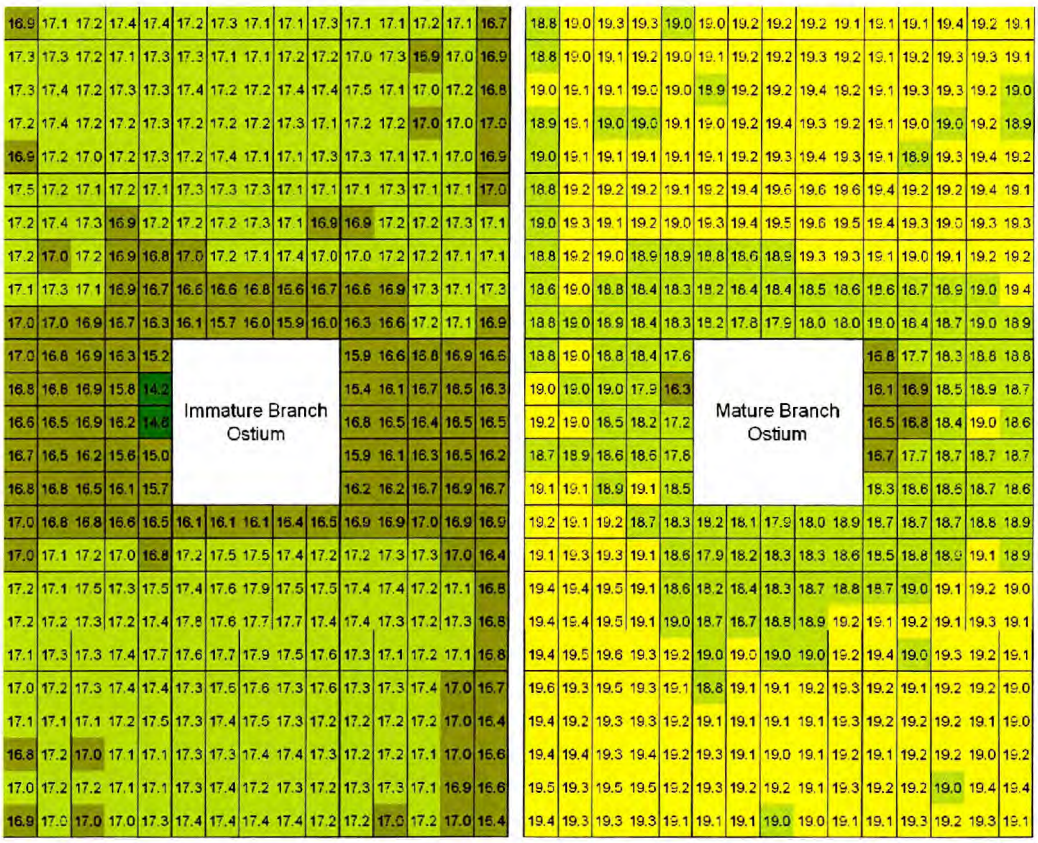

Fig. 5.27. Length (μm) of endothelial cell nuclei for all the branch ostia. Each square represents the data for a 100μm * 100μm region. The total area of the map is 3.75mm^2. n = 4 immature rabbits, n = 4 mature rabbits. Data are averages for 36 immature and 38 mature branches.

Table 5.18a. Immature rabbit endothelial cell nuclear lengths (μm) for sub-regions (100μm * 100μm) within upstream and lateral main-regions in "Zone A", where n equals the number of branches.

Immature	U2R1		U2		U2L1		U1R1		U1		U1L1		R1		L1	
Sub-Region	Mean	SEM	Mean	SEM	Mean	SEM	Mean	SEM	Mean	SEM	Mean	SEM	Mean	SEM	Mean	SEM
U2R2s	16.95	0.24	17.24	0.22	17.11	0.21	17.47	0.27	17.27	0.16	17.13	0.20	16.99	0.20	15.93	0.32
U2R1s	17.12	0.15	17.31	0.18	17.06	0.22	17.23	0.16	17.29	0.20	17.31	0.23	16.85	0.16	16.64	0.25
U2s	17.22	0.26	17.06	0.17	17.15	0.23	17.11	0.17	17.27	0.24	17.06	0.25	16.95	0.24	16.80	0.22
U2L1s	17.40	0.23	17.08	0.20	17.06	0.21	17.17	0.20	17.08	0.20	17.14	0.21	16.28	0.28	16.90	0.22
U2L2s	17.38	0.16	17.29	0.24	16.73	0.33	17.07	0.15	17.09	0.19	16.98	0.36	15.23	0.29	16.57	0.18
U1R2s	17.27	0.17	17.29	0.18	17.01	0.22	17.23	0.31	17.22	0.16	16.93	0.18	16.79	0.25	15.39	0.61
U1R1s	17.29	0.14	17.11	0.12	17.26	0.20	17.35	0.17	17.20	0.21	17.24	0.21	16.80	0.22	16.10	0.40
U1s	17.16	0.20	17.15	0.15	16.87	0.20	17.32	0.20	17.30	0.25	17.23	0.22	16.87	0.31	16.70	0.25
U1L1s	17.15	0.16	17.18	0.21	17.00	0.25	16.93	0.22	17.12	0.17	17.28	0.19	15.84	0.37	16.50	0.19
U1L2s	17.31	0.20	17.17	0.28	16.92	0.30	17.20	0.16	16.93	0.17	17.13	0.27	14.17	0.53	16.35	0.21
R2s	17.28	0.25	17.37	0.21	17.48	0.25	17.19	0.25	16.96	0.20	17.01	0.17	16.64	0.27	16.81	0.88
R1s	17.38	0.20	17.20	0.17	17.09	0.19	16.98	0.16	17.20	0.19	17.19	0.16	16.55	0.20	16.47	0.24
Cs	17.25	0.22	17.20	0.21	17.01	0.19	17.20	0.15	17.13	0.21	17.21	0.21	16.87	0.31	16.40	0.24
L1s	17.26	0.18	17.42	0.26	17.16	0.25	16.93	0.17	17.36	0.24	17.08	0.19	16.15	0.48	16.47	0.17
L2s	17.28	0.20	17.37	0.25	16.76	0.29	16.81	0.16	17.01	0.20	17.15	0.39	14.57	0.44	16.55	0.32
D1R2s	17.22	0.23	17.24	0.21	17.15	0.19	17.13	0.27	16.55	0.20	16.65	0.21	16.70	0.24	15.92	0.61
D1R1s	17.37	0.17	17.21	0.19	17.18	0.18	17.27	0.16	16.64	0.17	16.91	0.24	16.50	0.17	16.06	0.26
D1s	17.17	0.19	17.23	0.21	16.97	0.21	17.13	0.19	16.76	0.23	17.31	0.24	16.25	0.25	16.26	0.20
D1L1s	17.21	0.17	17.29	0.27	17.02	0.22	16.91	0.18	16.64	0.20	17.07	0.20	15.56	0.32	16.54	0.17
D1L2s	17.27	0.19	17.12	0.21	16.98	0.36	16.72	0.19	16.73	0.24	17.31	0.47	15.04	0.62	16.24	0.21
D2R2s	16.94	0.24	17.21	0.18	17.29	0.22	16.97	0.24	16.08	0.28	16.34	0.19	16.78	0.28	16.16	0.26
D2R1s	17.23	0.22	17.38	0.20	17.07	0.22	16.96	0.18	15.65	0.29	16.65	0.26	16.76	0.21	16.21	0.24
D2s	17.02	0.17	17.11	0.24	17.06	0.21	16.95	0.18	16.00	0.26	17.15	0.23	16.49	0.21	16.73	0.23
D2L1s	17.24	0.17	17.12	0.23	17.02	0.20	16.67	0.18	15.93	0.26	17.10	0.19	16.10	0.18	16.68	0.21
D2L2s	17.31	0.20	17.27	0.25	16.88	0.34	16.29	0.19	16.00	0.22	16.85	0.25	15.73	0.32	16.65	0.28

Table 5.18b. Immature rabbit endothelial cell nuclear lengths (μm) for sub-regions (100μm * 100μm) within downstream main-regions in "Zone A", where n equals the number of branches.

Immature	D1R1		D1		D1L1		D2R1		D2		D2L1	
Sub-Region	Mean	SEM	Mean	SEM	Mean	SEM	Mean	SEM	Mean	SEM	Mean	SEM
U2R2s	16.99	0.21	16.14	0.26	16.87	0.29	17.04	0.22	17.31	0.13	17.33	0.19
U2R1s	16.77	0.18	16.15	0.28	16.93	0.33	17.17	0.21	17.60	0.18	17.26	0.19
U2s	16.80	0.19	16.11	0.28	16.96	0.24	17.30	0.22	17.59	0.14	17.38	0.19
U2L1s	16.65	0.25	16.42	0.28	16.86	0.18	17.39	0.18	17.27	0.22	16.98	0.16
U2L2s	16.51	0.24	16.51	0.27	16.87	0.21	17.36	0.17	17.63	0.20	16.67	0.22
U1R2s	16.98	0.21	17.20	0.30	17.22	0.30	17.06	0.24	17.30	0.21	17.20	0.18
U1R1s	17.14	0.20	17.48	0.22	17.27	0.27	17.06	0.15	17.42	0.16	17.21	0.20
U1s	17.19	0.19	17.48	0.21	17.31	0.25	17.15	0.16	17.50	0.23	17.20	0.23
U1L1s	17.03	0.20	17.36	0.21	16.95	0.18	17.18	0.19	17.29	0.17	17.00	0.18
U1L2s	16.82	0.23	17.23	0.22	16.41	0.25	17.49	0.21	17.18	0.22	16.37	0.27
R2s	17.19	0.24	17.44	0.34	17.36	0.27	16.85	0.25	17.32	0.19	17.15	0.16
R1s	17.14	0.15	17.64	0.19	17.37	0.26	17.21	0.19	17.31	0.18	17.21	0.19
Cs	17.46	0.20	17.92	0.16	17.22	0.24	16.97	0.19	17.39	0.17	17.06	0.21
L1s	17.27	0.19	17.53	0.19	17.12	0.21	17.08	0.18	17.36	0.13	16.98	0.21
L2s	17.55	0.21	17.49	0.25	16.80	0.21	17.11	0.20	17.34	0.19	16.60	0.27
D1R2s	17.20	0.23	17.83	0.19	17.43	0.24	17.04	0.30	17.29	0.18	17.35	0.19
D1R1s	17.17	0.14	17.59	0.19	17.34	0.21	17.24	0.15	17.39	0.20	17.35	0.21
D1s	17.29	0.19	17.72	0.18	17.22	0.21	17.17	0.19	17.21	0.18	17.11	0.19
D1L1s	17.23	0.19	17.71	0.21	17.26	0.18	17.08	0.17	17.31	0.18	16.88	0.19
D1L2s	17.35	0.21	17.43	0.17	16.84	0.21	17.15	0.20	17.20	0.13	16.61	0.32
D2R2s	17.08	0.23	17.56	0.16	17.33	0.19	16.92	0.25	17.43	0.26	17.24	0.21
D2R1s	17.32	0.21	17.69	0.19	17.10	0.18	17.03	0.17	17.39	0.18	16.98	0.19
D2s	17.26	0.20	17.85	0.17	17.24	0.22	16.97	0.18	17.38	0.16	17.17	0.27
D2L1s	17.36	0.19	17.49	0.18	17.08	0.21	17.02	0.19	17.37	0.17	16.96	0.18
D2L2s	17.66	0.25	17.62	0.20	16.82	0.25	17.32	0.22	17.18	0.19	16.36	0.31

Table 5.19a. Mature rabbit endothelial cell nuclear lengths (μm) for sub-regions (100μm * 100μm) within upstream and lateral main-regions in "Zone A", where n equals the number of branches.

Mature	U2R1		U2		U2L1		U1R1		U1		U1L1		R1		L1	
Sub-Region	Mean	SEM	Mean	SEM	Mean	SEM	Mean	SEM	Mean	SEM	Mean	SEM	Mean	SEM	Mean	SEM
U2R2s	18.76	0.18	19.03	0.19	19.11	0.17	18.80	0.17	19.22	0.19	19.35	0.20	18.77	0.23	16.85	0.32
U2R1s	19.01	0.15	19.18	0.14	19.10	0.19	19.21	0.16	19.38	0.21	19.23	0.21	19.02	0.22	17.70	0.24
U2s	19.34	0.19	19.18	0.17	19.36	0.19	19.19	0.18	19.58	0.21	19.19	0.22	18.80	0.30	18.35	0.20
U2L1s	19.31	0.17	19.20	0.17	19.16	0.19	19.16	0.16	19.56	0.22	19.42	0.20	18.37	0.41	18.79	0.29
U2L2s	18.97	0.18	19.13	0.16	19.10	0.20	19.05	0.17	19.55	0.20	19.10	0.19	17.65	0.33	18.80	0.28
U1R2s	18.83	0.25	19.05	0.22	19.06	0.16	19.00	0.22	19.26	0.22	19.35	0.19	19.00	0.20	16.14	0.62
U1R1s	19.03	0.13	19.20	0.18	19.18	0.16	19.26	0.17	19.39	0.19	19.30	0.19	18.97	0.16	16.94	0.35
U1s	19.11	0.14	19.22	0.20	19.29	0.18	19.11	0.14	19.53	0.23	19.04	0.20	18.97	0.40	18.49	0.24
U1L1s	19.16	0.18	19.29	0.17	19.29	0.15	19.18	0.16	19.59	0.22	19.34	0.18	17.94	0.44	18.89	0.20
U1L2s	19.05	0.21	19.18	0.15	19.08	0.22	19.03	0.19	19.54	0.21	19.35	0.20	16.27	0.32	18.71	0.27
R2s	19.03	0.20	18.88	0.21	19.06	0.16	18.82	0.26	18.79	0.19	19.14	0.20	19.23	0.22	16.47	0.83
R1s	19.15	0.14	19.18	0.19	19.28	0.17	19.24	0.13	18.55	0.26	19.01	0.18	19.00	0.16	16.78	0.38
Cs	19.09	0.20	19.20	0.18	19.25	0.17	19.01	0.21	18.85	0.24	19.10	0.17	18.50	0.30	18.41	0.21
L1s	19.03	0.18	19.41	0.19	19.25	0.20	18.89	0.23	19.25	0.20	19.25	0.16	18.22	0.42	19.04	0.18
L2s	19.03	0.20	19.16	0.16	18.97	0.25	18.86	0.21	19.32	0.23	19.19	0.22	17.23	0.58	18.62	0.22
D1R2s	18.94	0.20	19.04	0.20	19.14	0.15	18.64	0.17	18.23	0.25	18.65	0.16	18.69	0.21	16.73	0.26
D1R1s	19.06	0.18	19.23	0.20	19.03	0.20	19.03	0.16	18.38	0.25	18.72	0.15	18.86	0.16	17.71	0.31
D1s	18.99	0.19	19.42	0.22	18.97	0.20	18.83	0.20	18.35	0.25	18.86	0.13	18.59	0.24	18.71	0.24
D1L1s	18.99	0.17	19.25	0.16	19.24	0.24	18.44	0.21	18.50	0.22	18.96	0.18	18.62	0.26	18.75	0.18
D1L2s	19.11	0.18	19.18	0.17	18.88	0.24	18.28	0.21	18.59	0.20	19.42	0.22	17.85	0.52	18.74	0.18
D2R2s	19.00	0.23	19.12	0.18	19.12	0.20	18.76	0.22	18.18	0.31	18.02	0.24	19.10	0.23	18.32	0.30
D2R1s	19.06	0.15	19.20	0.18	18.91	0.25	18.99	0.14	17.79	0.37	18.42	0.17	19.13	0.18	18.60	0.21
D2s	19.09	0.18	19.26	0.20	19.34	0.20	18.87	0.25	17.88	0.37	18.66	0.15	18.95	0.18	18.64	0.20
D2L1s	19.07	0.17	19.41	0.23	19.41	0.20	18.40	0.17	17.96	0.28	18.95	0.18	19.06	0.25	18.73	0.19
D2L2s	19.05	0.15	19.33	0.18	19.22	0.20	18.27	0.27	18.04	0.27	18.93	0.23	18.49	0.40	18.64	0.16

Table 5.19b. Mature rabbit endothelial cell nuclear lengths (μm) for sub-regions (100μm * 100μm) within downstream main-regions in "Zone A", where n equals the number of branches.

Mature	D1R1		D1		D1L1		D2R1		D2		D2L1	
Sub-Region	Mean	SEM	Mean	SEM	Mean	SEM	Mean	SEM	Mean	SEM	Mean	SEM
U2R2s	19.22	0.26	18.22	0.31	18.67	0.30	19.62	0.31	18.83	0.23	19.20	0.16
U2R1s	19.12	0.20	18.11	0.44	18.68	0.23	19.27	0.17	19.11	0.25	19.11	0.16
U2s	19.18	0.19	17.94	0.22	18.71	0.15	19.46	0.19	19.12	0.21	19.16	0.21
U2L1s	18.73	0.17	17.97	0.29	18.84	0.17	19.32	0.16	19.22	0.21	19.15	0.20
U2L2s	18.28	0.20	18.87	0.21	18.90	0.13	19.09	0.20	19.33	0.18	19.04	0.31
U1R2s	19.11	0.32	17.95	0.27	18.52	0.20	19.36	0.23	19.11	0.22	19.18	0.19
U1R1s	19.30	0.20	18.24	0.25	18.79	0.20	19.22	0.19	19.12	0.21	19.25	0.18
U1s	19.32	0.17	18.33	0.26	18.92	0.18	19.34	0.17	19.10	0.23	19.18	0.16
U1L1s	19.09	0.14	18.30	0.26	19.06	0.20	19.32	0.17	19.09	0.19	19.06	0.16
U1L2s	18.59	0.21	18.64	0.19	18.86	0.25	19.15	0.19	19.27	0.22	19.02	0.29
R2s	19.44	0.30	18.23	0.27	18.71	0.21	19.43	0.24	19.30	0.20	19.07	0.17
R1s	19.36	0.24	18.43	0.23	18.99	0.18	19.36	0.19	19.06	0.22	19.21	0.19
Cs	19.48	0.19	18.30	0.16	19.05	0.21	19.33	0.18	19.03	0.24	19.17	0.19
L1s	19.11	0.12	18.69	0.19	19.16	0.21	19.41	0.17	19.10	0.23	19.04	0.15
L2s	18.60	0.17	18.84	0.20	19.00	0.20	19.18	0.20	19.24	0.20	19.20	0.28
D1R2s	19.44	0.36	18.73	0.22	19.10	0.16	19.52	0.27	19.29	0.18	19.16	0.16
D1R1s	19.39	0.22	18.73	0.22	19.21	0.18	19.32	0.19	19.19	0.23	19.21	0.16
D1s	19.50	0.17	18.76	0.25	19.11	0.23	19.46	0.20	19.18	0.25	19.00	0.18
D1L1s	19.10	0.16	18.90	0.19	19.27	0.19	19.48	0.19	19.15	0.24	19.38	0.19
D1L2s	19.00	0.19	19.17	0.21	19.08	0.21	19.24	0.20	19.31	0.18	19.45	0.30
D2R2s	19.44	0.28	18.96	0.23	19.38	0.19	19.42	0.31	19.11	0.22	19.07	0.17
D2R1s	19.48	0.21	19.04	0.23	18.99	0.19	19.35	0.20	19.10	0.25	19.27	0.22
D2s	19.60	0.18	18.98	0.20	19.30	0.20	19.34	0.19	18.97	0.25	19.21	0.20
D2L1s	19.26	0.15	19.00	0.19	19.23	0.18	19.31	0.19	19.04	0.27	19.30	0.22
D2L2s	19.16	0.20	19.18	0.17	19.09	0.27	19.14	0.22	19.09	0.25	19.12	0.28

Tukey tests were performed on data for nuclear lengths for sub-regions in "Zone A" (Appendix B.3a-h).

5.3.3.3 "Zone B" (500μm * 500μm regions)

The lengths of the nuclei within Zone B are shown in Table 5.20. There were highly significant effects of age and region and an interaction between age and region (all $P<0.005$). Mean nuclear lengths were 16.72 ± 0.03μm (n = 1163 regions) and 19.13 ± 0.03μm (n = 1355 regions) for immature and mature rabbits respectively (a difference of 14.4%). Lengths ranged from 16.03 ± 0.23 ("U4L4", n = 16 branches) to 17.27 ± 0.14 ("U4R1", n = 34 branches) (7.7% difference) in immature rabbits, and from 18.47 ± 0.20 ("D3L4", n = 18 branches) to 19.39 ± 0.27 ("D4R2", n = 21 branches) (a 5.0% difference) in mature rabbits.

Table 5.20. Rabbit endothelial cell lengths (μm) for regions in "Zone B", where n equals the number of branches.

Region	Immature		Mature	
	Mean	SEM	Mean	SEM
U4R4	16.59	0.25	19.11	0.25
U4R3	16.83	0.21	19.09	0.24
U4R2	17.05	0.19	19.08	0.24
U4R1	17.27	0.14	19.35	0.13
U4	17.23	0.17	19.31	0.13
U4L1	17.07	0.18	19.31	0.15
U4L2	16.49	0.26	19.12	0.19
U4L3	16.22	0.26	19.19	0.18
U4L4	16.03	0.23	18.71	0.23
U3R4	16.58	0.25	19.14	0.21
U3R3	16.65	0.22	19.19	0.24
U3R2	17.07	0.18	19.01	0.26
U3R1	17.20	0.13	19.12	0.13
U3	17.16	0.16	19.23	0.12
U3L1	17.05	0.17	19.29	0.15
U3L2	16.58	0.25	19.14	0.17
U3L3	16.23	0.26	19.07	0.16
U3L4	16.10	0.24	18.73	0.19
U2R4	16.60	0.23	19.09	0.17
U2R3	16.74	0.19	19.16	0.21
U2L3	16.32	0.24	19.14	0.21
U2L4	16.16	0.28	18.77	0.21
U1R4	16.65	0.27	19.29	0.18
U1R3	16.84	0.22	19.24	0.21
U1L3	16.45	0.30	19.07	0.21
U1L4	16.12	0.27	18.68	0.24
R4	16.53	0.26	19.31	0.18
R3	16.84	0.25	19.16	0.24
L3	16.40	0.27	18.95	0.21
L4	16.08	0.28	18.67	0.24
D1R4	16.52	0.25	19.21	0.22
D1R3	16.81	0.21	19.19	0.31
D1L3	16.37	0.28	18.91	0.22
D1L4	16.19	0.33	18.58	0.23
D2R4	16.47	0.28	19.23	0.23
D2R3	16.75	0.21	19.25	0.25
D2L3	16.40	0.27	19.03	0.24
D2L4	16.21	0.37	18.48	0.20
D3R4	16.47	0.26	19.31	0.21
D3R3	16.66	0.21	19.25	0.23
D3R2	16.91	0.18	19.36	0.24
D3R1	17.05	0.13	19.34	0.16
D3	17.14	0.13	19.19	0.15
D3L1	17.04	0.13	19.27	0.14
D3L2	16.56	0.25	19.06	0.20
D3L3	16.32	0.26	18.91	0.22

D3L4	16.09	0.33	18.47	0.20
D4R4	16.43	0.25	19.26	0.24
D4R3	16.56	0.21	19.34	0.24
D4R2	16.86	0.17	19.39	0.27
D4R1	17.03	0.14	19.37	0.17
D4	17.12	0.14	19.27	0.16
D4L1	17.02	0.14	19.36	0.14
D4L2	16.48	0.21	19.03	0.20
D4L3	15.99	0.25	18.97	0.23
D4L4	16.10	0.35	18.52	0.21
Total mean	**16.72**	**0.03**	**19.13**	**0.03**

5.3.3.4 "Zone C" (500μm * 500μm regions)

The lengths of the nuclei within Zone C are shown in Table 5.21. There were highly significant effects of age and region and an interaction between age and region (all $P<0.005$). The mean lengths of nuclei in immature and mature rabbits were 16.50 ± 0.03μm (n = 1423 regions) and 19.01 ± 0.03μm (n = 1443 regions) respectively; a difference of 15.2%. Nuclear lengths were between 15.82 ± 0.32 ("U6L5", n = 12 branches) and 17.21 ± 0.17 ("U5R1", n = 33 branches) (8.8% difference) in immature rabbits, and ranged from 18.13 ± 0.41 ("D6L5", n = 5 branches) to 19.48 ± 0.23 ("U6R1", n = 20 branches) and 19.48 ± 0.21 ("D5R3", n = 20 branches) (7.4% difference).

Table 5.21. Rabbit nuclear length (μm) for regions in "Zone C", where n equals the number of branches.

Region	Immature		Mature	
	Mean	SEM	Mean	SEM
U6R6	16.09	0.37	19.06	0.29
U6R5	16.34	0.35	18.55	0.44
U6R4	16.41	0.37	18.88	0.36
U6R3	16.41	0.28	18.93	0.25
U6R2	16.52	0.22	18.92	0.22
U6R1	16.89	0.18	19.48	0.23
U6	16.85	0.20	19.28	0.22
U6L1	16.88	0.20	19.26	0.21
U6L2	16.49	0.33	19.47	0.33
U6L3	16.25	0.27	19.38	0.24
U6L4	16.18	0.36	19.25	0.25
U6L5	15.82	0.32	19.19	0.27
U6L6	16.28	0.34	19.04	0.33
U5R6	16.12	0.24	18.90	0.31
U5R5	16.14	0.25	18.93	0.25
U5R4	16.43	0.23	19.09	0.24
U5R3	16.64	0.20	18.94	0.22
U5R2	16.87	0.19	19.11	0.24
U5R1	17.21	0.17	19.22	0.17
U5	17.16	0.16	19.28	0.17
U5L1	17.09	0.18	19.24	0.16
U5L2	16.50	0.28	19.17	0.20
U5L3	16.37	0.27	19.32	0.21
U5L4	16.18	0.27	19.05	0.20
U5L5	16.26	0.29	18.91	0.25
U5L6	16.43	0.36	19.01	0.37
U4R6	16.22	0.28	18.92	0.27
U4R5	16.27	0.26	18.96	0.23
U4L5	16.15	0.27	18.70	0.19
U4L6	16.47	0.35	18.67	0.31
U3R6	16.40	0.25	19.06	0.20
U3R5	16.26	0.25	19.06	0.22
U3L5	16.08	0.28	18.70	0.20
U3L6	16.60	0.32	18.42	0.29
U2R6	16.33	0.22	18.67	0.23
U2R5	16.36	0.26	18.92	0.19
U2L5	16.12	0.29	18.45	0.17
U2L6	16.44	0.34	18.35	0.25
U1R6	16.24	0.24	18.92	0.21
U1R5	16.33	0.24	19.13	0.20
U1L5	16.37	0.36	18.68	0.17
U1L6	16.47	0.35	18.32	0.25
R6	16.29	0.24	18.91	0.20
R5	16.26	0.23	19.11	0.21
L5	16.24	0.31	18.53	0.18
L6	16.43	0.35	18.27	0.30

D1R6	16.31	0.25	18.85	0.22
D1R5	16.23	0.24	19.05	0.26
D1L5	16.33	0.32	18.65	0.21
D1L6	16.32	0.30	18.38	0.25
D2R6	16.30	0.26	18.89	0.20
D2R5	16.27	0.26	19.19	0.28
D2L5	16.22	0.33	18.48	0.18
D2L6	16.12	0.31	18.20	0.29
D3R6	16.43	0.30	18.89	0.20
D3R5	16.31	0.24	19.15	0.23
D3L5	16.38	0.37	18.49	0.24
D3L6	16.12	0.36	18.32	0.30
D4R6	16.30	0.25	19.07	0.24
D4R5	16.37	0.27	19.21	0.22
D4L5	16.40	0.40	18.59	0.25
D4L6	16.01	0.45	18.18	0.25
D5R6	16.17	0.31	19.05	0.27
D5R5	16.37	0.30	19.30	0.19
D5R4	16.44	0.29	19.41	0.29
D5R3	16.46	0.22	19.48	0.21
D5R2	16.80	0.21	19.40	0.22
D5R1	16.96	0.17	19.41	0.16
D5	17.07	0.14	19.31	0.16
D5L1	17.05	0.15	19.18	0.14
D5L2	16.54	0.26	19.04	0.27
D5L3	16.25	0.27	18.86	0.25
D5L4	16.15	0.29	18.64	0.22
D5L5	16.21	0.29	18.45	0.27
D5L6	16.19	0.39	18.25	0.24
D6R6	16.24	0.31	18.75	0.22
D6R5	16.45	0.30	19.31	0.24
D6R4	16.43	0.25	19.30	0.29
D6R3	16.59	0.28	19.46	0.26
D6R2	16.65	0.27	19.35	0.20
D6R1	16.92	0.18	19.46	0.16
D6	16.91	0.18	19.27	0.18
D6L1	16.98	0.18	19.29	0.17
D6L2	16.69	0.29	18.97	0.24
D6L3	16.28	0.29	18.98	0.30
D6L4	16.02	0.27	18.88	0.30
D6L5	16.13	0.37	18.13	0.41
D6L6	16.10	0.52	18.18	0.40
Total mean	**16.50**	**0.03**	**19.01**	**0.03**

5.3.3.5 Nuclear lengths around ostia in different parts of the descending thoracic aorta (500μm * 500μm regions)

Mean lengths for nuclei surrounding ostia within the upper portion and lower portion of the descending thoracic aorta, and ostia from the left and right hand side of this vessel are shown in Table 5.22. Data are further subdivided by the different zones around the ostia.

Data for nuclear lengths within individual regions in "Zone A" for the upper and lower portion and right and left portions of the descending thoracic aorta are shown in Table 5.23 and 5.24 respectively. Colour maps showing mean variations in nuclear length around the branch ostia at low resolution (averages per 500μm * 500μm regions) for different branch locations are shown in Figs 5.28-5.31.

Table 5.22. Rabbit endothelial cell lengths (μm) for all regions, separated by location of the branch, where n equals the number of regions.

Location of branch ostia	Region	Immature		Mature	
		Mean	SEM	Mean	SEM
Upper branch ostia	Zone A-C	16.53	0.02	18.70	0.03
	Zone A	16.87	0.05	18.73	0.06
	Zone B	16.57	0.04	18.76	0.04
	Zone C	16.32	0.04	18.63	0.04
Lower branch ostia	Zone A-C	16.87	0.03	19.46	0.02
	Zone A	17.15	0.05	19.33	0.04
	Zone B	16.92	0.04	19.53	0.03
	Zone C	16.71	0.04	19.46	0.03
Right branch ostia	Zone A-C	16.62	0.03	19.04	0.02
	Zone A	16.90	0.05	19.06	0.05
	Zone B	16.58	0.05	19.11	0.04
	Zone C	16.51	0.05	18.95	0.04
Left branch ostia	Zone A-C	16.75	0.03	19.31	0.02
	Zone A	17.11	0.05	19.16	0.05
	Zone B	16.87	0.04	19.41	0.04
	Zone C	16.49	0.04	19.31	0.03

Immature **Mature**

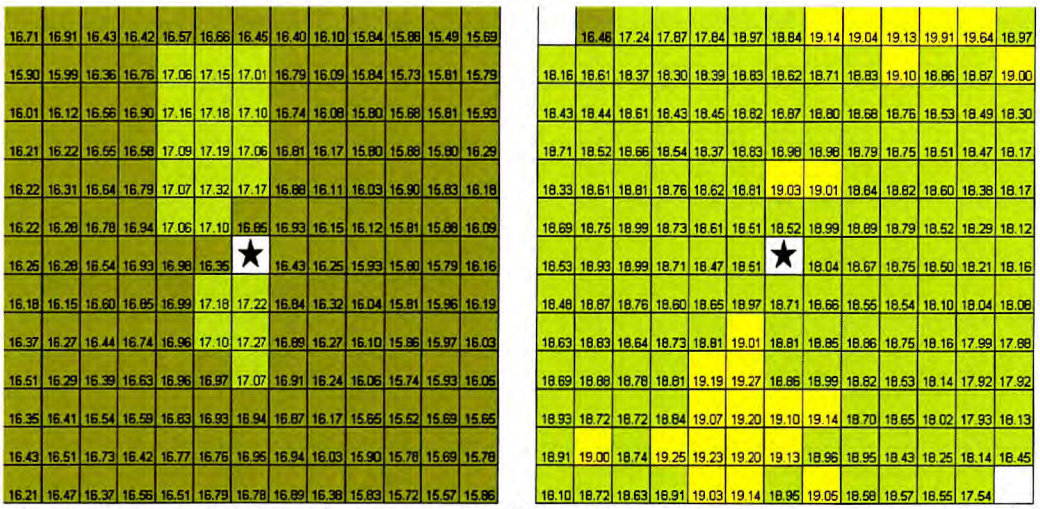

Fig. 5.28. Length (μm) of rabbit endothelial cell nuclei in the upper descending thoracic aorta. Values are averages for branches 1 to 6 (branch 1 being the first branch downstream from the aortic arch). Each square represents the average data for a 500μm*500μm region. The total area of map is 42.25mm^2. n = 4 immature rabbits, n = 4 mature rabbits. Data represent averages for 21 immature and 14 mature branches.

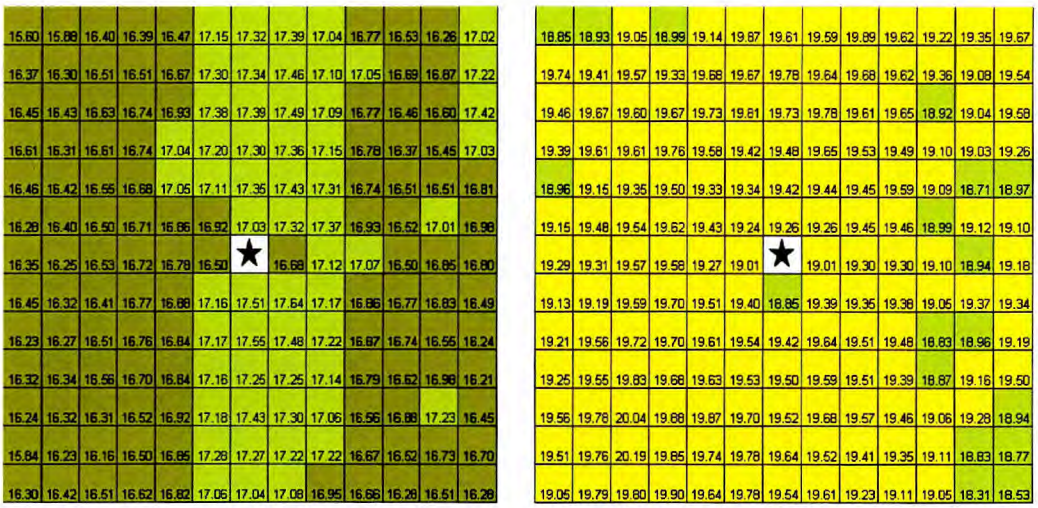

Fig. 5.29. Length (μm) of rabbit endothelial cell nuclei in the lower descending thoracic aorta. Values are averages for branches 7 to 12. Each square represents the average data for a 500μm * 500μm region. The total area of map is 42.25mm^2. n = 4 immature rabbits, n = 4 mature rabbits. Data represent averages for 15 immature and 20 mature branches.

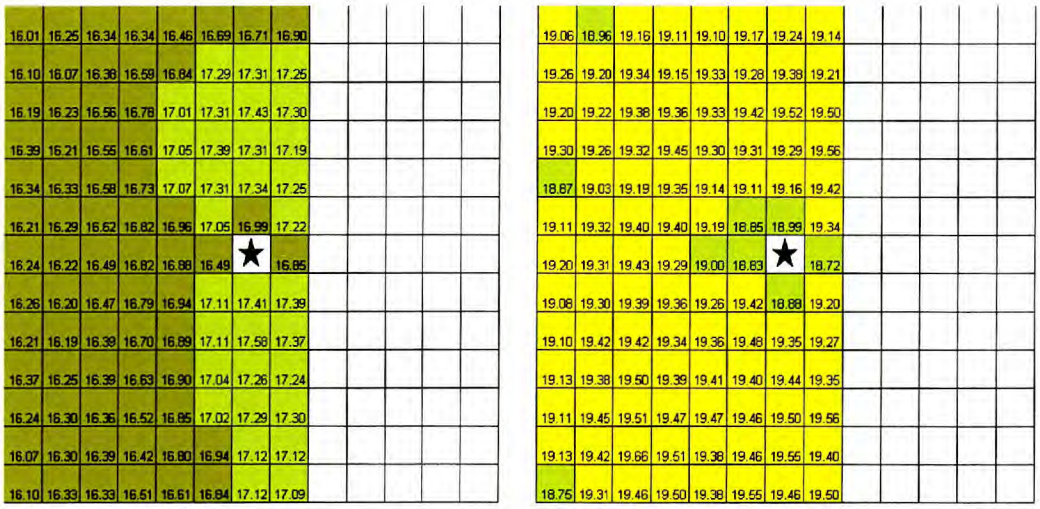

Fig. 5.30. Length (μm) of rabbit endothelial cell nuclei for branches on the anatomical right hand side of the aorta. (The map has been truncated to avoid affects of flow around ostia on the left hand side). Each square represents the average data for a 500μm*500μm region. The total area of map is 26.0mm^2. n = 4 immature rabbits, n = 4 mature rabbits. Data represent averages for 17 immature and 17 mature branches.

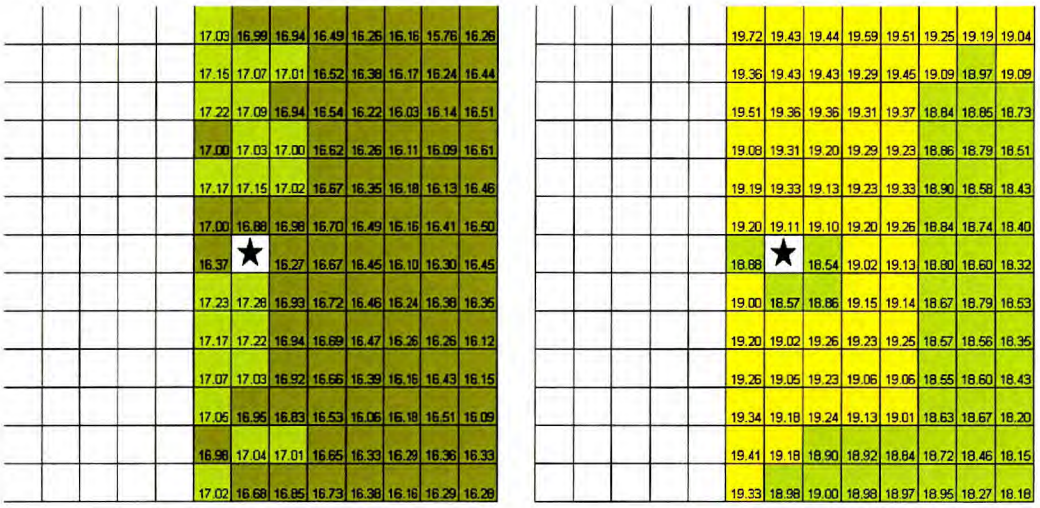

Fig. 5.31. Length (μm) of rabbit endothelial cell nuclei for branches on the anatomical left hand side of the aorta. (The map has been truncated to avoid affects of flow around ostia on the right hand side). Each square represents the average data for a 500μm * 500μm region. The total area of the map is 26.0mm^2. n = 4 immature rabbits, n = 4 mature rabbits. Data represent averages for 18 immature and 17 mature branches.

Table 5.23. Nuclear lengths (μm) for branch ostia within regions in the upper and lower portion of the descending thoracic aorta in "Zone A", where n equals the number of branches.

	UPPER AORTA				LOWER AORTA			
Region	Immature		Mature		Immature		Mature	
	Mean	SEM	Mean	SEM	Mean	SEM	Mean	SEM
U2R2	17.07	0.20	18.62	0.29	17.05	0.29	19.33	0.27
U2R1	17.32	0.18	18.81	0.22	17.11	0.19	19.34	0.18
U2	17.17	0.23	19.03	0.27	17.35	0.24	19.42	0.19
U2L1	16.88	0.24	19.01	0.26	17.43	0.19	19.44	0.17
U2L2	16.11	0.33	18.84	0.31	17.31	0.23	19.45	0.17
U1R2	17.06	0.23	18.61	0.27	16.86	0.36	19.43	0.24
U1R1	17.10	0.14	18.51	0.23	16.92	0.19	19.24	0.11
U1	16.85	0.20	18.52	0.31	17.03	0.23	19.26	0.14
U1L1	16.93	0.23	18.99	0.29	17.32	0.17	19.26	0.19
U1L2	16.15	0.31	18.89	0.34	17.37	0.28	19.45	0.18
R2	16.98	0.24	18.47	0.32	16.78	0.35	19.27	0.28
R1	16.35	0.22	18.51	0.30	16.50	0.21	19.01	0.15
L1	16.43	0.19	18.04	0.14	16.68	0.12	19.01	0.19
L2	16.25	0.28	18.67	0.34	17.12	0.27	19.30	0.19
D1R2	16.99	0.25	18.65	0.44	16.88	0.34	19.51	0.30
D1R1	17.18	0.20	18.97	0.25	17.16	0.18	19.40	0.16
D1	17.22	0.18	18.71	0.29	17.51	0.21	18.85	0.19
D1L1	16.84	0.21	18.66	0.18	17.64	0.22	19.39	0.19
D1L2	16.32	0.29	18.55	0.38	17.17	0.43	19.35	0.17
D2R2	16.96	0.27	18.81	0.38	16.84	0.34	19.61	0.26
D2R1	17.10	0.19	19.01	0.32	17.17	0.21	19.54	0.16
D2	17.27	0.15	18.81	0.36	17.55	0.22	19.42	0.20
D2L1	16.89	0.19	18.85	0.28	17.48	0.22	19.64	0.16
D2L2	16.27	0.26	18.86	0.36	17.22	0.45	19.51	0.19
Total Mean	**16.87**	**0.05**	**18.73**	**0.06**	**17.15**	**0.05**	**19.33**	**0.04**

Table 5.24. Nuclear lengths (μm) for the branch ostia on the anatomical right and left of the descending thoracic aorta, where n equals the number of branches.

	ANATOMICAL RIGHT				ANATOMICAL LEFT			
Region	Immature		Mature		Immature		Mature	
	Mean	SEM	Mean	SEM	Mean	SEM	Mean	SEM
U2R2	-	-	-	-	17.07	0.17	19.14	0.21
U2R1	17.17	0.20	19.19	0.18	17.31	0.19	19.11	0.22
U2	17.15	0.24	19.33	0.20	17.34	0.25	19.16	0.24
U2L1	17.02	0.25	19.13	0.19	17.25	0.24	19.42	0.22
U2L2	16.67	0.26	19.23	0.19	-	-	-	-
U1R2	-	-	-	-	16.96	0.21	19.19	0.19
U1R1	17.00	0.17	19.20	0.16	17.05	0.16	18.85	0.15
U1	16.88	0.24	19.11	0.23	16.99	0.20	18.99	0.20
U1L1	16.98	0.24	19.10	0.22	17.22	0.21	19.34	0.23
U1L2	16.70	0.26	19.20	0.22	-	-	-	-
R2	-	-	-	-	16.88	0.21	19.00	0.23
R1	16.37	0.24	18.88	0.23	16.49	0.21	18.83	0.16
L1	16.27	0.16	18.54	0.21	16.85	0.18	18.72	0.20
L2	16.67	0.22	19.02	0.23	-	-	-	-
D1R2	-	-	-	-	16.94	0.21	19.26	0.27
D1R1	17.23	0.21	19.00	0.18	17.11	0.19	19.42	0.22
D1	17.28	0.21	18.57	0.19	17.41	0.19	18.88	0.24
D1L1	16.93	0.27	18.86	0.19	17.39	0.20	19.20	0.25
D1L2	16.72	0.26	19.15	0.21	-	-	-	-
D2R2	-	-	-	-	16.89	0.22	19.36	0.24
D2R1	17.17	0.19	19.20	0.19	17.11	0.22	19.48	0.28
D2	17.22	0.16	19.02	0.28	17.58	0.19	19.35	0.27
D2L1	16.94	0.22	19.26	0.27	17.37	0.20	19.27	0.21
D2L2	16.69	0.25	19.23	0.24	-	-	-	-
Total Mean	**16.90**	**0.05**	**19.06**	**0.05**	**17.11**	**0.05**	**19.16**	**0.05**

5.3.3.5.1 Length of nuclei surrounding branch ostia within the upper and lower portion of the aorta

Mean nuclear lengths for immature rabbits, for ostia in the upper and lower portion of the descending thoracic aorta were 16.53 ± 0.02μm (n = 1854 regions) and 16.87 ± 0.03 (n = 1409 regions) respectively (2.1% difference) ($P<0.005$), and for mature rabbits were 18.70 ± 0.03μm (n = 1535 regions) and 19.46 ± 0.02μm (n = 1475 regions) respectively (4.1% difference) ($P<0.005$).

Nuclear lengths in regions within Zones A-C combined, in the upper portion of the descending thoracic aorta were significantly different between ages and regions and

there was a significant interaction between age and region (all P<0.005). This was the same for nuclei in the lower portion of the descending thoracic aorta (all P<0.005).

5.3.3.5.2 Length of nuclei surrounding branch ostia within the left hand and right hand side of the artery

Mean nuclear lengths surrounding ostia from the right and left side of the descending thoracic aorta, for immature rabbits, were 16.62 ± 0.03 (n = 1635 regions) and 16.75 ± 0.03 (n = 1460 regions) respectively (0.8% difference) (P<0.005), and for mature rabbits were 19.04 ± 0.02 (n = 1535 regions) and 19.31 ± 0.02 (n = 1475 regions) respectively (1.4% difference) (P<0.005).

Nuclear lengths in regions within Zones A-C combined, for ostia on the left hand side of the descending thoracic aorta were significantly different between ages and regions and there was a significant interaction between age and region (all P<0.005). This was the same for nuclei around ostia on the right hand side (all P<0.005).

5.3.4 Rabbit nuclear width

The mean nuclear widths for immature and mature rabbits for 500μm * 500μm regions in Zones A-C are shown in Fig. 5.32. There were highly significant differences in mean width between ages and regions and a highly significant interaction between age and region (age*region) (all P<0.005). Mean widths for individual rabbits are shown in Table 5.25. The mean nuclear widths were 7.02 ± 0.01μm (n = 3263 regions) and 5.95 ± 0.01μm (n = 3539 regions) for immature and mature rabbits respectively; a difference of 15.2%.

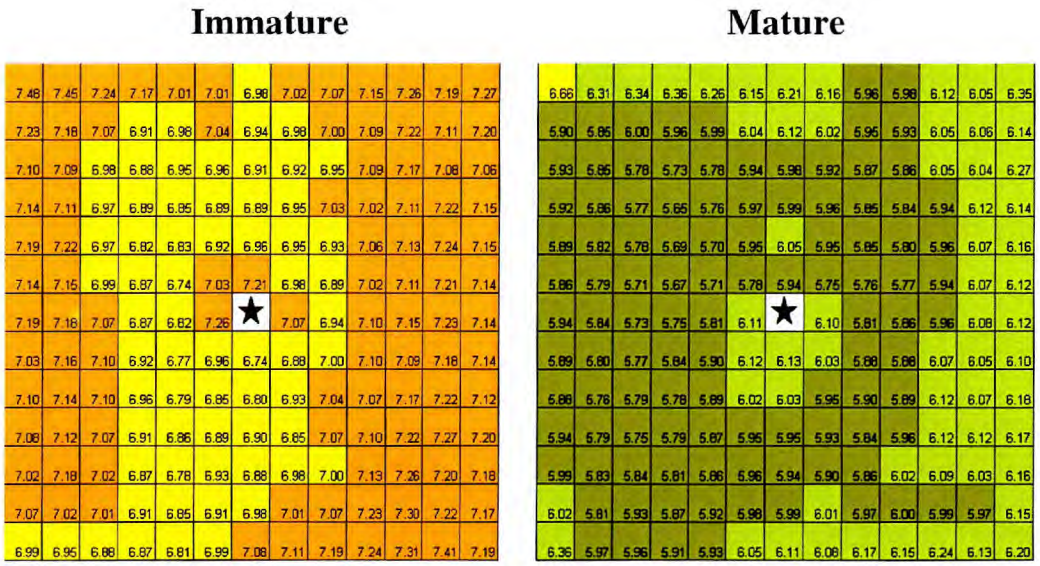

Fig. 5.32. Width (μm) of rabbit endothelial cell nuclei all branch ostia. Each square represents a 500μm * 500μm region. The total area of the map is 42.25mm^2. n = 4 immature rabbits, n = 4 mature rabbits. Data represent averages for 36 immature and 38 mature branches.

Table 5.25. Mean rabbit endothelial cell width (μm). n equals the number of regions.

Age Group	Rabbit	Width (μm)	
		Mean	SEM
Immature	I1	7.08	0.02
	I2	6.80	0.01
	I3	7.30	0.02
	I4	6.49	0.02
	All immature	7.02	0.01
Mature	M1	5.69	0.01
	M2	6.27	0.02
	M3	5.96	0.01
	M4	5.14	0.02
	All mature	5.95	0.01

5.3.4.1 "Zone A" (500μm * 500μm regions)

The mean widths of nuclei in "Zone A" are shown in Fig. 5.33. There was a highly significant effect of age and region and a highly significant interaction between age and region (all $P<0.005$).

The minimum mean width of the nuclei in immature rabbits (6.74 ± 0.13μm, "U1R2", n = 19 branches, and 6.74 ± 0.11μm, "D1", n = 34 branches) was greater than the maximum mean width of the nuclei in mature rabbits (6.13 ± 0.11μm, "D1", n = 38 branches). The ratio of the mean nuclear width upstream (7.21 ± 0.09μm, "U1", n = 36 branches) to the mean width downstream (6.74 ± 0.11μm, "D1", n = 34 branches) was 1.07 in immature rabbits, but in mature rabbits, the ratio was 0.97 ("U1": 5.94 ± 0.10μm; "D1": 6.13 ± 0.11μm – both n = 38 branches). Within Zone A, nuclear widths were generally greater immediately upstream and in the lateral regions, in immature rabbits. In mature rabbits, nuclei were wider at the lateral regions and immediately downstream of the ostia.

The significance of differences in nuclear width between individual regions for immature and mature rabbits, obtained using the Tukey test, are shown in Fig. 5.34.

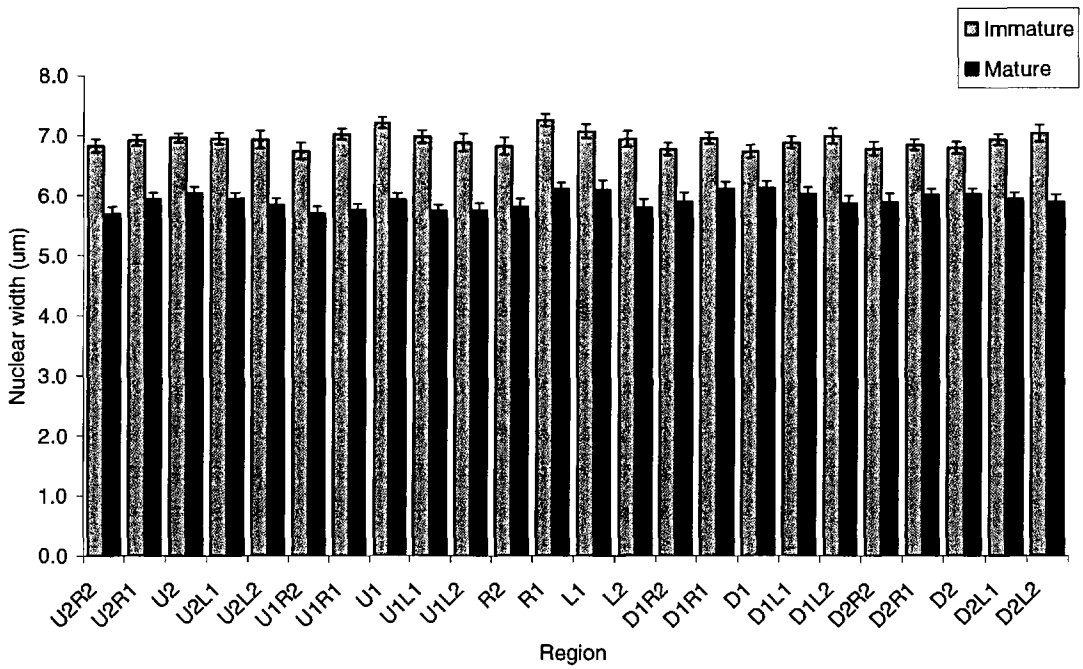

Fig. 5.33. Nuclear widths (μm) for regions within Zone A (defined in figure 5.1), in immature and mature rabbits. Bars show means ± SEM (n = number of branches).

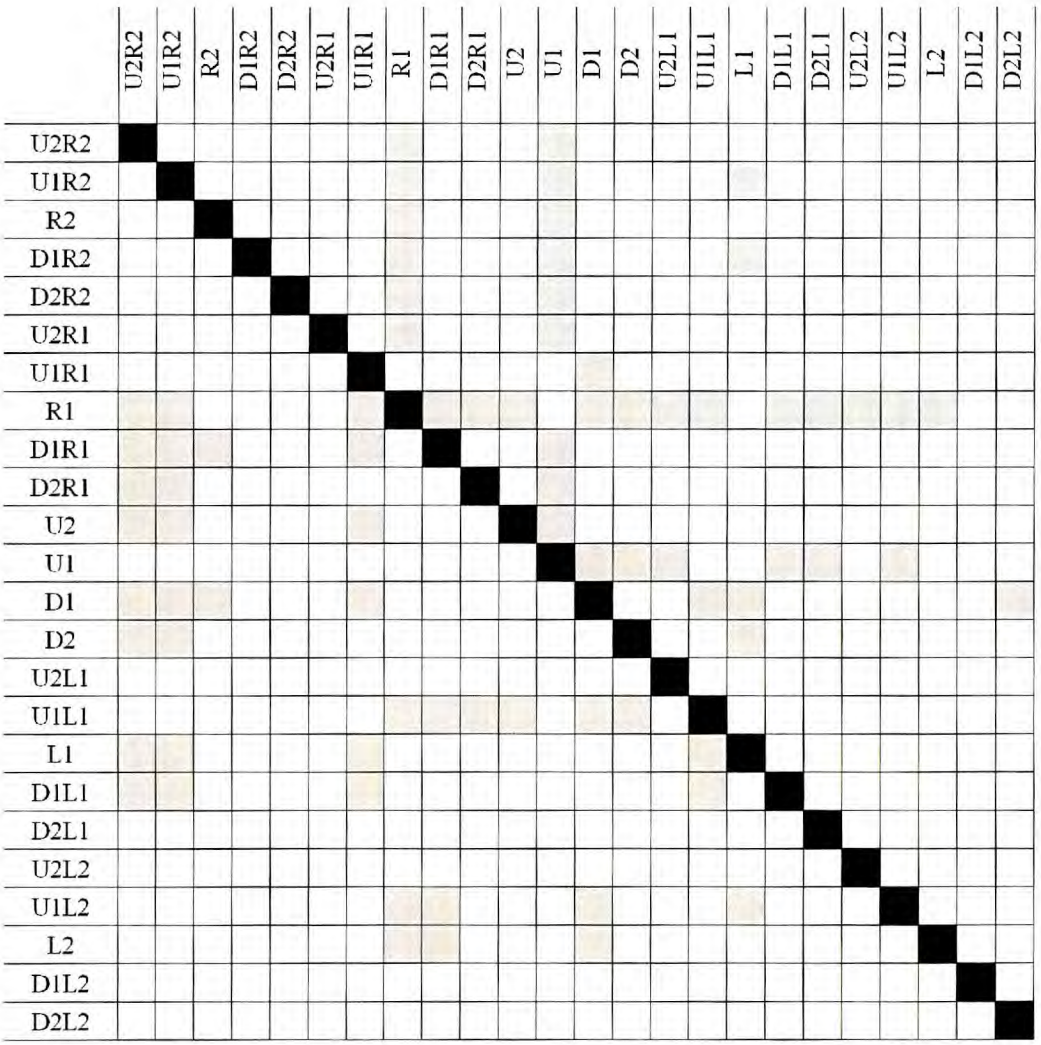

Fig. 5.34. Significance of differences in nuclear width between 500μm * 500μm regions within Zone A, determined by the Tukey test for multiple comparisons. Squares shaded in grey depict significant differences ($P<0.05$). Squares to the right of the black diagonal line indicate differences in immature rabbits. Squares to the left indicate differences in mature rabbits.

5.3.4.2 "Zone A" (100μm * 100μm sub-regions)

Data for the width of nuclei were split so that the 100μm * 100μm sub-regions in each of the 500μm * 500μm main regions nearest the branch ostia ("U2R1", "U2", "U2L1", "U1R1", "U1", "U1L1", "R1", "L1", "D1R1", "D1", "D1L1", "D2R1", "D2", "D2L1") were analysed individually rather than being combined (Fig. 5.35, Tables 5.26a,b and 5.27a,b). There were significant changes in nuclear width with age within all regions analysed ($P<0.05$), and significant effects of region for nuclei within main regions

"U1R1", "R1", "U1", "U1L1", "L1" (all P<0.005), "D1R1", "D2R1", and "D1" (P<0.05). There were significant interactions between age and region for main regions "R1", "L1" (both P<0.01), "D1" and "D1L1" (both P<0.05). In immature rabbits, in broad terms nuclei were wider upstream and at the sides of the ostia, whereas in mature rabbits they were wider downstream of the ostia, and in a region offset 500μm upstream of the branch.

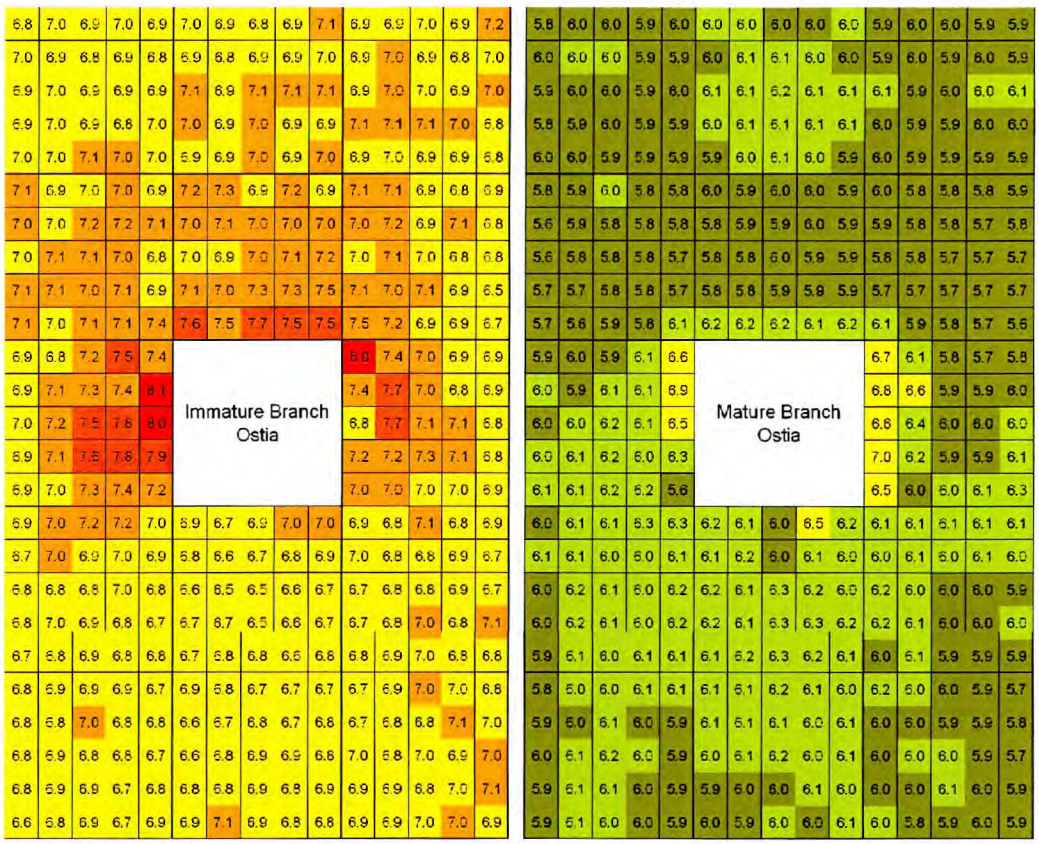

Fig. 5.35. Mean width (μm) of endothelial cell nuclei at high resolution for all branch ostia. Each square represents a 100μm * 100μm region. The total area of the map is 3.75mm^2. n = 4 immature rabbits, n = 4 mature rabbits. Data represent averages for 36 immature and 38 mature branches.

Table 5.26a. Immature rabbit endothelial cell nuclear widths (μm) for sub-regions (100μm * 100μm) within upstream and lateral main-regions in "Zone A", where n equals the number of branches.

Immature	U2R1		U2		U2L1		U1R1		U1		U1L1		R1		L1	
Sub-Region	Mean	SEM	Mean	SEM	Mean	SEM	Mean	SEM	Mean	SEM	Mean	SEM	Mean	SEM	Mean	SEM
U2R2s	6.77	0.16	6.97	0.14	6.94	0.13	7.11	0.15	7.25	0.13	7.07	0.13	6.87	0.20	8.02	0.51
U2R1s	6.96	0.13	6.87	0.13	6.93	0.13	6.91	0.13	7.27	0.13	7.13	0.11	6.81	0.13	7.36	0.25
U2s	6.91	0.15	6.79	0.11	6.95	0.14	6.95	0.10	6.94	0.09	6.95	0.15	7.17	0.17	7.02	0.18
U2L1s	7.00	0.13	6.93	0.11	6.87	0.11	7.04	0.12	7.16	0.09	6.80	0.13	7.53	0.21	6.90	0.19
U2L2s	6.85	0.13	7.13	0.15	7.19	0.26	6.90	0.12	6.92	0.12	6.93	0.24	7.37	0.21	6.86	0.23
U1R2s	6.95	0.17	6.91	0.11	6.87	0.15	7.04	0.19	7.04	0.11	7.01	0.09	6.89	0.20	7.44	0.25
U1R1s	6.92	0.11	6.79	0.10	7.01	0.12	7.00	0.12	7.14	0.12	7.18	0.12	7.11	0.17	7.68	0.31
U1s	6.84	0.14	6.94	0.11	6.89	0.10	7.19	0.13	7.01	0.10	6.93	0.14	7.34	0.15	7.00	0.19
U1L1s	6.88	0.13	6.93	0.12	6.85	0.11	7.20	0.12	7.04	0.11	7.08	0.18	7.43	0.26	6.76	0.13
U1L2s	6.81	0.12	6.95	0.09	6.97	0.24	7.10	0.14	7.05	0.12	6.79	0.19	8.12	0.69	6.86	0.17
R2s	6.93	0.19	7.09	0.13	6.88	0.14	6.99	0.25	6.97	0.14	6.98	0.13	6.99	0.13	6.82	0.21
R1s	6.98	0.15	6.86	0.13	7.02	0.14	7.09	0.13	6.92	0.12	7.08	0.15	7.22	0.16	7.73	0.33
Cs	6.87	0.12	7.06	0.11	6.96	0.11	7.14	0.11	7.02	0.13	6.95	0.15	7.52	0.19	7.12	0.17
L1s	6.88	0.12	7.11	0.11	6.87	0.10	7.00	0.12	7.13	0.13	6.80	0.17	7.77	0.23	7.09	0.16
L2s	6.93	0.13	7.09	0.10	7.04	0.19	6.84	0.09	7.18	0.11	6.79	0.22	8.03	0.45	6.79	0.20
D1R2s	6.89	0.20	7.00	0.13	7.14	0.15	7.12	0.24	7.09	0.15	7.08	0.12	6.90	0.16	7.21	0.23
D1R1s	6.96	0.12	6.93	0.12	7.08	0.17	7.08	0.13	7.04	0.11	7.02	0.15	7.14	0.12	7.21	0.21
D1s	6.86	0.12	7.01	0.11	7.06	0.13	7.05	0.14	7.26	0.18	7.07	0.17	7.59	0.17	7.32	0.18
D1L1s	6.77	0.11	6.86	0.08	7.02	0.15	7.06	0.13	7.30	0.15	6.94	0.19	7.78	0.24	7.09	0.19
D1L2s	6.97	0.10	6.86	0.11	6.82	0.19	6.89	0.12	7.48	0.28	6.55	0.20	7.90	0.61	6.79	0.17
D2R2s	6.97	0.17	6.93	0.11	6.91	0.12	7.09	0.22	7.56	0.25	7.48	0.26	6.94	0.14	7.01	0.20
D2R1s	6.98	0.16	6.86	0.11	6.99	0.15	6.98	0.15	7.48	0.21	7.18	0.26	6.99	0.12	7.04	0.17
D2s	7.07	0.14	7.03	0.11	6.91	0.13	7.12	0.14	7.70	0.22	6.92	0.17	7.26	0.12	7.00	0.12
D2L1s	7.03	0.12	6.93	0.12	6.92	0.16	7.10	0.13	7.52	0.19	6.88	0.14	7.37	0.20	6.96	0.13
D2L2s	6.99	0.14	7.01	0.14	6.78	0.16	7.43	0.19	7.52	0.16	6.68	0.17	7.18	0.29	6.89	0.15

Table 5.26b. Immature rabbit endothelial cell nuclear widths (μm) for sub-regions (100μm * 100μm) within downstream main-regions in "Zone A", where n equals the number of branches.

Immature	D1R1		D1		D1L1		D2R1		D2		D2L1	
Sub-Region	Mean	SEM	Mean	SEM	Mean	SEM	Mean	SEM	Mean	SEM	Mean	SEM
U2R2s	6.89	0.17	6.90	0.23	6.92	0.16	6.77	0.14	6.85	0.15	6.69	0.13
U2R1s	7.01	0.13	6.67	0.14	6.84	0.16	6.86	0.11	6.83	0.15	6.92	0.14
U2s	7.25	0.14	6.94	0.16	7.08	0.17	6.91	0.11	6.72	0.13	7.01	0.11
U2L1s	7.23	0.16	7.04	0.19	6.82	0.14	6.93	0.18	6.68	0.16	6.96	0.13
U2L2s	7.00	0.14	7.01	0.15	6.88	0.19	6.72	0.14	6.72	0.14	6.84	0.17
U1R2s	6.66	0.14	6.83	0.17	6.99	0.17	6.81	0.15	6.64	0.13	6.75	0.16
U1R1s	7.03	0.13	6.59	0.15	6.84	0.13	6.81	0.09	6.73	0.12	6.83	0.10
U1s	6.93	0.14	6.72	0.16	6.75	0.09	7.02	0.13	6.78	0.14	6.82	0.13
U1L1s	7.00	0.14	6.77	0.17	6.89	0.12	6.80	0.13	6.75	0.12	7.06	0.13
U1L2s	6.89	0.14	6.89	0.16	6.71	0.16	6.78	0.13	6.76	0.14	6.97	0.21
R2s	6.81	0.14	6.59	0.26	6.67	0.14	6.81	0.14	6.56	0.15	7.00	0.16
R1s	6.79	0.11	6.54	0.14	6.79	0.11	6.93	0.11	6.83	0.14	6.83	0.12
Cs	6.85	0.13	6.52	0.16	6.84	0.13	6.82	0.11	6.88	0.14	6.99	0.13
L1s	6.98	0.15	6.59	0.13	6.88	0.12	6.80	0.15	6.86	0.16	6.91	0.12
L2s	6.81	0.15	6.74	0.14	6.67	0.14	6.66	0.11	6.82	0.14	7.00	0.22
D1R2s	6.76	0.14	6.73	0.17	6.73	0.13	6.76	0.11	6.75	0.15	6.94	0.12
D1R1s	6.98	0.13	6.70	0.16	6.82	0.11	6.92	0.11	6.80	0.14	6.89	0.11
D1s	6.89	0.13	6.52	0.12	7.00	0.14	6.88	0.10	6.90	0.15	6.85	0.14
D1L1s	6.77	0.12	6.65	0.14	6.77	0.11	6.74	0.11	6.80	0.12	6.97	0.15
D1L2s	6.72	0.14	6.67	0.11	7.10	0.29	6.76	0.14	6.90	0.13	7.14	0.20
D2R2s	6.71	0.18	6.71	0.16	6.84	0.14	6.64	0.13	6.86	0.15	6.93	0.14
D2R1s	6.84	0.09	6.84	0.15	6.89	0.12	6.79	0.12	7.06	0.14	6.94	0.13
D2s	6.87	0.13	6.79	0.11	6.95	0.17	6.95	0.10	6.91	0.14	6.98	0.13
D2L1s	6.78	0.12	6.55	0.12	6.80	0.12	6.73	0.10	6.76	0.12	7.01	0.13
D2L2s	6.78	0.18	6.78	0.15	6.80	0.17	6.91	0.15	6.81	0.13	6.87	0.20

Table 5.27a. Mature rabbit endothelial cell nuclear widths (μm) for sub-regions (100μm * 100μm) within upstream and lateral main-regions in "Zone A", where n equals the number of branches.

Mature	U2R1		U2		U2L1		U1R1		U1		U1L1		R1		L1	
Sub-Region	Mean	SEM	Mean	SEM	Mean	SEM	Mean	SEM	Mean	SEM	Mean	SEM	Mean	SEM	Mean	SEM
U2R2s	5.79	0.15	6.01	0.13	5.95	0.12	5.81	0.12	5.95	0.12	6.00	0.13	5.90	0.18	6.75	0.30
U2R1s	5.98	0.10	6.02	0.10	6.00	0.12	5.90	0.13	5.95	0.12	5.83	0.12	5.96	0.16	6.07	0.17
U2s	5.99	0.11	5.97	0.10	5.98	0.11	6.00	0.11	5.96	0.11	5.75	0.10	5.91	0.13	5.80	0.12
U2L1s	5.93	0.11	6.00	0.11	5.88	0.09	5.81	0.13	5.96	0.13	5.78	0.11	6.15	0.16	5.74	0.11
U2L2s	5.99	0.13	6.03	0.11	5.94	0.16	5.84	0.12	5.92	0.14	5.89	0.14	6.59	0.22	5.82	0.13
U1R2s	6.00	0.17	5.98	0.13	5.87	0.16	5.61	0.13	5.85	0.11	5.92	0.12	6.00	0.19	6.83	0.36
U1R1s	6.03	0.10	6.06	0.12	5.99	0.11	5.86	0.12	5.91	0.12	5.81	0.12	5.93	0.12	6.62	0.32
U1s	6.03	0.11	6.13	0.10	5.94	0.10	5.82	0.11	5.94	0.13	5.83	0.11	6.07	0.14	5.89	0.12
U1L1s	5.89	0.11	6.01	0.10	5.99	0.09	5.79	0.12	5.99	0.12	5.75	0.11	6.13	0.19	5.87	0.11
U1L2s	5.91	0.12	5.99	0.12	5.91	0.14	5.82	0.12	5.94	0.13	5.77	0.16	6.91	0.30	5.98	0.19
R2s	5.92	0.15	6.08	0.12	6.05	0.14	5.63	0.12	5.83	0.12	5.82	0.13	5.99	0.20	6.63	0.77
R1s	5.97	0.11	6.14	0.12	5.95	0.11	5.77	0.12	5.84	0.13	5.79	0.13	6.05	0.12	6.43	0.34
Cs	5.98	0.13	6.18	0.12	5.97	0.10	5.78	0.11	5.96	0.11	5.71	0.13	6.16	0.20	5.96	0.14
L1s	5.93	0.12	6.08	0.12	6.02	0.10	5.77	0.11	5.88	0.13	5.68	0.10	6.07	0.25	5.99	0.12
L2s	5.97	0.13	6.11	0.11	6.06	0.14	5.75	0.12	5.90	0.14	5.71	0.16	6.53	0.37	6.02	0.17
D1R2s	5.79	0.12	6.02	0.12	5.99	0.13	5.65	0.12	5.79	0.11	5.66	0.13	6.04	0.20	6.98	0.43
D1R1s	5.93	0.12	6.09	0.12	5.89	0.11	5.71	0.11	5.83	0.13	5.70	0.13	6.08	0.13	6.18	0.26
D1s	5.96	0.13	6.09	0.12	5.89	0.11	5.76	0.13	5.87	0.13	5.71	0.13	6.16	0.14	5.88	0.11
D1L1s	5.94	0.12	6.07	0.12	5.98	0.12	5.76	0.11	5.88	0.13	5.71	0.10	6.04	0.19	5.95	0.15
D1L2s	5.87	0.12	6.08	0.14	5.95	0.16	5.73	0.11	5.89	0.13	5.71	0.15	6.32	0.69	6.08	0.20
D2R2s	5.95	0.13	5.94	0.12	5.98	0.13	5.74	0.16	6.22	0.20	6.12	0.14	6.12	0.19	6.54	0.35
D2R1s	5.96	0.13	6.02	0.12	5.91	0.14	5.63	0.11	6.19	0.18	5.93	0.13	6.15	0.13	5.99	0.16
D2s	5.94	0.13	6.11	0.12	5.87	0.12	5.90	0.14	6.24	0.21	5.79	0.13	6.18	0.13	6.05	0.12
D2L1s	5.85	0.13	6.01	0.13	5.90	0.12	5.82	0.14	6.15	0.22	5.66	0.11	6.18	0.15	6.06	0.13
D2L2s	5.87	0.12	5.94	0.14	5.87	0.16	6.08	0.18	6.18	0.18	5.61	0.13	5.55	0.36	6.32	0.27

Table 5.27b. Mature rabbit endothelial cell nuclear widths for sub-regions (100μm * 100μm) within downstream main-regions in "Zone A", where n equals the number of branches.

Mature	D1R1		D1		D1L1		D2R1		D2		D2L1	
Sub-Region	Mean	SEM	Mean	SEM	Mean	SEM	Mean	SEM	Mean	SEM	Mean	SEM
U2R2s	5.99	0.18	6.15	0.21	6.09	0.17	5.81	0.16	6.10	0.12	6.16	0.12
U2R1s	6.13	0.11	6.15	0.20	6.06	0.14	6.01	0.13	6.13	0.12	6.00	0.12
U2s	6.13	0.12	5.99	0.26	6.06	0.12	6.02	0.12	6.19	0.12	5.96	0.10
U2L1s	6.30	0.14	6.50	0.28	6.07	0.14	6.07	0.12	6.13	0.12	5.91	0.11
U2L2s	6.30	0.17	6.24	0.18	6.06	0.17	6.09	0.13	6.04	0.14	5.70	0.17
U1R2s	6.05	0.18	6.14	0.17	6.04	0.14	5.90	0.16	6.06	0.10	6.00	0.11
U1R1s	6.12	0.12	6.18	0.15	6.05	0.14	5.97	0.12	6.12	0.12	5.98	0.12
U1s	6.04	0.12	6.00	0.16	6.02	0.12	6.06	0.13	6.09	0.11	5.93	0.10
U1L1s	6.04	0.13	6.13	0.15	6.06	0.13	5.98	0.11	6.00	0.12	5.89	0.11
U1L2s	6.06	0.16	6.03	0.13	6.03	0.14	5.90	0.10	6.06	0.11	5.76	0.15
R2s	5.97	0.18	6.17	0.12	6.16	0.14	5.95	0.18	6.00	0.10	5.99	0.11
R1s	6.16	0.13	6.12	0.13	6.04	0.13	6.06	0.12	6.09	0.13	6.01	0.10
Cs	6.08	0.12	6.31	0.14	5.97	0.11	6.15	0.11	6.17	0.12	6.03	0.11
L1s	6.04	0.12	6.20	0.14	5.98	0.11	6.00	0.10	6.03	0.12	5.93	0.12
L2s	6.19	0.14	6.02	0.14	5.94	0.15	5.94	0.10	6.14	0.12	5.71	0.15
D1R2s	5.98	0.19	6.19	0.13	6.17	0.12	5.94	0.18	5.90	0.10	5.99	0.11
D1R1s	6.17	0.13	6.09	0.13	6.07	0.11	6.10	0.13	5.97	0.11	5.98	0.10
D1s	6.10	0.13	6.30	0.14	5.99	0.13	6.11	0.11	6.00	0.11	6.07	0.12
D1L1s	6.03	0.13	6.31	0.13	5.96	0.12	5.96	0.11	6.06	0.11	5.98	0.13
D1L2s	6.17	0.13	6.20	0.12	6.03	0.16	5.89	0.10	6.04	0.10	5.86	0.14
D2R2s	5.93	0.17	6.12	0.12	5.99	0.13	5.87	0.16	5.96	0.09	6.00	0.10
D2R1s	6.13	0.13	6.24	0.13	6.11	0.11	6.07	0.13	5.92	0.10	5.84	0.11
D2s	6.04	0.12	6.26	0.13	5.93	0.11	6.02	0.11	6.04	0.13	5.89	0.12
D2L1s	6.09	0.12	6.22	0.13	5.92	0.11	5.99	0.11	5.96	0.12	6.00	0.12
D2L2s	6.08	0.14	6.08	0.12	5.91	0.17	5.90	0.10	6.07	0.11	5.86	0.14

Tukey tests were performed on data for nuclear widths for sub-regions in "zone A". A matrix of the significant interactions between sub-regions, for each main region is shown in the Appendices (Appendix B.4a-f).

5.3.4.3 "Zone B" (500μm * 500μm regions)

The width of the nuclei within Zone B are shown in Table 5.28. Effects of age, region and the interaction between age and region were highly significant (all $P<0.005$). Mean values for immature and mature rabbits were 6.98 ± 0.02μm (n = 1163 regions) and 5.88 ± 0.01μm (n = 1355 regions) respectively; a 15.8% difference. Widths ranged from 6.82 ± 0.10μm ("U2R3", n = 19 branches) to 7.26 ± 0.15μm ("D4L4", n = 14 branches) (a 6.5% difference) in immature rabbits, and from 5.65 ± 0.12μm ("U3R3", n = 21 branches) to 6.12 ± 0.12μm ("D3L4", n = 18 branches) (an 8.3% difference) in mature.

Table 5.28. Rabbit endothelial cell nuclear widths (μm) for regions in "Zone B", where n equals the number of branches.

Region	Immature		Mature	
	Mean	SEM	Mean	SEM
U4R4	6.98	0.15	5.78	0.13
U4R3	6.88	0.13	5.73	0.13
U4R2	6.95	0.14	5.78	0.13
U4R1	6.96	0.10	5.94	0.09
U4	6.91	0.09	5.98	0.09
U4L1	6.92	0.10	5.92	0.09
U4L2	6.95	0.13	5.87	0.12
U4L3	7.09	0.15	5.86	0.11
U4L4	7.17	0.17	6.05	0.14
U3R4	6.97	0.13	5.77	0.13
U3R3	6.89	0.12	5.65	0.12
U3R2	6.85	0.12	5.76	0.13
U3R1	6.89	0.09	5.97	0.09
U3	6.89	0.09	5.99	0.09
U3L1	6.95	0.10	5.96	0.09
U3L2	7.03	0.17	5.85	0.12
U3L3	7.02	0.15	5.84	0.11
U3L4	7.11	0.17	5.94	0.11
U2R4	6.97	0.13	5.78	0.13
U2R3	6.82	0.10	5.69	0.11
U2L3	7.06	0.14	5.80	0.12
U2L4	7.13	0.16	5.96	0.12
U1R4	6.99	0.14	5.71	0.12
U1R3	6.87	0.13	5.67	0.12
U1L3	7.02	0.11	5.77	0.12
U1L4	7.11	0.18	5.94	0.12
R4	7.07	0.12	5.73	0.12
R3	6.87	0.12	5.75	0.14
L3	7.10	0.16	5.86	0.13
L4	7.15	0.22	5.96	0.11
D1R4	7.10	0.14	5.77	0.11
D1R3	6.92	0.12	5.84	0.13
D1L3	7.10	0.15	5.88	0.13
D1L4	7.09	0.20	6.07	0.10
D2R4	7.10	0.14	5.79	0.11
D2R3	6.96	0.13	5.78	0.13
D2L3	7.07	0.14	5.89	0.11
D2L4	7.17	0.15	6.12	0.12
D3R4	7.07	0.13	5.75	0.10
D3R3	6.91	0.12	5.79	0.13
D3R2	6.86	0.13	5.87	0.14
D3R1	6.89	0.09	5.95	0.10
D3	6.90	0.10	5.95	0.09
D3L1	6.85	0.10	5.93	0.10
D3L2	7.07	0.17	5.84	0.12
D3L3	7.10	0.16	5.96	0.11

D3L4	7.22	0.18	6.12	0.12
D4R4	7.02	0.14	5.84	0.13
D4R3	6.87	0.14	5.81	0.13
D4R2	6.78	0.13	5.86	0.13
D4R1	6.93	0.09	5.96	0.09
D4	6.88	0.09	5.94	0.08
D4L1	6.98	0.10	5.90	0.08
D4L2	7.00	0.17	5.86	0.09
D4L3	7.13	0.15	6.02	0.10
D4L4	7.26	0.15	6.09	0.11
Total mean	**6.98**	**0.02**	**5.88**	**0.01**

5.3.4.4 "Zone C" (500μm * 500μm regions)

The width of the nuclei within Zone C are shown in Table 5.29. Effects of age, region and the interaction between age and region were highly significant (all $P<0.005$). Mean values for immature and mature rabbits were 7.10 ± 0.02μm (n = 1423 regions) and 6.01 ± 0.01μm (n = 1443 regions) respectively; a 15.4% difference. Nuclear widths in immature rabbits were between 6.81 ± 0.18μm ("D6R2", n = 13 branches) and 7.48 ± 0.21μm ("U6R6", n = 9 branches) (a 9.8% difference), and between 5.76 ± 0.11μm ("D2R5", n = 19 branches) and 6.66 ± 0.32μm ("U6R6", n = 4 branches) (a 15.7% difference) in mature.

Table 5.29. Rabbit endothelial cell nuclear widths (μm) for regions in "Zone C", where n equals the number of branches.

Region	Immature		Mature	
	Mean	SEM	Mean	SEM
U6R6	7.48	0.21	6.66	0.32
U6R5	7.45	0.22	6.31	0.26
U6R4	7.24	0.19	6.34	0.25
U6R3	7.17	0.17	6.36	0.24
U6R2	7.01	0.12	6.26	0.24
U6R1	7.01	0.09	6.15	0.13
U6	6.98	0.10	6.21	0.14
U6L1	7.02	0.11	6.16	0.14
U6L2	7.07	0.14	5.96	0.14
U6L3	7.15	0.14	5.98	0.13
U6L4	7.26	0.14	6.12	0.17
U6L5	7.19	0.17	6.05	0.13
U6L6	7.27	0.19	6.35	0.20
U5R6	7.23	0.13	5.90	0.21
U5R5	7.18	0.14	5.85	0.18
U5R4	7.07	0.16	6.00	0.13
U5R3	6.91	0.15	5.96	0.14
U5R2	6.98	0.14	5.99	0.13
U5R1	7.04	0.09	6.04	0.09
U5	6.94	0.09	6.12	0.09
U5L1	6.98	0.11	6.02	0.09
U5L2	7.00	0.12	5.95	0.11
U5L3	7.09	0.14	5.93	0.11
U5L4	7.22	0.17	6.05	0.13
U5L5	7.11	0.15	6.06	0.11
U5L6	7.20	0.19	6.14	0.16
U4R6	7.10	0.15	5.93	0.21
U4R5	7.09	0.14	5.85	0.15
U4L5	7.08	0.15	6.04	0.14
U4L6	7.06	0.25	6.27	0.17
U3R6	7.14	0.12	5.92	0.17
U3R5	7.11	0.12	5.86	0.13
U3L5	7.22	0.19	6.12	0.14
U3L6	7.15	0.23	6.14	0.17
U2R6	7.19	0.13	5.89	0.14
U2R5	7.22	0.13	5.82	0.13
U2L5	7.24	0.17	6.07	0.14
U2L6	7.15	0.19	6.16	0.18
U1R6	7.14	0.14	5.86	0.18
U1R5	7.15	0.14	5.79	0.12
U1L5	7.21	0.16	6.07	0.13
U1L6	7.14	0.19	6.12	0.17
R6	7.19	0.14	5.94	0.17
R5	7.18	0.11	5.84	0.12
L5	7.23	0.18	6.08	0.11
L6	7.14	0.20	6.12	0.16

D1R6	7.03	0.12	5.89	0.15
D1R5	7.16	0.13	5.80	0.12
D1L5	7.18	0.18	6.05	0.11
D1L6	7.14	0.21	6.10	0.19
D2R6	7.10	0.12	5.88	0.16
D2R5	7.14	0.13	5.76	0.11
D2L5	7.22	0.16	6.07	0.11
D2L6	7.12	0.21	6.18	0.18
D3R6	7.08	0.13	5.94	0.16
D3R5	7.12	0.12	5.79	0.11
D3L5	7.27	0.17	6.12	0.13
D3L6	7.20	0.23	6.17	0.17
D4R6	7.02	0.11	5.99	0.14
D4R5	7.18	0.15	5.83	0.12
D4L5	7.20	0.18	6.03	0.11
D4L6	7.18	0.19	6.16	0.16
D5R6	7.07	0.14	6.02	0.14
D5R5	7.02	0.16	5.81	0.11
D5R4	7.01	0.15	5.93	0.13
D5R3	6.91	0.15	5.87	0.14
D5R2	6.85	0.16	5.92	0.14
D5R1	6.91	0.09	5.98	0.09
D5	6.98	0.10	5.99	0.09
D5L1	7.01	0.10	6.01	0.08
D5L2	7.07	0.21	5.97	0.11
D5L3	7.23	0.17	6.00	0.11
D5L4	7.30	0.19	5.99	0.11
D5L5	7.22	0.18	5.97	0.14
D5L6	7.17	0.22	6.15	0.19
D6R6	6.99	0.12	6.36	0.28
D6R5	6.95	0.17	5.97	0.14
D6R4	6.88	0.15	5.96	0.15
D6R3	6.87	0.20	5.91	0.15
D6R2	6.81	0.18	5.93	0.13
D6R1	6.99	0.14	6.05	0.08
D6	7.08	0.13	6.11	0.09
D6L1	7.11	0.13	6.08	0.08
D6L2	7.19	0.26	6.17	0.10
D6L3	7.24	0.23	6.15	0.13
D6L4	7.31	0.22	6.24	0.11
D6L5	7.41	0.21	6.13	0.14
D6L6	7.19	0.21	6.20	0.16
Total mean	**7.10**	**0.02**	**6.01**	**0.01**

5.3.4.5 Nuclear widths for different locations of branch ostia

Mean widths for nuclei surrounding ostia within the upper portion and lower portion of the descending thoracic aorta, and ostia from the left and right hand side of the vessel are shown in Table 5.30. Data are further subdivided according to the different zones around the ostia.

Data for nuclear widths within individual main regions in "Zone A" for the upper and lower portion and right and left portions of the descending thoracic aorta are shown in Table 5.31 and 5.32 respectively. Colour maps showing mean variations in nuclear width around the branch ostia at low resolution (averages per 500μm * 500μm regions) for different branch ostial locations are shown in Fig. 5.36-5.39.

Table 5.30. Rabbit endothelial cell nuclear widths (μm) for all regions, results separated by location of the branch ostia, where n equals the number of regions.

Location of branch ostia	Region	Immature		Mature	
		Mean	SEM	Mean	SEM
Upper branch ostia	Zone A-C	6.82	0.01	5.56	0.01
	Zone A	6.73	0.03	5.51	0.03
	Zone B	6.78	0.02	5.53	0.02
	Zone C	6.91	0.02	5.62	0.02
Lower branch ostia	Zone A-C	7.28	0.01	6.08	0.01
	Zone A	7.26	0.03	6.11	0.03
	Zone B	7.25	0.02	6.01	0.02
	Zone C	7.32	0.02	6.13	0.02
Right branch ostia	Zone A-C	7.06	0.02	6.07	0.01
	Zone A	6.96	0.03	6.02	0.03
	Zone B	7.02	0.03	6.02	0.02
	Zone C	7.14	0.03	6.16	0.02
Left branch ostia	Zone A-C	6.99	0.01	6.00	0.02
	Zone A	6.93	0.03	6.03	0.04
	Zone B	6.93	0.02	5.92	0.02
	Zone C	7.06	0.02	6.05	0.02

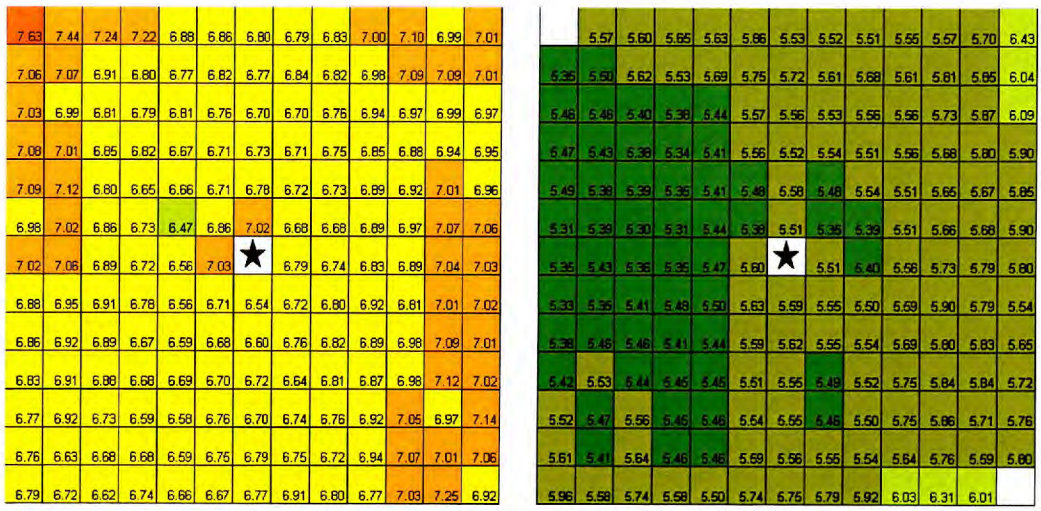

Fig. 5.36. Width (μm) of rabbit endothelial cell nuclei for branches within the upper portion of the descending thoracic aorta (branches 1 to 6, branch 1 being the first branch downstream from the aortic arch). Each square represents a 500μm * 500μm region. The total area of the map is 42.25mm^2. n = 4 immature rabbits, n = 4 mature rabbits. Data represent averages for 21 immature and 14 mature branches.

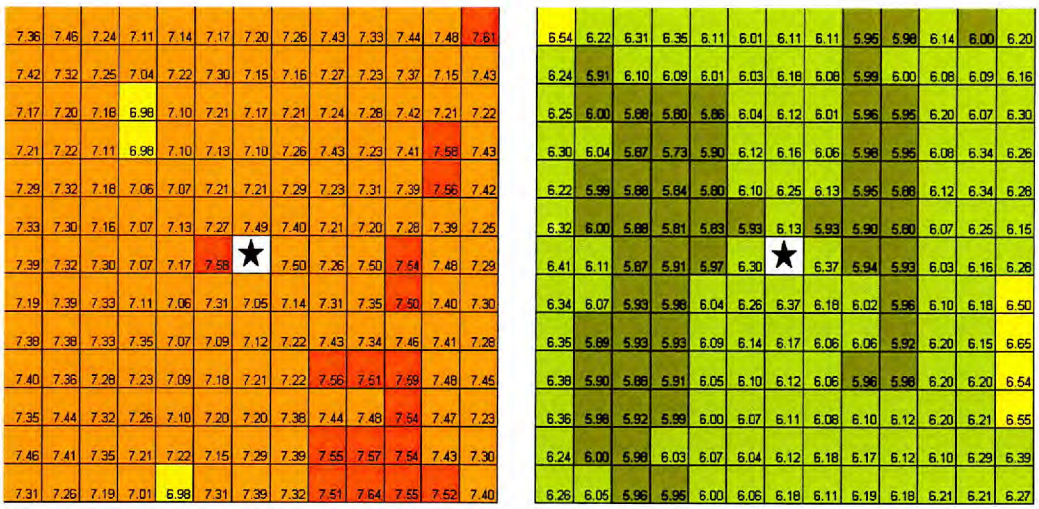

Fig. 5.37. Width (μm) of rabbit endothelial cell nuclei for branches within the lower portion of the descending thoracic aorta (branches 7 to 12). Each square represents a 500μm * 500μm region. The total area of the map is 42.25mm^2. n = 4 immature rabbits, n = 4 mature rabbits. Data represent the means for 15 immature and 20 mature branches.

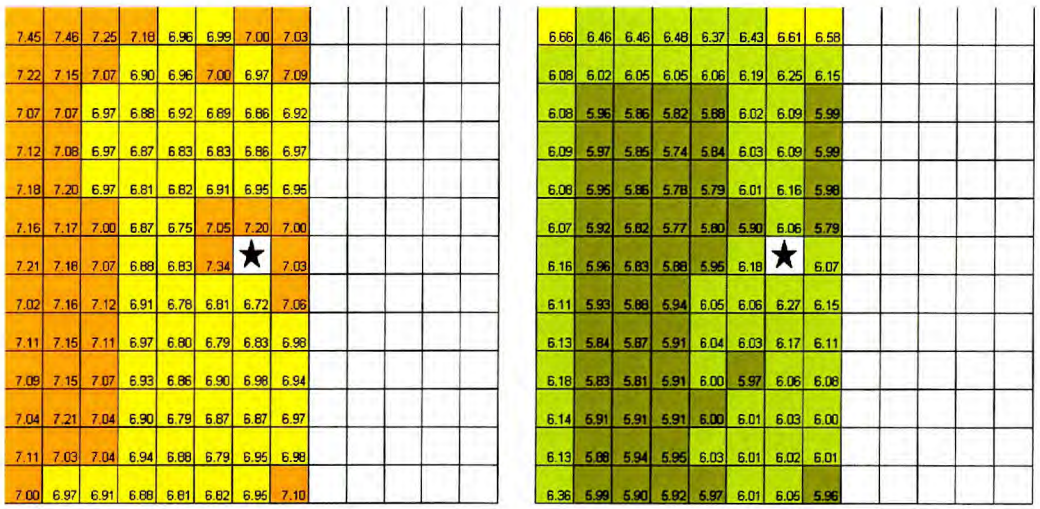

Fig. 5.38. Width (μm) of rabbit endothelial cell nuclei for branches in the anatomical right hand side of the descending thoracic aorta. (The maps are truncated to avoid effects of flow around ostia on the left hand side). Each square represents a 500μm * 500μm region. The total area of the map is 26.0mm^2. n = 4 immature rabbits, n = 4 mature rabbits. Data represent averages for 17 immature and 17 mature branches.

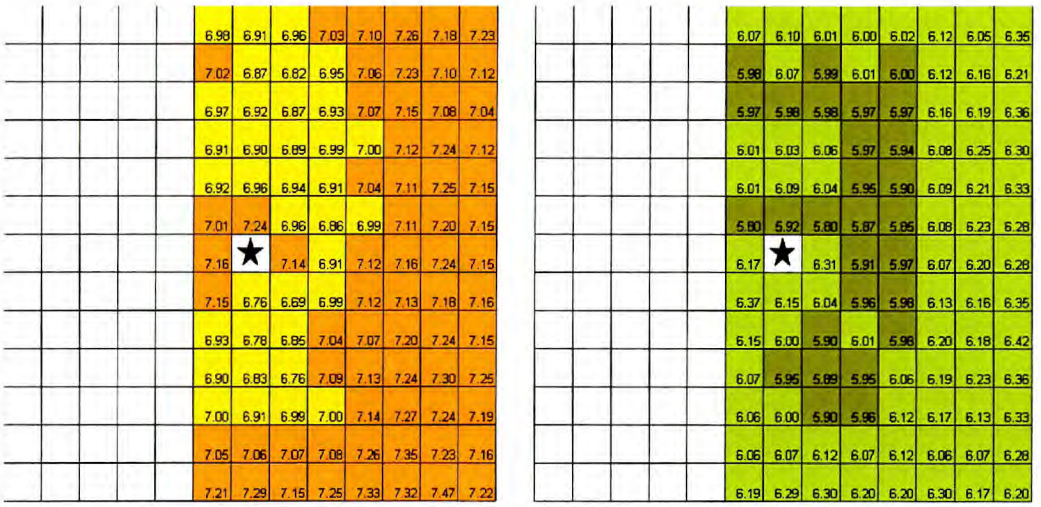

Fig. 5.39. Width (μm) of rabbit endothelial cell nuclei for branches in the anatomical left hand side of the descending thoracic aorta. (Maps are truncated to avoid affects of flow around ostia on the right hand side). Each square represents a 500μm * 500μm region. Total area of map is 26.0mm^2. n = 4 immature rabbits, n = 4 mature rabbits. Data represent averages for 18 immature and 17 mature branches.

Table 5.31. Nuclear widths (μm) for branch ostia within the upper and lower portion of the descending thoracic aorta in "Zone A", where n equals the number of branches.

	UPPER AORTA				LOWER AORTA			
Region	Immature		Mature		Immature		Mature	
	Mean	SEM	Mean	SEM	Mean	SEM	Mean	SEM
U2R2	6.66	0.14	5.41	0.15	7.07	0.15	5.80	0.13
U2R1	6.71	0.10	5.48	0.12	7.21	0.13	6.10	0.11
U2	6.78	0.08	5.58	0.12	7.21	0.12	6.25	0.12
U2L1	6.72	0.09	5.48	0.11	7.29	0.15	6.13	0.12
U2L2	6.73	0.17	5.54	0.12	7.23	0.25	5.95	0.12
U1R2	6.47	0.17	5.44	0.15	7.13	0.14	5.83	0.13
U1R1	6.86	0.11	5.38	0.12	7.27	0.14	5.93	0.10
U1	7.02	0.10	5.51	0.13	7.49	0.15	6.13	0.13
U1L1	6.68	0.11	5.35	0.12	7.40	0.15	5.93	0.13
U1L2	6.68	0.17	5.39	0.12	7.21	0.24	5.90	0.15
R2	6.56	0.19	5.47	0.17	7.17	0.15	5.97	0.16
R1	7.03	0.11	5.60	0.12	7.58	0.16	6.30	0.10
L1	6.79	0.14	5.51	0.12	7.50	0.14	6.37	0.23
L2	6.74	0.15	5.40	0.16	7.26	0.19	5.94	0.10
D1R2	6.56	0.13	5.50	0.18	7.06	0.09	6.04	0.12
D1R1	6.71	0.11	5.63	0.15	7.31	0.14	6.26	0.12
D1	6.54	0.11	5.59	0.16	7.05	0.18	6.37	0.11
D1L1	6.72	0.12	5.55	0.10	7.14	0.13	6.18	0.13
D1L2	6.80	0.15	5.50	0.13	7.31	0.20	6.02	0.11
D2R2	6.59	0.14	5.44	0.15	7.07	0.15	6.09	0.13
D2R1	6.68	0.10	5.59	0.11	7.09	0.13	6.14	0.11
D2	6.60	0.10	5.62	0.13	7.12	0.17	6.17	0.10
D2L1	6.76	0.10	5.55	0.11	7.22	0.14	6.06	0.12
D2L2	6.82	0.15	5.54	0.12	7.43	0.23	6.06	0.15
Total Mean	**6.73**	**0.03**	**5.51**	**0.03**	**7.26**	**0.03**	**6.11**	**0.03**

Table 5.32. Nuclear widths (μm) for branch ostia within the anatomical right and left of the descending thoracic aorta, where n equals the number of branches.

	ANATOMICAL RIGHT				ANATOMICAL LEFT			
Region	Immature		Mature		Immature		Mature	
	Mean	SEM	Mean	SEM	Mean	SEM	Mean	SEM
U2R2	-	-	-	-	6.82	0.11	5.79	0.13
U2R1	6.92	0.12	6.01	0.13	6.91	0.14	6.01	0.17
U2	6.96	0.12	6.09	0.14	6.95	0.11	6.16	0.16
U2L1	6.94	0.15	6.04	0.14	6.95	0.12	5.98	0.16
U2L2	6.91	0.16	5.95	0.11	-	-	-	-
U1R2	-	-	-	-	6.75	0.14	5.80	0.12
U1R1	7.01	0.12	5.80	0.14	7.05	0.14	5.90	0.12
U1	7.24	0.15	5.92	0.14	7.20	0.13	6.06	0.16
U1L1	6.96	0.18	5.80	0.15	7.00	0.14	5.79	0.15
U1L2	6.86	0.15	5.87	0.14	-	-	-	-
R2	-	-	-	-	6.83	0.15	5.95	0.15
R1	7.16	0.13	6.17	0.15	7.34	0.17	6.18	0.15
L1	7.14	0.18	6.31	0.29	7.03	0.16	6.07	0.17
L2	6.91	0.13	5.91	0.15	-	-	-	-
D1R2	-	-	-	-	6.78	0.11	6.05	0.15
D1R1	7.15	0.14	6.37	0.14	6.81	0.13	6.06	0.17
D1	6.76	0.17	6.15	0.16	6.72	0.14	6.27	0.16
D1L1	6.69	0.15	6.04	0.14	7.06	0.11	6.15	0.19
D1L2	6.99	0.14	5.96	0.14	-	-	-	-
D2R2	-	-	-	-	6.80	0.12	6.04	0.15
D2R1	6.93	0.15	6.15	0.13	6.79	0.10	6.03	0.16
D2	6.78	0.17	6.00	0.12	6.83	0.12	6.17	0.15
D2L1	6.85	0.16	5.90	0.13	6.98	0.10	6.11	0.17
D2L2	7.04	0.15	6.01	0.13	-	-	-	-
Total Mean	**6.96**	**0.03**	**6.02**	**0.03**	**6.93**	**0.03**	**6.03**	**0.04**

5.3.4.5.1 Width of nuclei surrounding branch ostia within the upper and lower portion of the descending thoracic aorta

Mean nuclear widths within Zones A-C combined, for immature rabbits and for ostia in the upper and lower portion of the descending thoracic aorta were 6.82 ± 0.01μm (n = 1854 regions) and 7.28 ± 0.01μm (n = 1409 regions) respectively (6.7% difference) ($P<0.005$), and for mature rabbits were 5.56 ± 0.01μm (n = 1378 regions) and 6.08 ± 0.01μm (n = 1755 regions) respectively (9.4% difference) ($P<0.005$).

Nuclear widths in the regions within Zones A-C combined, in the upper portion of the descending thoracic aorta were significantly different between ages and regions (both $P<0.005$) and there was a significant interaction between age and region ($P<0.01$). In

the lower descending thoracic aorta, there were also significant differences between ages ($P<0.01$) and regions ($P<0.005$) and a significant interaction between age and region ($P<0.005$).

5.3.4.5.2 Width of nuclei surrounding branch ostia in the left hand and right hand sides of the descending thoracic aorta

Mean nuclear widths around ostium from the right and left side of the aorta, for immature rabbits, were 7.06 ± 0.02 (n = 1635 regions) and 6.99 ± 0.01 (n = 1460 regions) respectively (1.0% difference) ($P<0.005$), and for mature rabbits were 6.07 ± 0.01 (n = 1535 regions) and 6.00 ± 0.02 (n = 1475 regions) respectively (1.2% difference) ($P<0.005$).

Nuclear widths in regions within Zones A-C combined, for ostia on the left hand side of the aorta were significantly different between ages and regions and there was a significant interaction between age and region (all $P<0.005$). There were also significant differences between ages ($P<0.01$) and regions ($P<0.005$) and a significant interaction between age and region ($P<0.005$) for ostia on the right hand side of the aorta.

5.3.5 Rabbit nuclear area

Endothelial nuclear areas are shown in pixels^2 as these are the units given by ImageTool. It measures the area as the number of pixels within an object, but it is not known whether pixels^2 can simply be converted into μm^2. For this reason, pixels^2 are used so comparisons can be made within our own data, however it may not be possible to compare our results with data from other researchers.

The area of endothelial nuclei within Zones A-C for immature and mature rabbits are shown in Fig. 5.40. There was no significant difference in mean area between ages ($P=0.88$) but there was a highly significant effect of region, and a significant interaction between age and region (both $P<0.005$). Mean nuclear areas are shown for individual rabbits in Table 5.33. Nuclei of immature rabbits had mean areas of 490.9 ± 1.01 pixels^2 (n = 3263) and mature rabbits had mean areas of 486.8 ± 0.77pixels^2 (n = 3539) (0.8% difference).

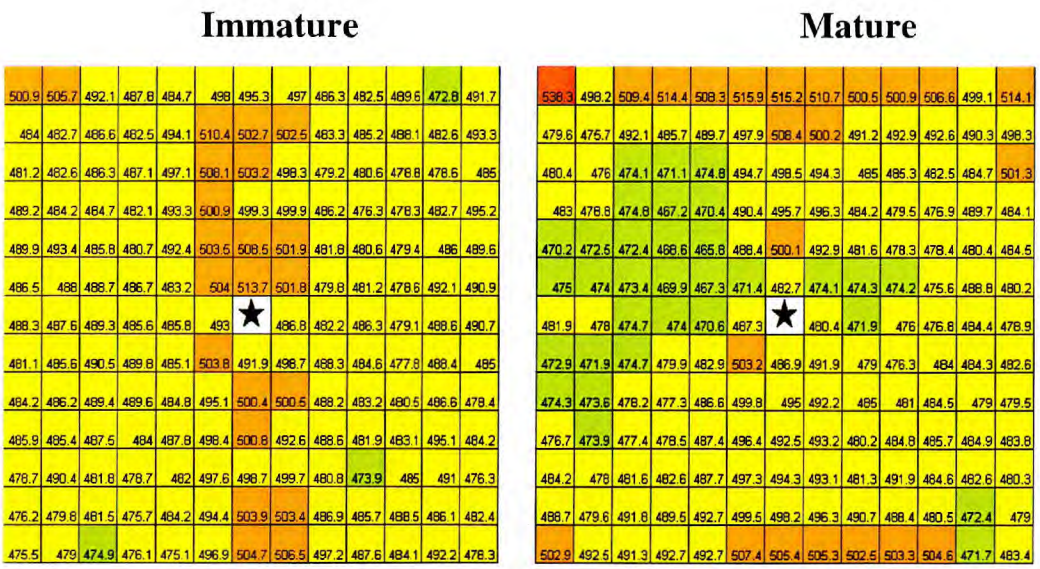

Fig. 5.40. Area (pixels^2) of rabbit endothelial cell nuclei all branch ostia imaged. Each square represents a 500μm * 500μm region. The total area of the map is 42.25mm^2. n = 4 immature rabbits, n = 4 mature rabbits. Data represent averages for 36 immature and 38 mature branches.

Table 5.33. Mean rabbit endothelial cell nuclear area (pixels^2), where n equals the number of regions.

Age Group	Rabbit	Area (Pixel^2)	
		Mean	SEM
Immature	I1	503.6	1.34
	I2	453.1	0.68
	I3	521.1	2.38
	I4	467.5	2.53
	All immature	490.9	1.01
Mature	M1	476.3	1.23
	M2	496.2	1.40
	M3	493.2	1.27
	M4	454.1	1.49
	All mature	486.8	0.77

5.3.5.1 "Zone A" (500μm * 500μm regions)

The areas of nuclei within Zone A are shown in and Fig. 5.41. There was no significant effect of age (P=0.56) (mean nuclear areas were 496.24 ± 1.65pixels^2 (n = 677) and 485.50 ± 1.77pixels^2 (n = 741) for immature and mature rabbits respectively; a 2.2% difference), but there was a significant effect of region and a significant interaction between age and region (both P<0.005).

In immature rabbits, nuclei were larger upstream of the branch than downstream; the ratio of upstream ("U1") to downstream ("D1") was 1.04. Nuclei in the lateral regions ("R1" and "L1") were smaller than those immediately upstream of the ostia. In mature rabbits, there was little change between upstream and downstream regions (ratio = 0.99). Lateral regions had nuclei of a very similar size to both immediate upstream and downstream regions. Values ranged from 479.93 ± 14.95pixels^2 ("U1L2", n = 18 branches) to 513.68 ± 9.38pixels^2 ("U1", n = 36 branches) (7.0% difference) in immature rabbits, and 465.84 ± 9.72pixels^2 ("U2R2", n = 21 branches) to 503.20 ± 7.85pixels^2 ("D1R1", n = 38 branches) (8.0% difference) in mature rabbits.

The significance of differences between individual regions for immature and mature rabbits, obtained using the Tukey test, are shown in Fig. 5.42.

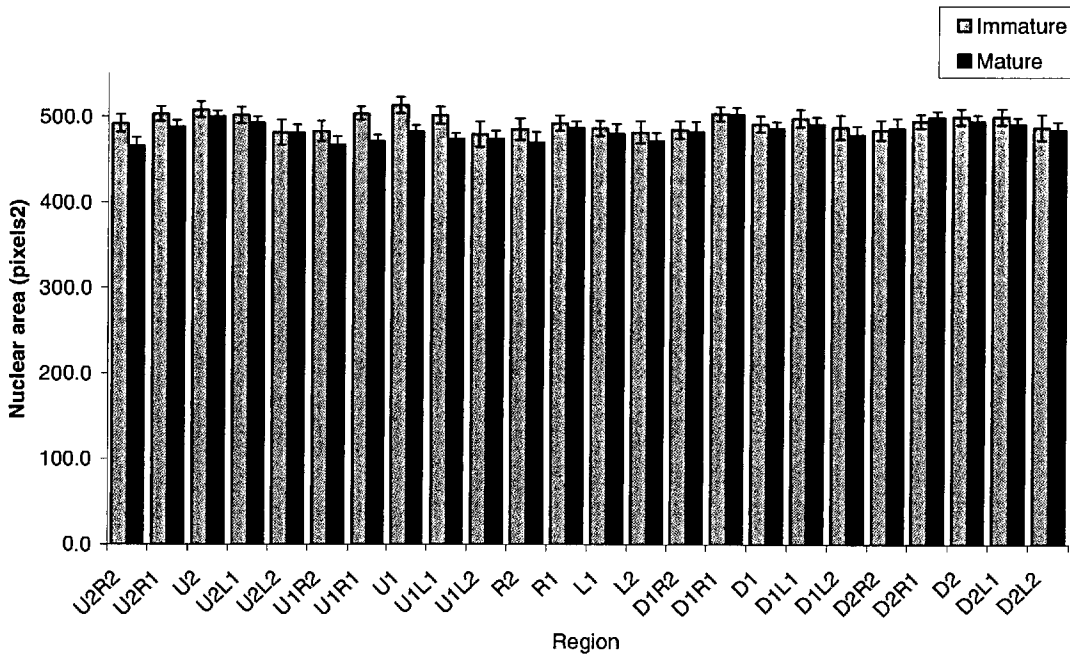

Fig. 5.41. Nuclear area (pixels^2) for regions within Zone A (defined in figure 5.1), in immature and mature rabbits. Bars show means ± SEM (n = number of branches).

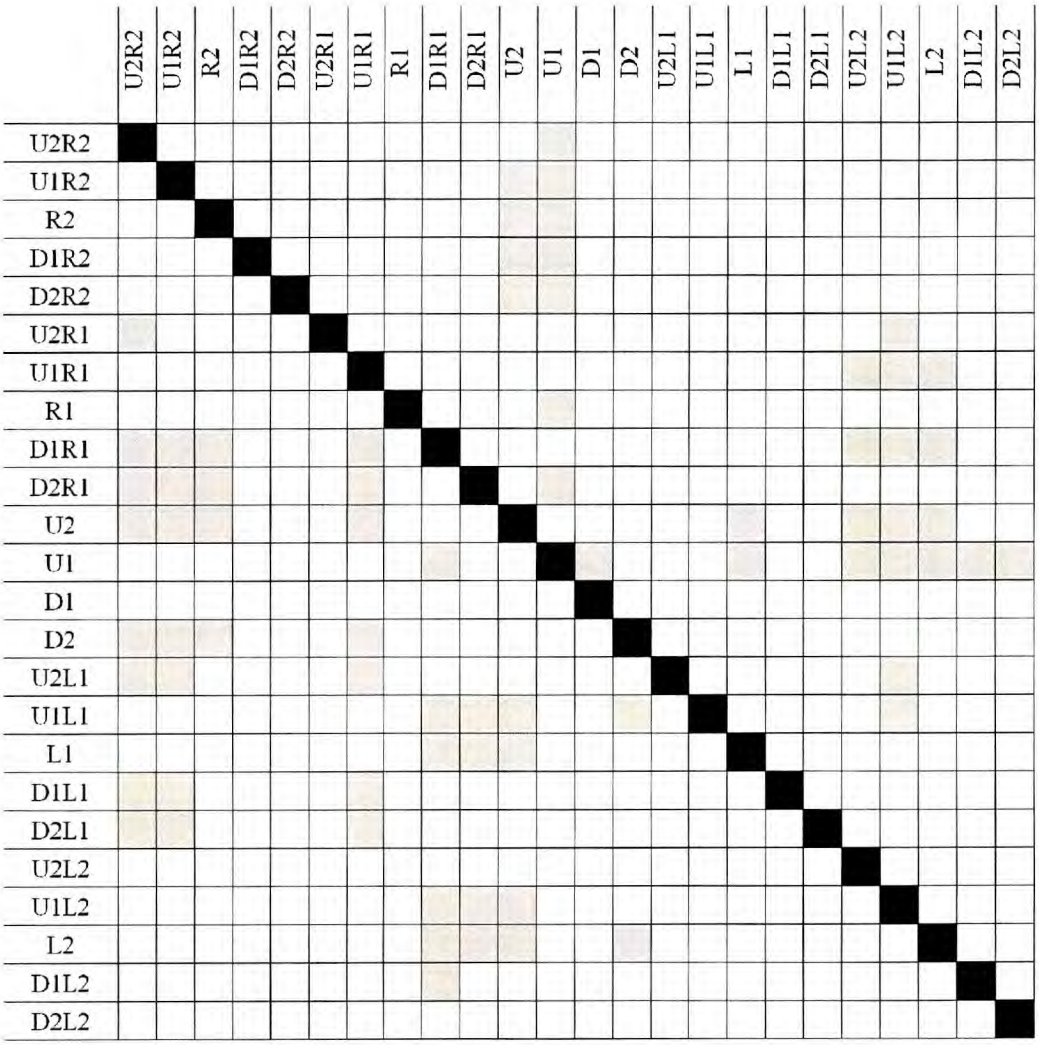

Fig. 5.42. Significance of differences in area of nuclei between 500μm * 500μm regions within Zone A, determined by the Tukey test for multiple comparisons. Squares shaded in grey depict significant differences ($P<0.05$) between regions. Squares to the right of the black diagonal line indicate differences in immature rabbits. Squares to the left indicate differences in mature rabbits.

5.3.5.2 "Zone A" (100μm * 100μm sub-regions)

Nuclear areas in the main regions nearest the branch ostia ("U2R1", "U2", "U2L1", "U1R1", "U1", "U1L1", "R1", "L1", "D1R1", "D1", "D1L1", "D2R1", "D2", "D2L1") were analysed at higher resolution, using data for individual 100μm * 100μm sub-regions (Fig.5.43, Table 5.34a, b and 5.35a,b). Data were examined for effects of age or region, or any interaction between age and region. There were no significant effects of age ($P>0.05$), but there were significant effects of region ($P<0.005$) for sub-regions

within main regions "U1R1", "R1", "D1R1", "D2R1", "U2", "U1", "D1", "U1L1" and "L1". There was a significant change with age in pattern (age*region interaction) for the regions "R1", "U1", "U1L1" and "L1" (all $P<0.005$). In general, nuclei upstream of the branch ostia in immature rabbits were larger than those downstream and in the lateral regions. In mature rabbits, the nuclear areas were much more uniform, with only small patches of larger nuclei upstream and downstream of the ostia.

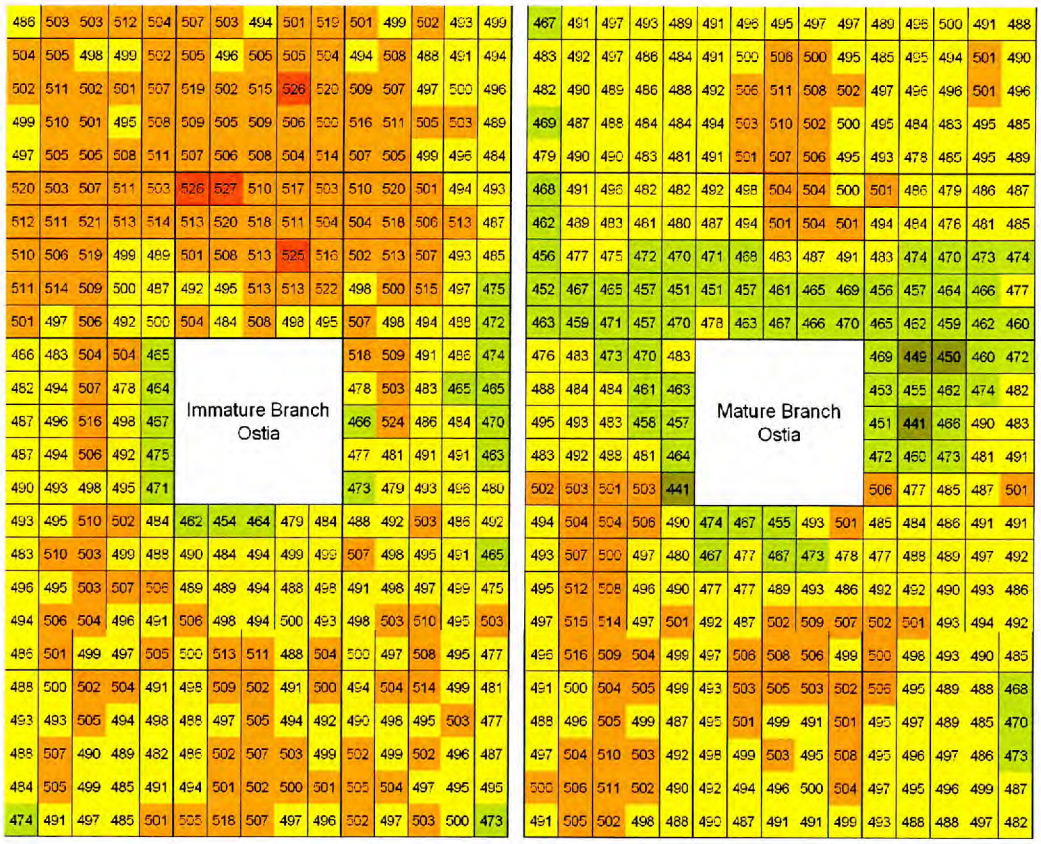

Fig. 5.43. Mean area (pixels^2) of endothelial cell nuclei for all the branch ostia. Each square represents a 100μm * 100μm region. The total area of the map is 3.75mm^2. n = 4 immature rabbits, n = 4 mature rabbits. Data represent averages for 36 immature and 38 mature branches.

Table 5.34a. Immature rabbit endothelial cell nuclear area (pixels^2) for sub-regions (100μm * 100μm) within upstream and lateral main-regions in "Zone A", where n equals the number of branches.

Immature	U2R1		U2		U2L1		U1R1		U1		U1L1		R1		L1	
Sub-Region	Mean	SEM	Mean	SEM	Mean	SEM	Mean	SEM	Mean	SEM	Mean	SEM	Mean	SEM	Mean	SEM
U2R2s	486.06	14.72	507.40	11.78	501.50	11.84	519.73	15.27	526.24	11.94	509.93	11.10	486.27	13.98	518.00	29.16
U2R1s	502.84	9.96	502.64	11.91	498.70	11.77	502.74	10.60	527.38	12.02	520.02	12.72	482.85	10.12	508.85	17.83
U2s	502.96	11.94	493.91	10.33	501.70	12.56	506.53	9.31	509.92	10.90	501.27	13.90	503.72	12.92	490.67	12.40
U2L1s	512.44	12.35	501.21	11.23	493.03	10.54	511.48	11.88	516.86	10.17	493.90	12.80	504.29	14.99	485.75	13.43
U2L2s	504.30	11.22	518.85	14.28	499.22	22.56	502.55	10.28	503.41	11.29	492.69	21.82	464.55	14.62	474.17	16.72
U1R2s	504.22	11.25	505.44	10.20	494.46	12.97	512.17	19.67	512.82	8.89	503.67	9.68	482.45	13.93	477.81	23.75
U1R1s	504.79	8.77	495.58	8.28	508.28	10.93	510.97	10.15	519.55	12.45	517.72	11.52	493.72	12.97	502.79	13.92
U1s	498.42	12.30	504.60	10.01	487.87	9.26	521.49	11.14	517.92	11.28	505.97	13.42	506.69	11.22	482.89	11.39
U1L1s	499.33	10.85	505.22	11.73	490.96	10.31	512.84	11.01	510.75	9.75	513.41	14.58	477.68	20.11	465.43	9.10
U1L2s	501.76	12.50	503.67	11.75	494.35	16.89	514.36	10.17	504.05	11.34	486.90	15.91	463.83	40.66	465.17	13.48
R2s	502.34	14.41	518.52	12.27	508.60	13.80	510.17	20.35	500.80	11.64	502.15	10.82	486.80	10.54	466.10	28.06
R1s	510.75	12.90	501.84	10.63	507.05	12.78	506.36	10.05	507.97	12.12	512.78	11.63	495.66	10.89	523.72	20.47
Cs	501.99	12.22	514.78	11.62	497.11	10.39	519.11	9.26	512.64	12.54	506.62	13.69	515.74	14.66	485.82	11.33
L1s	501.35	10.05	525.51	13.67	499.67	11.29	498.99	8.87	525.25	12.61	492.79	14.22	497.54	19.46	484.31	11.48
L2s	506.78	12.63	519.99	12.07	496.14	15.72	489.20	8.62	516.31	9.77	485.18	19.23	467.21	35.59	469.84	17.31
D1R2s	498.58	15.38	509.41	12.77	515.64	12.90	510.97	17.86	492.23	11.18	498.49	11.24	486.73	12.79	476.76	18.07
D1R1s	509.71	11.30	504.64	10.99	510.66	14.60	514.47	10.20	495.05	9.65	500.48	12.85	493.86	9.85	480.89	13.86
D1s	501.46	10.12	508.98	11.05	504.79	12.90	508.62	10.06	513.16	14.28	514.55	13.64	505.73	12.18	490.80	11.62
D1L1s	495.47	8.76	506.43	12.06	503.19	12.72	499.53	9.69	513.00	11.49	496.95	14.44	492.20	20.76	490.82	15.25
D1L2s	507.92	10.51	500.32	10.13	488.52	16.68	486.83	9.34	522.09	20.25	474.53	21.31	474.53	40.52	463.28	15.23
D2R2s	497.48	14.05	506.68	10.87	507.08	11.79	500.84	13.66	503.54	20.02	507.13	16.86	490.46	13.86	472.57	15.95
D2R1s	505.10	14.78	505.90	11.04	504.67	13.41	496.97	10.98	484.48	15.41	497.58	17.65	492.97	9.85	479.36	13.22
D2s	505.18	11.75	507.91	12.22	499.27	13.34	505.74	11.18	507.87	17.25	493.83	13.50	498.48	9.71	493.43	11.22
D2L1s	507.66	10.68	504.49	12.74	496.48	13.55	492.32	9.32	497.90	13.21	487.64	10.83	494.75	13.23	495.56	12.68
D2L2s	511.21	12.40	513.75	14.92	484.29	18.19	499.91	12.75	495.06	10.63	472.48	14.61	470.87	23.02	479.64	15.59

Table 5.34b. Immature rabbit endothelial cell nuclear area (pixels^2) for sub-regions (100μm * 100μm) within downstream main-regions in "Zone A", where n equals the number of branches.

Immature	D1R1		D1		D1L1		D2R1		D2		D2L1	
Sub-Region	Mean	SEM	Mean	SEM	Mean	SEM	Mean	SEM	Mean	SEM	Mean	SEM
U2R2s	493.46	14.78	461.88	15.88	466.05	15.61	488.17	11.35	497.72	10.24	493.58	11.93
U2R1s	495.48	9.47	454.44	11.83	491.78	18.36	499.97	10.10	508.54	12.79	503.71	11.81
U2s	510.09	12.24	463.53	12.51	502.92	15.04	502.40	10.60	501.75	9.59	513.88	10.99
U2L1s	501.61	13.26	479.20	13.14	486.43	12.57	503.70	12.79	491.05	14.20	498.75	11.99
U2L2s	483.78	10.95	484.38	14.50	491.67	17.42	490.84	10.32	500.47	12.71	481.48	15.64
U1R2s	482.61	11.63	489.97	14.68	506.58	16.56	493.47	14.75	488.18	11.75	490.05	12.62
U1R1s	509.65	11.41	484.37	10.15	498.10	13.76	492.80	7.76	497.22	9.97	497.53	10.75
U1s	502.87	10.94	493.52	12.38	494.90	11.59	505.01	9.99	505.42	12.71	495.32	13.10
U1L1s	499.17	10.84	498.68	15.09	491.41	10.14	493.51	11.05	493.70	10.42	502.84	10.95
U1L2s	487.77	12.17	499.02	12.90	465.48	16.18	497.98	11.23	492.20	12.56	476.81	16.46
R2s	495.85	11.99	489.09	17.75	490.66	13.77	488.24	13.42	485.70	12.27	501.97	11.20
R1s	495.05	9.42	486.96	9.42	498.10	13.07	506.95	11.16	501.96	12.40	498.69	11.15
Cs	502.69	10.64	494.31	10.57	497.00	13.34	490.07	10.48	507.14	10.80	502.25	12.23
L1s	506.69	11.01	487.59	11.25	498.87	11.78	486.54	11.94	502.72	11.59	495.86	11.20
L2s	505.63	11.86	497.51	12.63	475.01	12.18	481.74	9.91	499.32	12.32	486.73	17.63
D1R2s	494.04	11.98	506.22	11.28	498.10	12.21	484.46	12.27	494.24	12.69	504.84	11.08
D1R1s	505.90	9.24	498.40	12.16	502.75	11.41	504.61	10.27	501.20	12.29	503.80	11.82
D1s	503.62	11.18	493.59	10.75	509.65	14.01	499.39	9.89	501.65	12.49	497.39	12.49
D1L1s	495.54	9.59	499.99	11.03	494.98	10.60	484.82	9.81	500.33	10.90	495.26	11.80
D1L2s	490.70	11.51	493.25	9.39	503.03	19.92	490.80	12.60	500.87	10.79	494.73	18.10
D2R2s	485.58	14.87	499.96	12.37	499.69	11.66	473.78	12.31	504.97	14.78	502.45	12.12
D2R1s	500.99	9.65	513.10	12.76	496.87	10.32	491.04	10.28	518.15	12.96	497.06	12.60
D2s	498.63	11.14	510.90	10.55	508.26	15.58	496.78	9.95	507.01	11.05	502.83	12.76
D2L1s	496.68	10.03	488.12	10.92	495.18	14.01	484.54	10.58	497.12	10.62	499.97	11.36
D2L2s	504.52	14.39	504.01	13.00	477.26	14.19	501.36	13.65	496.27	12.68	472.83	18.14

Table 5.35a. Mature rabbit endothelial cell nuclear area (pixels^2) for sub-regions (100μm * 100μm) within upstream and lateral main-regions in "Zone A", where n equals the number of branches.

Mature	U2R1		U2		U2L1		U1R1		U1		U1L1		R1		L1	
Sub-Region	Mean	SEM	Mean	SEM	Mean	SEM	Mean	SEM	Mean	SEM	Mean	SEM	Mean	SEM	Mean	SEM
U2R2s	467.11	10.07	491.35	9.47	489.44	9.65	467.68	9.76	492.12	9.02	500.55	8.90	476.40	15.23	469.45	22.13
U2R1s	491.29	7.47	496.21	7.12	495.82	10.13	491.27	10.32	498.49	8.95	485.65	9.72	483.45	13.79	449.10	12.49
U2s	497.21	7.41	495.48	6.46	499.83	8.86	496.33	10.03	504.28	8.51	478.95	7.90	472.98	10.72	449.86	10.11
U2L1s	493.28	8.01	497.35	7.23	490.67	8.24	482.06	10.35	504.20	9.78	486.27	7.87	469.56	11.29	459.73	11.28
U2L2s	488.60	9.34	496.83	8.33	488.00	10.34	481.88	10.12	499.81	9.20	487.23	11.33	482.72	17.62	472.01	13.96
U1R2s	482.84	11.69	490.79	8.37	485.02	12.76	461.70	10.76	487.06	9.12	493.54	8.60	487.71	14.66	453.11	26.21
U1R1s	491.84	7.38	499.74	8.39	495.09	8.59	488.59	10.85	494.04	9.33	484.39	8.88	484.39	10.99	455.42	14.15
U1s	496.90	8.21	505.52	6.57	494.01	7.77	483.15	9.75	501.22	9.87	478.13	8.30	484.37	12.98	461.92	9.95
U1L1s	486.21	8.52	500.07	7.22	500.93	7.28	481.35	10.33	504.21	8.43	481.45	7.59	460.71	14.58	474.39	10.38
U1L2s	484.14	8.82	494.62	8.20	490.42	9.67	479.66	10.57	500.66	9.29	484.93	11.42	463.42	20.44	481.86	18.02
R2s	482.19	11.51	491.53	9.11	496.91	9.62	455.95	10.76	470.68	9.74	482.53	9.12	495.31	15.21	451.05	26.95
R1s	490.10	9.30	505.95	7.94	495.65	8.67	477.20	8.97	467.68	10.41	474.04	10.28	493.25	9.40	440.61	17.10
Cs	488.73	10.92	510.75	8.86	496.40	7.47	475.40	9.69	482.63	9.69	469.69	9.88	482.71	12.81	465.77	10.38
L1s	486.37	9.45	507.56	7.30	500.92	7.56	471.97	10.09	487.42	9.21	473.38	8.20	457.87	17.77	489.68	10.43
L2s	487.97	9.55	502.27	8.03	495.69	12.86	470.42	10.18	490.89	10.61	473.94	11.94	456.60	29.66	482.75	15.44
D1R2s	469.00	10.93	493.68	9.03	495.27	8.77	452.18	9.37	450.87	9.57	455.81	10.84	482.76	13.90	472.23	23.29
D1R1s	486.53	10.02	503.41	8.91	484.22	8.96	468.86	8.78	457.13	9.27	457.01	10.33	491.89	9.30	459.90	15.21
D1s	488.34	9.57	509.52	8.83	483.07	8.71	464.67	10.36	461.20	10.56	464.24	10.84	488.12	11.34	472.93	8.33
D1L1s	483.83	9.50	502.35	8.36	495.39	8.91	457.50	9.84	464.77	9.38	466.44	8.08	481.32	16.74	480.83	11.07
D1L2s	484.35	8.75	499.76	8.63	485.09	12.07	451.33	9.97	468.95	10.31	476.98	11.44	464.48	34.15	491.17	15.43
D2R2s	478.67	9.70	490.66	9.47	493.10	8.67	463.16	14.38	477.80	18.74	465.20	9.29	502.02	13.24	506.45	25.83
D2R1s	490.08	10.31	500.68	9.26	478.45	9.43	459.41	9.10	463.30	12.50	461.99	9.78	503.41	8.70	477.25	11.04
D2s	490.22	10.91	507.28	8.59	485.16	9.61	471.47	10.60	467.43	14.02	459.24	9.86	501.44	8.17	485.40	9.19
D2L1s	482.70	9.77	505.87	9.87	494.69	7.94	456.72	12.06	466.40	11.55	461.88	10.08	503.40	8.96	487.45	9.82
D2L2s	481.16	10.06	495.03	9.24	488.51	12.98	470.11	15.15	469.62	10.16	459.72	10.62	440.93	20.06	500.87	19.80

Table 5.35b. Mature rabbit endothelial cell nuclear area (pixels^2) for sub-regions (100μm * 100μm) within downstream main-regions in "Zone A", where n equals the number of branches.

Mature	D1R1		D1		D1L1		D2R1		D2		D2L1	
Sub-Region	Mean	SEM	Mean	SEM	Mean	SEM	Mean	SEM	Mean	SEM	Mean	SEM
U2R2s	493.60	14.21	473.70	15.73	485.15	11.92	490.82	13.26	493.15	10.33	505.72	8.46
U2R1s	503.84	9.31	467.30	11.71	484.08	9.92	499.84	9.47	502.73	10.47	494.86	9.82
U2s	504.00	8.35	455.40	17.77	486.07	8.37	504.20	10.01	504.76	9.44	489.03	9.17
U2L1s	506.50	10.05	492.60	15.83	490.66	9.50	504.59	10.28	503.07	8.34	488.25	7.70
U2L2s	490.44	10.37	501.48	12.54	490.85	13.35	499.19	9.64	501.88	9.86	468.44	11.41
U1R2s	492.59	12.84	466.90	10.79	477.13	10.65	487.91	11.94	494.76	8.56	495.48	7.93
U1R1s	507.33	9.35	477.37	11.03	488.21	10.85	495.66	8.93	501.21	9.09	496.64	8.76
U1s	500.31	9.06	466.76	10.71	488.90	9.00	504.92	9.66	498.60	7.89	489.26	7.47
U1L1s	497.02	9.36	472.96	10.86	497.14	10.36	498.53	8.45	491.09	7.66	485.25	8.63
U1L2s	479.53	11.24	478.12	8.97	492.11	13.42	486.79	8.56	501.32	7.57	469.76	9.62
R2s	494.86	12.94	477.00	10.39	491.63	9.85	497.22	14.89	497.98	8.73	494.75	7.67
R1s	512.40	9.66	476.72	9.53	492.10	10.04	503.85	8.90	499.05	10.23	496.09	7.28
Cs	507.90	9.55	488.84	9.39	490.13	8.47	510.38	7.79	503.33	9.67	496.72	8.49
L1s	495.74	8.96	492.50	9.54	492.61	8.97	503.41	8.08	495.00	8.53	486.45	9.04
L2s	490.46	9.67	485.65	9.40	486.17	13.60	491.85	8.17	508.46	8.66	472.51	10.22
D1R2s	496.65	13.56	491.77	9.11	501.92	8.76	500.03	15.50	492.03	8.47	497.45	8.95
D1R1s	514.82	9.68	486.91	9.80	501.12	8.26	505.93	9.34	493.72	10.10	494.61	7.53
D1s	513.55	10.75	502.09	10.00	492.98	10.15	510.91	8.51	496.15	9.97	496.03	9.51
D1L1s	496.97	10.33	508.98	9.93	493.68	8.70	501.52	8.35	499.78	8.80	498.69	8.20
D1L2s	501.43	9.98	507.15	9.11	492.05	12.26	490.23	9.04	503.71	8.39	487.38	8.92
D2R2s	496.19	13.38	497.09	9.09	500.05	8.20	490.84	14.48	489.92	9.07	493.28	9.04
D2R1s	516.24	9.99	505.75	9.69	497.61	9.24	505.22	10.40	486.68	10.17	487.79	8.76
D2s	508.65	10.25	507.78	10.23	493.00	8.13	502.16	8.89	491.23	11.79	488.14	9.68
D2L1s	504.45	10.16	506.05	8.69	490.09	7.87	498.43	8.50	490.52	11.65	497.46	9.20
D2L2s	499.05	10.50	499.25	8.69	485.23	13.43	488.28	9.21	498.87	10.36	481.58	11.24

Tukey tests were performed for nuclear areas in "Zone A" (in main regions "U1R1", "U1", "U1L1", "R1", "L1", "D1R1", "D1", "D1L1") to determine where significant differences existed between the sub-regions within each of these main regions (Appendix B.5a-g).

5.3.5.3 "Zone B" (500μm * 500μm regions)

The mean areas of nuclei within Zone B are shown in Table 5.36. There was no significant effect of age (P=0.81) but there was a highly significant effect of region (P<0.005) and a significant interaction between age and region (P<0.01). The mean nuclear area in immature rabbits was 489.59 ± 1.6pixels^2 (n = 1163) and in mature rabbits was 483.90 ± 1.21pixels^2 (n = 1355) (a difference of 1.2%). Areas ranged from 473.90 ± 15.02pixels^2 ("D4L3", n = 16 branches) to 508.12 ± 9.30pixels^2 ("U4R1", n = 34 branches) (7.2% difference) in immature rabbits, and from 468.59 ± 9.39pixels^2

("U2R3", n = 21 branches) to 498.51 ± 7.03pixels^2 ("U4", n = 38 branches) (a 6.4% difference) in mature.

Table 5.36. Rabbit endothelial cell nuclear area for "Zone B" regions, where n equals the number of branches.

Region	Immature		Mature	
	Mean	SEM	Mean	SEM
U4R4	486.27	14.15	474.06	10.39
U4R3	487.06	12.31	471.09	11.03
U4R2	497.14	13.21	474.76	11.21
U4R1	508.12	9.30	494.67	7.00
U4	503.15	9.20	498.51	7.03
U4L1	498.27	10.73	494.28	7.28
U4L2	479.25	13.44	484.99	9.52
U4L3	480.62	15.53	485.31	9.44
U4L4	478.79	15.05	482.54	10.50
U3R4	484.74	12.65	474.81	10.61
U3R3	482.07	12.29	467.16	10.57
U3R2	493.26	11.74	470.40	11.41
U3R1	500.91	7.76	490.36	6.86
U3	499.28	8.93	495.71	6.73
U3L1	499.89	10.20	496.31	6.94
U3L2	486.24	15.69	484.15	9.63
U3L3	476.29	15.62	479.47	9.23
U3L4	478.29	16.29	476.94	8.97
U2R4	485.82	12.89	472.38	9.41
U2R3	480.71	9.96	468.59	9.39
U2L3	480.59	13.57	478.27	9.38
U2L4	479.38	14.98	478.37	10.31
U1R4	488.67	13.91	473.44	9.73
U1R3	486.72	11.89	469.95	11.19
U1L3	481.20	13.40	474.15	9.34
U1L4	478.57	16.73	475.61	10.05
R4	489.28	11.89	474.69	9.27
R3	485.65	11.14	473.98	12.23
L3	486.27	16.57	476.00	9.71
L4	479.11	19.29	476.85	9.66
D1R4	490.46	12.80	474.73	9.90
D1R3	489.75	11.52	479.88	11.76
D1L3	484.56	15.72	476.31	10.91
D1L4	477.81	18.71	483.96	10.31
D2R4	489.37	13.74	478.24	10.38
D2R3	489.60	11.29	477.28	11.12
D2L3	483.15	15.15	480.96	8.81
D2L4	480.50	16.85	484.46	10.43
D3R4	487.49	13.43	477.44	9.11
D3R3	483.95	10.24	478.52	10.91
D3R2	487.81	11.10	487.38	9.95

D3R1	498.38	9.33	496.43	6.56
D3	500.76	9.83	492.51	6.79
D3L1	492.59	9.58	493.24	7.80
D3L2	488.59	16.07	480.24	9.24
D3L3	481.91	15.64	484.81	9.67
D3L4	483.06	18.85	485.69	10.18
D4R4	481.76	13.16	481.58	9.97
D4R3	478.73	11.13	482.64	10.76
D4R2	482.00	11.72	487.72	9.75
D4R1	497.58	9.05	497.33	6.16
D4	498.70	9.56	494.34	6.27
D4L1	499.69	9.73	493.05	6.84
D4L2	480.76	14.30	481.29	8.58
D4L3	473.90	15.02	491.95	8.68
D4L4	485.03	18.46	484.62	10.82
Total mean	**489.59**	**1.60**	**483.90**	**1.21**

5.3.5.4 "Zone C" (500μm * 500μm regions)

The mean nuclear areas for the regions within "Zone C" (2-4mm from branch ostia) defined in Fig. 5.1 are shown in Table 5.37. There was no significant effect of age ($P=1.00$) however there was a highly significant effect of region ($P<0.005$) and a significant interaction between age and region ($P<0.05$). The mean nuclear areas were 489.44 ± 1.01pixels^2 (n = 1423) and 490.18 ± 1.18pixels^2 (n = 1443) for immature and mature rabbits respectively. Values ranged from 472.80 ± 18.42pixels^2 ("U6L5", n = 12 branches) to 510.43 ± 9.18pixels^2 ("U5R1", n = 33 branches) in immature rabbits, and from 470.17 ± 13.56pixels^2 ("U2R6", n = 15 branches) to 538.30 ± 18.14pixels^2 ("U6R6", n = 4 branches) in mature; differences of 8.0% and 14.5% respectively.

Table 5.37. Rabbit endothelial cell area (pixels^2) for "Zone C", where n equals the number of branches.

Region	Immature		Mature	
	Mean	SEM	Mean	SEM
U6R6	500.94	21.70	538.30	18.14
U6R5	505.66	21.46	498.24	25.40
U6R4	492.09	17.72	509.44	19.88
U6R3	487.76	15.80	514.38	18.70
U6R2	484.73	10.26	508.26	20.07
U6R1	498.04	9.39	515.88	7.32
U6	495.35	10.96	515.20	9.38
U6L1	497.04	11.50	510.71	8.23
U6L2	486.28	16.21	500.54	9.80
U6L3	482.46	14.44	500.89	9.18
U6L4	489.56	17.98	506.60	10.88
U6L5	472.80	18.42	499.09	7.65
U6L6	491.68	22.10	514.11	13.53
U5R6	484.03	14.16	479.64	20.92
U5R5	482.74	14.47	475.74	14.84
U5R4	486.62	15.37	492.13	12.14
U5R3	482.48	12.99	485.67	12.18
U5R2	494.08	11.41	489.74	11.70
U5R1	510.43	9.18	497.95	6.86
U5	502.66	9.23	508.44	7.89
U5L1	502.47	10.97	500.17	7.45
U5L2	483.29	13.64	491.17	8.17
U5L3	485.17	15.35	492.85	8.76
U5L4	488.13	16.32	492.64	9.40
U5L5	482.61	15.74	490.29	10.53
U5L6	493.34	21.46	498.28	15.35
U4R6	481.22	16.60	480.37	17.30
U4R5	482.65	14.96	475.99	12.13
U4L5	478.61	16.32	484.74	11.13
U4L6	484.96	24.42	501.28	16.82
U3R6	489.24	14.14	482.97	15.08
U3R5	484.19	14.09	478.79	12.23
U3L5	482.70	18.77	489.68	11.34
U3L6	495.21	23.46	484.06	15.47
U2R6	489.90	12.63	470.17	13.56
U2R5	493.38	14.52	472.49	11.43
U2L5	486.03	18.09	480.40	12.14
U2L6	489.63	20.02	484.45	13.73
U1R6	486.52	14.16	474.99	15.61
U1R5	488.00	13.56	474.04	11.37
U1L5	492.08	20.12	488.78	10.83
U1L6	490.88	22.19	480.22	13.74
R6	488.29	14.96	481.88	15.12
R5	487.63	12.62	478.00	10.74
L5	488.62	19.56	484.36	9.00
L6	490.66	22.17	478.92	13.65

D1R6	481.12	14.76	472.92	13.26
D1R5	485.64	12.81	471.90	11.34
D1L5	488.36	18.97	484.29	10.71
D1L6	484.95	21.36	482.59	15.53
D2R6	484.21	13.21	474.33	13.36
D2R5	486.21	13.46	473.62	9.98
D2L5	486.62	19.39	479.02	10.19
D2L6	478.39	22.56	479.55	15.47
D3R6	485.87	15.12	476.74	12.54
D3R5	485.36	12.23	473.87	7.67
D3L5	495.14	19.52	484.89	11.05
D3L6	484.22	24.74	483.75	15.44
D4R6	478.66	12.25	484.21	11.60
D4R5	490.38	14.68	478.01	9.55
D4L5	491.03	21.80	482.58	12.58
D4L6	476.33	24.53	480.29	12.84
D5R6	476.19	11.99	488.70	10.12
D5R5	479.80	14.80	479.55	9.03
D5R4	481.53	14.11	491.77	10.39
D5R3	475.73	11.51	489.49	9.93
D5R2	484.20	12.71	492.65	9.23
D5R1	494.37	10.30	499.55	5.94
D5	503.91	9.69	498.23	6.20
D5L1	503.37	10.21	496.34	6.39
D5L2	486.87	18.73	490.69	9.47
D5L3	485.71	18.14	488.40	10.57
D5L4	488.50	18.84	480.54	10.93
D5L5	486.14	18.47	472.36	14.04
D5L6	482.36	23.52	479.00	14.37
D6R6	475.50	13.74	502.89	17.76
D6R5	479.02	16.95	492.47	9.78
D6R4	474.91	14.32	491.27	9.73
D6R3	476.12	15.18	492.73	10.84
D6R2	475.06	15.34	492.67	9.72
D6R1	496.91	12.28	507.42	5.77
D6	504.73	12.81	505.38	6.40
D6L1	506.54	12.56	505.35	5.40
D6L2	497.24	23.06	502.51	8.77
D6L3	487.61	19.82	503.31	13.74
D6L4	484.09	18.83	504.58	13.72
D6L5	492.23	23.00	471.69	21.31
D6L6	478.26	27.55	483.36	22.69
Total mean	**489.44**	**1.01**	**490.18**	**1.18**

5.3.5.5 Nuclear area for different locations of branch ostia (500μm * 500μm regions)

Mean nuclear areas for ostia within the upper portion and lower portion of the descending thoracic aorta, and ostia from the left and right hand side of the vessel are shown in Table 5.38. Data are further subdivided by region i.e. Zones A-C.

The mean areas of nuclei within individual regions in "Zone A" for the upper and lower portion and right and left portions of the descending thoracic aorta are shown in Table 5.39 and 5.40 respectively. Colour maps showing variations in the mean nuclear areas around the branch ostium at low resolution (averages for 500μm * 500μm regions) for different locations of branch ostia are shown in Fig. 5.44-5.47.

Table 5.38. Rabbit endothelial cell nuclear area averaged across all regions, results separated by location of the branch ostia, where n equals the number of regions.

Location of branch ostia	Region	Immature		Mature	
		Mean	SEM	Mean	SEM
Upper branch ostia	Zone A-C	474.15	1.30	448.11	0.90
	Zone A	479.3	2.53	444.93	1.99
	Zone B	473.04	2.09	447.4	1.37
	Zone C	472.43	2.15	450.52	1.49
Lower branch ostia	Zone A-C	512.96	1.38	507.92	0.79
	Zone A	521.16	2.92	506.57	1.89
	Zone B	512.73	2.28	504.49	1.24
	Zone C	509.67	2.12	511.85	1.18
Right branch ostia	Zone A-C	490.83	1.65	496.69	1.02
	Zone A	494.07	3.24	493.36	2.43
	Zone B	487.6	2.68	494.26	1.6
	Zone C	491.97	2.71	500.79	1.53
Left branch ostia	Zone A-C	491.57	1.34	496.06	1.12
	Zone A	499.6	2.82	494.39	2.63
	Zone B	492.08	2.18	493.33	1.83
	Zone C	487.43	2.10	499.37	1.68

5.3.5.5.1 Area of nuclei surrounding the branch ostia within the upper and lower portions of the descending thoracic aorta

The mean nuclear area for immature rabbits were 474.15 ± 1.3pixels^2 (n = 1854) and 512.96 ± 1.38pixels^2 (n = 1409) for ostia in the upper and lower portion of the vessel, respectively (P<0.005) (a difference of 8.2%), and for mature rabbits were 448.11 ± 0.90pixels^2 (n = 1378) and 507.92 ± 0.79pixels^2 (n = 1755) respectively (P<0.005) (a 13.3% difference).

The area of nuclei in the upper aorta were not significantly affected by age (P=0.20). However, there was an effect of region and a significant interaction between age and region (both P<0.005). In the lower portion, there was no significant difference between ages (P=0.67) and no interaction between age and region (P=0.34). There was, however, a significant effect of region (P<0.005).

5.3.5.5.2 The area of nuclei surrounding branch ostia within the left hand and right hand sides of the descending thoracic aorta

The mean areas of nuclei around ostium on the right and left side of the descending thoracic aorta in immature rabbits were 490.83 ± 1.65pixels^2 (n = 1460) and 491.57 ± 1.34pixels^2 (n = 1635) respectively (P=0.73) (a 0.2% difference), and for mature rabbits were 496.69 ± 1.02pixels^2 (n = 1475) and 496.06 ± 1.12 (n = 1535) respectively (P<0.005) (a 0.1% difference).

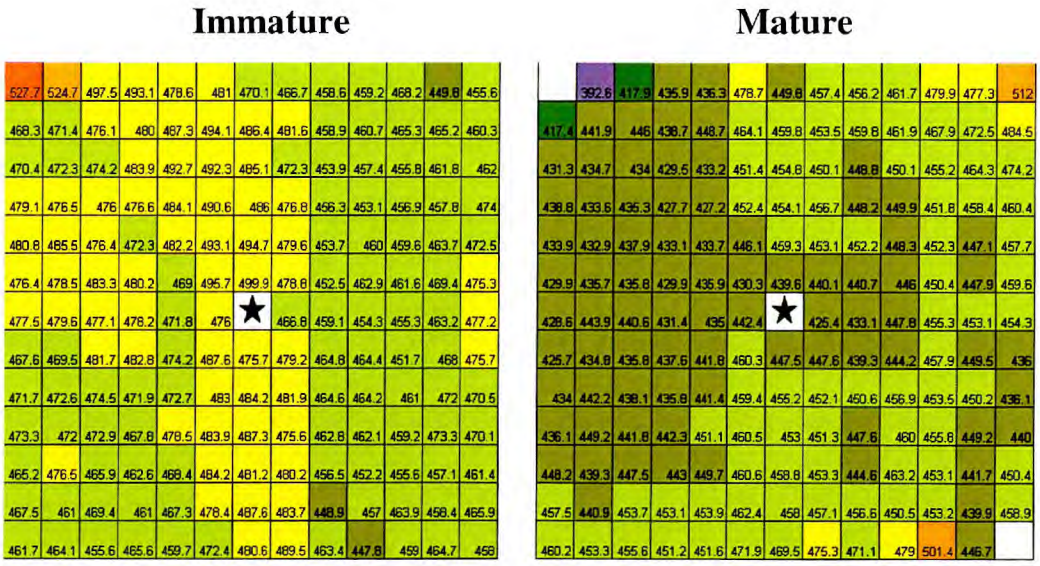

Fig. 5.44. Area (pixels^2) of rabbit endothelial cell nuclei for branches within the upper portion of the descending thoracic aorta (branches 1 to 6, branch 1 being the first branch downstream from the aortic arch). Each square represents a 500μm * 500μm region. The total area of the map is 42.25mm^2. n = 4 immature rabbits, n = 4 mature rabbits. Data represent averages for 21 immature and 14 mature branches.

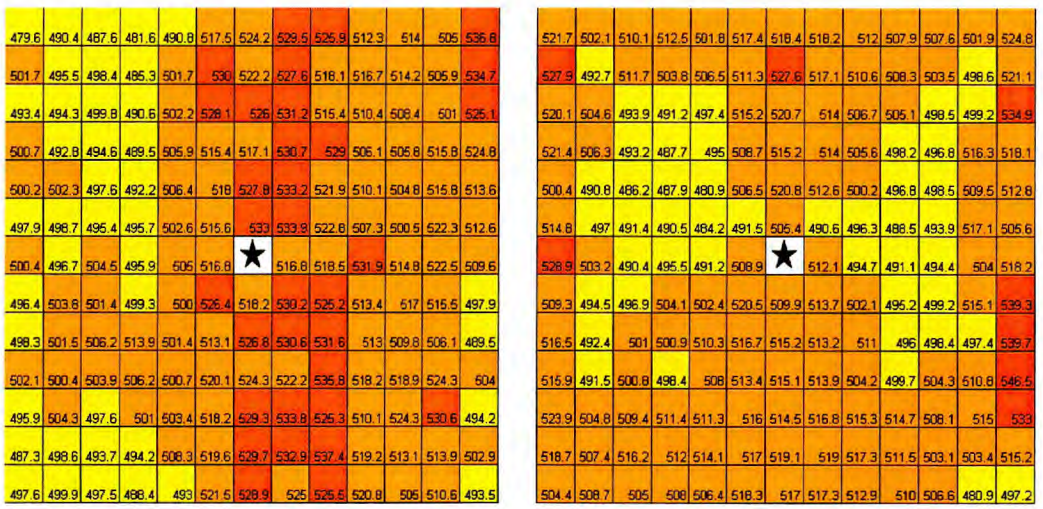

Fig. 5.45. Area (pixels^2) of rabbit endothelial cell nuclei for branches within the lower portion of the descending thoracic aorta (branches 7 to 12). Each square represents a 500μm * 500μm region. The total area of the map is 42.25mm^2. n = 4 immature rabbits, n = 4 mature rabbits. Data represent the means for 15 immature and 20 mature branches.

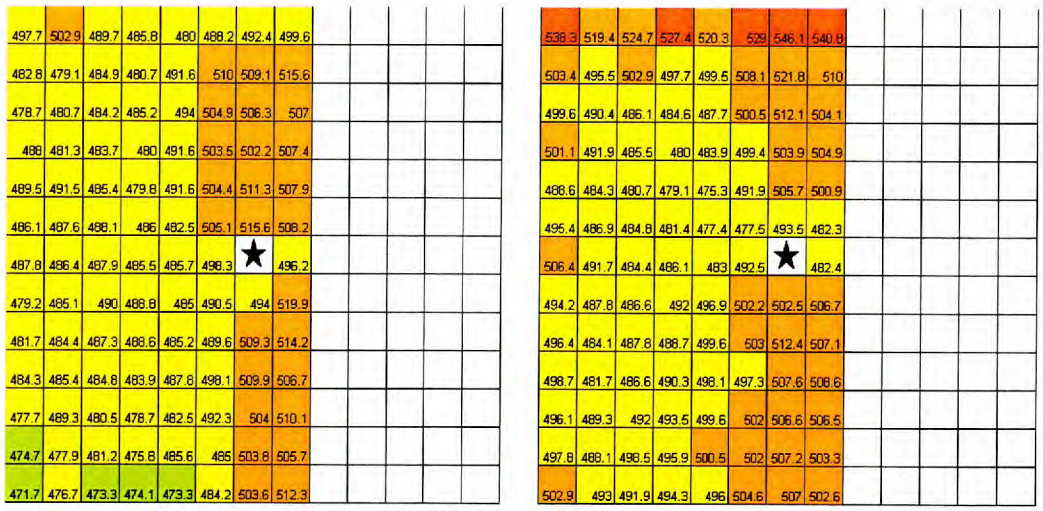

Fig. 5.46. Area (pixels^2) of rabbit endothelial cell nuclei for branches within the anatomical right hand side of the descending thoracic aorta. (Maps are truncated to avoid affects of flow around ostia on the left hand side). Each square represents a 500μm * 500μm region. The total area of the map is 26.0mm^2. n = 4 immature rabbits, n = 4 mature rabbits. Data represent averages for 17 immature and 17 mature branches.

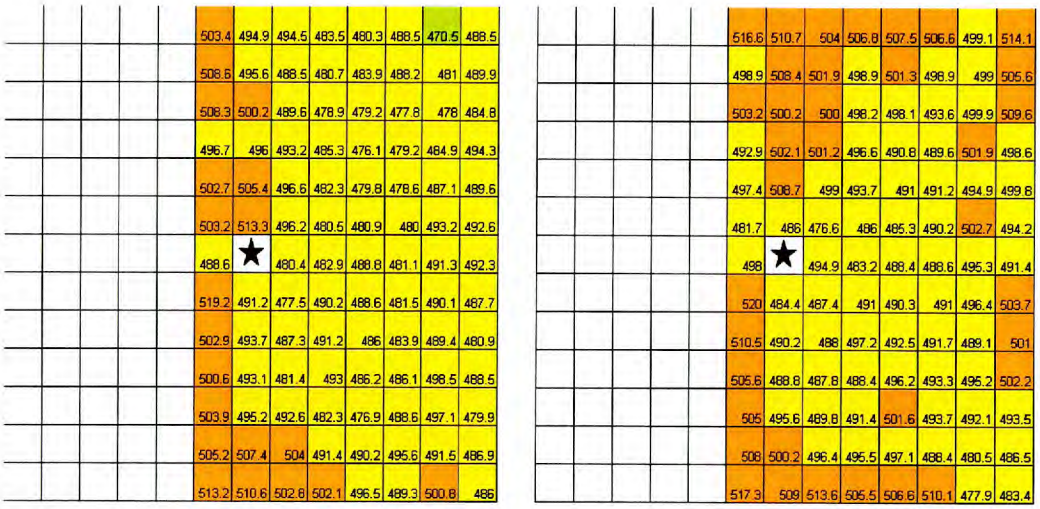

Fig. 5.47. Area (pixels^2) of rabbit endothelial cell nuclei for branches within the anatomical left hand side of the descending thoracic aorta. (Maps are truncated to avoid affects of flow around ostia on the right hand side). Each square represents a 500μm * 500μm region. The total area of the map is 26.0mm^2. n = 4 immature rabbits, n = 4 mature rabbits. Data represent averages for 18 immature and 17 mature branches.

Table 5.39. Area (pixels^2) of nuclei within Zone A, for branch ostia within upper and lower portion of the descending thoracic aorta, where n equals the number of branches.

	UPPER				LOWER			
Region	Immature		Mature		Immature		Mature	
	Mean	SEM	Mean	SEM	Mean	SEM	Mean	SEM
U2R2	482.20	13.63	433.73	11.53	506.42	15.87	480.92	8.68
U2R1	493.10	10.94	446.09	8.67	518.04	13.01	506.53	6.46
U2	494.74	11.23	459.29	7.55	527.83	14.06	520.83	5.94
U2L1	479.57	10.44	453.07	10.20	533.23	14.31	512.57	6.55
U2L2	453.69	15.80	452.24	13.17	521.94	19.18	500.25	10.04
U1R2	469.00	16.35	435.91	12.96	502.64	16.49	484.18	11.03
U1R1	495.74	9.80	430.26	10.62	515.62	11.54	491.52	8.03
U1	499.89	11.88	439.64	9.19	532.99	14.13	505.37	7.44
U1L1	478.85	12.70	440.14	9.78	533.93	12.56	490.62	7.57
U1L2	452.49	16.49	440.66	10.09	522.80	20.33	496.25	12.21
R2	471.78	17.56	434.99	13.75	504.97	16.38	491.18	13.83
R1	476.00	11.27	442.43	9.30	516.78	12.69	508.93	7.08
L1	466.83	10.99	425.40	8.00	516.79	10.28	512.09	16.51
L2	459.15	14.64	433.15	9.43	518.55	17.14	494.68	7.57
D1R2	474.17	13.95	441.78	12.62	500.01	14.02	502.36	9.90
D1R1	487.56	10.27	460.32	10.30	526.44	12.64	520.51	7.03
D1	475.66	10.90	447.47	10.13	518.19	14.29	509.86	7.99
D1L1	479.23	12.96	447.63	7.08	530.19	13.10	513.71	8.94
D1L2	464.80	14.38	439.31	9.33	525.19	22.08	502.08	11.24
D2R2	472.67	14.85	441.43	10.43	501.43	18.20	510.28	9.72
D2R1	483.02	10.30	459.36	7.86	513.15	12.60	516.65	6.52
D2	484.15	10.72	455.21	7.97	526.75	13.65	515.17	7.22
D2L1	481.95	10.84	452.11	7.12	530.57	13.79	513.19	7.60
D2L2	464.57	15.35	450.57	9.82	531.59	24.26	510.95	12.63
Total Mean	**479.30**	**2.53**	**444.93**	**1.99**	**521.16**	**2.92**	**506.57**	**1.89**

Table 5.40. Area (pixels^2) of nuclei within Zone A, for branch ostia within the anatomical right and left of the descending thoracic aorta, where n equals the number of branches.

	RIGHT				LEFT			
Region	Immature		Mature		Immature		Mature	
	Mean	SEM	Mean	SEM	Mean	SEM	Mean	SEM
U2R2	-	-	-	-	491.62	11.00	475.30	10.51
U2R1	502.66	12.38	497.42	9.47	504.37	12.73	491.90	11.60
U2	505.44	13.89	508.65	9.18	511.28	12.93	505.65	9.16
U2L1	496.61	15.25	499.03	8.86	507.85	12.70	500.87	11.50
U2L2	482.32	15.41	493.73	8.93	-	-	-	-
U1R2	-	-	-	-	482.46	12.75	477.36	10.70
U1R1	503.15	11.42	481.67	9.78	505.12	10.88	477.51	11.04
U1	513.34	14.09	485.99	9.36	515.64	13.52	493.51	11.91
U1L1	496.23	16.48	476.61	9.71	508.18	13.03	482.26	10.56
U1L2	480.46	15.85	485.99	9.85	-	-	-	-
R2	-	-	-	-	485.72	13.29	483.00	12.85
R1	488.63	13.47	498.01	9.12	498.35	12.92	492.52	12.17
L1	480.44	12.61	494.90	21.37	496.17	12.57	482.39	11.87
L2	482.93	13.68	483.17	9.43	-	-	-	-
D1R2	-	-	-	-	485.04	10.77	496.93	12.20
D1R1	519.24	12.87	519.99	9.37	490.51	11.17	502.25	12.04
D1	491.24	14.71	484.40	11.48	494.05	12.66	502.52	9.71
D1L1	477.48	15.60	487.45	10.39	519.86	12.80	506.66	12.94
D1L2	490.15	14.57	491.01	10.86	-	-	-	-
D2R2	-	-	-	-	485.18	12.34	499.61	12.48
D2R1	502.89	13.49	510.50	8.60	489.58	10.73	503.02	11.36
D2	493.73	13.97	490.20	9.87	509.30	12.29	512.42	10.23
D2L1	487.26	14.60	487.97	8.50	514.16	12.21	507.10	12.06
D2L2	491.23	15.62	497.18	9.62	-	-	-	-
Total Mean	**494.07**	**3.24**	**493.36**	**2.43**	**499.60**	**2.82**	**494.39**	**2.63**

5.3.6 Endothelial cell density

Within the regions outlined in Fig. 5.3, there was no significant change in the number of nuclei with age (P=0.77), but there was a highly significant effect of region and a significant interaction between age and region (both P<0.005).

Within Zone A* there was no significant change in the number of cells with age (P=0.34) but there was significant difference between regions, and a significant interaction between age and region (both P<0.005) (Fig. 5.48, Table 5.41). The mean number of nuclei per region ranged from 119.7 ± 4.9 ("U3L1", n = 34 branches) to 146.7 ± 2.7 ("U1L3", n = 32 branches), a 22.6% difference, in immature rabbits, and

between 117.1 ± 3.0 ("D2R3", n = 32 branches) and 157.3 ± 4.4 ("U2", n = 32 branches) in mature rabbits (a 34.3% difference). The ratio of the number of nuclei upstream of the ostia (region "U2") to the number of nuclei downstream (region "D2"), was 1.00 and 1.19 in immature and mature rabbits respectively. The significance of differences in cell density between regions in Zone A are shown in Fig. 5.49.

The number of cells in Zone B* were also not significantly different between ages (P=0.54), but there was a difference between regions (P<0.005) (Fig. 5.48, Table 5.42). There was no significant interaction between age and region (P=0.09). The number of nuclei within regions in Zone B* ranged from 123.4 ± 4.7 ("U4", n = 34 branches) to 146.4 ± 2.7 ("U1L4", n = 27 branches), a difference of 18.6% in immature rabbits, and in mature rabbits the number of cells ranged from 121.4 ± 3.3 ("D3R4", n = 28 branches) to 146.6 ± 3.6 ("U1L4", n = 30 branches); a 20.8% difference.

In immature rabbits the mean number of cell nuclei within Zone A* (133.0 ± 0.6 nuclei, n = 1320 regions) was significantly lower than the mean number in Zone B* (134.9 ± 0.7 nuclei, n = 976 regions) (a 1.4 % difference) (P<0.05). In mature rabbits, there was a higher nuclear density in Zone A* (135.4 ± 0.7 nuclei, n = 1320 regions) than in Zone B* (131.1 ± 0.6 nuclei, n = 992 regions) (3.3% difference) (P<0.005).

Fig. 5.48. The number of endothelial cell nuclei for all branch ostia. Each square represents the data for a 250μm*250μm region. Total area of map is 6.25mm^2. n = 4 immature rabbits, n = 4 mature rabbits. Data represent average for 36 immature and 38 mature branches.

Table 5.41. Mean number of endothelial cell nuclei within each region in Zone A*, where n equals the number of branches.

	Immature		Mature	
Zone A*	Mean	SEM	Mean	SEM
U3R3	135.4	2.3	137.2	3.9
U3R2	124.5	4.1	132.7	3.9
U3R1	122.3	4.6	135.7	4.1
U3	124.1	3.7	130.9	4.5
U3L1	119.7	4.9	139.8	3.3
U3L2	132.2	4.1	140.2	3.7
U3L3	135.1	3.8	137.7	3.1
U2R3	137.8	2.5	146.9	3.4
U2R2	127.8	2.5	148.5	4.8
U2R1	124.3	5.0	154.0	4.7
U2	130.3	3.6	157.3	4.4
U2L1	129.1	4.5	156.6	4.5
U2L2	133.5	5.0	151.4	5.2
U2L3	137.0	4.7	147.4	3.3
U1R3	145.6	2.2	146.8	3.1
U1R2	135.4	5.0	136.8	7.7
U1L2	139.0	4.2	153.3	6.6
U1L3	146.7	2.7	152.7	3.3
R3	139.6	2.4	131.3	4.1
R2	131.9	3.2	131.3	6.3
L2	130.3	5.7	148.6	4.5
L3	139.1	4.6	140.5	4.2
D1R3	138.1	2.3	123.4	3.4
D1R2	129.8	3.0	126.6	3.9
D1L2	139.2	3.1	132.4	4.0
D1L3	139.1	3.0	130.7	3.6
D2R3	130.2	2.7	117.1	3.0
D2R2	127.9	3.4	121.9	4.3
D2R1	129.7	5.7	131.4	5.2
D2	130.9	5.3	131.9	4.9
D2L1	133.8	4.2	124.9	4.0
D2L2	132.8	3.5	123.2	3.1
D2L3	137.9	3.7	127.1	3.6
D3R3	132.6	2.8	123.1	3.2
D3R2	127.8	4.7	120.8	3.5
D3R1	128.7	4.8	123.4	4.2
D3	132.7	4.6	126.9	4.3
D3L1	139.5	2.6	123.2	3.5
D3L2	135.7	2.7	123.9	2.9
D3L3	137.7	2.9	126.4	3.3
Total mean	**133.0**	**0.6**	**135.4**	**0.7**

Table 5.42. Mean number of endothelial cell nuclei within each region in Zone B*, where n equals the number of branches.

Zone B*	Immature		Mature	
	Mean	SEM	Mean	SEM
U4R4	133.7	4.8	139.5	3.3
U4R3	136.4	2.6	133.3	2.4
U4R2	131.6	3.0	128.6	2.6
U4R1	128.4	4.0	126.5	3.1
U4	123.4	4.7	125.2	3.1
U4L1	129.6	2.7	132.1	3.2
U4L2	128.7	4.9	136.4	3.0
U4L3	134.8	3.3	134.4	2.7
U4L4	138.6	5.6	136.9	3.4
U3R4	140.4	2.1	135.4	3.6
U3L4	138.9	4.7	137.4	3.5
U2R4	141.9	2.8	137.2	5.7
U2L4	144.5	3.7	142.9	3.2
U1R4	139.4	3.4	136.5	5.9
U1L4	146.4	2.7	146.6	3.6
R4	144.1	2.6	130.3	4.9
L4	145.0	2.2	142.4	4.1
D1R4	133.1	4.7	125.9	3.7
D1L4	134.3	5.2	137.1	3.5
D2R4	127.7	4.7	123.9	3.2
D2L4	134.5	5.5	127.9	3.4
D3R4	135.5	3.2	121.4	3.3
D3L4	134.1	3.4	127.0	3.6
D4R4	134.2	2.9	125.2	2.7
D4R3	127.9	4.6	124.1	2.6
D4R2	127.8	3.3	125.5	2.7
D4R1	127.9	4.2	123.8	3.7
D4	137.0	3.3	129.0	3.4
D4L1	134.9	2.9	125.6	3.2
D4L2	140.1	2.1	125.1	2.8
D4L3	133.6	4.4	128.4	2.9
D4L4	139.3	2.6	128.3	3.0
Total mean	**134.9**	**0.7**	**131.1**	**0.6**

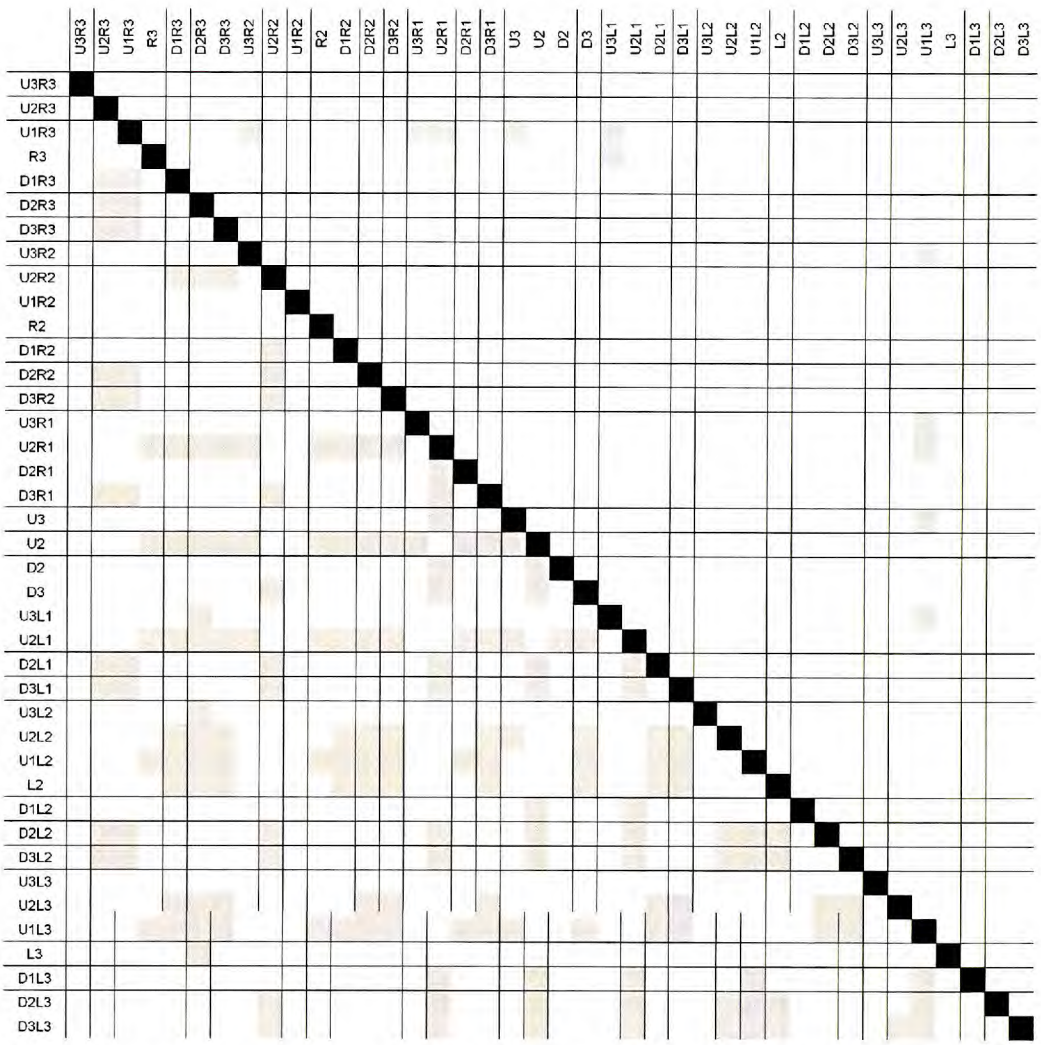

Fig. 5.49. Significant differences in number of endothelial cell nuclei within 250μm * 250μm regions in Zone A* (see Fig 5.1). Squares shaded in grey depict where there are significant differences ($P<0.05$) between regions. Squares to the right of the black diagonal line indicate where differences lie, in immature rabbits. Squares to the left indicate differences in mature rabbits.

5.3.7 Summary of main rabbit results

- There were significant differences between immature and mature rabbits for endothelial nuclear LW ratio, length and width, but no significant change for nuclear orientation, nuclear area or cell density
- There was a significant effect of region for all nuclear parameters analysed
- There was a significant interaction between age and region (suggesting a change in pattern) for all nuclear parameters analysed

- Nuclei were more elongated in mature rabbits than in immature
- In immature rabbits nuclei were in general more elongated downstream than upstream of branch ostia. This pattern reversed in mature rabbits; nuclei were more elongated upstream than downstream
- Change in pattern of nuclear length resembled the change in pattern of LW ratio, but nuclear width showed the opposite change
- Nuclei became less elongated as the distance from the aortic arch increased in both age groups
- Nuclear orientations in lateral regions of branch ostia had their distal ends angled sharply towards the ostium, the sharpest angles being level with the proximal edge of the ostium
- Downstream of the flow divider, orientations almost align parallel to the aortic axis
- In general, away from ostia, on the anatomical right of the aorta, nuclei lean to the anatomical left and vice versa

5.3.8 Results from Mouse aortas

Results are presented as colour maps to show the mean nuclear LW ratios, angle of orientation and area for a Balb/c mouse (Fig. 5.50), an eNOS-GFP mouse (Fig. 5.51), and a Wild-type (WT) mouse (Fig. 5.52). Statistical analyses were not carried out due to the small number of aortas examined. The mean LW ratios for the Balb/c, eNOS-GFP, and WT mice were 2.62 (range 1.55 to 5.84), 1.92 (range 1.23 to 3.71) and 1.98 (range 1.10 to 3.65) respectively. For all mice, there appeared to be strips of high and low nuclear LW ratios and large or small nuclear areas running diagonally down the aortas. This diagonal pattern was not visible in maps of nuclear orientations as the angles were normalised so that the mean was zero for each mouse. The mean nuclear area was 477pixels^2 (range 148 to 636pixels^2), 425pixels^2 (range 159 to 644pixels^2) and 431pixels^2 (range 199 to 679pixels^2) for Balb/c, eNOS-GFP and WT mice respectively. Nuclei just distal to the aortic arch appeared to have much lower nuclear areas than those elsewhere.

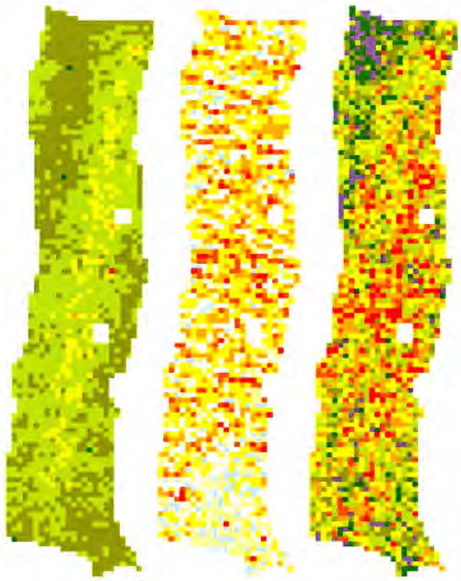

Fig. 5.50. Colour maps produced of nuclear morphologies from an EStAR preparation of the descending thoracic aorta of one Balb/c mouse. Each coloured square represents the nuclear LW ratio (left), angle of orientation (centre), and area (pixels^2) (right) for 100μm * 100μm regions. The length of the section of aorta is approximately 11.4mm. Mean blood flow is from top to bottom of the image.

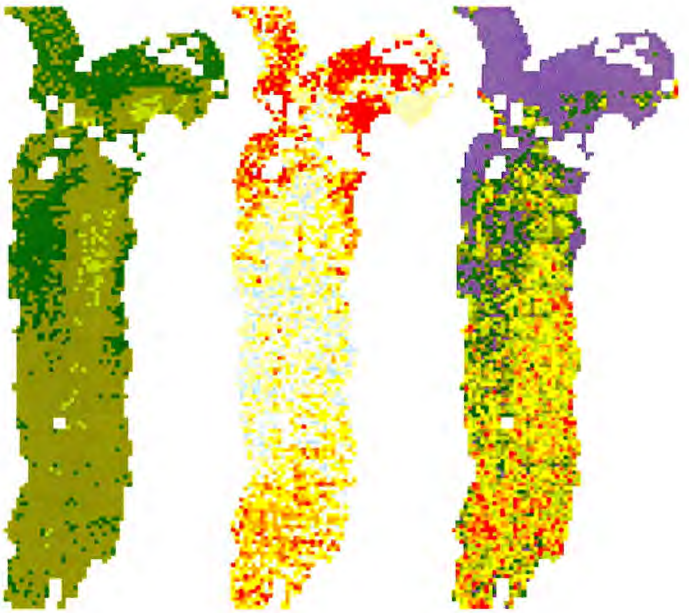

Fig. 5.51. Colour maps produced of nuclear morphologies from an EStAR preparation of the descending thoracic aorta of one eNOS-GFP mouse. Each coloured square represents the nuclear LW ratio (left), angle of orientation (centre), and area (pixels^2) (right) for 100μm * 100μm regions. The length of the section of aorta is approximately 16.0mm and includes the aortic arch at the top of the image. Mean blood flow is from top to bottom of the image.

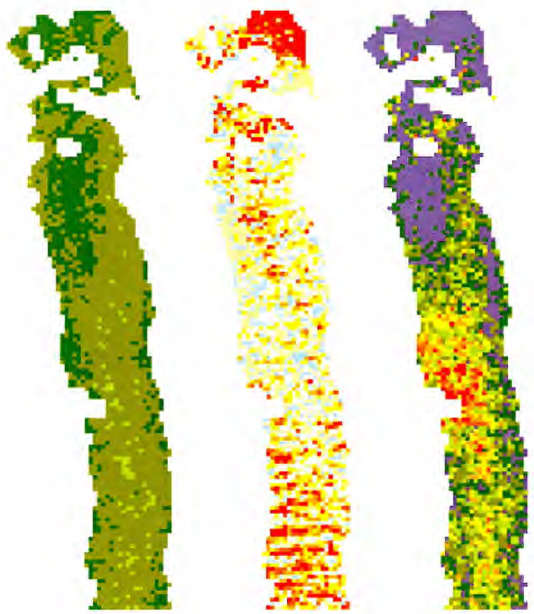

Fig. 5.52. Colour maps produced of nuclear morphologies from an EStAR preparation of the descending thoracic aorta of one wild-type mouse. Each coloured square represents the nuclear LW ratio (left), angle of orientation (centre), and area (pixels^2) (right) for 100μm * 100μm regions. The length of the section of aorta is approximately 15.5mm and includes the aortic arch at the top of the image. Mean blood flow is from top to bottom of the image.

5.3.9 Results for pig aortas

The mean LW ratio, angle of orientation, and area of endothelial cell nuclei in regions near a branch of one pig aorta (Fig. 5.53) are shown in Fig. 5.54. The mean LW ratio was 1.60 ± 0.01, and values ranged from 1.38 to 2.15. The mean angle of orientation was normalised as has been described previously and was therefore zero degrees; values ranged from -29.81 to 23.43°. The mean area was 297.4 ± 2.16pixels^2 and values ranged from 226.0 pixels^2 to 453.1 pixels^2.

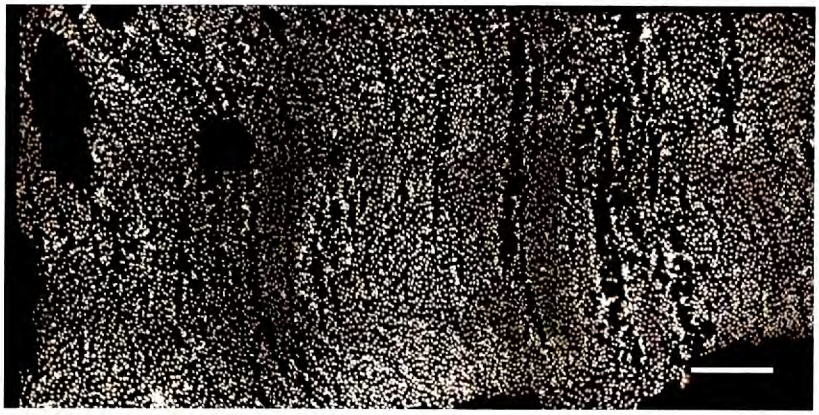

Fig. 5.53. *En face*, EStAR, preparation of propidium iodide stained nuclei in the region analysed around a pig aortic branch. The branch ostium is located at the bottom right of the image. Mean blood flow is from top to bottom. Bar = 200μm.

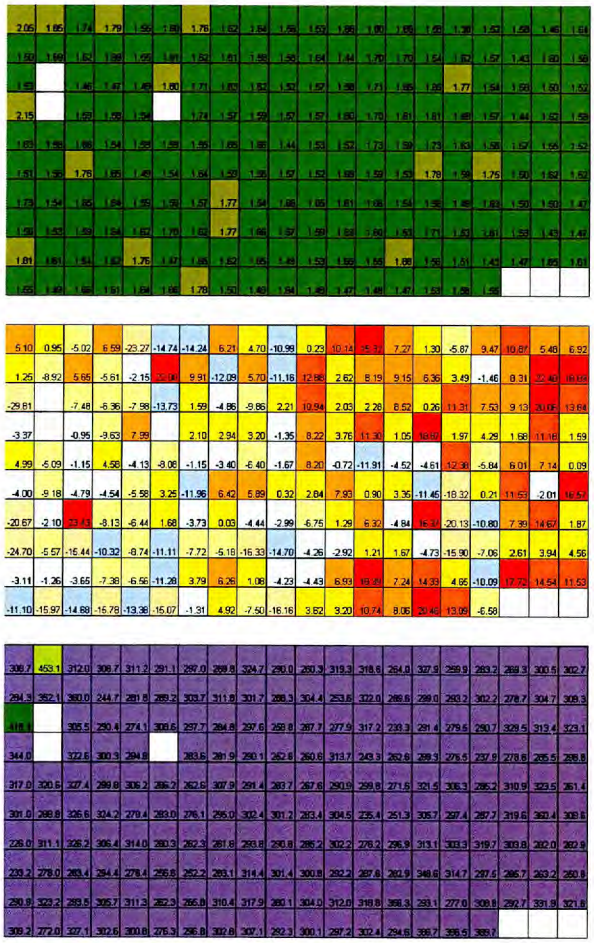

Fig. 5.54. Colour maps showing average nuclear LW ratio (top), angle of orientation (°) (middle) and area (pixels^2) (bottom) in 100μm*100μm regions in an area upstream of a pig aortic branch (see Fig. 5.53). The total area of the map is 2mm^2.

5.4 Discussion

This study has shown that it is possible to produce detailed maps of the shape of endothelial cell nuclei surrounding intercostal branch ostia in the thoracic aortas of rabbits and pigs, and it is possible to produce maps of the whole descending aorta, including the aortic arch, in mice. The maps produced have enabled us to observe changes in nuclear shape over small areas of the aortic wall ($0.01mm^2$) in considerable detail. As described previously, changes in shape and orientation of endothelial cells and their nuclei have been shown to be dependent on blood flowing across the endothelium, cells and nuclei elongating in regions of higher flow rates, and aligning with the time averaged flow direction.

5.4.1 Nuclear elongation in rabbits

Mature rabbits had more elongated nuclei than immature rabbits in all regions. The pattern of nuclear elongation also changed with age. Between 1.5 and 11 months (or 1.6 and 3.8kg), nuclei become relatively more elongated in regions upstream of the branch; the ratio of LW values upstream to those downstream changed from <1 to >1 when looking at regions measuring $0.25mm^2$. In immature rabbits this difference was significant. When nuclei within the sub-regions immediately upstream and downstream of the branch ostia (within 100μm of the branch) were examined, in both age groups, the ratio was <1, the nuclei being more elongated downstream than upstream. This may be due to faster flowing blood from the centre of the aorta impinging on the flow divider as postulated by Caro *et al* (1985) (Fig. 1.10). In the region 100-200μm upstream and downstream of the ostia, the ratio changed from <1 to >1 with age. Figure 5.8 shows the nuclear LW ratios along a longitudinal line through the centre of the branch ostium. Although LW ratios are higher in mature rabbits, upstream of the branch the pattern of elongation is very similar; LW ratios remain fairly constant up to approximately 500μm upstream, and then the nuclei become less elongated the closer they are to the branch. In both immature and mature rabbits, within approximately 200μm downstream of the branch, the nuclei are more elongated than those in the regions on the proximal ostial lip, but at this point the patterns change. In immature rabbits the nuclei become more elongated within the next 100μm, before gradually becoming less elongated the further away they are from the branch ostia. In mature rabbits, approximately 300μm

downstream of the branch, the nuclei become less elongated before gradually becoming more elongated further away from the branch.

Our data for nuclear elongation are in agreement with those of Al-Musawi *et al* (2004). However, they contradict earlier theories concerning atherogensis and flow. As described previously in this thesis, the consensus is that lipid deposition and atherosclerosis develop in regions of low shear stress (Caro et al., 1971, Zarins et al., 1983, Asakura and Karino, 1990, Gnasso et al., 1997). Previous work has shown that lipid deposition and atherosclerosis are greatest downstream of branch ostia in immature rabbits (Ivey et al., 1995, Barnes and Weinberg, 1998) and humans (Sinzinger et al., 1980), and greatest upstream and laterally in mature rabbits (Barnes and Weinberg, 1998, 1999) and humans (Sloop et al., 1998), the downstream region being free of disease. If the low shear stress theories of disease development are true we would expect to see more rounded nuclei downstream than upstream in young, and more rounded upstream than downstream in old; this is the reverse of what our data show. Our data imply that atherosclerosis develops in regions of higher shear stresses as previously proposed by Fry (1969). However, a more recent theory is that atherosclerosis develops in regions of oscillatory flow, where the shear fluctuates in magnitude over the period of the cardiac cycle, yielding time-averaged shear values close to zero. This occurs primarily downstream of stenoses, at the lateral walls of bifurcations, and in the vicinity of branch points (reviewed by Chatzizisis et al., 2007). It could be that with age the oscillatory nature of flow changes in the vasculature, causing changes in shear stress values around branches.

The change in pattern of nuclear length resembled the change in LW ratio, in that the ratio of length upstream to downstream (within $0.25mm^2$ regions) changed with age from <1 to >1. Nuclear width showed the opposite pattern, changing from >1 to <1 with age. Nuclei within 1000μm of the branch ostia (Zone A) were 14% longer and 15% narrower in mature rabbits than in immature. These data suggest that LW ratio, at least in these regions, is the most sensitive indicator, combining the effects of opposite trends in length and width. Changes in nuclear morphology are relatively small. In immature rabbits, the differences between minimum and maximum values were only 5% and 8%

for length and width respectively, and in mature rabbits the differences were only 4% and 8% for length and width. Hence the advantage gained from combining both trends, by using LW ratios, is significant.

High resolution colour maps produced for nuclear lengths (Fig.5.27) do appear to correlate with the disease patterns seen in the different age groups (if small regions at the branch lip are ignored), and maps produced for nuclear widths (Fig. 5.35) inversely correlate with disease. Shorter and wider nuclei were located upstream of the branch ostia in immature rabbits, a region of lower lipid deposition, and in the mature rabbits the shorter and wider nuclei are downstream of the branch, in a triangular pattern that correlates with the region spared of disease at that age (see Fig. 1.3).

Nuclei in regions further away from the branch (2000-3000μm) had lower LW ratios than those in regions nearer to the branch (when looking at branch ostia from the whole aorta). This could be due to these regions being beyond the influence of altered haemodynamics caused by the flow divider and branch ostium.

Nuclei in the regions surrounding ostia from the lower portion of the descending thoracic aorta were significantly more elongated than nuclei in the upper portion for both age groups. This could be due to an increase in shear stress caused by the decreasing diameter of the aorta (Fig. 5.55). As a vessel becomes narrower, such as during a stenosis, the shear stress increases (Levesque *et al.*, 1986). If branch ostia in the abdominal aorta had also been studied here, it is thought that the ECn would have become even more elongated due to the increased shear stress. This has previously been shown using vascular casts to look at EC shape in rabbits (Cornhill *et al.*, 1980); the postulate flow patterns perhaps provide an explanation for the increased disease prevalence in this region (compared to the thoracic aorta) in humans (Glagov et al., 1961).

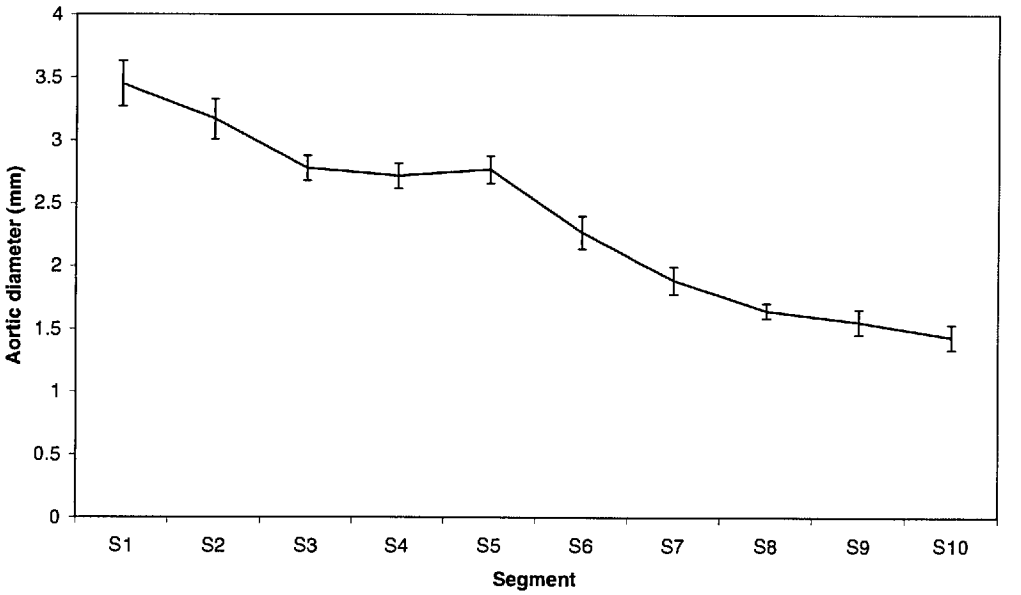

Fig. 5.55. Adult New Zealand White rabbit aortic diameters (mm). Segments 1 to 5 are from the thoracic aorta, 6 to 10 are from the abdominal aorta (Segment 1 - within ascending aortic arch, 10 = level of the caudal mesenteric artery). Graph produced from data in Dabanoglu, 2000).

Nuclei surrounding ostia on the anatomical left side were significantly longer than those surrounding ostia from the right of the aorta, in both age groups. Out of the 35 pairs of branch ostia analysed, the anatomical left hand ostia was situated further upstream than the right in only four of the pairs. This may have caused the flow patterns impinging on the left hand ostia to have been affected by those flowing over the right.

5.4.2 Nuclear orientation in rabbits

Our study has shown that it is important to look at the changes in nuclear morphology at high resolution. An example of this arose when examining nuclear orientation. Data for nuclear orientation within 0.25mm^2 regions enable us to see general changes, such as that the majority of nuclei on the anatomical right of the branch ostia have nuclei leaning to the anatomical left, and vice versa. However, it was possible to see other changes around the branch ostia when looking at 0.01mm^2 regions. Nuclear orientations around the branch ostia in 0.25mm^2 regions within Zone A did not change significantly with age

but when examining 0.01mm^2 regions (Fig. 5.16-5.18) there were substantial changes between regions.

In both age groups, the nuclei in the lateral regions had their distal ends angled sharply towards the ostium, the sharpest angles being level with the proximal edge of the ostium. Directly upstream of the ostia, nuclei to the anatomical right and left of the longitudinal midline again had negative and positive angles respectively. These results suggest that blood is entering the branch from its sides as well as from upstream. In line with the distal edge of the ostium, the angles suddenly change from being positive to negative, or vice versa. It is thought that this line corresponds approximately to where the flow divider extends out from the distal lip of the ostia. Although no measurements were made, and no previous data have been found, the impression was gained that the flow divider was more pronounced (wider and deeper) in mature rabbits. If the flow divider were larger, the blood may get drawn into the ostium from a larger region, hence causing a change in nuclear orientation. The colour maps appear to show that this is the case; the distance upstream from the ostium where the nuclei are oriented away from the longitudinal axis by more than 5° is larger in mature rabbits (~400μm) than in immature ones (~200μm). Another explanation for this may be the presence of an intimal cushion on the upstream margin of branches, previously seen in mature, but not immature rabbits (Staughton & Weinberg, unpublished data, 2000). A cushion may cause the flow of blood to be diverted away from the longitudinal axis of the aorta, further upstream, more than if no cushion were present. It is surprising that nuclear elongation did not also change visibly at the level of the flow divider. It may have been that, within the 100μm * 100μm regions observed, changes in the LW ratios upstream and downstream of the flow divider averaged each other out. Measuring nuclei within even smaller regions (e.g. 50μm * 50μm) would allow this to be confirmed or ruled out.

The mean orientation of nuclei within a sub-region was never exactly aligned with the longitudinal axis of the aorta (0°), suggesting that blood flow is rarely axial. Within the regions surrounding the branch ostium, we did not observe a double spiral pattern that would provide evidence of counter-rotating Dean vortices within the aorta (Fig. 5.56), as has been suggested by other investigators (Flaherty et al., 1972, Chien, 2003), but this

may reflect the fact that the ostia we examined do not lie on the dorsal or ventral midline of the aorta. Dean vortices are established within the aortic arch when the faster moving blood in the centre of the flow stream has too much inertia to turn and follow the curve of the arch. The velocity profile becomes skewed towards the outer wall causing the faster moving blood to impinge on the wall itself. This results in secondary flows in which the blood moves in opposite directions, forming the vortices shown. If present, it is thought that the nuclei in one half of the aorta would have predominantly positive angles, whilst those in the other half would have negative angles.

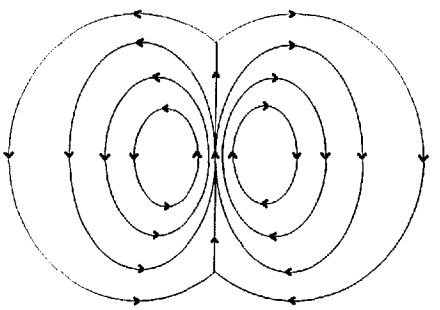

Fig. 5.56. Simplified diagram of Dean vortices in cross-section through a curved pipe. Arrows indicate direction of blood flow in the plane of the section. The vortices rotate in opposite directions.

Individual colour maps of nuclear orientation were pieced together to reconstruct the majority of the aorta (Figs. 5.57 and 5.58). Longitudinal stripes of oppositely aligned nuclei (positive vs. negative angles) were visible next to each other, and could have been caused by such Dean vortices. The patterns differ from those seen in mice (Figs. 5.50-5.52). 3-D modelling of the aorta showing the alignment of the nuclei would enable the helical arrangement to be visualised.

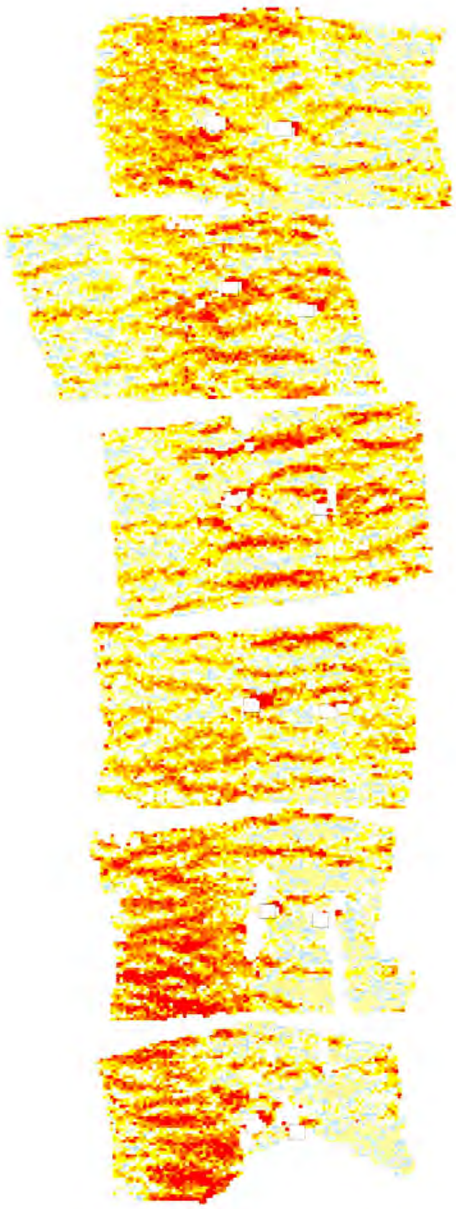

Fig. 5.57. Colour maps depicting the nuclear orientation within the aorta of an immature rabbit (I1). The orientation within each separate EStAR preparation was normalised by a constant that made the mean angle zero. Blood flow is from the top to bottom of the image. Branch ostia (n = 12) are marked with squares. The length of the aorta analysed is approximately 40mm. Nuclei with their upstream end leaning to the left of the longitudinal axis, as viewed on the screen, have negative angles (coloured blue, pink and yellow), and conversely, those with their upstream end leaning to the right were assigned positive angles (coloured red and orange) – See Fig. 4.5 for key.

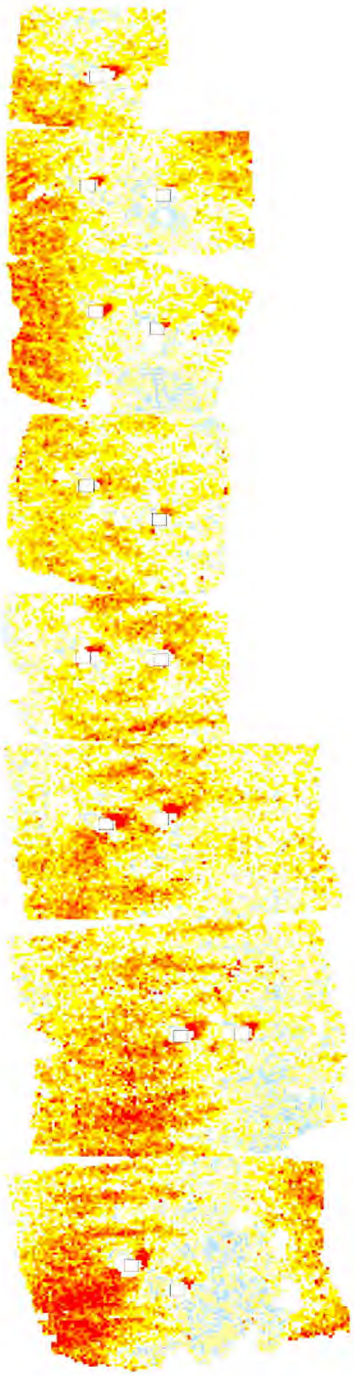

Fig. 5.58. Colour map depicting the nuclear orientation within the aorta of a mature rabbit (M2). The orientation within each separate EStAR preparation was normalised by a constant that made the mean angle zero. Blood flow is from the top to bottom of the image. Branch ostia (n = 15) are marked with a square. The length of the aorta analysed is approximately 56mm. Colour coding is the same as in Fig. 5.57.

5.4.3 Nuclear Area in rabbits

Our study has shown that there is no significant change in nuclear area with age in regions surrounding the branch ostia (Zone A) or further away from the branch (Zones B and C). In immature rabbits the nuclei were larger upstream of the branch than at the lateral regions or downstream. In mature rabbits the nuclei were smaller at the lateral regions, upstream of the approximate level of the flow divider, and upstream of the branch. Eskin (1984) suggested that cells undergo hypertrophy in regions of low shear stress under pulsatile conditions, so it would be expected that larger nuclei would be found upstream of the branch in immature rabbits, and downstream in old (due to shear stresses predicted from our ECn LW ratio data). In immature rabbits this is true, but in mature rabbits immediately downstream the nuclei were smaller than upstream of the branch, although there was a region of larger nuclei 400μm downstream of the ostia. In both immature and mature rabbits, nuclei surrounding ostia in the upper aorta were smaller than nuclei in the lower aorta, again suggesting that nuclei become larger in areas of increased shear stress.

5.4.4 Cell density in rabbits

The number of ECn can be used as a measure of the number of endothelial cells, as every cell has one nucleus. It was thought that the cell density would be greater in immature rabbits than mature rabbits, as this pattern has previously been shown in young and old humans (Repin *et al.*, 1984). However, our study found no significant change in the mean number of nuclei per region with age. This could be due to genuine differences between rabbits and humans, the presence of atherosclerotic lesions in the adult human vessels, or to different methods of counting cells (measured by hand vs. measured automatically by image analysis software). In immature rabbits the ratio of the number of cells upstream to downstream was 1.00 suggesting that the number of cells did not change in regions of higher shear stresses. However, in mature rabbits the ratio was 1.19, demonstrating that there were more cells upstream of the ostia than downstream.

5.4.5 Nuclear shape and orientation in mouse aortas

In all three mice studied, there appeared to be large variations in nuclear elongation, orientation and size. This may reflect lack of practice making EStAR preparations of whole aortas, which led to regions where the endothelium was missing or damaged, particularly in the aortic arch (where present). It is felt that with practice this problem could be alleviated and the EStAR technique will be a valuable tool in studying the endothelium of mice.

The nuclear LW ratios of the Balb/c mouse were approximately 30% higher than those in the other mice. Unfortunately, due to the small number of mice studied it is unclear whether this is a genuine difference or a statistical fluctuation. In all mice there was a spiral pattern running down the length of the aorta where nuclei are more elongated, implying a region of higher shear stress. However, despite deviations away from the longitudinal axis, nuclear orientations do not give the impression of spiralling flow (Fig. 5.51 and 5.52). Blood flow in mice is less inertial than in rabbits, having peak Reynolds numbers of ~250, and in mice secondary flows are fewer (Feintuch *et al.*, 2007) and less significant than in e.g. humans (Suo *et al.*, 2007).

The area of the nuclei did not appear to change much between mice. However, within the region of the aortic arch, the nuclei were much smaller than in the rest of the aorta. Our work with rabbits appeared to suggest that nuclear area increases in regions of higher shear stress. It could therefore be suggested that in mice the aortic arch is a region of lower shear stress. Again, interpretation of these results requires caution due to the small numbers of aortas observed, and possible damage to the endothelium.

5.4.6 Nuclear shape and orientation in a pig aorta

Endothelial cell nuclei in the aorta of a pig were more rounded, and had a smaller area, than those in mice or rabbits. The aorta was not fixed at pressure before excision so when removed it is likely to have contracted and may have caused the nuclei to have an inaccurate shape. Due to the small region of endothelium observe, it is unclear how accurate the data for orientation of the nuclei are. Again due to the lack of pressure fixation, the results may be inaccurate. It is felt that this technique will be valid for

observation of endothelial changes within the porcine vasculature once a method for *in vivo* fixation at physiological pressure has been determined.

Chapter 6: Development of staining techniques for endothelial cell borders

6.1 Introduction

As described elsewhere, it has been shown that EC nuclei align with the predominant direction of blood flow and elongate in regions of higher shear stress. Endothelial cells have also previously been shown to align and elongate in the same manner as their nuclei in the presence of blood flow (Dewey *et al.*, 1981, Langille and Adamson, 1981), so methods for staining EC borders using the EStAR technique were developed to try to confirm this.

As with the staining techniques for EC nuclei, the resulting images should ideally be analysable automatically using image analysis software. Staining therefore had to be very distinct, if possible with a uniform expression of stain to prevent gaps in the EC borders. Immunohistochemical staining was attempted as it is highly specific and should enable cell borders to be clearly observed. The ideal protein targets are those found within intercellular junctions, such as occludin, claudin, junctional adhesion molecule (JAM), zonula occludens-1 (ZO-1), catenins, platelet endothelial cell adhesion molecules (PECAM), or cadherins (Levick, 2003). Images of antibodies to PECAM-1 (Scholz and Schaper, 1997) and pan-Cadherin conjugated to fluorescent secondary antibodies (Abcam plc, 2006), revealed distinct EC borders with minimal background noise so these targets were attempted in the present study.

As with all prior staining procedures, problems were encountered with the curvature of the arterial wall and to alleviate this we carried out antibody staining on EStAR preparations. This also prevented staining becoming masked by autofluorescence from underlying tissue not associated with the endothelium.

There are standard protocols for antibody staining of animal tissue, however these generally seem to involve either cells in culture or thin (μm) sections taken from paraffin embedded or frozen tissue, as opposed to tissue fixed and stored *ex vivo* in fixatives such as formalin and Karnovsky's fixative. The protocols were used as a guideline and the staining techniques modified.

Immunohistochemistry procedures contain the same general steps for different species, preparations (i.e. whole mount, cell culture), and antibodies. A typical procedure is as follows:

1) Permeabilise cell membranes with detergent
2) Incubate in blocking buffer
3) Incubate with primary antibody
4) Wash in buffer
5) Incubate with secondary antibody (conjugated to fluorescence protein)
6) Rinse in buffer

Each of the above steps involves a great deal of variability (e.g. concentration/dilution, duration, temperature) and has to be adjusted until the optimum staining procedure is discovered.

6.2 Methods

6.2.1 Cadherin Staining

An antibody to the vascular endothelial (VE) cadherin, pan-cadherin was obtained that was claimed (Abcam plc, 2006) to react with rabbit tissue. After numerous attempts at finding the optimum concentration, staining time, and temperature of the antibody, and trying different detergents (Triton X-100 (Sigma), Digitonin (Sigma)) to increase membrane permeability, no staining was observed. It was concluded that the antibody either did not react with rabbit tissue, or that the EStAR technique was somehow preventing binding of the antibody to the antigen.

6.2.2 PECAM-1 Staining

Platelet endothelial cell adhesion molecule-1 (PECAM-1) (CD31) is a member of the immunoglobulin superfamily (Jackson, 2003), and spans the junctions between endothelial cells. It is expressed at high density at the lateral borders of EC (Newman, 1997). Antibodies to PECAM-1 have previously been used to visualise endothelial cells of mice (Nakashima *et al.*, 1998), rabbits (Sho *et al.*, 2003) and in HUVECs (Dusserre *et al.*, 2004).

Two approaches to PECAM-1 antibody staining were attempted; pre- and post-EStAR preparation.

6.2.2.1 Staining pre-EStAR

During the initial fixation process antigens become masked by protein cross-linking and thus are not accessible to the antibody binding sites. To overcome this, antigen retrieval treatment with Target Retrieval Solution (TRS) (Dakocytomation) was necessary. Manufacturer's recommendations suggest boiling the tissue in TRS however this was not possible as it caused severe damage to the tissue that prevented the production of EStARs. Instead, before staining could commence, aortic rings were placed in eppendorf tubes containing TRS, and placed in an incubator (45 min, 37°C). The tissue was then permeabilised with the detergent Triton X-100 (Sigma, 1% in PBS, 1 min), as detergents enable target proteins located intracellularly to be exposed to antigens by making the cell membranes 'leaky'. Tissue was then incubated in blocking buffer (1% Bovine Serum Albumin (BSA) in PBST (PBS + Tween-20) + 0.01% Sodium Azide, 10 min), before being incubated in PECAM-1 primary antibody (Clone JC70A, DakoCytomation, 1:5, 37°C, 30 min), diluted in blocking buffer. During the stages leading up to antibody staining i.e. antigen retrieval treatment, making the tissue permeable, blocking and washing, aortic rings were placed into solutions in 1ml eppendorf tubes. For the actual antibody staining (primary and secondary), this would have required large volumes that would have proved costly. To overcome this, a 10ul drop of antibody was placed onto a glass slide and the aortic ring was cut longitudinally and placed endothelium side down onto the drop. Another glass slide was placed on top of this to maintain antibody-endothelium contact, and both were placed into a humidified chamber in an incubator. The tissue was then rinsed in PBS (15 min) to remove all unbound antibody before being incubated in TRITC-conjugated rabbit anti-mouse IgG secondary antibody (Abcam plc, 1:40, 37°C, 30 min). Tissue then underwent a final PBS (15 min) rinse to remove unbound secondary antibody. The stained tissue was then dehydrated in a graded ethanol series and the EStAR technique carried out as previously described.

6.2.2.2 Staining post-EStAR

Having carried out the EStAR technique, tissue was rinsed in PBS (Sigma, 2 min) to remove remaining glycerol from the endothelial layer (EL) before undergoing the same antigen retrieval (TRS, 45 min, 37°C) and staining protocol as for the pre-EStAR technique. Post-EStAR, it was not possible to boil the tissue in TRS as the tape melted, and consequently wrinkled, causing damage to the tissue. Solutions were applied as a drop (sufficient quantity to cover surface) to the EStAR preparation before being placed in a humid chamber in an incubator to prevent evaporation. 7ul of antibody was added as a drop to the surface as this was deemed the optimum amount necessary to bind, whilst preventing excess cost. When tissue underwent any washing or rinsing, no running solutions were used. Instead a large drop of solution was added as shall be discussed later.

For both pre-and post-EStAR staining approaches, before microscopy, the endothelium was rinsed in distilled water and the region surrounding the EL was dabbed dry, care being taken not to touch the endothelium, before being mounted in FluorSave (Calbiochem) under glass coverslips.

The luminal surface of the tissue was viewed *en face* using an epifluorescence microscope and a filter for rhodamine. Images were captured with a low light CCD camera coupled to a software package, Maxim DL (Diffraction Limited, Canada) at 100x or 200x magnification. Images were taken in a grid-like formation surrounding branch ostia, as previously described, to enable montage images to be produced.

6.3 Results and Discussion

Both approaches had drawbacks. Pre-EStAR staining did enable visualisation of PECAM-1 location and hence outlines of EC were visible (Fig. 6.1). However, to produce EStARs, tissue had to be dehydrated in alcohol overnight. This led to the intensity of the stain dropping drastically, making it virtually impossible to produce montages of the intercostal branch ostia (in the absence of an automated stage) as the cells could not be seen by eye.

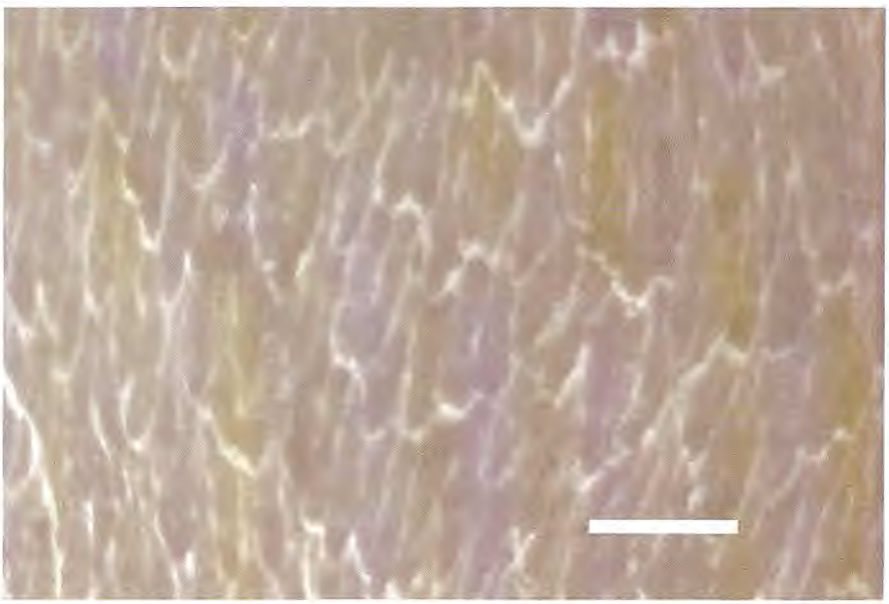

Fig. 6.1. Pre-EStAR staining with an antibody to PECAM-1. Blood flow is from top to bottom of image. Scale bar = 100μm.

Post-EStAR staining produced much brighter staining (Fig. 6.2) and, on rare occasions, enabled imaging of the EL in one focal plane. However, due to the long period of time spent in solution (>2 hours), the endothelial layer usually started to unstick from the tape (a problem not seen when staining EC nuclei, due to the shorter incubation times (<30mins)). At best, this led to difficulties imaging ELs due to an increased number of focal planes. At worst, after lifting up, the endothelial layer would fold slightly, giving a wrinkled appearance (Fig. 6.3). Initial attempts resulted in endothelium being lost entirely due to washing the EL by spraying or running solutions over the surface, so to try to alleviate this, a stationary drop was added. This prevented total loss of EL, but did not stop sections lifting up and wrinkling. To reduce this wrinkling effect, all incubation times were minimised as far as possible to reduce immersion time. This also caused its own problems. ELs were not washed as fully as necessary and bright spots were often visible (Fig. 6.4), possibly caused by either remaining unbound TRITC-labelled secondary antibody, or TRITC-labelled secondary antibody bound to unbound primary antibody.

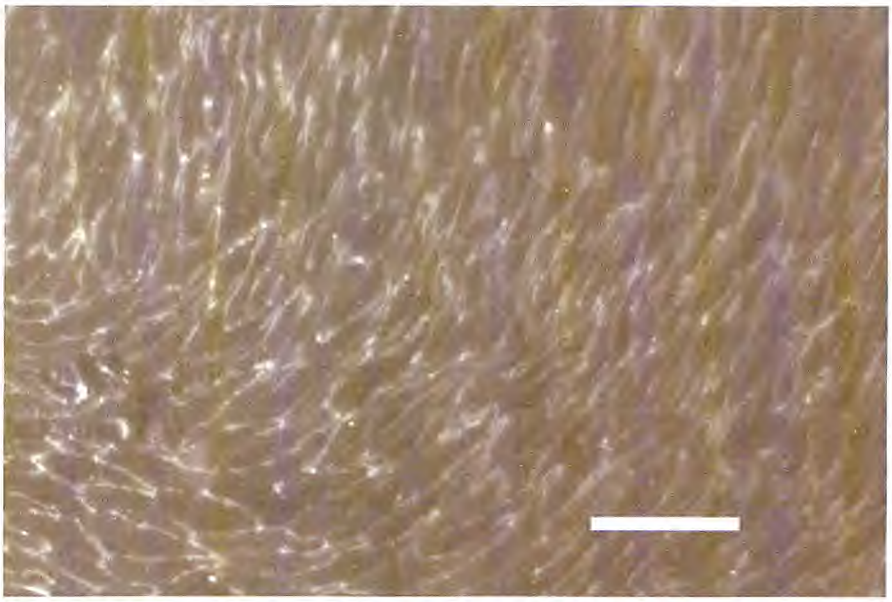

Fig. 6.2. Post-EStAR staining with an antibody to PECAM-1. Blood flow is from top to bottom of image. Scale bar = 100μm.

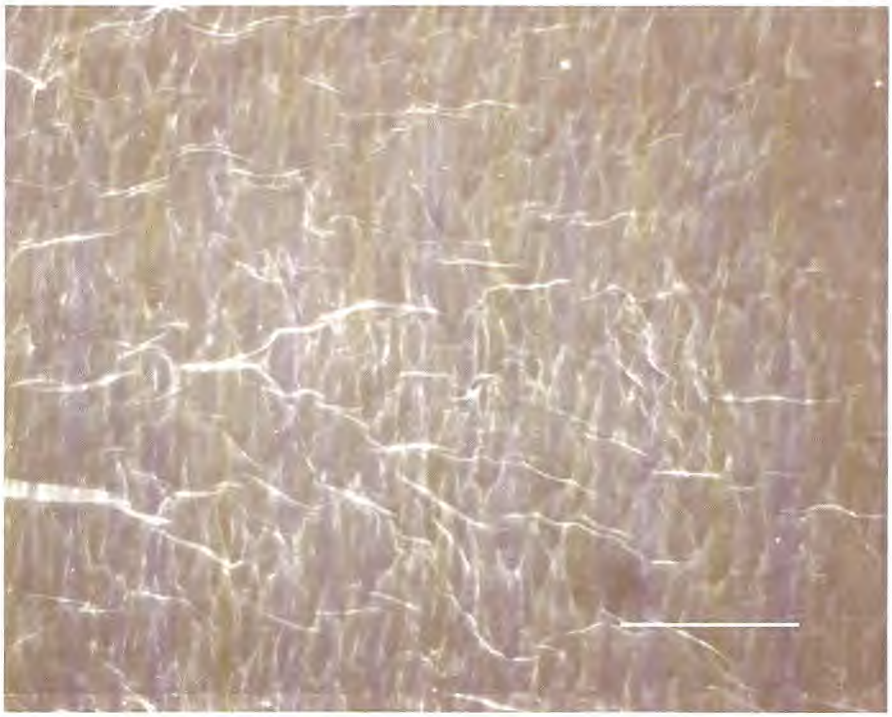

Fig. 6.3. Post-EStAR staining with an antibody to PECAM-1 demonstrating wrinkles that appear in tissue due to long period of time endothelial layer spends in solution. Blood flow is from top to bottom. Scale bar = 100μm.

Fig. 6.4. Post-EStAR staining with an antibody to PECAM-1 demonstrating bright spots that occur if endothelial layer not rinsed properly after staining. Blood flow is from top to bottom. Scale bar = 100μm.

As a final attempt to prevent this problem, mechanical solutions were sought. Rings were cut from acetate sheets and stuck onto the tape so as to impinge on the corners of the tissue without masking too much of the endothelium. This did not work as, despite best efforts to produce a perfect seal, solutions simply leaked out from under the rings, causing the ELs to dry out, damaging them. Instead, drops of cyanoacrylate glue (3M Vetbond) were used as rivets at the tissue corners. This would have worked had the tissue not had to be kept moist, as this allowed the glue to run over the EL damaging it, or preventing it from being imaged.

On the few occasions when, following post-EStAR staining, the EL did not become unstuck from the tape it was possible to see very clear cell boundaries in the peri-ostial regions, usually within the branch mouth, suggesting that the staining technique had worked very well (Fig. 6.5).

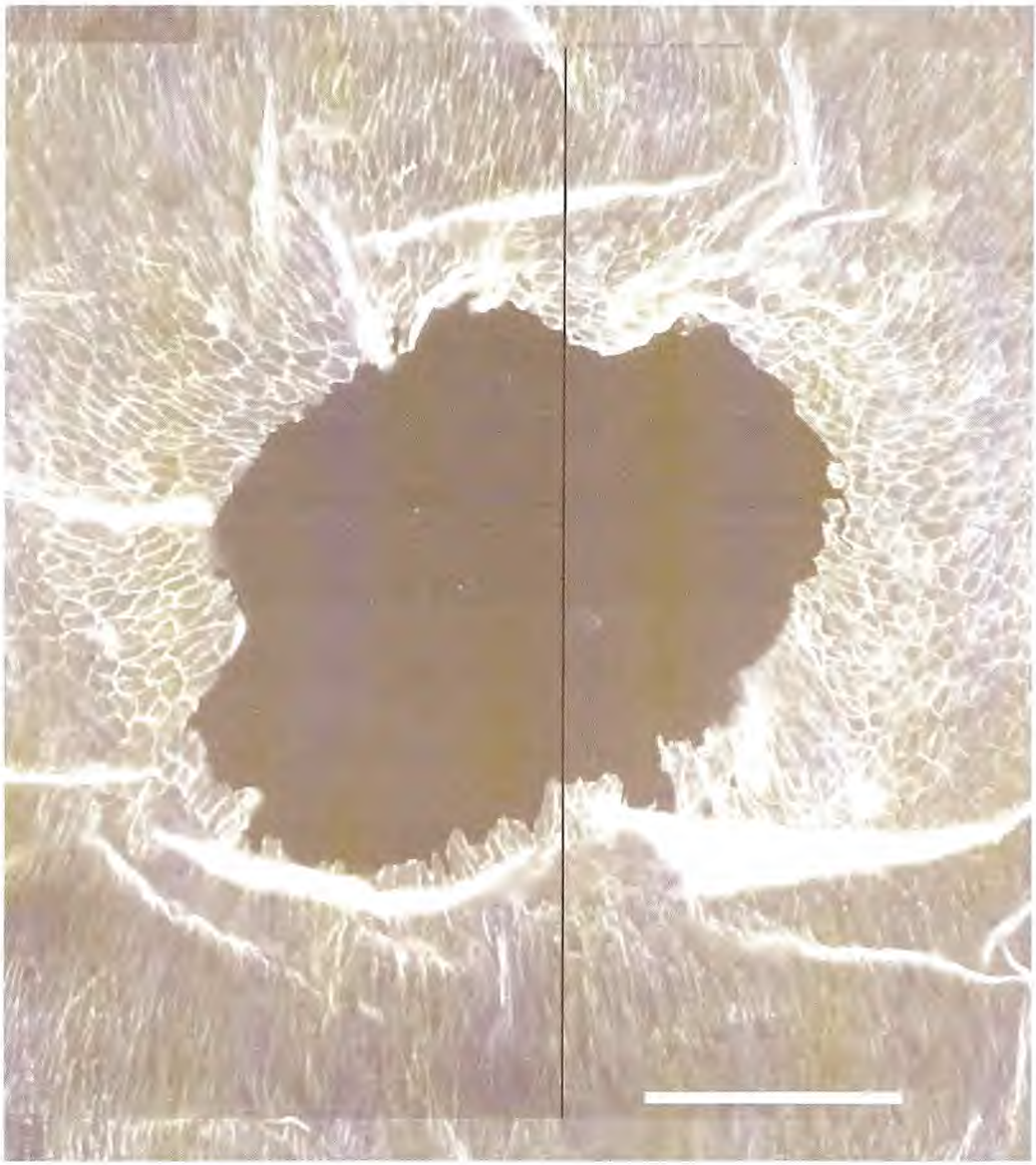

Fig. 6.5. EStAR preparation of endothelium stained with an anti-PECAM-1 antibody labelled with rhodamine to show endothelial cell boundaries. Cell definition appears to be improved upstream of, and within the branch ostia. Scale bar = 200μm. Blood flow is from top to bottom.

Despite clear antibody staining in some regions i.e. within the branch ostia, the intensity was not very uniform throughout all regions observed. The lack of uniformity of staining could be due to the tissue lifting off the adhesive tape, and causing regions of the EL to be out of focus, giving the impression cells were not stained as well. Perhaps a more likely explanation is that PECAM-1 is being expressed at different levels around

the branch ostium. Although only two branches, both from immature rabbits, were stained well enough to image, by eye staining appeared to be stronger upstream and within the branch ostia. A study in which a shear stress modifier was applied to the carotid artery of eNOS-GFP mice, and regions exposed to varying shear stresses were quantified for PECAM-1 expression, showed that expression was increased in regions of higher shear stress (Cheng *et al.*, 2005). Our data for endothelial cell nuclear elongation suggest that in immature rabbits, shear stresses are higher downstream of the branch, not upstream, so the pattern of PECAM-1 staining appears to be the reverse of that expected.

Despite cell boundaries being visible by eye it still would not have been possible to carry out automated image analysis. It would have been possible to measure cells by hand, as has previously been done for EC nuclei (Al-Musawi *et al.*, 2004). The optimum staining technique developed was as follows (unless stated, steps were carried out at room temperature):

1) EStAR produced
2) PBS rinse (2 min)
3) Antigen retrieval treatment - TRS (45min at 37°C)
4) Triton X-100 (1% in PBS, 1min)
5) Blocking buffer (1% BSA, 10min)
6) Primary antibody against PECAM-1 – (7µl, 1:5, 30min at 37°C)
7) PBS rinse (15min)
8) Secondary antibody (7µl, 1:40, 30min at 37°C)
9) PBS rinse (15min)

With further time, the problem of ELs becoming unstuck may have been overcome, either by decreasing the time the EL was immersed in solutions, or by developing ways of keeping the EL stuck to the tape.

Chapter 7: Changes in endothelial cell shape around intercostal branch ostia in rabbits, determined by silver staining

7.1 Introduction

Although antibodies to PECAM-1 did enable imaging of EC borders, it was not possible automatically to obtain cell dimensions. A method that has previously been used for visualisation of EC borders is to stain with a silver nitrate ($AgNO_3$) solution (e.g. Florey et al., 1959, Reidy and Levesque, 1977, He and Adamson, 1995, Hirata et al., 1995). It has previously been shown that $AgNO_3$ stains EC borders sufficiently well that their shape and size can be quantified computationally (Dyck *et al.*, 2001). It is not known exactly what $AgNO_3$ stains, but it is thought to stain an element of the intercellular junction at the abluminal surface of the EC (Hirata *et al.*, 1995) which subsequently shows up as a network of dark brown lines, allowing visualisation of the cell boundaries, and therefore the orientation and elongation of the cells. Early work by Florey *et al* (1959) suggested that staining depends on the presence of chloride, iodide or bromide ions, and it was thought that the silver is deposited at the "cement" between EC. They thought that the silver was deposited to some extent on all surfaces of EC, but predominantly along cell junctions. A general build up of the stain at the cell edges, and some degree of overlap between cells, perhaps caused the visible lines. Techniques found in the literature involve "developing" the stain, to make lines appear darker, varying from exposure to light (Hirata *et al.*, 1995), to the addition of chemicals such as ammonium sulphide (Nakatsu *et al.*, 1988) or solutions of cobalt and ammonium bromide (Florey *et al.*, 1959).

7.2 Methods

All animal procedures complied with the Animal (Scientific Procedures) Act 1986. Endothelial cells were examined in male New Zealand White rabbits (Harlan Interfauna strain) aged 2.3 months (n=4) or 4-11months (n=4).

Fixation methods were developed from those previously described. Rabbits were injected with heparin (Sigma, ~2000 USP Units in 1.5ml Ringers i.v) which was allowed to circulate for 2 minutes, before euthanasia by intravenous injection of pentobarbitone. Following thoracotomy and laparotomy along the ventral midline, a retrograde cannula was inserted into the thoracic aorta at the level of the diaphragm and tied in place using silk suture. The aorta was flushed at physiological pressure with 50ml Ringers solution

(n=6) or PBS (n=1) containing 1.5ml heparin followed by perfusion at the same pressure with 10% neutral buffered formalin for 1.5mins. Pressure fixation was then discontinued and 20ml of a $AgNO_3$ solution (2.5mg/ml, Sigma) was introduced through the cannula before pressure formalin perfusion was restarted and continued for 30mins. After one minute the aortic arch was clamped. Aortas were excised and stored in formalin for a minimum of 16 hours to allow complete fixation.

Prior to staining multiple aortas, a pilot experiment was carried out to test that the staining technique described above was viable. A section of stained aorta was removed from fixative and placed in PBS for an hour, before being cut open longitudinally and mounted *en face* on the microscope to check whether the staining survived storage in formalin. Dark lines were visible using transmitted light on the microscope (Fig. 7.1) but as previously discussed (and visible in Fig, 7.1), the problem of wall curvature would have prevented rapid imaging; EStAR preparations were required. A section of aorta was placed into 100% ethanol for 30mins on a suspension mixer, to gently agitate the tissue, to determine whether staining would withstand alcohol dehydration, which is necessary for EStAR preparations. The section was again placed as a whole mount onto the microscope and brown lines were visible, suggesting alcohol does not remove or fade the stain.

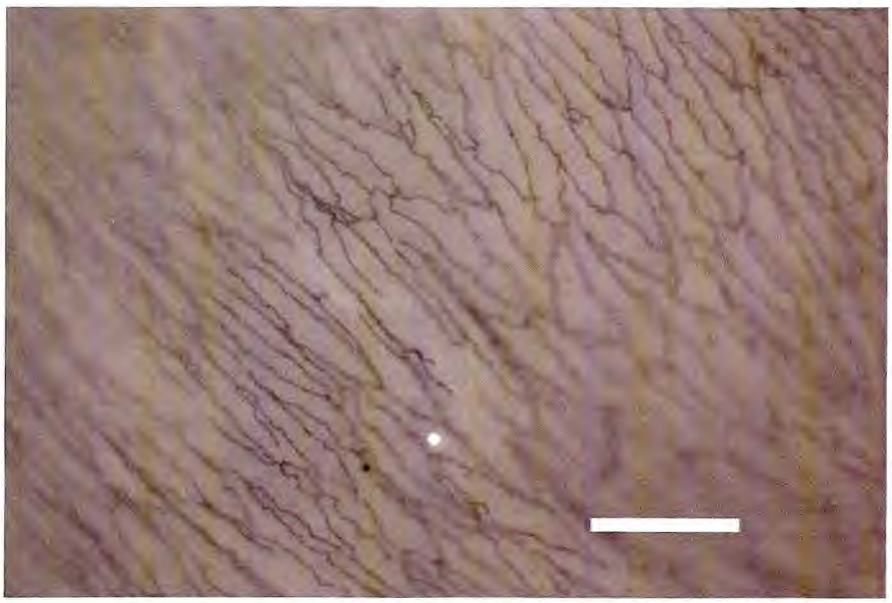

Fig. 7.1. *En face* view of whole mount preparation of silver stained tissue. Endothelial cell borders are visible as dark lines. Scale bar = 50μm.

Having determined that staining was still present in the test aorta, all stained aortas were dehydrated in a graded alcohol series and EStAR preparations made as described previously. Once the EStARs had been produced it was observed that at first the stain was very faint. However, the longer the stain was exposed to light the darker the EC borders became, although the exact time required was not quantified. The lines became darker over time even after the EL had been mounted under a coverslip with Fluorsave.

EStARs were viewed using an Axioplan epifluorescence microscope (Zeiss) and images obtained using a low light CCD camera with a Kodak KF1600 chip, coupled to the software package Maxim DL (Diffraction Limited, Canada), at 200x magnification using a 20x objective lens (NA 0.45). Although the silver lines, in most cases, were clearly visible by eye, various methods were attempted to improve the images obtained with the camera, to enable easier analysis. Images were taken using 1) transmitted light through the EL, 2) epifluorescence illumination using a fluorescein filter (usually used for detection of autofluorescence), 3 and 4) same methods as 1) and 2) respectively, but with a piece of white paper underneath the slide (see Figs. 7.2a-d).

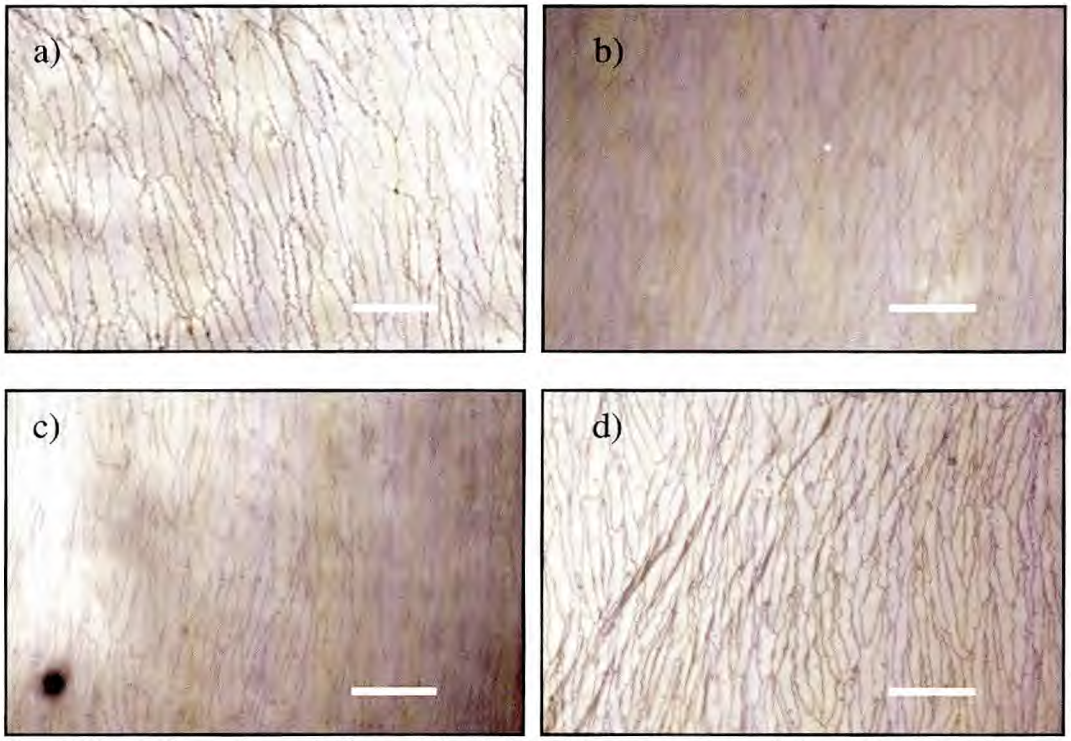

Fig. 7.2. *En face* view of silver stained EStAR preparations of thoracic aorta taken using a) transmitted light, b) epifluorescence with a fluoroscein filter, c) transmitted light with a piece of white paper underneath slide, d) epifluorescence with a fluorescein filter and piece of white paper underneath slide. Scale bar = 50μm.

Despite producing EStARs of the $AgNO_3$ stained tissue, the problem of the arterial wall not being flat, particularly around branch ostia, was still encountered, causing areas of the images to be out of focus. To overcome this, an optical stack of images was taken so that all the focal planes were included in each region viewed i.e. an image was taken with an area being in-focus, the distance between the slide and the lens was manually adjusted so another area was in-focus and another image taken. This process was repeated until all areas within a region had been imaged. The images within the optical stack were then opened in Adobe Photoshop, placed on top of each other and out-of focus regions in each layer were erased. The stack was made semi-transparent so all in-focus regions were visible, and the stack merged to form one in-focus image (Fig. 7.3).

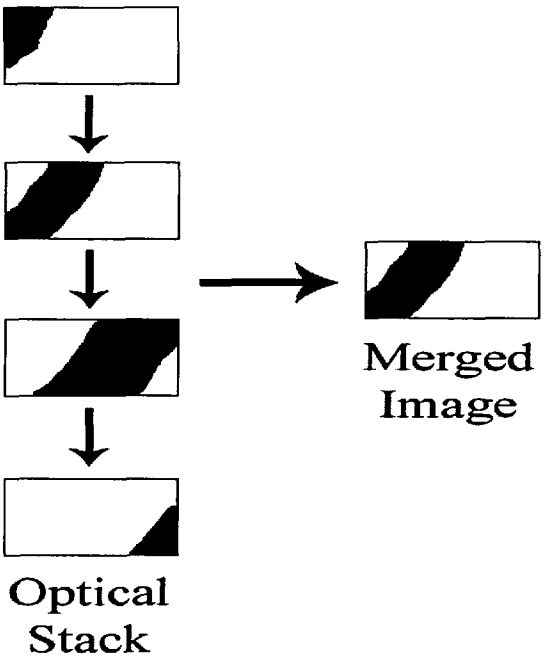

Fig. 7.3. Separate images were taken to produce an optical stack, with each image containing areas of in-focus (black) and out-of-focus (white) regions. Out-of-focus regions were deleted from each image before merging the optical stack to produce a final image containing in-focus regions only.

Images of the endothelium were taken in a grid-like pattern over the aortic region of interest, ensuring each image overlapped slightly with its neighbours, and their location was noted. Individual images could then be copied to a new blank canvas in Photoshop, destined to become a final montage, made semi-transparent so the previous image could be seen underneath, and the silver stained EC borders towards the edges aligned with the previous image. This process was continued until all the images for each branch/pair of intercostal branches were aligned and in the final montage image.

7.2.1 Measurement of endothelial cells

When images of silver-stained tissue were captured it was not possible to perform automated object analysis as the staining intensity was inconsistent around the cell borders. In particular, there were small gaps in the lines (perhaps representing real breaks in junctional structures) so that when object analysis was attempted in ImageTool, the software could not always distinguish between neighbouring cells.

However, the borders were clear enough to see by eye. Therefore, to allow subsequent automatic analysis, the outlines were traced manually. Montage images of branch ostia were opened and overlaid with a transparent blank layer, in Adobe Photoshop. Using a graphics tablet and pen (Volito2, Wacom Co. Ltd.), cell borders were traced onto the new layer using the pencil tool set at a width of 1-2 pixels (Fig. 7.4).

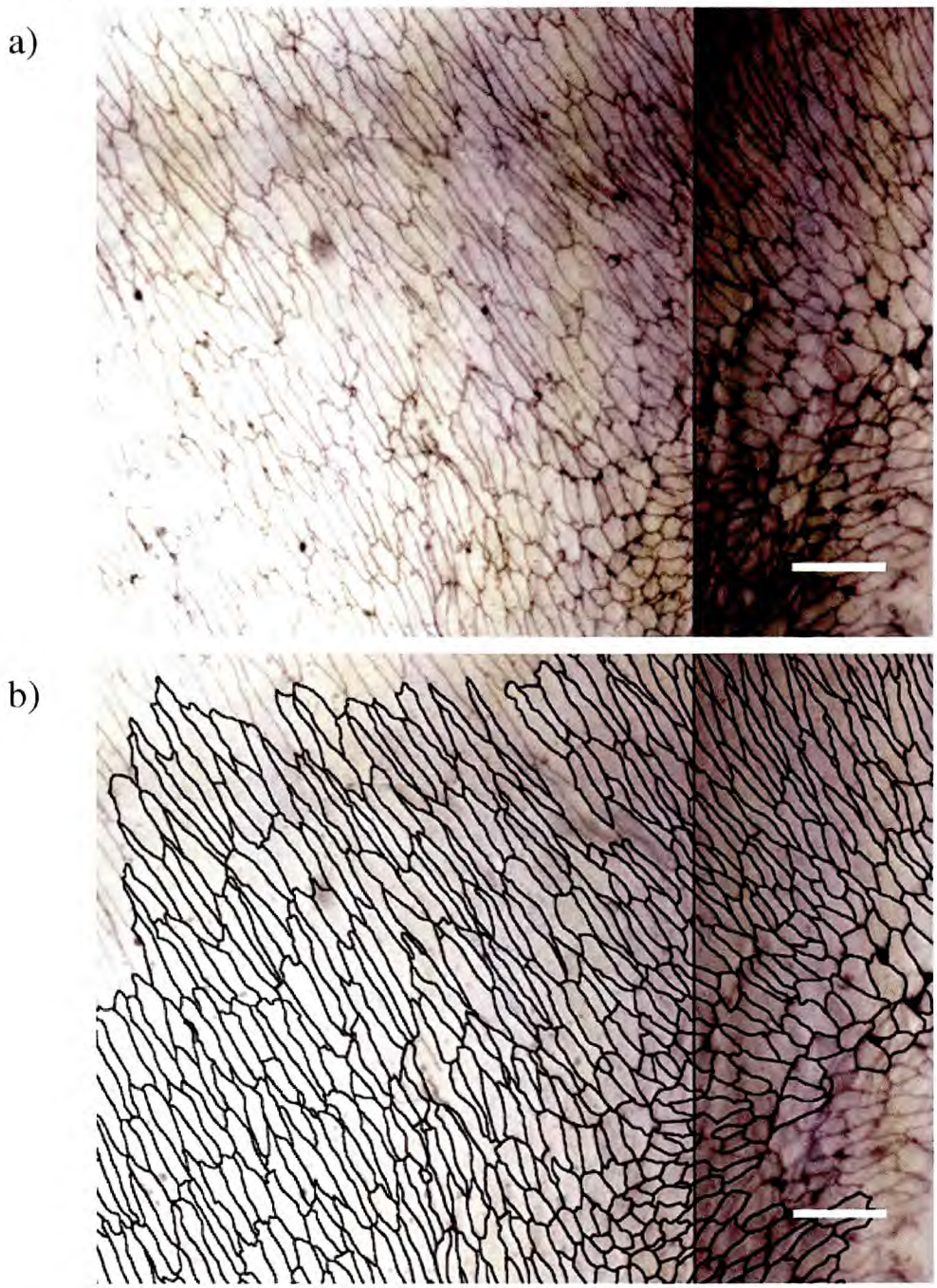

Fig. 7.4. a) EStAR preparation of rabbit endothelium stained with silver nitrate, and b) same image with outlines of endothelial cells drawn for image analysis. Bars = 50μm.

Once the borders were complete, a region measuring 600μm * 600μm was selected upstream and downstream of each branch, with the lower and upper edge of the region respectively aligned with the upper and lower edge of the ostium (Fig. 7.5). The selected regions were opened in ImageTool and thresholded to produce a binary image that could be analysed using the "Analyze" tool. Tables containing the parameters for each object in the image were produced and were saved as text files to be transferred to Microsoft Excel.

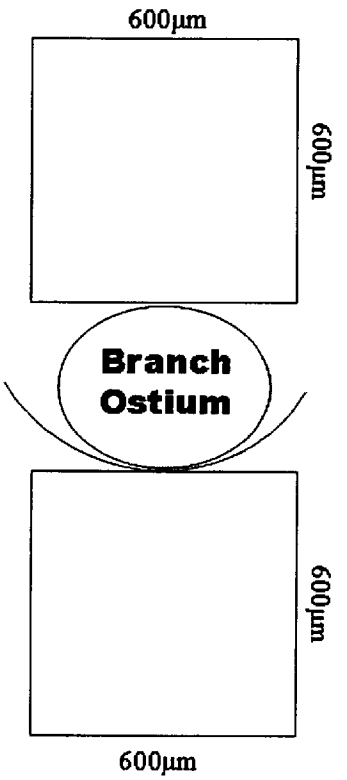

Fig. 7.5. Location of upstream and downstream region in which silver stained endothelial cells were analysed. Mean aortic blood flow is from top to bottom.

When drawing the outlines of cells, the lines did not always meet, or lines were missed due to the silver stain being too faint to discern by eye. When this happened, objects analysed in ImageTool would be measured as two or more adjacent cells, producing inaccurate results. To avoid this problem, as with the previous analysis of endothelial

cell nuclei, the data were filtered by the objects area and perimeter. The literature was searched for previously published parameters for endothelial cells (Table 7.1).

Table 7.1. Previously published dimensions of endothelial cells.

Investigator	**Endothelial cell length (μm)**	**Endothelial cell width (μm)**
(Cornhill *et al.*, 1980)	63	19
(Nerem *et al.*, 1981)	66.2	14.0
(Levesque and Nerem, 1985)	42.7	20.5
Average	**57.3**	**17.8**

By trial and error it was determined that a 60% increase in average area and perimeter encompassed changes in elongation upstream and downstream of branch ostia, but excluded pairs of cells where lines were not connected. The minimum area was determined by the results of our previous endothelial cell nuclei experiments. We found that the average area of a nucleus was 488.9 pixels, and cells must be larger than their nuclei. The average length and width of our nuclei were 39.7 pixels and 14.4 pixels respectively, and from these values the average perimeter was calculated as being 90 pixels. These values are summarised below:

Average endothelial cell length (literature values) = 57.3μm = 127.2 pixels
Average endothelial cell width (literature values) = 17.8μm = 39.6 pixels

A 60% variation above the average nuclear length and width = 203.5 pixels and 63.3 pixels respectively.

Therefore, a 60% increase in area and perimeter = 10,100 pixels and 633 pixels respectively.

Average endothelial cell nuclear area (our data) = 488.9 pixels
Average endothelial cell nuclear length (our data) = 39.7 pixels
Average endothelial cell nuclear width (our data) = 14.4 pixels

Therefore, the average endothelial cell nuclei perimeter (calculated) = 90 pixels

Thus,

minimum and maximum area of ellipse = **489** pixels^2 and **10,100** pixels^2 respectively.

minimum and maximum perimeter of ellipse = **90** pixels and **633** pixels respectively.

The range of values for the perimeter and area were then included in a macro code (Appendix C - Macro 12) to exclude objects outside these ranges. Other than a different range of values, the macro used was identical to that used in the analysis of EStARs stained for endothelial cell nuclei. Angles were adjusted to convert the data so that if a cell were aligned along the longitudinal axis rather than the horizontal axis it would be assigned an angle of zero degrees, and results were averaged over 100μm * 100μm regions, as previously described.

7.2.2 Propidium iodide and silver staining combined

In 3 rabbits, having produced EStARs from tissue stained *in situ* with silver, the EStARs were also stained with propidium iodide, following protocols described above. This enabled the cells and their nuclei to be observed in the same EL (but imaged separately), and correlations in their respective dimensions to be studied. ELs were imaged at 200x magnification using transmitted light (3 seconds exposure) (with a sheet of white paper under the slide) for silver-stained EC borders, and with epifluorescence illumination and rhodamine filters (3 seconds exposure) (without paper under the slide) for PI stained nuclei. The silver stained images could then be made semi-transparent and overlaid onto the PI stained images, using Adobe Photoshop, to see both images at once. The technique of simultaneously recording silver stain and a nuclear stain has previously been demonstrated in frog and hamster microvessels, using confocal reflectance for the silver stain, and fluorescence imaging for the nuclei (He and Adamson, 1995).

Two upstream, and two downstream regions were selected per branch, each measuring 250μm * 500μm, and containing silver stained ECs and PI stained nuclei. The first upstream and downstream regions were aligned so their lower (upstream region) and upper (downstream region) edges were aligned with the proximal and distal edge of the branch ostia respectively. The second upstream and downstream regions were offset

250μm proximally and distally, respectively, from the first regions. The outlines of approximately 20 silver stained cells were drawn as previously described, using the "pen tool" in Adobe Photoshop, with a graphics tablet and pen, and were pasted into a new image. Cells were selected if their nuclei were not touching neighbouring nuclei because this would have caused problems during the analysis. Having drawn the outlines of the cells, a high-pass filter (10 pixel radius) was applied to the layer containing nuclei, and the nucleus of each cell was selected using the "polygonal lasso" tool to cut them from the original image and paste them next to their respective cell (see Fig. 7.6 for an example). The images containing EC and ECn were thresholded in ImageTool and analysed to produce a results table containing parameters for each object in the image.

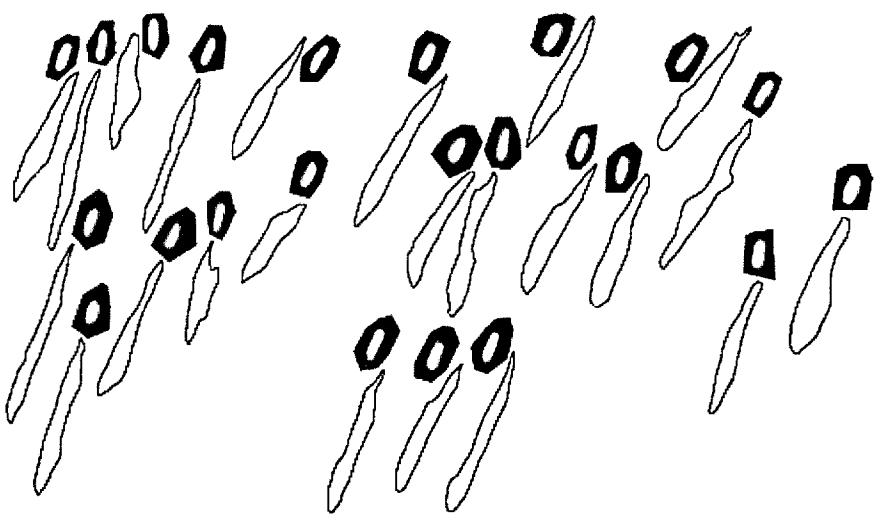

Fig. 7.6. Propidium iodide stained endothelial cell nuclei next to their respective endothelial cell outline, drawn from silver stained images.

The results tables were opened in Microsoft Excel and each cell with its corresponding nucleus was assigned an individual number to enable statistical analysis to be performed. The angle of the major axis for each object was adjusted using the following equation for the reasons previously explained:

IF (Angle>0) then (Angle*-1) +90

IF (Angle<0) then (Angle*-1) -90

7.2.3 Statistical Analysis

The significance of differences between silver stained cells in the upstream and downstream regions was determined using an independent samples t-test (SPSS version 14.0) (where n equals the number of branches). The correlation between the parameters of EC and ECn was determined using a Pearson correlation test (SPSS version 14.0). All data are represented as mean ± SEM.

7.3 Results

7.3.1 Morphology of endothelial cells

The LW ratios, angle of orientation, length, width and area of silver stained endothelial cells, averaged within 600μm * 600μm regions upstream and downstream of the branch ostia, are shown in Table 7.2.

Table 7.2. Endothelial cell shape in regions upstream and downstream of branch ostia in immature and mature rabbits, where n equals the number of branches.

		Immature		Mature	
		Mean	SEM	Mean	SEM
LW	**Upstream**	7.16	0.31	9.22	0.58
	Downstream	7.75	0.16	8.72	0.67
Angle (°)	**Upstream**	-1.85	2.48	1.26	2.46
	Downstream	-0.31	1.85	-0.95	1.53
Length (μm)	**Upstream**	59.56	2.57	64.92	3.03
	Downstream	63.61	1.28	76.42	2.76
Width (μm)	**Upstream**	8.81	0.25	7.63	0.41
	Downstream	8.75	0.10	9.71	0.72
Area ($pixels^2$)	**Upstream**	1681.7	93.8	1521.6	90.6
	Downstream	1793.5	38.3	2265.1	157.8

The LW ratios of ECs in immature rabbits were 7.16 ± 0.31 and 7.75 ± 0.16 in upstream and downstream regions respectively (8% difference; P=0.12), and the ratio of the LW ratio upstream to the LW ratio downstream was 0.92. In mature rabbits the LW ratios were 9.22 ± 0.58 and 8.72 ± 0.67 (6% difference; P=0.59) in upstream and downstream regions, and the ratio of the LW ratio upstream to the LW ratio downstream was 1.06.

The normalised nuclear orientations in immature rabbits were -1.85 ± 2.48° upstream, and -0.31 ± 1.85° downstream (P=0.63), and in mature rabbits they were 1.26 ± 2.46° and -0.95 ± 1.53° (P=0.46) in upstream and downstream regions respectively.

Nuclear lengths were 59.56 ± 2.57μm and 63.61 ± 1.28μm (7% difference; P=0.19) in upstream and downstream regions respectively in immature rabbits. In mature rabbits, the lengths were 64.92 ± 3.03μm and 76.42 ± 2.76μm (18% difference; P<0.05) in upstream and downstream regions. The ratio of the nuclear length upstream to the length downstream was 0.94 and 0.85 in immature and mature rabbits respectively.

Nuclear widths in immature rabbits were 8.81 ± 0.25μm and 8.75 ± 0.10μm (1% difference; P=0.84) in upstream and downstream regions respectively; the ratio of the width upstream to the width downstream was 1.01. In mature rabbits, the nuclear widths were 7.63 ± 0.41μm and 9.71 ± 0.72μm (27% difference; P<0.05) upstream and downstream respectively and the ratio of widths upstream to downstream was 0.79.

The area of the nuclei in immature rabbits was 1681.7 ± 93.8pixels^2 and 1793.5 ± 38.3pixels^2 (7% difference; P=0.30) upstream and downstream respectively, and the ratio between areas upstream to downstream was 0.94. In mature rabbits the nuclear area upstream of branch ostia was 1521.6 ± 90.6pixels^2 and downstream was 2265.1 ± 157.8pixels^2 (49% difference; P<0.005). The ratio of upstream to downstream widths was 0.67.

7.3.2 Correlation between the morphology of endothelial cells and their nuclei

In total, 350 ECs were compared with their nuclei to determine whether the cell shape correlated with the shape of the nucleus. Data were not split into age groups due to the small sample size. When looking at all nuclei, for all parameters there was a significant ($P<0.005$) positive correlation between the endothelial cells and their nuclei (Fig. 7.7a-e). The r^2 values for cells versus their nuclei were 0.38, 0.88, 0.52, 0.33 and 0.52 for the LW ratio, angle of orientation, length, width, and area respectively.

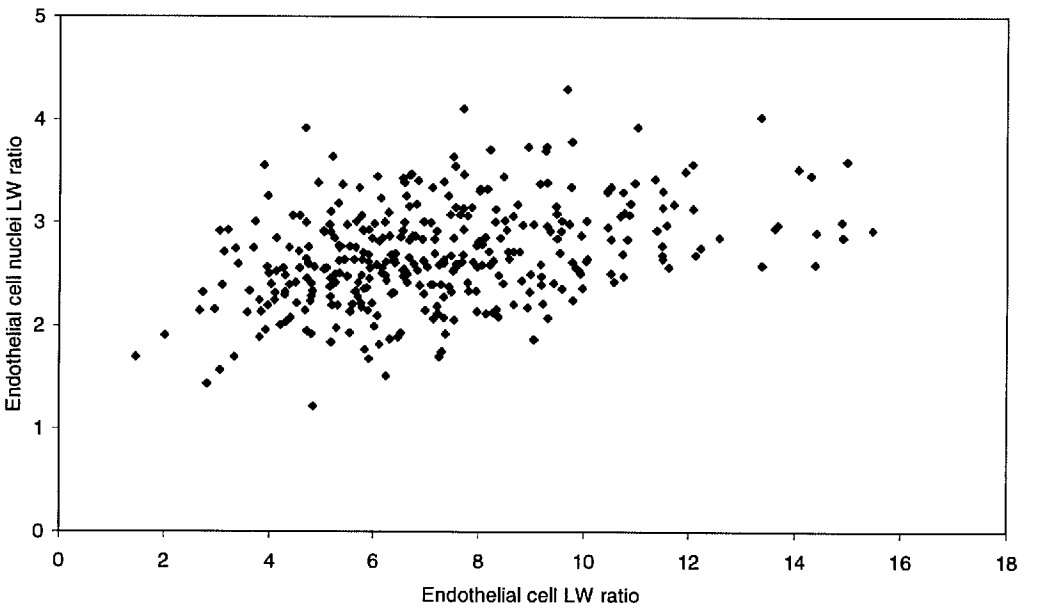

Fig. 7.7a. Correlation between the LW ratios of endothelial cells and their nuclei. R^2 = 0.38.

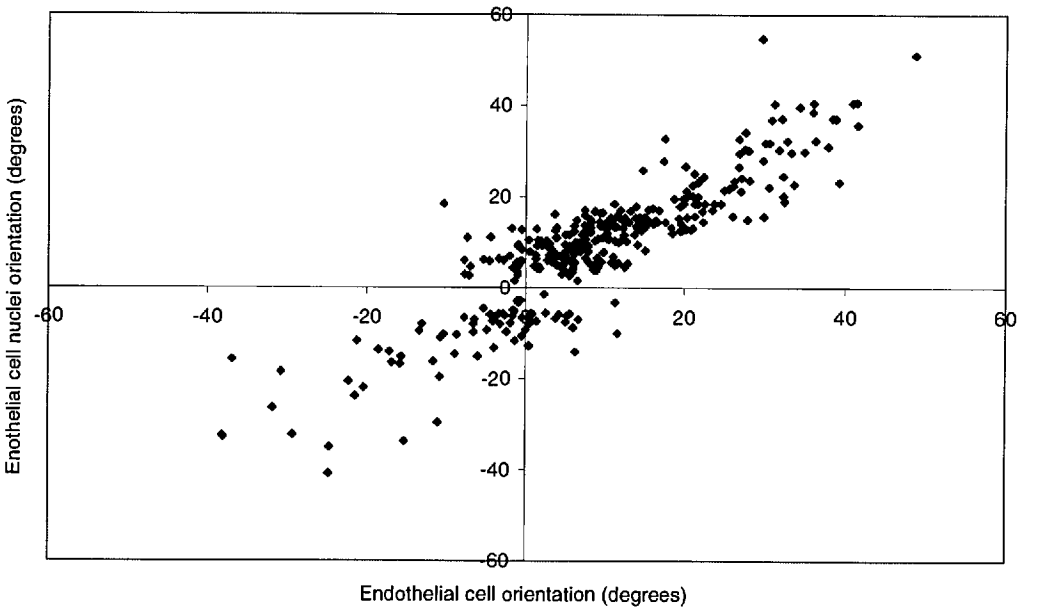

Fig. 7.7b. Correlation between the orientation (°) of endothelial cells and their nuclei. $R^2 = 0.88$.

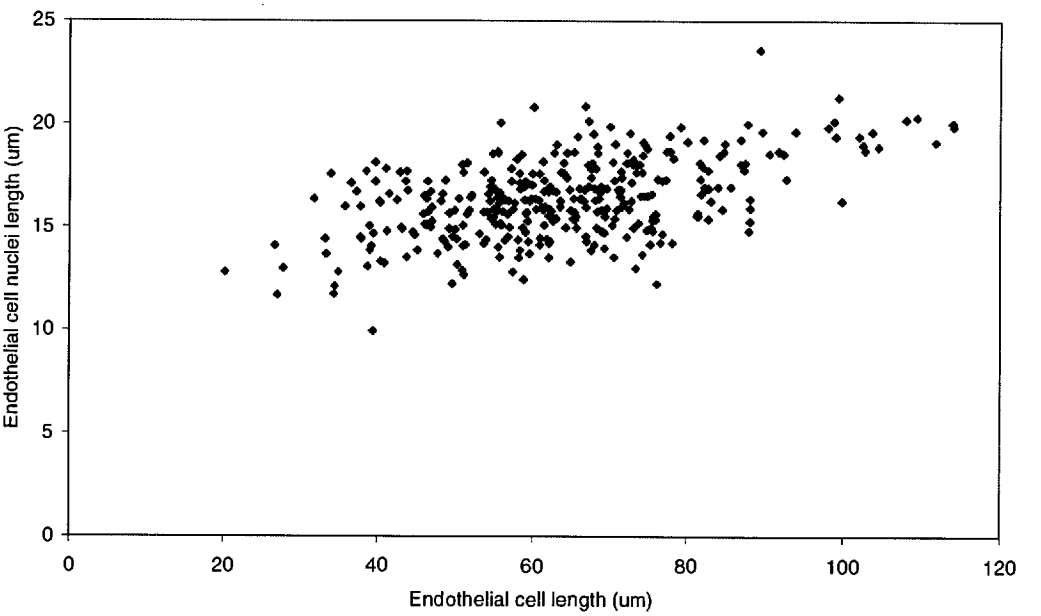

Fig. 7.7c. Correlation between the length (μm) of endothelial cells and their nuclei. $R^2 = 0.52$.

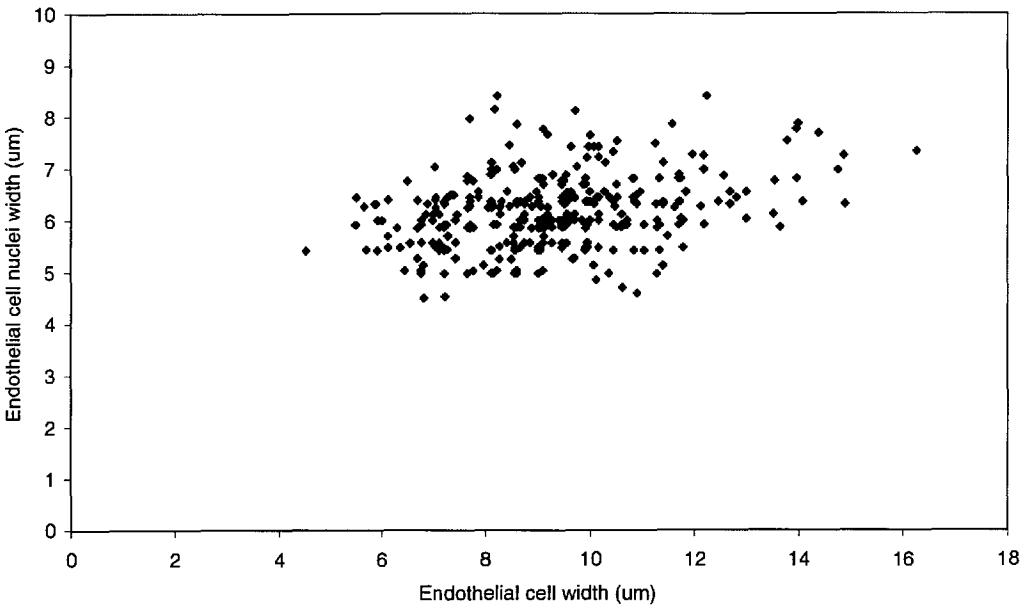

Fig. 7.7d. Correlation between the width (μm) of endothelial cells and their nuclei. R^2 = 0.33.

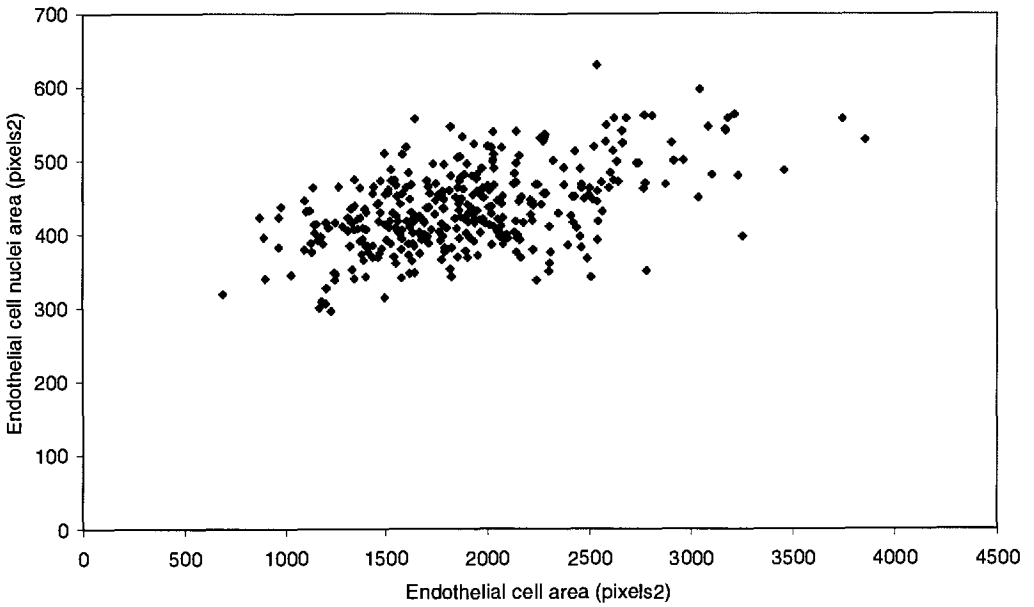

Fig. 7.7e. Correlation between the area (pixels^2) of endothelial cells and their nuclei. R^2 = 0.52.

Cells and nuclei within the first upstream region (0-250μm upstream of the ostia) were significantly ($P<0.01$) positively correlated for LW ratio ($r^2=0.29$), orientation ($r^2=0.92$),

length (r^2=0.48) and area (r^2=0.34). The width of nuclei were not significantly correlated with the width of the cells (r^2=0.06, P=0.60).

In the second upstream region (250-500μm upstream of the branch), there was a positive significant (P<0.001) correlation between cells and their nuclei for all parameters. R^2 values were 0.48, 0.91, 0.39, 0.54 and 0.25 for LW ratio, orientation, length, width and area respectively.

In the first downstream region (0-250μm downstream of branch ostia) there were significant (P<0.05) positive correlations between cells and their nuclei for all parameters. R^2 values were 0.45, 0.66, 0.66, 0.31 and 0.61 for the LW ratio, orientation, length, width and area respectively.

In the second downstream region (250-500μm downstream of branch ostia), there were positive significant correlations between the cells and nuclei for orientation (r^2=0.76), length (r^2=0.44), width (r^2=0.38) and area (r^2=0.72). The LW ratio of the nuclei were very weakly correlated with the LW ratio of the cells (r^2=0.18, P=0.01).

The differences in p values between these four regions may reflect the smaller sample sizes.

7.4 Discussion

Our study has shown that it is possible to utilise the EStAR preparation, in conjunction with silver nitrate, to stain the borders of ECs in regions surrounding branch ostia of immature and mature rabbits. In a number of EStAR preparations of both ages, cell borders were not visible in the region immediately downstream of the branch ostium, despite ECn being visible (in sections also stained with PI) suggesting the endothelium was intact. This finding has also been observed previously (Reidy and Bowyer, 1977), the authors stating that "it was consistently observed that the distal lip of the branch and the tissue immediately below it stained poorly with silver". Other work however has shown that silver stained cell boundaries cannot be visualised upstream of branch ostia in young rabbits (Sebkhi and Weinberg, 1996). This perhaps suggests that in regions

surrounding branches, the intercellular junctions have unusual properties that prevent consistent silver staining. Despite the small size of study, our data have shown that there is a change in the pattern of EC elongation upstream and downstream of the branch ostia. The ratio of LW values upstream of the branch to those downstream changed from <1 to >1 with age. This change was not significant, presumably due to the small sample size. The change in pattern of elongation was similar to that seen in ECn by Al-Musawi *et al* (2004) and in our study looking at ECn in rabbits using the confocal technique. There were significant changes in cell length and width from upstream to downstream regions in mature rabbits, but not in immature, but the ratio of cell length upstream to downstream was <1 in both ages groups. The ratio of the cell width upstream to downstream showed an inverse pattern to the LW ratio, changing from >1 to <1 with age. In immature rabbits there was a larger percentage difference in cell length (7%) from upstream to downstream, than there was for cell width (1%) suggesting the length of the cell has the dominant effect on LW ratios. In mature rabbits, the opposite occurred and there was a larger percentage difference in cell width (27%) than length (18%) from upstream to downstream regions, suggesting that the width is the cause for the change in LW ratios. The area of the cells did not differ significantly between the upstream and downstream regions in immature rabbits, although there was a trend for the cells downstream to be larger than upstream. In mature rabbits, there was a highly significant difference between upstream to downstream regions, the cells downstream being nearly 50% larger than those upstream. The mature pattern is the same as that seen in ECn, albeit larger. The immature pattern of EC area is the opposite of that seen in ECn.

No previous evidence has been found for how the shape and orientation of ECs correlates with the shape and orientation of their nuclei. For all of the parameters studied, there were positive correlations between cell and nuclei i.e. as the cell size/shape changed, the nuclei also changed in the same direction. A single exception to this was the correlation between cell and nuclear widths 0-250μm upstream of the branch ostia, where there was no significant correlation. The strongest correlation was for the angle of orientation. Despite the close correlation between the angle of the cells and their nuclei, there was still a mean difference of approximately 5°, the minimum and

maximum differences being 0.1° and 29° respectively. The mean differences between EC and ECn were 4.5, 47.3μm, 3.1μm and 1466 pixels^2 for LW ratio, length, width and area respectively. The differences between orientation and LW ratio may suggest that the nuclei are experiencing different shear stresses over their surface causing them to align differently to the cells. Hazel & Pedley (2000) described how cells align themselves to the blood flow in such a way as to minimize the total force on their nuclei i.e. they make themselves streamlined to the flow. The nuclei are elevated slightly above the basal membrane and are thicker than the junctions between the cells (Masuda *et al.*, 2003) and so are more likely to be affected by the flow of blood over their surface than the remainder of the cell.

Parenthetically it was observed that when imaging PI stained nuclei in EStAR preparations, it was usually possible to get good images from one focal plane, whereas both PECAM-1 and silver stained EC borders frequently required imaging in multiple planes. Other than the problems of ELs lifting up, this could have been due to the thickness of the nuclei. This means that if the EL was slightly undulating, some part of the nucleus might always be in the focal plane whereas this would be less likely for the thinner cell borders.

Silver staining in the rabbit vasculature has proved a reliable method for staining the borders of endothelial cells, and double staining of cell borders and nuclei in conjunction with a nuclear stain, in regions surrounding branch ostia. The method developed is rather time consuming as it requires a large amount of manual input when drawing the cell outlines, but without this input it would not be possible to analyse the morphology of the cells due to the uneven intensity of the stain, and the variable wall background. The ability to double stain both cells and nuclei in the same section of arterial wall will prove invaluable in further elucidating the mechanisms behind changes in shear stress over the endothelial surface.

Chapter 8: General Discussion

8.1 Technique Development

During the course of this project, new techniques have been developed with the aim of furthering our understanding of local blood flow near the endothelium, and how these flows can be correlated with the location of atherosclerosis. Initially it was hoped that a technique could be developed to visualise ECn in the aorta without staining the nuclei of underlying SMC, thus enabling automated analysis of large regions of endothelium. Staining with propidium iodide, having first treated the tissue with detergents and RNase, did allow clear visualisation of the ECn but did not totally eliminate SMCn staining. A technique was then developed to study patterns of ECn shape in the descending thoracic aortas of mice and rabbits, using confocal microscopy and manually selecting ECn from optical stacks through the arterial wall. Although this allowed the removal of SMCn, the technique proved extremely time consuming so alternative methods were sought. The development of a modified Häutchen technique, subsequently named the EStAR technique, enabled visualisation of large sheets of endothelium devoid of SMCs from the aortas of immature and mature rabbits. These permitted automated analysis of millions of nuclei, to produce detailed maps of the patterns of nuclear shape and orientation around intercostal branch ostia, areas that have a predilection for developing atherosclerotic lesions (Cornhill and Roach, 1976). Having produced maps for ECn, attempts were made to develop techniques for visualisation and automatic analysis of the ECs themselves. First, antibodies to PECAM-1 were used in immunofluorescence studies of EStAR preparations. These did enable cell borders to be visualised, but the staining intensity was very variable and would not have permitted automated analysis. The fact that staining EStAR preparations with antibodies worked at all suggests that there is great potential for this technique in staining e.g. mechanosensors, and determining regions where these are up- or down-regulated, and whether these correlate with high or low shear stress regions. However, the issues involved in staining antigens that are on the luminal surface of the ECs, and hence in contact with the tape, needs to be resolved. Having not been able to produce data of sufficient quality for ECs using antibodies, staining ELs with silver nitrate was attempted instead. This proved more successful than PECAM-1 and produced very clearly defined borders. However the staining still was not quite uniform enough to enable automated analysis. This was overcome by manually completing the cell outlines

in regions of interest (i.e. upstream and downstream regions around branch ostia) and then analysing these semi-automatically using image analysis techniques previously developed. As with ECn it was then possible to observe whether the patterns of cell elongation changed with age.

8.2 Changes in blood flow patterns with age

The evidence accumulated in this study points to an age-related change in the pattern of elongation around rabbit intercostal branch ostia. Increased cellular and nuclear elongation downstream of the branch ostia changes to increased elongation upstream, after the age of sexual maturity. There are a number of possible haemodynamic explanations for this change with age. 1) It has been shown that arteries generally become stiffer with age (even in the absence of atherosclerosis) in mice (Reddy *et al.*, 2003), pigs (Greenwald *et al.*, 1982), and humans (Vaitkevicius *et al.*, 1993). (Aortic stiffness has been shown to decrease sharply with age in humans until the age of approximately 10, and then shows a progressive increase with age (Laogun and Gosling, 1982)). Sloop et al (1998) suggested that greater arterial elasticity allows increased volume and duration of retrograde blood flow during late systole/early diastole, thus allowing the propagation of retrograde flow through the entire length of the aortic branch and moving the location of the region of lower shear stress away from the branch ostium. 2) The branch diameter in rabbits does not appear to change substantially with age (Al-Musawi *et al.*, 2004). Therefore increasing the flow into the branch, as would be expected with age due to increased body weight, would cause a region of higher shear stress upstream of the ostium relative to that downstream (Cheer *et al.*, 1998). 3) Intimal cushions are regions of the intima that protrude into the lumen of the artery, and may alter blood flow patterns. Work in our group has suggested that they are present upstream of branches in mature but not immature rabbits (Staughton & Weinberg, unpublished data, 2000). 4) Although no measurements were taken, the flow dividers observed in the present study appeared more pronounced in mature rabbits than immature ones, even after the arterial wall was flattened during the EStAR preparation. A larger flow divider would enable blood from a larger region upstream and laterally around the ostia to be drawn into the branch. There would also be a larger affect on blood flow downstream of the flow divider.

It is unclear which of the above, if any, are responsible for age-related changes in blood flow. It may be that the change in lesion location is partly due to properties of the arterial wall changing with age, perhaps making some parts of the intima more susceptible to atherogenic stimuli. It has been shown that components at the cellular level change with age e.g. age causes decreased intracellular free magnesium levels (Resnick *et al.*, 1997), decreased release of nitric oxide (Haendeler, 2005), decreased responsiveness of arterial wall to endothelin (a vasoconstrictor synthesised by the endothelium), and increased oxygen-derived free radicals due to decreased natural antioxidant defences (reviewed by Marin, 1995). The carotid arterial wall has been shown to adapt to chronic changes in blood flow differently in young and old rabbits (Langille *et al.*, 1989). In young, decreased blood flow (imposed by stenosing the artery) caused an inhibition of wall tissue growth that involved cellular and elastic but not collagenous elements. In old, decreased flow did not cause any inhibition of wall growth, elastin or collagen. A study looking at the endothelium in rabbits has shown that the planar cell polarity (PCP) is age and blood vessel specific (McCue *et al.*, 2006). PCP occurs when cell organelles, cytoskeleton, and/or adhesion complexes align along a unidirectional axis that lies in the plane of a cell monolayer, and is thought to have implications in the repair of damaged endothelium. In adult rabbits, microtubule organising centres (MTOCs) were downstream of nuclei in the vena cava, upstream in the carotid artery, reversed polarity with age in the abdominal aorta, but were unpolarized in the thoracic aorta. However, it is unlikely that the regions examined were around branch ostia. If cells around intercostal branches are polarized, as in the abdominal aorta, then this could play a role in the change in disease pattern with age in these regions.

As already mentioned, the release of nitric oxide (NO) decreases with age (Haendeler, 2005). NO is a free radical gas with a half-life of several seconds (Napoli *et al.*, 2006) that plays an important role in regulating the functional integrity of the endothelium. It is synthesised from L-arginine via the action of nitric oxide synthases of which there are 3 isoforms; only endothelial nitric oxide synthase (eNOS) is of relevance here. NO has been found to have a role in inhibiting platelet adherence, leuckocyte chemotaxis, SMC

proliferation and migration, promoting endothelial regrowth and vasorelaxation (Barbato and Tzeng, 2004), all of which are atheroprotective. Forster & Weinberg (1997) have shown that administering the NO-synthase inhibitor N^{ω}-monomethyl-L-arginine (L-NMMA), to the thoracic aorta causes a change to the pattern of albumin uptake around branch ostia in mature rabbits. The usual pattern of uptake upstream of the branch was reversed, uptake becoming greater downstream (as in immature rabbits). In immature rabbits, the pattern of uptake was not changed by L-NMMA. The fact that the vessels were perfused at a constant rate and pressure throughout this procedure, and that side-branch flow did not change significantly, suggests that the mature pattern, but not the immature, depends on direct effects of NO on the arterial wall. A study that followed on from this (Staughton *et al.*, 2001) tested whether the mature pattern was also flow dependent, as NO synthesis is thought to be influenced by blood flow. Intercostal arteries of rabbits were occluded to stop the flow into the branch, and uptake of rhodamine-labelled albumin around the branch was measured. As with administering L-NMMA, reducing side-branch flow caused the mature pattern of uptake to reverse (uptake became greater downstream than upstream of ostia).

As described elsewhere, a transgenic eNOS-GFP mouse has been developed to observe how the expression of eNOS changes throughout the vasculature, in regions of differing shear stresses (Cheng *et al.*, 2005). In eNOS-GFP mice, regions expressing eNOS fluoresce when viewed through filter sets for fluorescein. Cheng *et al* showed that eNOS is mainly located at a perinuclear site that coincides with the location of the Golgi complex, and the plasma membrane. Application of a shear modifying cuff showed that in regions of high shear stress, levels of eNOS increase in the Golgi complex and cell membrane when compared with undisturbed shear stress or low shear stress.

Using the EStAR technique it was possible to produce an EL containing a branch ostium from one of these mice (Fig. 8.1).

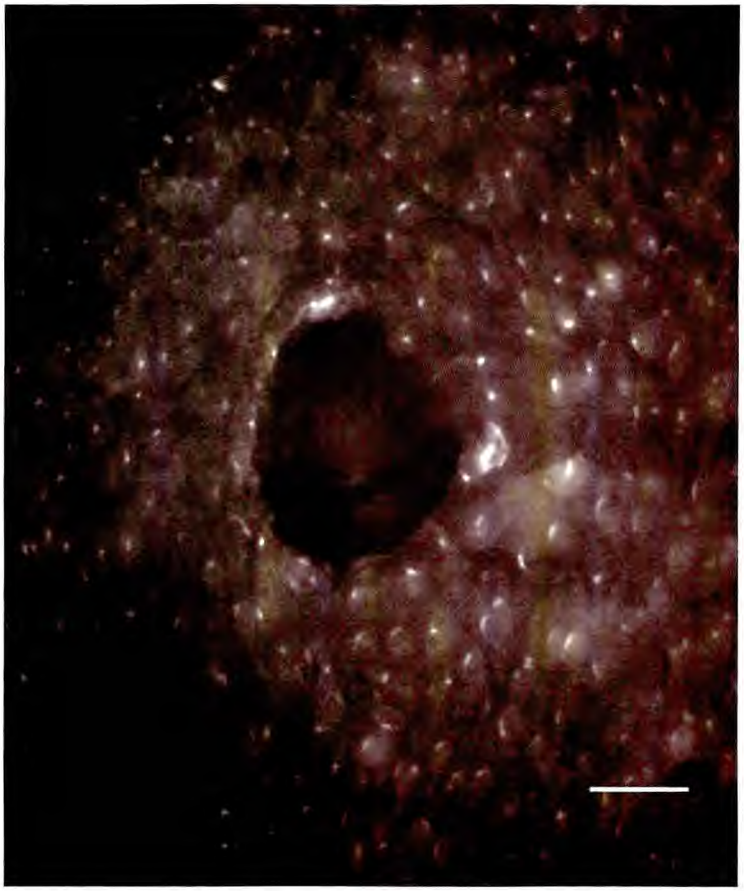

Fig. 8.1. EStAR preparation of endothelium in the region surrounding an intercostal branch ostium (centre of the image) of an eNOS-GFP mouse. eNOS shows up as bright spots. Blood flow is from top to bottom of image. Scale bar = 50μm.

In our images, eNOS appears to be located uniformly around the ostium and to be present in all of the cells. The brighter fluorescence in "spots" corresponds well with the appearance of eNOS in low shear stress regions seen by Cheng *et al* (2005) in the carotid artery of eNOS-GFP mice. The uniform distribution of eNOS around the ostium suggest a relatively uniform and low level of wall shear stress, and could provide clues as to why the pattern of lesion development in mice is different to that of rabbits and humans. Further studies using the EStAR technique would be a useful method of mapping the location and intensities of eNOS in the transgenic mouse to determine whether the location corresponds with the location of lesions in $LDLR^{-/-}/ApoE^{-/-}$ double knockout mice.

8.3 Differences in blood flow patterns between species

It is clear that there is a difference in blood flow patterns around intercostal ostia between mice and rabbits, and these differences may partly explain the different pattern of lesion prevalence. In mice aortas, lesions are located relatively uniformly around branch ostia, and this pattern does not change significantly with age (McGillicuddy *et al.*, 2001). This is partly reflected in the pattern of nuclear elongation; there was no significant change in pattern between age groups (although nuclei in mature mice were generally more elongated than in immature). There were, however, differences between regions around the ostia, namely nuclei at the lateral regions were more elongated than in all other regions. Lipid deposition occurs downstream of the branch in immature rabbits (Ivey *et al.*, 1995), and upstream and at the lateral regions in mature rabbits (Barnes and Weinberg, 1999). These distributions were also reflected in the pattern of nuclear elongation. ECn were more elongated downstream than upstream of the ostia in immature rabbits, and this pattern reversed with age. These differences may provide an explanation as to why mice and rabbits have different lesion locations. A geometrical difference between species was the presence of a large arterial cushion upstream of the mice ostia in all ages; no such feature was observed in rabbits (although smaller upstream cushions have been seen in mature rabbits by Staughton and Weinberg. Explanations for differences between nuclear orientations are given elsewhere.

The mean nuclear LW ratios determined by the different techniques used in this project are shown in Fig. 8.2. The two techniques gave similar results in immature and mature rabbits. In mice the LW ratios were about 10% lower for the EStAR technique. The most likely explanation for this is that the confocal technique in mice only looked at regions surrounding branch ostia, whereas the EStAR technique produced data for the whole aortas of mice, including the aortic arch. Genuine differences between techniques (for example that the aortas in the confocal technique were only partially flattened before microscopy and were not dehydrated at any point, whereas in the EStAR technique they were flattened fully having first been dehydrated in alcohol) leading to variable data are made unlikely by the fact that rabbit data is comparable between techniques. The nuclear LW ratios in pigs were much lower than for all other species

but this is almost certainly due to the lack of pressure fixation causing the arterial wall to contract, shortening the nuclei with it.

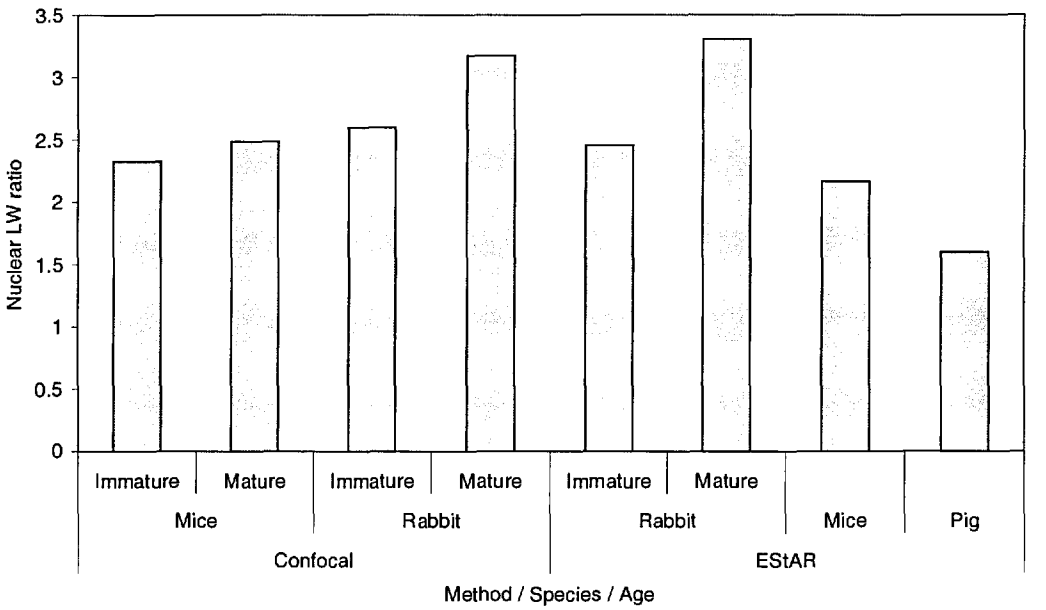

Fig. 8.2. Comparison of total mean nuclear LW ratios determined by the confocal microscopy technique and the EStAR technique, in mice, rabbits, and pigs. SEMs are not shown due to variable sample sizes.

8.4 Future Studies

This project has enabled endothelial cell nuclear morphology to be mapped in significant detail in the thoracic aortas of rabbits and mice of different ages. Rabbits have previously been shown to be a good model for the location of atherosclerotic lesions in humans. Mapping the changes in nuclear shape in human aortas, especially around intercostal branch ostia, using the EStAR technique would prove extremely useful in further validating the rabbit model, although there would be difficulties in obtaining vessels fixed at *in vivo* dimensions, as with the pig.

Despite there being evidence that nuclei elongate in regions of higher shear stress, it is currently unknown by how much cells of different ages elongate at different levels of shear stress and under different flow waveforms. Using cultured endothelial cells and parallel plate flow chambers to apply a known shear stress over the cell surface, it would

be possible to use the image analysis techniques developed for this project to produce accurate data to show how the cell and nuclear shape changes. Using cultured cells from immature and mature animals would then be useful to see if their responses to increased shear stress differed. It has previously been argued (Al-Musawi *et al*, 2004) that EC and ECn must elongate with increased shear at both ages, since cell culture experiments reporting such behaviour have used cells from immature and mature animals. However, there may be quantitative differences in the response.

The problem of how to automate the analysis of images of endothelial cells might at first sight appear to be a trivial one. However, this turns out not to be the case. S. Iftikhar and A. Bharath, at Imperial College London, are attempting to automate the analysis of our images with modern techniques, but several problems have still not been overcome. They have used the images of endothelium double stained with PI and $AgNO_3$. Using the nuclei as central points of reference, radial lines were drawn to enable ellipses to be drawn to fit to the cell borders (Fig. 8.3). The ellipses could then be analysed to determine the shape and alignment of the ECs, and these could be correlated with the shape and alignment of ECn.

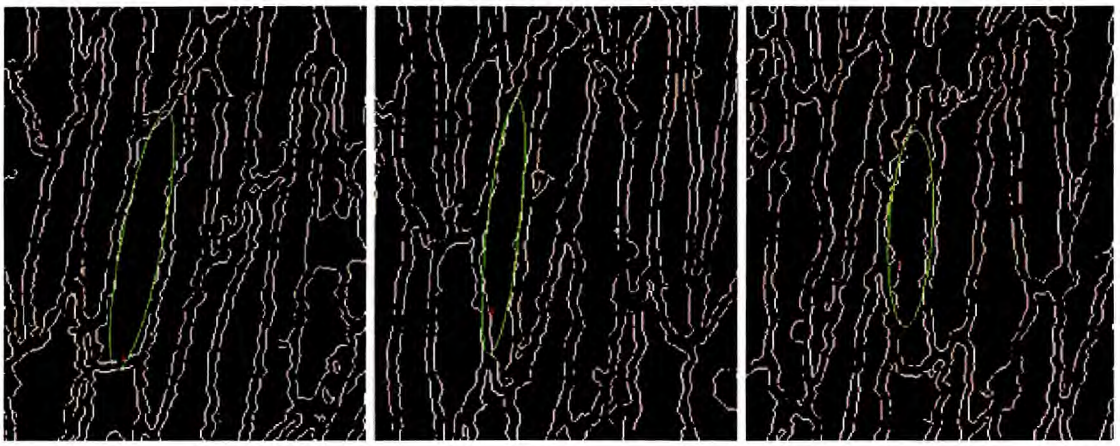

Fig. 8.3. Ellipses (green) drawn using an automated technique to represent endothelial cell borders. The white lines are the edges of the silver stained cells after thresholding.

The technique currently cannot accurately fit ellipses to the borders of all the cells, and would not give results that are as good as those we obtained by manually drawing the outline of cells. However, it is a good example of how staining endothelial layers

prepared using the EStAR technique might be utilised in the future to determine cell shapes.

Attempts were made to stain the endothelial cytoskeleton with rhodamine-phalloidin, as the distribution of microfilaments changes under altered flow conditions (Kim *et al.*, 1989a). Other studies have shown this to be a reliable technique both *in vitro* (Cucina *et al.*, 1995) and *in vivo* (Kim et al., 1989b, Colangelo et al., 1994, Kiosses et al., 1997), but our experiments were unsuccessful. This could be due to the EStAR technique damaging the cytoskeleton, either during the removal of the underlying SMCs or during alcohol deydration. It seems unlikely that removing underlying SMCs would prevent staining as MFs are found within the cell itself, and through PI staining and silver staining it has been shown that the endothelial layer is still present. A study by Small (1981) examined the influence of dehydration on MFs in cultured cells. Their findings suggested that dehydration leads to a thickening or distortion of MFs, but not total removal, so some staining should have been seen in our preparations. Further studies are required to improve the staining procedure (possibly staining *in situ*, or prior to dehydration steps), and to observe whether the cytoskeleton is altered in regions around branches in the thoracic aorta and whether there is a change in pattern between immature and mature aortas.

Using the EStAR technique it was possible to stain PECAM-1 within the endothelium. This suggests it would also be possible to use antibody staining for other proteins within the wall, in particular ones that are up- or down-regulated in changing shear stress such as Kruppel-like factor-2 (Wang *et al.*, 2006).

In conclusion, the work that has been carried out in this project furthers our understanding of blood flow patterns around intercostal branch ostia. There appear to be distinct differences in flow patterns between mice and rabbits, and around rabbit intercostal branch ostia there are definite changes with age. These differences could help explain the patchy nature of atherosclerotic lesions within the vasculature.

References

ABCAM PLC (2006) pan Cadherin antibody datasheet. www.abcam.co.uk.

AL-MUSAWI, S. L., BISHTON, J., DEAN, J., WILLIAMS, S., CREMERS, S. G. & WEINBERG, P. D. (2004) Evidence for a reversal with age in the pattern of near-wall blood flow around aortic branches. *Atherosclerosis,* 172, 79-84.

ALBERTS, B., BRAY, D., LEWIS, J., RAFF, M., ROBERTS, K. & WATSON, J. D. (1994) Vesicular traffic in the secretory and endocytic pathways *Molecular Biology of the cell.* New York, Garland Publishing.

ALEVRIADOU, B. R., ESKIN, S. G., MCINTIRE, L. V. & SCHILLING, W. P. (1993) Effect of shear stress on 86Rb+ efflux from calf pulmonary artery endothelial cells. *Ann Biomed Eng,* 21, 1-7.

ANITSCHKOW, N. (1933) Experimental atherosclerosis in animals. IN COWDRY, E. V. (Ed.) *Arteriosclerosis.* New York, Macmillan.

ASAKURA, T. & KARINO, T. (1990) Flow patterns and spatial distribution of atherosclerotic lesions in human coronary arteries. *Circ Res,* 66, 1045-66.

BACK, L. H., CRAWFORD, D. W. & BARNDT, R., JR. (1976) Flow field and mass transport analysis in arteries with longitudinal ridges. *J Appl Physiol,* 41, 910-9.

BADEER, H. S. (2001) Hemodynamics for medical students. *Adv Physiol Educ,* 25, 44-52.

BARBATO, J. E. & TZENG, E. (2004) Nitric oxide and arterial disease. *J Vasc Surg,* 40, 187-93.

BARNES, S. E. & WEINBERG, P. D. (1998) Contrasting patterns of spontaneous aortic disease in young and old rabbits. *Arterioscler Thromb Vasc Biol,* 18, 300-8.

BARNES, S. E. & WEINBERG, P. D. (1999) Two patterns of lipid deposition in the cholesterol-fed rabbit. *Arterioscler Thromb Vasc Biol,* 19, 2376-86.

BERCELI, S. A., WARTY, V. S., SHEPPECK, R. A., MANDARINO, W. A., TANKSALE, S. K. & BOROVETZ, H. S. (1990) Hemodynamics and low density lipoprotein metabolism. Rates of low density lipoprotein incorporation and degradation along medial and lateral walls of the rabbit aorto-iliac bifurcation. *Arteriosclerosis,* 10, 686-94.

BERK, B. C., CORSON, M. A., PETERSON, T. E. & TSENG, H. (1995) Protein kinases as mediators of fluid shear stress stimulated signal transduction in endothelial cells: a hypothesis for calcium-dependent and calcium-independent events activated by flow. *J Biomech,* 28, 1439-50.

BIRUKOV, K. G., BIRUKOVA, A. A., DUDEK, S. M., VERIN, A. D., CROW, M. T., ZHAN, X., DEPAOLA, N. & GARCIA, J. G. (2002) Shear stress-mediated cytoskeletal

remodeling and cortactin translocation in pulmonary endothelial cells. *Am J Respir Cell Mol Biol,* 26, 453-64.

BRADDOCK, M., SCHWACHTGEN, J. L., HOUSTON, P., DICKSON, M. C., LEE, M. J. & CAMPBELL, C. J. (1998) Fluid Shear Stress Modulation of Gene Expression in Endothelial Cells. *News Physiol Sci,* 13, 241-246.

BRITISH HEART FOUNDATION (2004) British Heart Foundation Statistics Website. www.heartstats.org.

BUGELSKI, P. J., MALEEFF, B. E., KLINKNER, A. M., LOUDEN, C. S. & HART, T. K. (2000) Nonlinear Dynamics in the Progression of Atherosclerotic Fatty Streaks: Morphometric Analysis. *Microscopy and Microanalysis,* 6, 532-541.

CAI, J. M., HATSUKAMI, T. S., FERGUSON, M. S., SMALL, R., POLISSAR, N. L. & YUAN, C. (2002) Classification of human carotid atherosclerotic lesions with in vivo multicontrast magnetic resonance imaging. *Circulation,* 106, 1368-73.

CARO, C. G. (1978) *The Mechanics of the Circulation,* Oxford, Oxford University Press.

CARO, C. G. (1982) Arterial fluid mechanics and atherogenesis. *Clinical Hemorheology,* 2, 131-136.

CARO, C. G., FITZ-GERALD, J. M. & SCHROTER, R. C. (1969) Arterial wall shear and distribution of early atheroma in man. *Nature,* 223, 1159-60.

CARO, C. G., FITZ-GERALD, J. M. & SCHROTER, R. C. (1971) Atheroma and arterial wall shear. Observation, correlation and proposal of a shear dependent mass transfer mechanism for atherogenesis. *Proc R Soc Lond B Biol Sci,* 177, 109-59.

CARO, C. G., PARKER, K. H., FISH, P. J. & LEVER, M. J. (1985) Blood flow near the arterial wall and arterial disease. *Clinical Hemorheology,* 5, 849-871.

CHANDRAN, K. B., MUN, J. H., CHOI, K. K., CHEN, J. S., HAMILTON, A., NAGARAJ, A. & MCPHERSON, D. D. (2003) A method for in-vivo analysis for regional arterial wall material property alterations with atherosclerosis: preliminary results. *Med Eng Phys,* 25, 289-98.

CHATZIZISIS, Y. S., COSKUN, A. U., JONAS, M., EDELMAN, E. R., FELDMAN, C. L. & STONE, P. H. (2007) Role of endothelial shear stress in the natural history of coronary atherosclerosis and vascular remodelling: molecular, cellular, and vascular behaviour. *Journal of the American College of Cardiology,* 49, 2379-2393.

CHEER, A. Y., DWYER, H. A., BARAKAT, A. I., SY, E. & BICE, M. (1998) Computational study of the effect of geometric and flow parameters on the steady flow field at the rabbit aorta-celiac bifurcation. *Biorheology,* 35, 415-435.

CHENG, C., VAN HAPEREN, R., DE WAARD, M., VAN DAMME, L. C., TEMPEL, D., HANEMAAIJER, L., VAN CAPPELLEN, G. W., BOS, J., SLAGER, C. J.,

DUNCKER, D. J., VAN DER STEEN, A. F., DE CROM, R. & KRAMS, R. (2005) Shear stress affects the intracellular distribution of eNOS: direct demonstration by a novel in vivo technique. *Blood,* 106, 3691-8.

CHIEN, S. (2003) Molecular and mechanical bases of focal lipid accumulation in arterial wall. *Prog Biophys Mol Biol,* 83, 131-51.

CHUANG, P. T., CHENG, H. J., LIN, S. J., JAN, K. M., LEE, M. M. & CHIEN, S. (1990) Macromolecular transport across arterial and venous endothelium in rats. Studies with Evans blue-albumin and horseradish peroxidase. *Arteriosclerosis,* 10, 188-97.

CLEAVE BOOKS (2004) The Ellipses Calculator. *Specialist Calculators on Line.* www.cleavebooks.co.uk/scol/callipse.htm.

COLANGELO, S., LANGILLE, B. L. & GOTLIEB, A. I. (1994) Three patterns of distribution characterize the organization of endothelial microfilaments at aortic flow dividers. *Cell Tissue Res,* 278, 235-42.

CORNHILL, J. F., BARRETT, W. A., HERDERICK, E. E., MAHLEY, R. W. & FRY, D. L. (1985) Topographic study of sudanophilic lesions in cholesterol-fed minipigs by image analysis. *Arteriosclerosis,* 5, 415-26.

CORNHILL, J. F., LEVESQUE, M. J., HERDERICK, E. E., NEREM, R. M., KILMAN, J. W. & VASKO, J. S. (1980) Quantitative study of the rabbit aortic endothelium using vascular casts. *Atherosclerosis,* 35, 321-37.

CORNHILL, J. F. & ROACH, M. R. (1976) A quantitative study of the localization of atherosclerotic lesions in the rabbit aorta. *Atherosclerosis,* 23, 489-501.

COX, R. H. (1977) Effects of age on the mechanical properties of rat carotid artery. *Am J Physiol,* 233, H256-63.

CUCINA, A., STERPETTI, A. V., PUPELIS, G., FRAGALE, A., LEPIDI, S., CAVALLARO, A., GIUSTINIANI, Q. & SANTORO D'ANGELO, L. (1995) Shear stress induces changes in the morphology and cytoskeleton organisation of arterial endothelial cells. *Eur J Vasc Endovasc Surg,* 9, 86-92.

DABANOGLU, I. (2000) A quantitative study of the aorta of the New Zealand rabbit (Oryctolagus cuniculus L.). *Anat Histol Embryol,* 29, 145-7.

DEWEY, C. F., JR., BUSSOLARI, S. R., GIMBRONE, M. A., JR. & DAVIES, P. F. (1981) The dynamic response of vascular endothelial cells to fluid shear stress. *J Biomech Eng,* 103, 177-85.

DEWEY JR, C. F. (1979) Fluid mechanics of arterial flow. IN WOLF, S. & WERTHESSEN, N. T. (Eds.) *Dynamics of arterial flow: Advances in experimental medicine and biology.*

DUSSERRE, N., L'HEUREUX, N., BELL, K. S., STEVENS, H. Y., YEH, J., OTTE, L. A., LOUFRANI, L. & FRANGOS, J. A. (2004) PECAM-1 interacts with nitric oxide

synthase in human endothelial cells: implication for flow-induced nitric oxide synthase activation. *Arterioscler Thromb Vasc Biol,* 24, 1796-802.

DYCK, J., LOO, S., ZACHER, N., WONG, D., MCDONALD, P. C., WALKER, D. C., WILSON, J. E. & MCMANUS, B. M. (2001) Use of en face silver nitrate staining to assess endothelial gaps and vascular permeability in rat coronary artery transplant vasculopathy. *J Heart Lung Transplant,* 20, 229-230.

EFUNDA (2003) Reynolds Number Calculator. http://www.efunda.com/formulae/fluids/calc_reynolds.cfm.

ERIKSSON, M. (2002) Primary prevention of clinical atherosclerosis. IN CARLSON, L. (Ed.) *Lectures in clinical atherosclerosis and dyslipidaemia.* London, Science Press Ltd.

ESKIN, S. G., IVES, C. L., MCINTIRE, L. V. & NAVARRO, L. T. (1984) Response of cultured endothelial cells to steady flow. *Microvasc Res,* 28, 87-94.

EWINS, B. A., MAJEWICZ, J., STAUGHTON, T. J. & WEINBERG, P. D. (2002) Two-dimensional maps of short-term albumin uptake by the immature and mature rabbit aortic wall around branch points. *J Biomech Eng,* 124, 684-90.

EZEILO, G. C. (2005) *Textbook of Physiology,* Oxford, Oxford University Press.

FEINTUCH, A., RUENGSAKULRACH, P., LIN, A., ZHANG, J., ZHOU, Y. Q., BISHOP, J., DAVIDSON, L., COURTMAN, D., FOSTER, F. S., STEINMAN, D. A., HENKELMAN, R. M. & ETHIER, C. R. (2007) Hemodynamics in the mouse aortic arch as assessed by MRI, ultrasound, and numerical modeling. *Am J Physiol Heart Circ Physiol,* 292, H884-92.

FLAHERTY, J. T., PIERCE, J. E., FERRANS, V. J., PATEL, D. J., TUCKER, W. K. & FRY, D. L. (1972) Endothelial nuclear patterns in the canine arterial tree with particular reference to hemodynamic events. *Circ Res,* 30, 23-33.

FLOREY, H. W., POOLE, J. C. & MEEK, G. A. (1959) Endothelial cells and cement lines. *J Pathol Bacteriol,* 77, 625-36.

FORSTER, B. A. & WEINBERG, P. D. (1997) Changes with age in the influence of endogenous nitric oxide on transport properties of the rabbit aortic wall near branches. *Arterioscler Thromb Vasc Biol,* 17, 1361-1368.

FOURMAN, J. & MOFFAT, D. B. (1961) The effect of intra-arterial cushions on plasma skimming in small arteries. *J Physiol,* 158, 374-80.

FRANKE, R. P., GRAFE, M., SCHNITTLER, H., SEIFFGE, D., MITTERMAYER, C. & DRENCKHAHN, D. (1984) Induction of human vascular endothelial stress fibres by fluid shear stress. *Nature,* 307, 648-9.

FRIMERMAN, A., MILLER, H. I., SIEGEL, R. J., ROSENSCHEIN, U., ROTH, A. & KEREN, G. (1999) Intravascular ultrasound imaging of myocardial-infarction-related

arteries after percutaneous transluminal coronary angioplasty reveals significant plaque burden and compensatory enlargement. *Int J Cardiovasc Intervent,* 2, 101-107.

FRY, D. L. (1969) Certain chemorheologic considerations regarding the blood vascular wall interface with particular reference to coronary artery disease. *Circulation,* 40 (Suppl. IV), 38-59.

GETZ, G. S. & REARDON, C. A. (2006) Diet and murine atherosclerosis. *Arterioscler Thromb Vasc Biol,* 26, 242-9.

GLAGOV, S., ROWLEY, D. A. & KOHUT, R. I. (1961) Atherosclerosis of human aorta and its coronary and renal arteries. A consideration of some hemodynamic factors which may be related to the marked differences in atherosclerotic involvement of the coronary and renal arteries. *Archives of Pathology,* 72, 558-71.

GNASSO, A., IRACE, C., CARALLO, C., DE FRANCESCHI, M. S., MOTTI, C., MATTIOLI, P. L. & PUJIA, A. (1997) In vivo association between low wall shear stress and plaque in subjects with asymmetrical carotid atherosclerosis. *Stroke,* 28, 993-8.

GORGAS, K. & BOCK, P. (1975) Studies on intra-arterial cushions. I. Morphology of the cushions at the origins of intercostal arteries in mice. *Anat Embryol (Berl),* 148, 59-72.

GOUVERNEUR, M., BERG, B., NIEUWDORP, M., STROES, E. & VINK, H. (2006a) Vasculoprotective properties of the endothelial glycocalyx: effects of fluid shear stress. *J Intern Med,* 259, 393-400.

GOUVERNEUR, M., SPAAN, J. A., PANNEKOEK, H., FONTIJN, R. D. & VINK, H. (2006b) Fluid shear stress stimulates incorporation of hyaluronan into endothelial cell glycocalyx. *Am J Physiol Heart Circ Physiol,* 290, H458-2.

GREENWALD, S. E., BERRY, C. L. & HAWORTH, S. G. (1982) Changes in the distensibility of the intrapulmonary arteries in the normal newborn and growing pig. *Cardiovasc Res,* 16, 716-25.

GUZMAN, R. J., KRYSTKOWIAK, A. & ZARINS, C. K. (2002) Early and sustained medial cell activation after aortocaval fistula creation in mice. *J Surg Res,* 108, 112-21.

HAENDELER, J. (2005) Nitric oxide and endothelial cell aging. *Eur J Clin Pharmacol,* 1-4.

HAZEL, A. L. & PEDLEY, T. J. (2000) Vascular endothelial cells minimize the total force on their nuclei. *Biophys J,* 78, 47-54.

HE, P. (1998) Confocal reflectance and fluorescence imaging of post-capillary venules. *Bio-Rad Application Note 26.* Bio-Rad Laboratories.

HE, P. & ADAMSON, R. H. (1995) Visualization of endothelial clefts and nuclei in living microvessels with combined reflectance and fluorescence confocal microscopy. *Microcirculation,* 2, 267-76.

HEIDGER, P. M., JR., VAN ORDEN, D. E. & FARLEY, D. B. (1983) Electron microscopic and histochemical characterization of intra-arterial cushions of the rat and porcine uterine vascular bed. *Acta Anat (Basel),* 117, 239-47.

HELMLINGER, G., GEIGER, R. V., SCHRECK, S. & NEREM, R. M. (1991) Effects of pulsatile flow on cultured vascular endothelial cell morphology. *J Biomech Eng,* 113, 123-31.

HESSE, M. & BOCK, P. (1980) Studies on intra-arterial cushions. III. The cushions at the origin of the rat carotid body artery (CBA). *Z Mikrosk Anat Forsch,* 94, 471-8.

HIRATA, A., BALUK, P., FUJIWARA, T. & MCDONALD, D. M. (1995) Location of focal silver staining at endothelial gaps in inflamed venules examined by scanning electron microscopy. *Am J Physiol,* 269, L403-18.

HIRSCH, E. Z., MARTINO, W., ORR, C. H., WHITE, H. & CHISOLM, G. M., 3RD (1980) A simple rapid method for the preparation of en face endothelial (Hautchen) monolayers from rat and rabbit aortas. *Atherosclerosis,* 37, 539-48.

HOSSLER, F. E. (1998) Vascular corrosion casting can provide quantitiative as well as morphological information on the microvasculature of organs and tissues. *Microscopy Today,* 6, 14-15.

INGBER, D. E. (1998) Cellular basis of mechanotransduction. *Biol Bull,* 194, 323-5; discussion 325-7.

IVEY, J., ROACH, M. R. & KRATKY, R. G. (1995) A new probability mapping method to describe the development of atherosclerotic lesions in cholesterol-fed rabbits. *Atherosclerosis,* 115, 73-84.

JACKSON, D. E. (2003) The unfolding tale of PECAM-1. *FEBS Lett,* 540, 7-14.

JOHNSON, J. L. & JACKSON, C. L. (2001) Atherosclerotic plaque rupture in the apolipoprotein E knockout mouse. *Atherosclerosis,* 154, 399-406.

KAZAKIDI, A., SHERWIN, S. J. & WEINBERG, P. D. (2006) Alteration of Reynolds number and flow partition modify wall shear stresses at arterial branches in a way that can explain age- and species-dependent patterns of arterial disease. *Journal of Biomechanics,* 39, Suppl. 1, S611.

KIM, D. W., GOTLIEB, A. I. & LANGILLE, B. L. (1989a) In vivo modulation of endothelial F-actin microfilaments by experimental alterations in shear stress. *Arteriosclerosis,* 9, 439-45.

KIM, D. W., LANGILLE, B. L., WONG, M. K. & GOTLIEB, A. I. (1989b) Patterns of endothelial microfilament distribution in the rabbit aorta in situ. *Circ Res,* 64, 21-31.

KIOSSES, W. B., MCKEE, N. H. & KALNINS, V. I. (1997) Relationship between the distribution of stress fibers and centrosomes in endothelial cells of the rat aorta. *Cell Motil Cytoskeleton,* 36, 228-35.

KRATKY, R. G. & ROACH, M. R. (1987) Endothelial cell morphometry near branch junctions of rabbit aortae. *Can J Physiol Pharmacol,* 65, 1864-71.

KRATKY, R. G., ZEINDLER, C. M., LO, D. K. & ROACH, M. R. (1989) Quantitative measurement from vascular casts. *Scanning Microscopy,* 3, 937-943.

LABARBERA, M. (1990) Principles of design of fluid transport systems in zoology. *Science,* 249, 992-1000.

LANGILLE, B. L. & ADAMSON, S. L. (1981) Relationship between blood flow direction and endothelial cell orientation at arterial branch sites in rabbits and mice. *Circ Res,* 48, 481-8.

LANGILLE, B. L., BENDECK, M. P. & KEELEY, F. W. (1989) Adaptations of carotid arteries of young and mature rabbits to reduced carotid blood flow. *Am J Physiol,* 256, H931-9.

LAOGUN, A. A. & GOSLING, R. G. (1982) In vivo arterial compliance in man. *Clin Phys Physiol Meas,* 3, 201-12.

LARZUL, C. & DE ROCHAMBEAU, H. (2004) Comparison of ten rabbit lines of terminal bucks for growth, feed efficiency and carcass traits. *Animal Research,* 53, 535-545.

LEE, B. K., KWON, H. M., HONG, B. K., PARK, B. E., SUH, S. H., CHO, M. T., LEE, C. S., KIM, M. C., KIM, C. J., YOO, S. S. & KIM, H. S. (2001) Hemodynamic effects on atherosclerosis-prone coronary artery: wall shear stress/rate distribution and impedance phase angle in coronary and aortic circulation. *Yonsei Med J,* 42, 375-83.

LEE, T. Y. & GOTLIEB, A. I. (2003) Microfilaments and microtubules maintain endothelial integrity. *Microsc Res Tech,* 60, 115-27.

LEVESQUE, M. J., CORNHILL, J. F. & NEREM, R. M. (1979) Vascular casting. A new method for the study of the arterial endothelium. *Atherosclerosis,* 34, 457-67.

LEVESQUE, M. J., LIEPSCH, D., MORAVEC, S. & NEREM, R. M. (1986) Correlation of endothelial cell shape and wall shear stress in a stenosed dog aorta. *Arteriosclerosis,* 6, 220-9.

LEVESQUE, M. J. & NEREM, R. M. (1985) The elongation and orientation of cultured endothelial cells in response to shear stress. *J Biomech Eng,* 107, 341-7.

LEVICK, J. R. (2003) *An Introduction to Cardiovascular Physiology,* UK, Arnold.

LI, Y. S., HAGA, J. H. & CHIEN, S. (2005) Molecular basis of the effects of shear stress on vascular endothelial cells. *J Biomech,* 38, 1949-71.

LICHTMAN, A. H., CLINTON, S. K., IIYAMA, K., CONNELLY, P. W., LIBBY, P. & CYBULSKY, M. I. (1999) Hyperlipidemia and atherosclerotic lesion development in

LDL receptor-deficient mice fed defined semipurified diets with and without cholate. *Arterioscler Thromb Vasc Biol,* 19, 1938-44.

LIN, S. J. (1996) Risk factors, endothelial cell turnover and lipid transport in atherogenesis. *Zhonghua Yi Xue Za Zhi (Taipei),* 58, 309-16.

LIN, S. J., JAN, K. M. & CHIEN, S. (1990) Role of dying endothelial cells in transendothelial macromolecular transport. *Arteriosclerosis,* 10, 703-9.

LUPINETTI, F. M., TSAI, T. T., KNEEBONE, J. M. & BOVE, E. L. (1993) Effect of cryopreservation on the presence of endothelial cells on human valve allografts. *J Thorac Cardiovasc Surg,* 106, 912-917.

MACARI, M. & MACHADO, C. R. (1978) Sexual maturity in rabbits defined by the physical and chemical characteristics of the semen. *Lab Anim,* 12, 37-39.

MALINAUSKAS, R. A., SARRAF, P., BARBER, K. M. & TRUSKEY, G. A. (1998) Association between secondary flow in models of the aorto-celiac junction and subendothelial macrophages in the normal rabbit. *Atherosclerosis,* 140, 121-34.

MANN, M. J., GIBBONS, G. H., KERNOFF, R. S., DIET, F. P., TSAO, P. S., COOKE, J. P., KANEDA, Y. & DZAU, V. J. (1995) Genetic engineering of vein grafts resistant to atherosclerosis. *Proc Natl Acad Sci U S A,* 92, 4502-6.

MARIN, J. (1995) Age-related changes in vascular responses: a review. *Mech Ageing Dev,* 79, 71-114.

MASUDA, H., KAWAMURA, K., NANJO, H., SHO, E., KOMATSU, M., SUGIYAMA, T., SUGITA, A., ASARI, Y., KOBAYASHI, M., EBINA, T., HOSHI, N., SINGH, T. M., XU, C. & ZARINS, C. K. (2003) Ultrastructure of endothelial cells under flow alteration. *Microsc Res Tech,* 60, 2-12.

MCCUE, S., DAJNOWIEC, D., XU, F., ZHANG, M., JACKSON, M. R. & LANGILLE, B. L. (2006) Shear stress regulates forward and reverse planar cell polarity of vascular endothelium in vivo and in vitro. *Circ Res,* 98, 939-46.

MCCUE, S., NORIA, S. & LANGILLE, B. L. (2004) Shear-induced reorganization of endothelial cell cytoskeleton and adhesion complexes. *Trends Cardiovasc Med,* 14, 143-51.

MCGILLICUDDY, C. J., CARRIER, M. J. & WEINBERG, P. D. (2001) Distribution of lipid deposits around aortic branches of mice lacking LDL receptors and apolipoprotein E. *Arterioscler Thromb Vasc Biol,* 21, 1220-5.

MITCHELL, J. R. A. & SCHWARTZ, C. J. (1965) *Arterial Disease.* Oxford, Blackwell.

MOLECULAR PROBES (2004) Acridine Orange - Product information Sheet. www.probes.com.

NAKASHIMA, Y., RAINES, E. W., PLUMP, A. S., BRESLOW, J. L. & ROSS, R. (1998) Upregulation of VCAM-1 and ICAM-1 at atherosclerosis-prone sites on the endothelium in the ApoE-deficient mouse. *Arterioscler Thromb Vasc Biol,* 18, 842-51.

NAKATSU, K., KAWAMOTO, J. H., BRIEN, J. F. & MARKS, G. S. (1988) A facile, reliable method for staining blood vessel endothelium. *J Pharmacol Methods,* 19, 149-54.

NAPOLI, C., DE NIGRIS, F., WILLIAMS-IGNARRO, S., PIGNALOSA, O., SICA, V. & IGNARRO, L. J. (2006) Nitric oxide and atherosclerosis: an update. *Nitric Oxide,* 15, 265-79.

NEREM, R. M., LEVESQUE, M. J. & CORNHILL, J. F. (1981) Vascular endothelial morphology as an indicator of the pattern of blood flow. *J Biomech Eng,* 103, 172-6.

NEREM, R. M. & SEED, W. A. (1983) Coronary artery geometry and its fluid mechanical implications. IN SCHETTLER, G., NEREM, R. M., SCHMID-SCHÖNBEIN, G. W., MÖRL, H. & DIEHM, C. (Eds.) *Fluid dynamics as a localizing factor for atherosclerosis.* Heidelberg, Springer-Verlag.

NEWMAN, P. J. (1997) The biology of PECAM-1. *Journal of Clinical Investigation,* 100, S25-S29.

NICHOLS, W. W. & O'ROURKE, M. F. (1998) *McDonald's Blood Flow in Arteries: Theoretic, experimental and clinical principles,* London, Arnold.

OKANO, M. & YOSHIDA, Y. (1993) Influence of shear stress on endothelial cell shapes and junction complexes at flow dividers of aortic bifurcations in cholesterol-fed rabbits. *Front Med Biol Eng,* 5, 95-120.

ORLANDI, A., MARCELLINI, M. & SPAGNOLI, L. G. (2000) Aging influences development and progression of early aortic atherosclerotic lesions in cholesterol-fed rabbits. *Arterioscler Thromb Vasc Biol,* 20, 1123-36.

OSHINSKI, J. N., CURTIN, J. L. & LOTH, F. (2006) Mean-average wall shear stress measurements in the common carotid artery. *J Cardiovasc Magn Reson,* 8, 717-22.

PARKER, K. H. & GIBSON, D. G. (2005) Cardiovascular fluid dynamics. *BSc Undergraduate Lecture notes - Imperial College London.*

PATTERSON, C. E., RHOADES, R. A. & GARCIA, J. G. (1992) Evans blue dye as a marker of albumin clearance in cultured endothelial monolayer and isolated lung. *J Appl Physiol,* 72, 865-73.

PEARSON, J. D., MORRELL, C. H., BRANT, L. J., LANDIS, P. K. & FLEG, J. L. (1997) Age-associated changes in blood pressure in a longitudinal study of healthy men and women *The journals of gerontology. Series A, Biological sciences and medical sciences,* 52, M177-M183.

PISSINATTI, A., FREITAS BURITY, C. H. & MANDARIM-DE-LACERDA, C. A. (2000) Morphological and morphometric age-related changes of the upper thoracic aorta in Leontopithecus (Lesson, 1840) (callitrichidae--primates). *J Med Primatol,* 29, 421-6.

REDDY, A. K., LI, Y. H., PHAM, T. T., OCHOA, L. N., TREVINO, M. T., HARTLEY, C. J., MICHAEL, L. H., ENTMAN, M. L. & TAFFET, G. E. (2003) Measurement of aortic input impedance in mice: effects of age on aortic stiffness. *Am J Physiol Heart Circ Physiol,* 285, H1464-70.

REIDY, M. A. & BOWYER, D. E. (1977) Scanning electron microscopy of arteries. The morphology of aortic endothelium in haemodynamically stressed areas associated with branches. *Atherosclerosis,* 26, 181-94.

REIDY, M. A. & LEVESQUE, M. J. (1977) A scanning electron microscopic study of arterial endothelial cells using vascular casts. *Atherosclerosis,* 28, 463-70.

REPIN, V. S., DOLGOV, V. V., ZAIKINA, O. E., NOVIKOV, I. D., ANTONOV, A. S., NIKOLAEVA, M. A. & SMIRNOV, V. N. (1984) Heterogeneity of endothelium in human aorta. A quantitative analysis by scanning electron microscopy. *Atherosclerosis,* 50, 35-52.

RESNICK, L. M., MILITIANU, D., CUNNINGS, A. J., PIPE, J. G., EVELHOCH, J. L. & SOULEN, R. L. (1997) Direct magnetic resonance determination of aortic distensibility in essential hypertension: relation to age, abdominal visceral fat, and in situ intracellular free magnesium. *Hypertension,* 30, 654-9.

RICHARDS, J. P. & WEINBERG, P. D. (2000) Distribution of disease around the aortocoeliac branch of white carneau pigeons at different ages. *Exp Mol Pathol,* 68, 95-103.

ROSS, R. (1993) The pathogenesis of atherosclerosis: a perspective for the 1990s. *Nature,* 362, 801-9.

SATO, M. & OHASHI, T. (2005) Biorheological views of endothelial cell responses to mechanical stimuli. *Biorheology,* 42, 421-41.

SCHACHNER, T., LAUFER, G. & BONATTI, J. (2006) In vivo (animal) models of vein graft disease. *Eur J Cardiothorac Surg,* 30, 451-63.

SCHOLZ, D. & SCHAPER, J. (1997) Platelet/endothelial cell adhesion molecule-1 (PECAM-1) is localized over the entire plasma membrane of endothelial cells. *Cell Tissue Res,* 290, 623-31.

SCHWARTZ, M. A. (2001) Integrin signaling revisited. *Trends Cell Biol,* 11, 466-70.

SEBKHI, A. & WEINBERG, P. D. (1994) Age-related variations in transport properties of the rabbit arterial wall near branches. *Atherosclerosis,* 106, 1-8.

SEBKHI, A. & WEINBERG, P. D. (1996) Effect of age on the pattern of short-term albumin uptake by the rabbit aortic wall near intercostal branch ostia. *Arterioscler Thromb Vasc Biol,* 16, 317-327.

SENIS, Y. A., RICHARDSON, M., TINLIN, S., MAURICE, D. H. & GILES, A. R. (1996) Changes in the pattern of distribution of von Willebrand factor in rat aortic endothelial cells following thrombin generation in vivo. *Br J Haematol,* 93, 195-203.

SHASBY, D. M., SHASBY, S. S., SULLIVAN, J. M. & PEACH, M. J. (1982) Role of endothelial cell cytoskeleton in control of endothelial permeability. *Circ Res,* 51, 657-61.

SIGMA-ALDRICH (2003) Accustain Harris Hematoxylin Solution (Procedure no.HHS) - Data Sheet. www.sigmaaldrich.com.

SINZINGER, H., SILBERBAUER, K. & AUERSWALD, W. (1980) Quantitative investigation of sudanophilic lesions around the aortic ostia of human fetuses, newborn and children. *Blood Vessels,* 17, 44-52.

SKANTZE, H. B., KAPLAN, J., BONDJERS, G., MANUCK, S. & PETTERSSON, K. (1998) Endothelial injury and leukocyte adherence in Hautchen preparations from coronary arteries and aorta of cynomolgus monkeys. *Atherosclerosis,* 136, 33-42.

SLOOP, G. D., PERRET, R. S., BRAHNEY, J. S. & OALMANN, M. (1998) A description of two morphologic patterns of aortic fatty streaks, and a hypothesis of their pathogenesis. *Atherosclerosis,* 141, 153-60.

SMALL, J. V. (1981) Organization of actin in the leading edge of cultured cells: influence of osmium tetroxide and dehydration on the ultrastructure of actin meshworks. *J Cell Biol,* 91, 695-705.

SMITH, J. M., MEINKOTH, J. H., HOCHSTATTER, T. & MEYERS, K. M. (1996) Differential distribution of von Willebrand factor in canine vascular endothlieum. *American Journal of Veterinary Research,* 57, 750-755.

STANTON, A. V. (1999) Haemodynamics, wall mechanics and atheroma: a clinician's perspective. *Proc Inst Mech Eng [H],* 213, 385-90.

STARMANS-KOOL, M. J., STANTON, A. V., ZHAO, S., XU, X. Y., THOM, S. A. & HUGHES, A. D. (2002) Measurement of hemodynamics in human carotid artery using ultrasound and computational fluid dynamics. *J Appl Physiol,* 92, 957-61.

STARY, H. C. (2000) Natural history and histological classification of atherosclerotic lesions: an update. *Arterioscler Thromb Vasc Biol,* 20, 1177-8.

STARY, H. C., BLANKENHORN, D. H., CHANDLER, A. B., GLAGOV, S., INSULL, W., JR., RICHARDSON, M., ROSENFELD, M. E., SCHAFFER, S. A., SCHWARTZ, C. J., WAGNER, W. D. & ET AL. (1992) A definition of the intima of human arteries and of its atherosclerosis-prone regions. A report from the Committee on Vascular

Lesions of the Council on Arteriosclerosis, American Heart Association. *Circulation,* 85, 391-405.

STARY, H. C., CHANDLER, A. B., DINSMORE, R. E., FUSTER, V., GLAGOV, S., INSULL, W., JR., ROSENFELD, M. E., SCHWARTZ, C. J., WAGNER, W. D. & WISSLER, R. W. (1995) A definition of advanced types of atherosclerotic lesions and a histological classification of atherosclerosis. A report from the Committee on Vascular Lesions of the Council on Arteriosclerosis, American Heart Association. *Arterioscler Thromb Vasc Biol,* 15, 1512-31.

STARY, H. C., CHANDLER, A. B., GLAGOV, S., GUYTON, J. R., INSULL, W., JR., ROSENFELD, M. E., SCHAFFER, S. A., SCHWARTZ, C. J., WAGNER, W. D. & WISSLER, R. W. (1994) A definition of initial, fatty streak, and intermediate lesions of atherosclerosis. A report from the Committee on Vascular Lesions of the Council on Arteriosclerosis, American Heart Association. *Circulation,* 89, 2462-78.

STAUGHTON, T. J., LEVER, M. J. & WEINBERG, P. D. (2001) Effect of altered flow on the pattern of permeability around rabbit aortic branches. *Am J Physiol Heart Circ Physiol,* 281, H53-9.

STAUGHTON, T. J. & WEINBERG, P. D. (2004) Effect of time of day and rabbit strain on patterns of aortic wall permeability. *Exp Physiol,* 89, 109-18.

STEIN, Y. & STEIN, O. (2001) Does therapeutic intervention achieve slowing of progression or bona fide regression of atherosclerotic lesions? *Arterioscler Thromb Vasc Biol,* 21, 183-8.

STONE, P. H., COSKUN, A. U., KINLAY, S., CLARK, M. E., SONKA, M., WAHLE, A., ILEGBUSI, O. J., YEGHIAZARIANS, Y., POPMA, J. J., ORAV, J., KUNTZ, R. E. & FELDMAN, C. L. (2003) Effect of endothelial shear stress on the progression of coronary artery disease, vascular remodeling, and in-stent restenosis in humans: in vivo 6-month follow-up study. *Circulation,* 108, 438-44.

SUO, J., FERRARA, D. E., SORESCU, D., GULDBERG, R. E., TAYLOR, W. R. & GIDDENS, D. P. (2007) Hemodynamic shear stresses in mouse aortas: implications for atherogenesis. *Arterioscler Thromb Vasc Biol,* 27, 346-51.

TAYLOR, C. A., CHENG, C. P., ESPINOSA, L. A., TANG, B. T., PARKER, D. & HERFKENS, R. J. (2002) In vivo quantification of blood flow and wall shear stress in the human abdominal aorta during lower limb exercise. *Ann Biomed Eng,* 30, 402-8.

TAYLOR, C. A., HUGHES, T. J. & ZARINS, C. K. (1998) Finite element modeling of three-dimensional pulsatile flow in the abdominal aorta: relevance to atherosclerosis. *Ann Biomed Eng,* 26, 975-87.

TRAUB, O. & BERK, B. C. (1998) Laminar shear stress: mechanisms by which endothelial cells transduce an atheroprotective force. *Arterioscler Thromb Vasc Biol,* 18, 677-85.

TRAUB, O., ISHIDA, T., ISHIDA, M., TUPPER, J. C. & BERK, B. C. (1999) Shear stress-mediated extracellular signal-regulated kinase activation is regulated by sodium in endothelial cells. Potential role for a voltage-dependent sodium channel. *J Biol Chem,* 274, 20144-50.

TRUSKEY, G. A., ROBERTS, W. L., HERRMANN, R. A. & MALINAUSKAS, R. A. (1992) Measurement of endothelial permeability to 125I-low density lipoproteins in rabbit arteries by use of en face preparations. *Circ Res,* 71, 883-97.

UEMATSU, M., KITABATAKE, A., TANOUCHI, J., DOI, Y., MASUYAMA, T., FUJII, K., YOSHIDA, Y., ITO, H., ISHIHARA, K., HORI, M. & ET AL. (1991) Reduction of endothelial microfilament bundles in the low-shear region of the canine aorta. Association with intimal plaque formation in hypercholesterolemia. *Arterioscler Thromb,* 11, 107-15.

VAITKEVICIUS, P. V., FLEG, J. L., ENGEL, J. H., O'CONNOR, F. C., WRIGHT, J. G., LAKATTA, L. E., YIN, F. C. & LAKATTA, E. G. (1993) Effects of age and aerobic capacity on arterial stiffness in healthy adults. *Circulation,* 88, 1456-62.

VAN HAPEREN, R., CHENG, C., MEES, B. M., VAN DEEL, E., DE WAARD, M., VAN DAMME, L. C., VAN GENT, T., VAN AKEN, T., KRAMS, R., DUNCKER, D. J. & DE CROM, R. (2003) Functional expression of endothelial nitric oxide synthase fused to green fluorescent protein in transgenic mice. *Am J Pathol,* 163, 1677-86.

VAN TEEFFELEN, J. W., BRANDS, J., STROES, E. S. & VINK, H. (2007) Endothelial glycocalyx: sweet shield of blood vessels. *Trends Cardiovasc Med,* 17, 101-5.

VIRMANI, R., KOLODGIE, F. D., BURKE, A. P., FARB, A. & SCHWARTZ, S. M. (2000) Lessons from sudden coronary death: a comprehensive morphological classification scheme for atherosclerotic lesions. *Arterioscler Thromb Vasc Biol,* 20, 1262-75.

WAGENVOORT, C. A. (1954) The significance of arterial rings for the blood circulation. *Acta Anat (Basel),* 21, 70-99.

WANG, N., MIAO, H., LI, Y. S., ZHANG, P., HAGA, J. H., HU, Y., YOUNG, A., YUAN, S., NGUYEN, P., WU, C. C. & CHIEN, S. (2006) Shear stress regulation of Kruppel-like factor 2 expression is flow pattern-specific. *Biochem Biophys Res Commun,* 341, 1244-51.

WANG, S., OKANO, M. & YOSHIDA, Y. (1991) Ultrastructure of endothelial cells and lipid deposition on the flow dividers of brachiocephalic and left subclavian arterial bifurcations of the rabbit aorta. *J Jpn Atheroscler Soc,* 19, 1089-1100.

WANG, Y., MIAO, H., LI, S., CHEN, K. D., LI, Y. S., YUAN, S., SHYY, J. Y. & CHIEN, S. (2002) Interplay between integrins and FLK-1 in shear stress-induced signaling. *Am J Physiol Cell Physiol,* 283, C1540-7.

WARD, M. R., PASTERKAMP, G., YEUNG, A. C. & BORST, C. (2000) Arterial remodeling. Mechanisms and clinical implications. *Circulation,* 102, 1186-91.

WEINBAUM, S., TARBELL, J. M. & DAMIANO, E. R. (2007) The structure and function of the endothelial glycocalyx layer. *Annu Rev Biomed Eng,* 9, 121-67.

WEINBERG, P. D. (2002) Disease patterns at arterial branches and their relation to flow. *Biorheology,* 39, 533-7.

WEINBERG, P. D. (2004) Rate-limiting steps in the development of atherosclerosis: the response-to-influx theory. *J Vasc Res,* 41, 1-17.

WEINBERG, P. D. & ETHIER, R. C. (2007) Twenty-fold difference in hemodynamic wall shear stress between murine and human aortas. *J Biomech,* 40, 1594-8.

WILLIAMS, P. L., WARWICK, R., DYSON, M. & BANNISTER, L. H. (Eds.) (1989) *Gray's Anatomy,* London, Churchill Livingstone.

WORLD HEART ORGANISATION (2000) WHO World Health Report. www.worldheart.org.

XU, X. Y., LONG, Q., COLLINS, M. W., BOURNE, M. & GRIFFITH, T. M. (1999) Reconstruction of blood flow patterns in human arteries. *Proc Inst Mech Eng [H],* 213, 411-21.

YOSHIDA, K. & SUGIMOTO, K. (1996) Morphological and cytoskeletal changes in endothelial cells of vein grafts under arterial hemodynamic conditions in vivo. *J Electron Microsc (Tokyo),* 45, 428-35.

ZARINS, C. K., GIDDENS, D. P., BHARADVAJ, B. K., SOTTIURAI, V. S., MABON, R. F. & GLAGOV, S. (1983) Carotid bifurcation atherosclerosis. Quantitative correlation of plaque localization with flow velocity profiles and wall shear stress. *Circ Res,* 53, 502-14.

ZHANG, S. H., REDDICK, R. L., PIEDRAHITA, J. A. & MAEDA, N. (1992) Spontaneous hypercholesterolemia and arterial lesions in mice lacking apolipoprotein E. *Science,* 258, 468-71.

ZHAO, S., SUCIU, A., ZIEGLER, T., MOORE, J. E., JR., BURKI, E., MEISTER, J. J. & BRUNNER, H. R. (1995) Synergistic effects of fluid shear stress and cyclic circumferential stretch on vascular endothelial cell morphology and cytoskeleton. *Arterioscler Thromb Vasc Biol,* 15, 1781-6.

Appendices

Appendix A – Results Tables

See supplementary CD.

Appendix B - Tukey matrices

See supplementary CD.

Appendix C – Macro Codes

See supplementary CD.

Macro-1 - Editing data from confocal images of propidium iodide stained nuclei, from mice

Macro-2 - Editing propidium iodide stained EStAR images, at 20x (magnification) - dividing results into 100um regions

Macro-3 - Counting nuclei

Macro-4 - Colour coding Excells in LW ratio maps for rabbits

Macro-5 - Colour coding Excells in angle of orientation maps for rabbits, mice and pigs

Macro-6 - Colour coding Excells in length maps for rabbits (values in microns)

Macro-7 - Colour coding Excells in width maps for rabbits (values in microns)

Macro-8 - Colour coding Excells in area maps for rabbits, mice and pigs

Macro-9 - Colour coding Excells in LW ratio maps for mice and pigs

Macro-10 - Colour coding Excells in nuclear density maps for mice and pigs

Macro-11 - Removing Excells from maps when neighbouring Excell contains no value

Macro-12 - Editing data from images of silver stained EStARs, at 20x (magnification) - dividing results into 100um regions.